Imperial College London

Comparing the blast tolerance of different composite structures

Mark Kelly

Department of Mechanical Engineering

Imperial College London

A thesis submitted for the degree of Doctor of Philosophy

of Imperial College London and the Diploma of Imperial College

August 2016

Acknowledgements

There are many people who have helped me along the way in completing this PhD, and first and foremost my thanks go to my supervisors John Dear and Hari Arora who have guided me along the way. My thanks also go to Paul Hooper who has provided a lot of technical expertise to the project, and Paolo Del Linz, Alex Worley, Michael Kaye, Joanna Li-Mayer and Vim Patel who have all helped out with my blast testing and made it possible for me to successfully complete the blast trials. I have learnt a great deal from all of you, and your help has always been much appreciated.

Secondly, my thanks go to Dr Yapa Rajapakse in the Office of Naval Research (ONR) for sponsoring this PhD and to the Centre for the Protection of National Infrastructure (CPNI), for funding the blast trials. I am grateful to DNV GL for allowing me to use their test site at RAF Spadeadam for the blast trials, and acknowledgments are due for the hard work of everyone there who were critical to the success of the tests. Specifically I would like to thank Ian Graham and Paul Cronin for organising the blast trials and your help in performing them. Thanks are also due to LaVision and Slowmo Camera Hire for loaning high speed cameras to me for air blast tests, and I would like to acknowledge the support of Rob Wood from GOM UK for his continued support in digital image correlation.

I am also grateful to everyone at Imperial for their continued support during my PhD. Amit, Tony, and Phil in the workshop have taught me huge amounts about machining and have always been willing to help me out when I needed it. I would also like to thank Suresh for all of his help in the lab over the three years. Thanks are due to everyone

in both offices for your input both academically and socially. Yatish and Tino for providing breakfast motivation to wake up to write my thesis, Declan for all of his technical debates and James for his sense of humour. I would also like to thank Ian for his skiing company, Idris for his help with Abaqus and always having a Natwest card reader, and Tom for his rewarding conversation.

Thanks must also go out to my fellow wardening friends made in Paragon and Wilson House over the three years, you have really provided me with a great home life away from the office, and for this I am indebted. Planning events and dealing with unpredictable situations in the middle of the night has provided me with unique experiences which I couldn't have gained anywhere else. I will always look back on even the stressful call-outs fondly!

Huge thanks are due to my parents, who have supported me in achieving all of my goals, and without whom I would not be in the position I am today. I am grateful to my Dad for all of his engineering and design help over the years, and to my Mum for her unfaltering support and encouragement. Finally, and by no means least importantly, I would like to thank my wonderful girlfriend Kirsty, who has lived and breathed my PhD as much as me. Your companionship in all of our endeavours makes them both manageable and enjoyable. The support of all three of you has made this journey much easier.

Abstract

Large surface ships have traditionally used steel for their construction, which provides good blast resistance and predictable behaviour in use. This research project, however, considered the use of polymeric foam core sandwich panels for the construction of ship hulls, with the intention of reducing the radar signature of the vessel; increasing the maximum speed; reducing fuel consumption; and providing control over desired mechanical properties for specific applications. This project specifically considered the resistance of the sandwich composites to non-contact explosives, specifically sea mines and areal blast.

This research project firstly presents air blast testing performed on polymeric foam core sandwich panels with glass fibre face-sheets. The foam polymer type, the effect of the face-sheet material and the effect of using a graded density foam core for blast wave attenuation were all investigated. When subjected to air blast loading it was found that by grading the core density a smoother back face-sheet displacement was witnessed. This was a significant discovery as protecting the back face-sheet is key to maintaining structural integrity of the ship hulls. In a comparison of foam polymers in the cores of the sandwich panel it was concluded that styrene acrylonitrile offers optimum fracture and adhesion properties. Furthermore, it was found that by interleaving high modulus polypropylene fibres between the glass fibre front face-sheets, front face-sheet cracking and delamination can be prevented, restricting water ingress into the sandwich panel if it were subjected to blast loading. Advances in using 3D high speed imaging for digital image correlation were also achieved, whereby the results were used to estimate core shear strain during deformation, and the kinetic energy

and strain energy in the sandwich panel were estimated by comparison with blast wave pressure simulations.

The residual flexural and edgewise compression properties of the air blasted sandwich panels were then determined to calculate the flexural stiffness and strength and edgewise stiffness and strength with varying damage. It was found that the construction of the sandwich panel properties were unaffected by the construction, and that debonding of the face-sheets and the core was the key performance reducing damage mechanism. Residual properties were determined for the sandwich materials, with the intention that these could be used in simulations to predict performance of the ship hulls after successfully withstanding a blast.

In underwater blast scenarios it was discovered that using a graded density foam core reduced the central deflection of the sandwich panel due to the increase in energy absorption due to crushing of the stepwise increase in foam core density. This effect was greater in carbon fibre sandwich panels than in glass fibre panels, due to the increased stiffness of the face-sheets. The central deflection was calculated by averaging the strains measured on the two face-sheets with electronic strain gauges, which was a novel technique and took advantage of the symmetry present in the square sandwich panels.

As the focus of this research project was on foam core properties, the polymeric foam materials were characterised in quasi-static and dynamic tension, and quasi-static and dynamic compression. Dynamic compression tests were performed using a split-Hopkinson pressure bar which was designed specifically for testing low density foam materials. Stress equilibrium was achieved in these tests using a textured polypropylene pulse shaper. Stress equilibrium was checked for by performing high speed digital image correlation during deformation, to ensure that core crushing did not begin at the incident bar.

The final stage of the research project was to construct finite element simulations of the air blast tests, using the polymeric foam material

properties measured in the quasi-static and dynamic tests. A large number of simulations were performed with varying charge sizes and stand-off distances, to determine a combination of blast peak pressure and impulse values at which the sandwich panels failed. Developments were achieved in the use of a brittle cracking material model and the effect of the boundary conditions on the simulations was also studied.

This research project furthered the understanding of sandwich composite materials to air and underwater blast loading. Advancements were made into the use of stepwise graded density foam cores and in characterising foams at dynamic tensile and compressive rates. A major conclusion of the project is that the use of graded density cores can be utilised to prevent damage of the sandwich panel on the rear side and can be used to absorb blast energy due to core crushing. The results of the project aid in simulating the response of composite ship hulls to blast loading and better predict the usability of the ships after being subjected to a blast event.

Declarations

I, the author, declare that this work is my own unless otherwise stated, and any other contributors are appropriately acknowledged.

The copyright of this thesis rests with the author and is made available under a Creative Commons Attribution Non-Commercial No Derivatives licence. Researchers are free to copy, distribute or transmit the thesis on the condition that they attribute it, that they do not use it for commercial purposes and that they do not alter, transform or build upon it. For any reuse or redistribution, researchers must make clear to others the licence terms of this work

Contents

Contents vii

List of Figures xiii

List of Tables xxvii

Nomenclature xxix

Acronyms xxxiv

1 Introduction 1

1.1 Composites in Naval Vessels 2
1.2 Blast Loading of Sandwich Composites 5
1.3 Research Objectives 5
1.4 Thesis Outline 9
1.4.1 Literature Review 9
1.4.2 Full Scale Air Blast Testing 9
1.4.3 Strength After Blast Testing 10
1.4.4 Full Scale Underwater Blast Testing 10
1.4.5 Foam Characterisation 11
1.4.6 Finite Element Modeling 11
1.4.7 Conclusions 11
1.5 Published Literature 12
1.5.1 Book Chapter 12
1.5.2 Journal Articles 12

2 Literature Review **13**
2.1 Introduction . . . 13
2.2 Blast Resistance of Composite Materials . . . 14
2.3 Strength After Blast . . . 18
2.4 Foam Characterisation . . . 21
2.4.1 Core and Face-Sheet Interface Properties . . . 22
2.4.2 Split-Hopkinson Pressure Bar Compression Tests . . . 24
2.5 Simulating Blast of Composites . . . 25
2.6 Summary . . . 28

3 Full Scale Air Blast Testing **30**
3.1 Introduction . . . 30
3.2 Materials . . . 31
3.2.1 Face-Sheets . . . 31
3.2.2 Polymeric Foams . . . 37
3.3 Experimental Methods . . . 39
3.3.1 Blast Wave Modelling . . . 39
3.3.2 Air Blast Testing . . . 40
3.3.2.1 Analytical Prediction . . . 42
3.3.2.2 Blast Test Design . . . 43
3.3.3 Digital Image Correlation . . . 47
3.3.3.1 Digital Image Correlation Data Processing . . . 52
3.3.4 Post-Blast Damage Assessment . . . 55
3.4 Results . . . 58
3.4.1 Blast Pressure . . . 58
3.4.2 Out-of-Plane Displacement . . . 62
3.4.2.1 Foam Polymer Comparison . . . 62
3.4.2.2 Graded Density Core . . . 65
3.4.2.3 Compliant Face-Sheet . . . 67
3.4.3 Core Shear Strain . . . 70
3.4.3.1 Foam Polymer Comparison . . . 70
3.4.3.2 Graded Density Core . . . 71
3.4.3.3 Compliant Face-Sheet . . . 73

3.4.4 Energy Balance . . . 73
3.4.4.1 Foam Polymer Comparison . . . 74
3.4.4.2 Graded Density Core . . . 75
3.4.4.3 Compliant Face-Sheet . . . 75
3.4.5 Post-Blast Damage Assessment . . . 75
3.4.5.1 Foam Polymer Comparison . . . 79
3.4.5.2 Graded Density Core . . . 79
3.4.5.3 Compliant Face-Sheet . . . 80
3.5 Discussion . . . 86
3.5.1 Air3D and Digital Image Correlation . . . 86
3.5.2 Out-of-Plane Displacement . . . 87
3.5.3 Core Shear Strain . . . 89
3.5.4 Energy Balance . . . 90
3.5.5 Post-Blast Damage Assessment . . . 91
3.6 Conclusion . . . 92

4 Strength After Blast Testing **96**
4.1 Introduction . . . 96
4.2 Materials . . . 97
4.3 Experimental Methods . . . 98
4.3.1 Flexural Testing . . . 98
4.3.1.1 Data Processing . . . 99
4.3.2 Edgewise Compression Testing . . . 101
4.3.2.1 Data Processing . . . 102
4.3.3 Damage Quantification . . . 103
4.4 Results . . . 104
4.4.1 Flexural Testing . . . 104
4.4.1.1 Rate Effects . . . 104
4.4.1.2 Stiffness . . . 107
4.4.1.3 Strength . . . 113
4.4.2 Edgewise Compression Testing . . . 116
4.4.2.1 Rate Effects . . . 116
4.4.2.2 Stiffness . . . 118

4.4.2.3 Strength . . . 121
4.5 Discussion . . . 125
4.5.1 Flexural Tests . . . 125
4.5.2 Edgewise Compression Tests . . . 128
4.6 Conclusion . . . 129

5 Full Scale Underwater Blast Testing 131
5.1 Introduction . . . 131
5.2 Materials . . . 132
5.3 Experimental Methods . . . 137
5.3.1 Underwater Blast Testing . . . 137
5.3.2 Pressure Gauges . . . 139
5.3.3 Electronic Strain Gauges . . . 140
5.3.4 Data Processing . . . 142
5.4 Results . . . 145
5.4.1 Selecting and Filtering Raw Data . . . 145
5.4.2 Pressure Traces . . . 146
5.4.3 Strain Measurements . . . 149
5.4.3.1 Single Core GFRP Sandwich Panel . . . 149
5.4.3.2 Graded Core GFRP Sandwich Panel . . . 155
5.4.3.3 Single Core CFRP Sandwich Panel . . . 161
5.4.3.4 Graded Core CFRP Sandwich Panel . . . 166
5.4.4 Out-Of-Plane Displacement Calculations . . . 171
5.4.4.1 Single Core GFRP Sandwich Panel . . . 172
5.4.4.2 Graded Core GFRP Sandwich Panel . . . 172
5.4.4.3 Single Core CFRP Sandwich Panel . . . 176
5.4.4.4 Graded Core CFRP Sandwich Panel . . . 176
5.5 Discussion . . . 179
5.5.1 Effect of Using a Graded Density Core . . . 179
5.5.2 The Effect of Glass Versus Carbon Fibre Face-Sheets . . . 180
5.6 Conclusion . . . 181

6 Foam Characterisation **185**
6.1 Introduction . . . 185
6.2 Quasi-Static Compression . . . 186
6.2.1 Experimental Methods . . . 186
6.2.2 Results . . . 189
6.2.2.1 SAN Foam . . . 189
6.2.2.2 PVC Foam . . . 190
6.2.2.3 PMI Foam . . . 193
6.3 Dynamic Compression Using a Split-Hopkinson Pressure Bar . . . 196
6.3.1 Experimental Methods . . . 196
6.3.1.1 Digital Image Correlation . . . 199
6.3.1.2 Test Parameters . . . 199
6.3.2 Results . . . 202
6.3.2.1 Raw Data . . . 202
6.3.2.2 Strain Equilibrium . . . 203
6.3.2.3 Compressive Modulus . . . 205
6.3.2.4 Crushing Strength . . . 206
6.4 Quasi-Static Tension . . . 209
6.4.1 Experimental Methods . . . 209
6.4.2 Results . . . 209
6.4.2.1 SAN Foam . . . 209
6.4.2.2 PVC Foam . . . 210
6.4.2.3 PMI Foam . . . 212
6.4.3 Dynamic Tension . . . 216
6.4.3.1 Experimental Methods . . . 216
6.4.4 Results . . . 216
6.4.4.1 SAN Foam . . . 216
6.4.4.2 PVC Foam . . . 219
6.4.4.3 PMI Foam . . . 221
6.5 Discussion . . . 224
6.5.1 Quasi-Static Properties . . . 224
6.5.2 Split-Hopkinson Pressure Bar . . . 225
6.5.3 Dynamic Tension . . . 228

6.6 Conclusion . . . 229

7 Finite Element Modelling **231**
7.1 Introduction . . . 231
7.2 Simulation Methods . . . 232
7.2.1 Finite Element Mesh . . . 232
7.2.2 Material Models . . . 233
7.2.3 Simulation Parameters and Results Processing . . . 236
7.2.4 Results . . . 237
7.2.4.1 Boundary Conditions . . . 237
7.2.4.2 Elastic Simulation Results . . . 241
7.2.4.3 Damage Simulation Results . . . 244
7.3 Discussion . . . 251
7.4 Conclusion . . . 252

8 Conclusions **254**
8.1 Full Scale Air Blast Testing . . . 255
8.2 Strength After Blast Testing . . . 257
8.3 Full Scale Underwater Blast Testing . . . 259
8.4 Foam Characterisation . . . 260
8.5 Finite Element Modelling . . . 261
8.6 Future Work . . . 262
8.7 Research Impact . . . 263

References **266**

A - Digital Image Correlation Contour Plots **280**

B - Air Blast Digital Image Correlation Uncertainty Analysis **282**

List of Figures

1.1 Photographs of the Royal Navy Type 45 destroyer composite radar dome (left), from [1], and the completed vessel (right), from [2]. . . 3
1.2 Photographs of the US Navy Zumwalt Class destroyer composite deck housing (left), from [3], and the completed vessel (right), from [4]. 3
1.3 Deflection schematics of a polymeric foam sandwich composite subjected to a) air blast loading; and b) underwater blast loading. . . . 6

3.1 Schematic of the layup method of the sandwich panels. 32
3.2 Schematic of the layup of the single core sandwich panels, incorporating a 40 mm thick foam core, with two plies of quadriaxial QE1200 GFRP either side. 34
3.3 Schematic of the layup of the graded core sandwich panel, incorporating three 10 mm thick SAN foam layers, with two plies of quadriaxial QE1200 GFRP either side. 34
3.4 Schematic of the layup of the single PVC core sandwich panel, incorporating a 40 mm thick foam core, with two plies of quadriaxial QE1200 GFRP either side and Innegra PP plies interleaved between the glass plies in the front face-sheet. 35
3.5 Air blast wave loading on a structure. 41
3.6 Schematic of the steel front of the test cubicle. 45
3.7 Schematic of the test cubicle, showing the concrete culverts. 45
3.8 Schematic of the front of the test cubicle and the test panels. Also shown is the clamping arrangement of the sandwich panels onto the cubicle front. 46

3.9 Schematic of the blast test layout. 46
3.10 Schematic of the reflected pressure gauge. 46
3.11 Schematic of the static pressure gauge. 47
3.12 Top and bottom camera images of the CC20 calibration cross. . . . 49
3.13 Pixel filter order in a Bayer sensor. 50
3.14 Schematic of the high speed camera equipment inside the test cubicle. 52
3.15 Calculation of the camera locations for 3D DIC. 53
3.16 Diagram showing the definition of α and β in calculating the core shear strain. 54
3.17 Damage mapping of a section of the PVC Airex C70.90 blast panel. 57
3.18 Post-blast section dimension key. 57
3.19 Mesh convergence study using element sizes of 25 mm, 50 mm, 75 mm, 100 mm and 150 mm, for the Air3D blast wave simulation. 59
3.20 Comparison of the pressure calculated at the gauge location using the Friedlander equation and using Air3D, and the pressure measured during the first blast test. 60
3.21 Pressure distribution across the front face of the sandwich panel as a percentage of the pressure at the reflected gauge location. 60
3.22 Frames taken from an external camera during blast testing of the PMI Rohacell 110SL sandwich panel and the PP fibre Innegra front face-sheet sandwich panel. Also shown is the time from detonation, at the top of each frame. 61
3.23 Contour plots of out-of-plane displacement of the 40 mm thick PVC Airex C70.90 foam core sandwich panel. 63
3.24 Out-of-plane displacement of the horizontal centre section of the 40 mm thick PVC Airex C70.90 foam core sandwich panel for a) the initial displacement; and b) the rebound. 64
3.25 Out-of-plane displacement of the horizontal centre section of the 40 mm thick SAN Corecell M100 foam core sandwich panel for a) the initial displacement; and b) the rebound. 64
3.26 Out-of-plane displacement of the horizontal centre section of the 40 mm thick PMI Rohacell SL110 foam core sandwich panel for a) the initial displacement; and b) the rebound. 65

3.27 Out-of-plane displacement of the centre, and left and right quarters of the 40 mm thick PVC Airex C70.90 foam core sandwich panel. . 66
3.28 Out-of-plane displacement of the centre, and left and right quarters of the 40 mm thick SAN Corecell M100 foam core sandwich panel. . 66
3.29 Out-of-plane displacement of the centre, and left and right quarters of the 40 mm thick PMI Rohacell SL110 foam core sandwich panel. 67
3.30 Out-of-plane displacement of the horizontal centre section of the 30 mm thick SAN graded density foam core sandwich panel for a) the initial displacement; and b) the rebound. 68
3.31 Out-of-plane displacement of the centre, and left and right quarters of the 30 mm thick SAN graded density foam core sandwich panel. 68
3.32 Out-of-plane displacement of the centre, and left and right quarters of the 40 mm thick PVC Airex C70.90 core sandwich panel, with compliant PP plies in the front face-sheet. 69
3.33 Out-of-plane displacement of the horizontal centre section of the 40 mm thick PVC Airex C70.90 core sandwich panel, with compliant PP plies in the front face-sheet for a) the initial displacement; and b) the rebound. 70
3.34 Shear strain in the core of the 40 mm thick PVC Airex C70.90 core sandwich panel, where the black lines are up until failure, and the red lines are post-failure. 71
3.35 Shear strain in the core of the 40 mm thick SAN Corecell M100 core sandwich panel, where the black lines are up until failure, and the red lines are post-failure. 72
3.36 Shear strain in the core of the 40 mm thick PMI Rohacell 110SL core sandwich panel, where the black lines are up until failure, and the red lines are post-failure. 72
3.37 Shear strain in the core of the 30 mm thick SAN Corecell graded core sandwich panel, where the black lines are up until failure, and the red lines are post-failure. 73

3.38 Shear strain in the core of the 40 mm thick PVC Airex C70.90 core sandwich panel, containing compliant PP plies in the front face-sheet, where the black lines are up until failure, and the red lines are post-failure. 74
3.39 Cumulative work done, kinetic energy and strain energy in the 40 mm thick PVC Airex C70.90 core sandwich panel. 76
3.40 Cumulative work done, kinetic energy and strain energy in the 40 mm thick SAN Corecell M100 core sandwich panel. 76
3.41 Cumulative work done, kinetic energy and strain energy in the 40 mm thick PMI Rohacell 110SL core sandwich panel. 77
3.42 Cumulative work done, kinetic energy and strain energy in the 30 mm thick SAN Corecell graded core sandwich panel. 77
3.43 Cumulative work done, kinetic energy and strain energy in the 40 mm thick PVC Airex C70.90 core sandwich panel, containing compliant PP plies in the face-sheet. 78
3.44 Damage map of the 40 mm thick PVC Airex C70.90 foam core sandwich panel, showing a) debonding between the back face-sheet and core; b) cracks in the foam core and c) debonding between the front face-sheet and core. 81
3.45 Damage map of the 40 mm thick SAN Corecell M100 foam core sandwich panel, showing a) debonding between the back face-sheet and core; b) cracks in the foam core and c) debonding between the front face-sheet and core. 81
3.46 Damage map of the 30 mm thick SAN Corecell M130 foam core sandwich panel, showing a) debonding between the back face-sheet and core; b) cracks in the foam core and c) debonding between the front face-sheet and core. 82
3.47 Damage map of the 30 mm thick SAN Corecell graded foam core sandwich panel, showing a) debonding between the back face-sheet and core; b) cracks in the foam core and c) debonding between the front face-sheet and core. 82

3.48 Damage map of the 40 mm thick PVC Airex C70.90 foam core sandwich panel, with compliant PP plies in the front face-sheet, showing a) debonding between the back face-sheet and core; b) cracks in the foam core and c) debonding between the front face-sheet and core. 84
3.49 Central out-of-plane displacement of the five air blast tested sandwich panels for which DIC data was available. 88

4.1 Locations of the flexural; edgewise compression; and flatwise compression test samples, cut from the air blast tested sandwich panels. 98
4.2 Schematic of the three point bending test method. 100
4.3 Schematic of the edgewise compression test method. 102
4.4 Effective stiffness of 30 mm thick SAN Corecell M130 core sandwich beams, tested at high, medium and quasi-static speeds. All of the test samples contained no visible damage prior to flexural testing. . 105
4.5 a) Direct face-sheet stress and b) core shear stress at failure of 30 mm thick SAN Corecell M130 core sandwich beams, tested at high, medium and quasi-static speeds. All of the test samples contained no visible damage prior to flexural testing. 105
4.6 a) Quasi-static and b) high speed compressive strain of two 30 mm thick SAN Corecell M130 core sandwich beams. These test samples contained no visible damage prior to flexural testing. 106
4.7 Effective stiffness versus visible damage for the 30 mm thick SAN Corecell graded core sandwich panel, tested at three different rates. 108
4.8 Effective Stiffness versus visible damage for the 40 mm thick SAN Corecell M100 core sandwich panel, tested at two different rates. . . 110
4.9 Effective stiffness versus visible damage for the 40 mm thick PVC Airex C70.90 core sandwich panel, tested at two different rates. . . 111
4.10 Effective stiffness versus visible damage for the 40 mm thick PVC Airex C70.90 sandwich panel with PP front face-sheet fibres, tested at two different rates. 112

4.11 a) Maximum shear stress and b) maximum direct face-sheet stress versus visible damage for the 30 mm thick SAN Corecell graded core sandwich panel, tested at three different rates. 113
4.12 a) Maximum shear stress and b) maximum direct face-sheet stress versus visible damage for the 40 mm thick SAN Corecell M100 core sandwich panel, tested at two different rates. 114
4.13 a) Maximum shear stress and b) maximum direct face-sheet stress versus visible damage for the 40 mm thick PVC Airex C70.90 core sandwich panel, tested at two different rates. 115
4.14 a) Maximum shear stress and b) maximum direct face-sheet stress versus visible damage for the 40 mm thick PVC Airex C70.90 sandwich panel with PP front face-sheet fibres, tested at two different rates. 115
4.15 Compressive modulus of 30 mm thick SAN Corecell M130 core sandwich beams, tested at medium and quasi-static speeds. All of the test samples contained no visible damage prior to edgewise compression testing. 117
4.16 Compressive modulus of 30 mm thick SAN graded core sandwich beams, tested at medium and quasi-static speeds. All of the test samples contained no visible damage prior to edgewise compression testing. 117
4.17 Maximum in-plane stress of 30 mm thick SAN Corecell M130 core sandwich beams, tested at medium and quasi-static speeds. All of the test samples contained no visible damage prior to edgewise compression testing. 118
4.18 Compressive strength of 30 mm thick SAN Corecell graded core sandwich beams, tested at medium and quasi-static speeds. All of the test samples contained no visible damage prior to edgewise compression testing. 119
4.19 Compressive modulus versus visible damage for the 30 mm thick SAN Corecell M130 core sandwich panel, tested at two different rates. 120

4.20 Compressive modulus versus visible damage for the 30 mm thick SAN graded density core sandwich panel, tested at two different rates. . . . 120
4.21 Compressive modulus versus visible damage for the 40 mm thick SAN Corecell M100 core sandwich panel, tested at two different rates. 121
4.22 Compressive modulus versus visible damage for the 40 mm thick PVC Airex C70.90 core sandwich panel, tested at two different rates. 122
4.23 Compressive modulus versus visible damage for the 40 mm thick PVC Airex C70.90 core sandwich panel with Innegra PP plies in the front face-sheet, tested at two different rates. . . . 122
4.24 Compressive strength versus visible damage for the 30 mm thick SAN Corecell M130 core sandwich panel, tested at two different rates. 123
4.25 Compressive strength versus visible damage for the 30 mm thick SAN Corecell graded density core sandwich panel, tested at two different rates. . . . 123
4.26 Compressive strength versus visible damage for the 40 mm thick SAN Corecell M100 core sandwich panel, tested at two different rates. 124
4.27 Compressive strength versus visible damage for the 40 mm thick PVC Airex C70.90 core sandwich panel, tested at two different rates. 124
4.28 Compressive strength versus visible damage for the 40 mm thick PVC Airex C70.90 core sandwich panel with Innegra PP plies in the front face-sheet, tested at two different rates. . . . 125

5.1 Schematic of the layup of the single core sandwich panels. . . . 133
5.2 Schematic of the layup of the graded core sandwich panels. . . . 135
5.3 Schematic of the underwater blast test frame. . . . 138
5.4 Schematic of the underwater blast test charge and pressure gauge layout. . . . 139
5.5 Schematic of the reflected pressure gauge. . . . 140
5.6 Locations of the 30 electronic strain gauges attached to the sandwich panels. . . . 142

5.7 Photographs of the underwater blast test setup showing a) the single core CFRP test panel before the charge was assembled; b) the single core CFRP sandwich panel with the charge assembled; and c) the whole test setup of the single core GFRP sandwich panel test, before the charge was assembled. 143
5.8 Schematic of the iterative method for calculating out-of-plane displacement. 144
5.9 Raw strain gauge data versus time, and a moving average filter applied. Detonation is shown as a spike in the data, due to radiation from the charge. 145
5.10 Side-on, reflected and adjusted pressure traces recorded for a) the single core GFRP test; b) the graded core GFRP test; c) the single core CFRP test; and d) the graded core CFRP test. 147
5.11 Side-on, reflected and adjusted impulse traces recorded for a) the single core GFRP test; b) the graded core GFRP test; c) the single core CFRP test; and d) the graded core CFRP test. 148
5.12 Raw strain gauge data for the horizontal strain gauges on the single core GFRP sandwich panel. 151
5.13 Raw strain gauge data for the vertical strain gauges on the single core GFRP sandwich panel. 152
5.14 Raw maximum principal strain gauge data for the diagonal strain gauges on the single core GFRP sandwich panel. 153
5.15 Variation of strain with time for a) the horizontal section of the front face; b) the horizontal section of the back face; c) the vertical section of the front face; d) the vertical section of the back face; e) the diagonal section of the front face; and f) the diagonal section of the back face, for the single core GFRP sandwich panel. 154
5.16 Photographs of the single core GFRP sandwich panel after blast testing. 155
5.17 Raw strain gauge data for the horizontal strain gauges on the graded core GFRP sandwich panel. 157
5.18 Raw strain gauge data for the vertical strain gauges on the graded core GFRP sandwich panel. 158

5.19 Raw maximum principal strain gauge data for the diagonal strain gauges on the graded core GFRP sandwich panel. 159
5.20 Variation of strain with time for a) the horizontal section of the front face; b) the horizontal section of the back face; c) the vertical section of the front face; d) the vertical section of the back face; e) the diagonal section of the front face; and f) the diagonal section of the back face, for the graded core GFRP sandwich panel. 160
5.21 Photographs of the graded core GFRP sandwich panel after blast testing. 161
5.22 Raw strain gauge data for the horizontal strain gauges on the single core CFRP sandwich panel. 162
5.23 Raw strain gauge data for the vertical strain gauges on the single core CFRP sandwich panel. 163
5.24 Raw maximum principal strain gauge data for the diagonal strain gauges on the single core CFRP sandwich panel. 164
5.25 Variation of strain with time for a) the horizontal section of the front face; b) the horizontal section of the back face; c) the vertical section of the front face; d) the vertical section of the back face; e) the diagonal section of the front face; and f) the diagonal section of the back face, for the single core CFRP sandwich panel. 165
5.26 Photographs of the single core CFRP sandwich panel after blast testing. 166
5.27 Raw strain gauge data for the horizontal strain gauges on the graded core CFRP sandwich panel. 167
5.28 Raw strain gauge data for the vertical strain gauges on the graded core CFRP sandwich panel. 168
5.29 Raw maximum principal strain gauge data for the diagonal strain gauges on the graded core CFRP sandwich panel. 169
5.30 Variation of strain with time for a) the horizontal section of the front face; b) the horizontal section of the back face; c) the vertical section of the front face; d) the vertical section of the back face; e) the diagonal section of the front face; and f) the diagonal section of the back face, for the graded core CFRP sandwich panel. 170

5.31 Photographs of the graded core CFRP sandwich panel after blast testing. . . . 171
5.32 a) The horizontal centre section displacement; b) the vertical centre section displacement; c) the diagonal section displacement; and d) the central deflection and the measured side-on blast pressure, of the single core GFRP sandwich panel. The time step between the section displacement plots is 0.01 ms. . . . 174
5.33 a) The horizontal centre section displacement; b) the vertical centre section displacement; c) the diagonal section displacement; and d) the central deflection and the measured side-on blast pressure of the graded core GFRP sandwich panel. . . . 175
5.34 a) The horizontal centre section displacement; b) the vertical centre section displacement; c) the diagonal section displacement; and d) the central deflection and the measured side-on blast pressure of the single core CFRP sandwich panel. . . . 177
5.35 a) The horizontal centre section displacement; b) the vertical centre section displacement; c) the diagonal section displacement; and d) the central deflection and the calculated side-on blast pressure of the graded core CFRP sandwich panel. . . . 178

6.1 Schematic of the quasi-static compression test setup used to characterise SAN, PVC and PMI foams. . . . 188
6.2 Engineering stress versus engineering strain for the three SAN Corecell M100 test samples. . . . 191
6.3 DIC contour plots of engineering compressive strain for one of the SAN Corecell M100 test samples. The image on the left shows the strain captured at the peak stress following the linear elastic compression of the sample, and the image on the right shows the strain when cell collapse has fully developed. The strain value above each image is the average strain in the specimen, measured using DIC. . . . 191
6.4 Engineering stress versus engineering strain for the three SAN Corecell M130 test samples. . . . 192

6.5 Engineering stress versus engineering strain for the three SAN Corecell M200 test samples. . . . 192
6.6 Engineering stress versus engineering strain for the three PVC Airex C70.90 test samples. . . . 193
6.7 Engineering stress versus engineering strain for the three PMI Rohacell 110SL test samples. . . . 194
6.8 Schematic of the split-Hopkison pressure bar setup used to characterise SAN foams in dynamic compression. . . . 198
6.9 Schematic of the pulse shaper used in the SHPB tests. The diameter ranged from 4 mm to 10 mm depending on test parameters. . . . 199
6.10 Images of the cell structure of the three foams tested using a SHPB. The images were captured using a microscope and show the SAN M100 foam structure in the top image; the SAN M130 foam structure in the middle image; and the SAN M200 foam structure in the bottom image. . . . 201
6.11 Raw Data of an M100 SHPB test at 1,430 s^{-1}. . . . 203
6.12 Test results of an M100 SHPB test at 1,430 s^{-1}, with a low pass moving average filter applied, using a 100 data point span. . . . 204
6.13 Equilibrium of an M130 sample tested at 2,710 s^{-1}, showing the DIC maximum principal strain contour plot in the frame immediately before crushing. . . . 204
6.14 Compressive modulus versus strain rate of the SAN M200; M130; and M100 foam samples. . . . 206
6.15 Compressive modulus versus strain rate of 4 mm, 5 mm and 6 mm thick SAN M200 foam samples. . . . 207
6.16 Crushing strength versus strain rate of the SAN M200; M130; and M100 foam samples. . . . 208
6.17 Crushing strength versus strain rate of 4 mm, 5 mm and 6 mm thick SAN M200 foam samples. . . . 208
6.18 Dimensions of the quasi-static tension foam dog bone test specimens. 210
6.19 Quasi-static tension results of the SAN M100 foam. . . . 211
6.20 Quasi-static tension results of the SAN M130 foam. . . . 211
6.21 Quasi-static tension results of the SAN M200 foam. . . . 212

6.22 Quasi-static tension results of the PVC C70.90 foam. 213
6.23 Quasi-static tension results of the PMI 110 SL foam. 213
6.24 DIC contour plots of the quasi-static tensile strain in a PMI 110 SL foam sample. The average DIC strain in each image is shown at the top, where the 2.0% image was captured during the yielding of the material, and the 6.2% image was captured near to fracture. 214
6.25 Schematic of the dynamic tension test setup. 217
6.26 Dimensions of the dynamic tension test samples. 218
6.27 Tensile stress versus strain curves for the SAN M100 foam, tested at a) 180 s^{-1} and b) 365 s^{-1}. 219
6.28 Tensile stress versus strain curves for the SAN M130 foam, tested at a) 180 s^{-1} and b) 365 s^{-1}. 220
6.29 Tensile stress versus strain curves for the SAN M200 foam, tested at a) 180 s^{-1} and b) 365 s^{-1}. 220
6.30 Tensile stress versus strain curves for the PVC C70.90 foam, tested at a) 180 s^{-1} and b) 365 s^{-1}. 221
6.31 Tensile stress versus strain curves for the PMI 110SL foam, tested at a) 180 s^{-1} and b) 365 s^{-1}. 222
6.32 DIC contour plots of the 180 s^{-1} tensile strain in a PMI 110 SL foam sample. The average DIC strain in each image is shown at the top, where the 2.3% image was captured immediately before fracture. 222
6.33 Dynamic compressive engineering stress versus engineering strain curves for the M100, M130 and M200 SAN foams, constructed from the strains measured in the quasi-static compression tests. 227

7.1 Schematic of the steel front of the test cubicle, with the section modelled with FEA highlighted in red. 233
7.2 Screenshot of the Abaqus model of the cubicle front and sandwich panel as a) a solid model; and b) a meshed solid model. The red line indicates the area of the sandwich panel modelled with the test cubicle sections omitted. 234

7.3 A comparison of the FEA plots with and without the test cubicle, and the results from the DIC. Also shown are plots of the central displacement with the response time factored down to match each other, to highlight the effect of the boundary conditions. 239
7.4 FEA results showing out-of-plane displacement of the SAN M100 single core sandwich panel with the steel test cubicle included, at 1.6 ms, 3.7 ms and 8.1 ms after the blast wave arrival. The sandwich panel displacement measurement point and steel cubicle displacement measurement point are also highlighted. 240
7.5 FEA results showing out-of-plane displacement of the SAN M100 single core sandwich panel at 1.2 ms, 2.6 ms and 4.5 ms after the blast wave arrival. The sandwich panel displacement measurement point is also highlighted. 241
7.6 Central and quarter point out-of-plane displacements of the SAN M100 sandwich panel, from FEA results and DIC results. 242
7.7 Central and quarter point out-of-plane displacements of the PVC C70.90 sandwich panel, from FEA results and DIC results. 243
7.8 Pressure versus impulse curves for the front face-sheet, foam core and rear face-sheet in the SAN M100 simulations using elastic material models. 244
7.9 Pressure versus impulse curves for the front face-sheet, foam core and rear face-sheet in the PVC C70.90 simulations using elastic material models. 245
7.10 FEA deflection shape of the horizontal centre of the SAN M100 sandwich panel, subjected to a 100 kg charge at 15 m. The contour plots show shear strain in the sandwich panel. 247
7.11 Central and quarter point out-of-plane displacements of the SAN M100 sandwich panel incorporating damage modelling, from FEA results and DIC results. 248
7.12 Central and quarter point out-of-plane displacements of the PVC C70.90 sandwich panel incorporating damage modelling, from FEA results and DIC results. 248

7.13 Pressure versus impulse curves for the front face-sheet, foam core and rear face-sheet in the SAN M100 simulations using material models incorporating damage. 249
7.14 Pressure versus impulse curves for the front face-sheet, foam core and rear face-sheet in the PVC C70.90 simulations using material models incorporating damage. 250

A1 Out-of-plane displacement (U_Z) and maximum principal strain (MPS) DIC contour plots for the five air blasted sandwich panels. The reference to each test panel is shown on the left hand side, and the colour scales are shown on the right hand side. 281

B1 Standard deviation of out-of-plane displacement of the air blast test panels, measured prior to blast wave arrival. 283
B2 Error calculated in the α component of the shear strain, for each of the five air blast tested sandwich panels, across the horizontal centre section at maximum displacement. 285

List of Tables

3.1 Panel construction identification. 35
3.2 Constitutive and bulk face-sheet mechanical properties. 36
3.3 Mechanical properties of the foam polymers, including quasi-static (QS) and 180 s^{-1} (HR) rate test results. 38
3.4 Damage results according to the analytical solution proposed by Andrews and Moussa [5]. 43
3.5 Specifications for the high speed cameras used to record the panel responses to blast loading [6] [7]. 50
3.6 Summary of core cracks caused by blast testing. 83
3.7 Summary of debonding caused by blast testing. 85
3.8 Summary of the air blast test results. 95

4.1 Post-blast flexural test results summary for the five air blasted sandwich panels. 127
4.2 Post-blast edgewise compression test result summary for the five air blasted sandwich panels. 129

5.1 Constitutive and bulk face-sheet mechanical properties. 134
5.2 Mechanical properties of the foam polymers, including quasi-static (QS) and 180 s^{-1} (HR) rate test results. 136
5.3 Summary of the underwater blast test results from the graded density and single density GFRP and CFRP sandwich panels. 184

6.1 Summary of the quasi-static compressive properties of the five foam polymers used in air and underwater blast testing. 195

6.2 Summary of the quasi-static tensile properties of the five foam polymers used in air and underwater blast testing. 215
6.3 Summary of the dynamic tensile properties of the five foam polymers used in air and underwater blast testing. The dynamic tensile tests were performed at strain rates of 180 s^{-1} and 365 s^{-1}. 223

7.1 Material properties of the polymeric foams and GFRP face-sheets used in the finite element simulations. 236

Nomenclature

Symbol	Units	Description
A_A	mm	Cross sectional area of the solid aluminium SHPB bars
A_C	m^2	Total surface area of all cracks in the foam core
A_S	mm	Cross sectional area of the SHPB samples
A_t	mm	Cross sectional area of the hollow aluminium SHPB transmission bar
BV	V	Wheatstone bridge voltage
C_0	m/s	Wave speed in aluminium SHPB bars
Cf	$-$	Correction factor applied to FEA simulations
C_s	m/s	Wave speed in a foam SHPB specimen
D_1	m	Distance from the centre of the sandwich panel to the camera beam in the air blast tests
D_2	m	Distance between the camera sensors in the air blast tests
D	Nm^2	Bending stiffness of a sandwich beam
D_C	m	Distance from the centre of the sandwich panel to each camera sensor in the air blast tests

E	MPa, GPa	Elastic modulus
E_c	kJ	Energy to crush the foam core
E_{eff}	GPa	Effective edgewise compressive stiffness of a sandwich specimen
E_f	GPa	Fibre elastic modulus
E_m	GPa	Matrix elastic modulus
E_s	MPa	Elastic modulus of the bulk polymer in a foam SHPB specimen
E^*	MPa	Elastic modulus of a foam SHPB specimen
F	kN	Applied edgewise compressive force
G	MPa	Shear modulus of a foam core
GF	$-$	Electronic strain gauge factor
I_r	$kPa.ms$	Reflected air blast impulse
KE	kJ	Kinetic energy
K_{eff}	N/m	Effective flexural stiffness of a sandwich beam
L	mm	Length of the long edge of the sample
L_C	mm	Length of cracks along the long edge of the sample
L_S	mm	Undeformed length of the SHPB samples
N_C	$-$	Number of through-thickness cracks in the foam core
N_{CL}	$-$	Number of through-thickness cracks in the foam core along the long edge of a sample
N_{CW}	$-$	Number of through-thickness cracks in the foam core along the short edge of a sample
P	kPa	Air blast overpressure
P_c	N	Central load in flexural tests
PE	kJ	Plastic energy

P_H	MPa	Hydrostatic underwater pressure
P_m	MPa	Peak hydrostatic underwater pressure
P_r	kPa	Peak reflected air blast overpressure
P_s	kPa	Peak static air blast overpressure
Q	MPa	Foam densification constant
R	m	Stand-off distance from the charge
Rc	$-$	Foam material constant
S	mm	Span of the flexural test specimen
SE	kJ	Strain energy
T	mm	Face-sheet thickness
T_g	$^\circ K$	Glass transition temperature of the bulk polymer in a foam material
U	N	Shear rigidity of a sandwich beam
W	mm	Length of the short edge of the sample
W_C	mm	Length of cracks along the short edge of the sample
WD	kJ	Work done
W_{TNT}	kg	TNT equivalent charge weight
X	mm	Distance between interpolated points on underwater blast panels
Z	$m/kg^{\frac{1}{3}}$	Scaled distance
b	$-$	Friedlander blast waveform parameter
c	mm	Sandwich specimen thickness
d	mm	Incremental out-of-plane facet displacement in air and underwater blast panels
d_n	mm	Relative displacement of the node at position 'n' with the node at position 'n-1'
e_n	%	In-plane centreline strain in a sandwich panel, at position 'n'
h	mm	Foam core thickness
t	s	Time
t^+	s	Air blast positive pressure duration

v	m/s^2	Out-of-plane DIC facet velocity
v_f	$-$	Fibre volume fraction
v_m	$-$	Matrix volume fraction
x	mm	Facet size in DIC
Δx	mm	In-plane horizontal displacement measured using DIC
y	mm	Total out-of-plane displacement
y_n	mm	Total out-of-plane displacement of the node 'n'
z	mm	Core crushing displacement
α	$^\circ$	In-plane component of through thickness core shear strain
β	$\circ$	Out-of-plane component of through thickness core shear strain
γ	$\circ$	Through thickness core shear strain
δ	mm	Central displacement in flexural tests
$\dot{\varepsilon_0}$	s^{-1}	Foam material constant
ε	%	In-plane face-sheet strain
ε_D	%	Strain at which foam densification begins
ε_i	%	Incident SHPB strain pulse
ε_M	%	Strain measured using the test machine displacement
ε_r	%	Reflected SHPB strain pulse
ε_s	%	Strain in an SHPB specimen
$\dot{\varepsilon_s}$	s^{-1}	Strain rate in an SHPB specimen
ε_t	%	Transmitted SHPB strain pulse
ε_X	%	In-plane horizontal face-sheet strain
ε_{xy}	%	Through thickness core shear strain
ε_Y	%	In-plane vertical face-sheet strain
ε_y	%	Edgewise compressive strain in a sandwich specimen
ζ	$-$	General error term

η	$-$	Krenchel factor for composite plies
θ	ms	Underwater blast waveform parameter
κ	$-$	General error term
λ	$-$	Foam densification constant
ν	$-$	Poisson's ratio
ξ	$-$	General error term
ρ	kg/m^3	Bulk density of composite plies
ρ_f	kg/m^3	Fibre density
ρ_m	kg/m^3	Matrix density
ρ_s	kg/m^3	Density of the bulk polymer in a foam SHPB specimen
σ	MPa	Direct stress in composite plies
σ_f	MPa	Direct tensile or compressive failure stress of a composite ply
σ_{ff}	MPa	Direct tensile or compressive failure stress of a fibre
σ_{fm}	MPa	Direct tensile or compressive failure stress of a matrix
σ_p	MPa	Compressive plateau stress of polymeric foam
σ_s	%	Stress in an SHPB specimen
σ_y	MPa	Edgewise compressive stress in a sandwich specimen
τ	MPa	Shear stress in a foam core
ϕ	$-$	Volume fraction of a polymeric foam
χ	$-$	General error term

Acronyms

ADC	Analogue to Digital Converter
BNC	Bayonet Neill-Concelman
C4 / PE4	Composition 4 / Plastic Explosive 4
CFD	Computational Fluid Dynamics
CFRP	Carbon Fibre Reinforced Polymer
DIC	Digital Image Correlation
DSLR	Digital Single-Lens Reflex
FEA	Finite Element Analysis
FSI	Fluid Structure Interaction
GFRP	Glass Fibre Reinforced Polymer
HR	High Rate (Dynamic)
MPS	Maximum Principal Strain
PMI	Polymethacrylimid
PP	Polypropylene
PU	Polyurethane
PVC	Polyvinyl chloride
QS	Quasi-Static
SAN	Styrene Acrylonitrile
SHPB	Split-Hopkinson Pressure Bar
TNT	Trinitrotoluene
TTL	Transistor-Transistor-Logic
VFM	Virtual Field Method

Chapter 1

Introduction

This research project considers the blast resistance of various constructions of polymeric foam sandwich composite materials for use in naval applications. Polymeric composite materials possess a lower radar signature than their metallic counterparts, so enable stealth ships to be developed to avoid detection. Furthermore, sandwich composite materials are much less dense than the metals used in ship building, allowing composite warships to move much faster in water. Finally, by using composite materials in the construction of naval vessels it is possible to design such that the optimum mechanical properties are obtained. The research presented in this thesis forms part of an international research initiative funded by the Office of Naval Research, USA, investigating all aspects of materials for use in military marine applications. In this project, however, the research is focussed on the resistance of the materials to blast loads.

When at sea the threat to a naval vessel can be categorised into torpedoes, missiles and sea mines. Torpedoes and missiles generally will detonate in contact with the ship, so protection from these threats is usually by avoiding detection, or destroying the weapon or source. Certain non-contact sea mines, however, are detonated such that their blast wave energy can be withstood with a suitability designed hull. Sea mines are detonated by three different methods: by physical contact with the naval vessel; by the displacement of the water from the ship; or by radio detonation using radar to establish the proximity of the ship. Physical contact of the sea mine to the ship hull generates a very large amount of energy,

which is unrealistic to protect against, meaning that this type of attack must be avoided. Proximity charges, however, decay the blast energy significantly before contact with the naval structure. It is to these threats that the responses of sandwich materials are tested in this project.

In order to test against this threat, composite sandwich panels were tested in air blast and underwater blast scenarios. This was done to simulate both subsurface mines and floating mines. The strength after air blast properties of the sandwich panels were also tested, to assess the capabilities of ships made from these materials for continued service after withstanding an air blast attack. The polymeric foam cores were also characterised using quasi-static and dynamic tension, and quasi-static and dynamic compression, in an attempt to understand the various responses to blast loading. Air blast finite element models were generated to simulate the response of the sandwich composites, including fracture of the foam core.

1.1 Composites in Naval Vessels

Composite materials were first incorporated into US naval vessels in 1947, in a prototype 8.5 m long boat, and between 1955 and 1962 a total of 32 glass fibre reinforced polymer (GFRP) boats were built, each between 10 m and 17 m long. The first submarine use of GFRP was in USS Halfbeak in 1953, where the material was used for the fairwater, and seven more were fitted by 1960. In 1965 the GFRP deckhouse of USS Asheville was blast tested, before 17 were built by 1971 [8].

In more recent years composites have been utilised in numerous fast attack boats. The Finish Hamina Class patrol boat utilises a carbon fibre reinforced polymer (CFRP) superstructure [9] to allow low water displacement and manoeuvrability . The design is similar to the Norwegian Skjold class corvette, which has a CFRP and GFRP superstructure [10], the Turkish Ada class frigates [11] and various other small stealth vessels.

Bigger ships to incorporate composite materials into their design include the Type 45 Destroyer, part of the UK Royal Navy fleet, and the Zumwalt Class Destroyer, part the US Navy fleet. The Type 45 destroyer has a fibre composite radar dome [12] to reduce interference, and the Zumwalt Class has a composite deck housing to reduce weight, radar signature and to increase corrosion resistance

[13]. Photographs of the Royal Navy Type 45 destroyer radar dome and complete vessel are shown in Figure 1.1, and photographs of the US Navy Zumwalt Class composite deck housing and the complete vessel are shown in Figure 1.2.



Figure 1.1: Photographs of the Royal Navy Type 45 destroyer composite radar dome (left), from [1], and the completed vessel (right), from [2].



Figure 1.2: Photographs of the US Navy Zumwalt Class destroyer composite deck housing (left), from [3], and the completed vessel (right), from [4].

These examples show that composites in warships are considered for fairly non-structural components, simply to reduce weight and radar signature. The research presented in this thesis considers the materials for structural use in the ship hull. If the composite materials are suitable for this application there are large prospective weight gains, as well as cost savings in propulsion and increased vessel speed. The lack of metallic materials would also reduce the radar signature of the vessels.

There are many considerations to be undertaken in the consideration of sandwich composite materials for use in ship hulls. The movement of the naval vessel through the water resulting in cyclic flexural loading the panels from the movement of the ship in the water as wells as from waves slamming against the side of the ship. This would cause cyclic strain of materials which could cause the opening of voids present from the manufacturing process, specifically in the face-sheet laminates and in the interface between the face-sheet and foam core.

Another aspect to be addressed would be the design of the ship hull itself, using the sandwich composites as structural members stiffened with fibre composite supports. The design of this is arguably more flexible than with a steel structure, due to the possible of achieving very complex shapes, and the possible variations in the constituent composite materials and constructions. However, the use of composite materials in such large structures is expensive in terms of materials, labour and testing. The manufacturing processes involved in steel ship construction are now well established, and rules and regulations for design and construction are well developed over time. However, this cannot be stated for composite materials used in ship hull construction.

The response of composite hulls to impact is another important factor. In the event of collisions with rocks and other marine structures steel hulls undergo significant ductile damage which limits the loss of structural integrity of the hull. Furthermore, it is a relatively simple process to repair the damage with welding, even if the damage is underwater. The response of composite materials can be much more brittle in behaviour and repair can be more complicated, but the design of the materials can be tailored such that impact brittle fracture can be inhibited and repair can take place.

Due to the varied use of naval vessels, the hulls are expected to perform in a wide variation in temperature and conditions such as ice, fresh water and sea water. A large proportion of composite materials are polymeric, so it is important to assess the temperature affects on their properties. However, there is a huge benefit to be realised in that composite materials can be selected such that they are not affected by the range of chemicals a naval vessel might be subject to.

Finally, for naval vessels a significant threat to the structural integrity of the hull is due to blast loading. This forms the research performed in this project, and

the details of the blast threat to naval vessels is outlined subsequently.

1.2 Blast Loading of Sandwich Composites

When a polymeric foam core sandwich panel is subjected to load, failure is possible in numerous forms. With high intensity loading, or localised loading such as three point bending, the failure mode is often first dominated by foam core crushing. This is immediately followed by front face-sheet compressive failure. When the sandwich composites are loaded in edgewise compression the failure mode is generally in the form of edge-wise compression of the face-sheets or bowing of the face-sheets causing debonding from the core. The various modes of failure of sandwich composites are discussed in detail in [14].

When subjected to blast loads with low pressure amplitudes, but high blast energy, the sandwich panels generally undergo gross bending into a "bathtub" shape, which causes shear cracks to form in the polymeric foam. These core shear cracks cause localised bending, which in turn cause debonding of the face-sheet and foam core at these locations. This type of low pressure magnitude loading is typical of the air blast tests performed in this research, which were achieved using high charge sizes at large stand-off distances. When subjected to underwater blast loads, on the other hand, the energy transmitted to the sandwich panel is much lower, but with a large peak pressure amplitude. This large peak pressure amplitude causes crushing of the foam core upon arrival, before the sandwich panel begins to bend. The core crushing reduces the flexural stiffness of the sandwich panel, causing greater bending damage in the second stage of deflection. Schematics of polymeric foam core sandwich panel deflections under air blast and underwater blast are shown in Figure 1.3a and Figure 1.3b respectively. These mechanisms of failure were all witnessed in the blast research presented in this thesis.

1.3 Research Objectives

One of the primary goals of this research project was to assess the benefits of using a graded density foam core in sandwich composite hull designs, specifically when

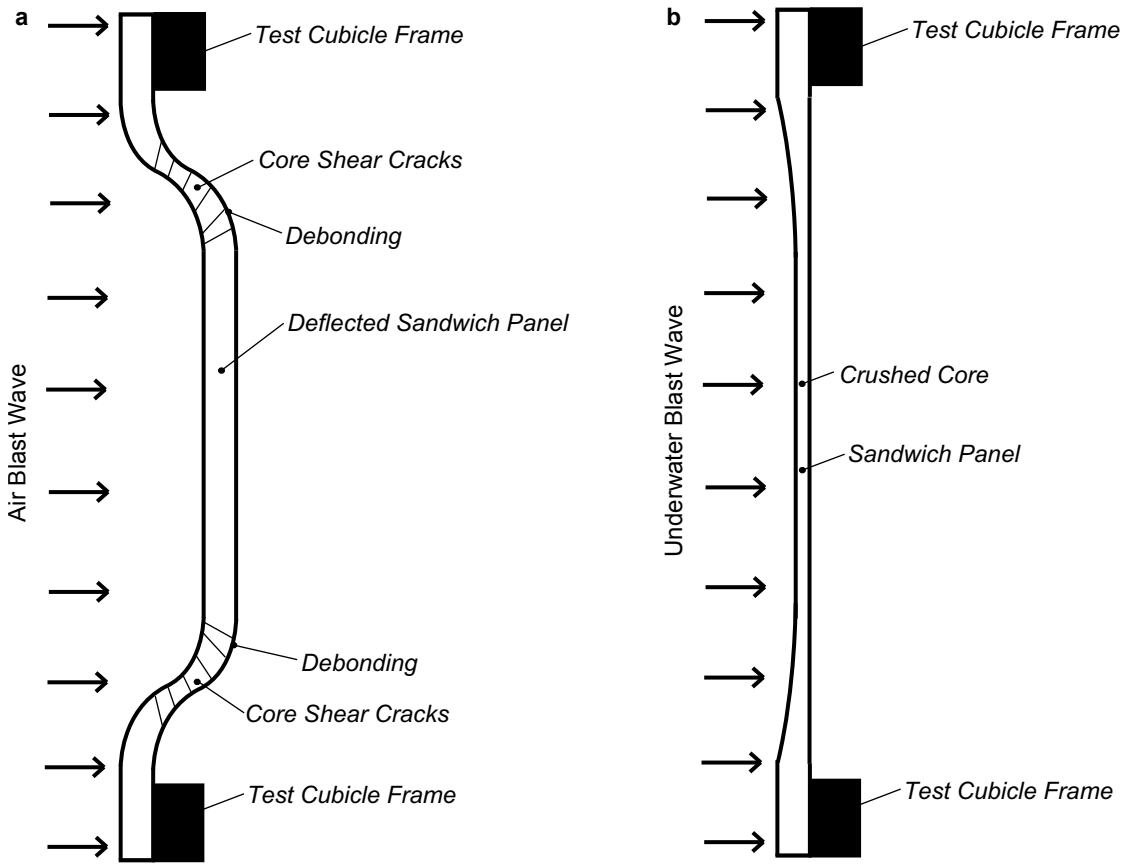


Figure 1.3: Deflection schematics of a polymeric foam sandwich composite subjected to a) air blast loading; and b) underwater blast loading.

subjected to air and underwater blast loading. It was hypothesised that by using a graded density foam core in the air blast tests, cracking would be encouraged in the front, lower density foam layers, providing a smoother displacement at the rear of the sandwich panel. This is desired as a smoother rear face-sheet displacement implies that it is less likely to suffer catastrophic failure, which is important for retaining structural integrity. In underwater blast, where the peak pressures are high enough to crush the polymeric foam cores inside the sandwich panels, it was expected that more blast energy would be absorbed in crushing a stepwise graded core than a single density core. By absorbing more energy, and attenuating the shock wave at the foam layer interfaces, the panel was expected to undergo less damage. The increased energy absorbed in crushing the graded density core than the single density core was to be examined using a split-Hopkinson pressure bar (SHPB), with the test setup specifically designed for use with rigid polymeric foam materials.

Another objective set out in this project was to assess the air blast responses of different foam polymer types used in the core of the sandwich panels. Styrene acrylonitrile (SAN) and polyvinyl chloride (PVC) are common cores used in marine applications, and polymethacrylimid (PMI) is common in helicopter blades. PMI is stiffer and stronger, but was expected to be much more brittle than the SAN and PVC core, which is detrimental in the large displacement witnessed in pressure loading of large panels. This research was expanded upon by characterising the three foams in quasi-static and dynamic tension, to assess the different fracture behaviours. The fracture mechanism in the foam core of a sandwich panel is dominated by shear loading, but as the manufacturer shear properties of the foams were very similar it was expected that different fracture behaviour would be due to varying tensile failure strains.

As stated previously the intention of using a graded density foam core was to protect the rear face-sheet from damage, to maintain the integrity of a ship hull. However, it would also be beneficial to prevent water ingress into the sandwich panels if they were to withstand a blast load but with front face-sheet cracking. In order to achieve this a compliant front face-sheet was required, and in this research Innegra polypropylene (PP) plies were distributed between the GFRP plies in the front face-sheet. It was expected that even with the presence of cracks in the

GFRP front face-sheet plies, and in the core, the PP plies would not fracture. This would, therefore, prevent water ingress into the sandwich panel.

A comparison of CFRP versus GFRP for the face-sheets was required in underwater blast, to assess the different central displacement profiles and failure mechanisms caused by the much stiffer CFRP material. It was expected that the CFRP sandwich panels would create a much higher bending moment at the boundaries, to the point of fracture of the rear face-sheet. As such the central displacement would be much lower, as the sandwich panel would be able to deflect less.

Residual flexural and edgewise compressive properties of the sandwich panels after being subjected to air blast were examined, and this was to characterise the sandwich constructions with damage present. The intention of this data would be to simulate the continued use of a naval vessel after withstanding a blast. Due to decoupling of the face-sheets it was expected that the presence of any damage would cause a significant reduction in stiffness and strength. In flexural loading the foam core acts to transmit shear load between the face-sheets, so with debonding present no shear would be transmitted. In edgewise compression the foam core acts to prevent buckling of the face-sheets, so decoupling would cause earlier buckling.

The ultimate aim of this research project is to develop an understanding of blast mechanics in sandwich structures, and to compare various sandwich composite materials for use in naval vessels. Due to the expense and uncertainty involved in full scale blast testing the use of simulations for predicting the response of ship hulls is desired. The residual material properties and the foam characterisation results presented in this thesis aid in developing simulations, and the air and underwater blast results provide validation of the simulation results. Finite element simulations were produced in this project to assess sandwich panels subjected to air blast loading, with the use of a tensile brittle cracking model. As the failure of the cores are dominated by shear loading and debonding between the face-sheets and the core, this was expected to only provide an indication of the onset of damage during deformation to blast loading. The intention was to better predict the responses of the sandwich composites to air blast loading than those obtained using linear elastic material models, and to produce failure curves for the two face-sheets and the foam core for various charge sizes and stand-off distances.

1.4 Thesis Outline

1.4.1 Literature Review

The first chapter in this thesis, Chapter 2, provides a review of current published research relevant to the project. The literature review first considers the blast resistance of composite materials, specifically the properties and characteristics observed by other researchers, as well as the experimental techniques used to test the materials. This provided insight into the testing techniques used to perform full scale air and underwater blast tests for this research project. The literature review also investigates published work on the strength after blast and strength after impact of sandwich composite materials. As this is a fairly non-standard investigation it was important to learn from the work of other researchers in designing the tests, and to be able to compare results with those obtained in literature. The third topic covered by the literature review summarises current progress in the area of foam and sandwich composite characterisation. The literature review section specifically considers the interfacial properties between the foam core and face-sheets, as well as SHPB testing of foam materials. The interfacial properties were investigated as no tests were performed in this project to characterise these, yet they play an important role in the response of sandwich composites to blast loading. SHPB tests were considered in order to design a system for the high strain rate characterisation of polymeric foam materials, as witnessed in underwater blast loading. The final section of the literature review looks at the simulation of sandwich composites, both numerically and analytically. This provided insight into the modelling techniques utilised in this project and by considering research into the simulation of sandwich materials to blast it was possible to highlight areas of necessary research, and to understand the requirements in material properties for blast resistance.

1.4.2 Full Scale Air Blast Testing

Chapter 3 is the first technical chapter of the thesis, and presents the results of full scale air blast tests, which were performed at a DNV GL test site at the Royal Air Force Spadeadam test site. These tests used 100 kg nitromethane charges and high

speed cameras were used to track the in-plane strain and out-of-plane displacement of the sandwich panels, using three dimensional digital image correlation (DIC). The tests investigated the use of a stepwise graded density sandwich panel which was expected to reduce the damage to the back face-sheet, due to cracks being encouraged in the lower density foam on the blast side of the construction. The air blast tests also compared three foam polymer cores: SAN, PVC and PMI. These polymers possess very different quasi-static material properties, so it was expected that their dynamic properties under blast would be vastly different. The final air blast comparison considered the use of PP plies interleaved between the glass plies in the front face-sheet of a PVC core sandwich panel. This was expected to reduce the front face-sheet cracking in compression, due to the higher strain to failure of the PP plies.

1.4.3 Strength After Blast Testing

The next stage of this research project was to assess the post-blast material properties of the blast tested sandwich composites, and these tests are documented in Chapter 4. The composites were sectioned into three point bending samples and edgewise compression samples, and the edges photographed to quantify the amount of damage present. The three point bend tests and edgewise compression tests were performed at various speeds and the responses were captured using two dimensional DIC. From these results the residual effective elastic moduli and residual strengths were determined against the varying amounts of damage present, and the strain rate at which the sandwich panels were tested. The intention of these findings was to input the results into finite element models for continued service of ship hulls. However this was not possible within the time constraints of the research project.

1.4.4 Full Scale Underwater Blast Testing

As with the air blast tests presented in Chapter 3, the underwater blast tests were performed at the DNV GL Spadeadam test site. The results of these tests are presented in Chapter 5. The tests compared the responses of SAN foam core sandwich panels with glass fibre and carbon fibre face-sheets. Also compared were

the responses of single density foam cores and graded density foam cores. The responses of the sandwich panels were measured using electronic strain gauges adhered to the front and rear face-sheets of the sandwich panels.

1.4.5 Foam Characterisation

Chapter 6 details foam characterisation tests performed in the project. The foams were characterised in quasi-static and dynamic tension, as well as quasi-static and dynamic compression. The quasi-static tests were performed to provide the full stress versus strain responses of the materials, and to provide a benchmark for comparison. Dynamic tension provided an insight into the different responses of the SAN, PVC and PMI foams in air blast, and dynamic compression helped to explain the responses of the SAN core graded density sandwich panels in underwater blast. The high strain rates in dynamic compression were achieved using a SHPB, and in dynamic tension by using a servo-hydraulic tensile testing machine.

1.4.6 Finite Element Modeling

Initial finite element analysis (FEA) research was performed to simulate the SAN and PVC core sandwich panels subjected to air blast in Chapter 3. The results of the FEA simulations are presented in Chapter 7. The FEA study included the comparison of fully elastic sandwich panels, and sandwich panels with fracture properties included in the foam core material models. Furthermore, a comparison was made between the sandwich panel responses when the test cubicle was included in the simulation, and when the test cubicle was omitted. The simulations resulted in pressure versus impulse failure curves, highlighting the charge and stand-off distance combinations to cause failure in the two face-sheets and the foam core.

1.4.7 Conclusions

The conclusions drawn from the research project are presented in Chapter 8. This chapter summarises the major findings in all of the research performed, and highlights the contribution made to the research area. Shortcomings in the research are also discussed in the chapter, and recommended areas of improvements for the

tests performed. A future work section is provided to identify areas to strengthen this area of research, and to recommend research areas in which the results could be used, such as in further simulating blast of sandwich composites.

1.5 Published Literature

The following list provides publications resulting from, or relating to the research presented in this thesis, into which the author has directly contributed.

1.5.1 Book Chapter

M. Kelly, H. Arora, and J. P. Dear. Blast resistance of polymeric composite sandwich structures. In P. W. R Beaumont, C. Soutis, and A. Hodzic, editors, *Structural Integrity and Durability of Advanced Composites*, chapter 20, pages 513-538. Woodhead publishing, London, 2015. ISBN 978-0-08-100137-0.

1.5.2 Journal Articles

H. Arora, M. Kelly, A. Worley, P. Del Linz, A. Fergusson, P. A. Hooper, and J. P Dear. Compressive strength after blast of sandwich composite materials. *Philosophical Transactions of the Royal Society of London A: Mathematical, Physical and Engineering Sciences*, 372(2015), 2014.

M. Kelly, H. Arora, A. Worley, M. Kaye, P. Del Linz, P. A. Hooper, and J. P Dear. Sandwich panel pore for blast applications: materials and graded density. *Experimental Mechanics*, 56(4), pages 523-544, 2015.

Chapter 2

Literature Review

2.1 Introduction

This chapter provides an overview of the current published research in the field of blast and impact loading of composite materials. Full scale blast testing is performed infrequently due to high costs, and the qualitative nature of the results. However, full scale tests are performed to compare different material responses as well as to validate finite element and analytical simulations. This chapter provides a summary of available literature considering full scale air and underwater blast testing, and the techniques used to perform the tests and to capture the results. Furthermore, the use of shock tubes is considered, which replicate the blast loading of structures by using a bursting diaphragm to generate a shock wave.

Another area of research reviewed in this chapter is quantification of residual mechanical properties after impact and blast. The focus of a significant amount of composites research is on the initial resistance to impact or blast, but the ability of the material in continued service is often neglected. As something which was researched in this project, it was important to consider the current literature in this area.

The third section presented in this chapter is in the area of foam characterisation. Due to the low stiffness of foam materials they are often difficult to test with laboratory apparatus due to the material crushing at the grips. Also, due to the high wave impendence, achieving stress equilibrium in dynamic testing is

challenging. There is a fair amount of literature available which addresses these challenges, and it is summarised in this chapter to highlight the considerations taken for the characterisation of foam in this project.

Finally, a section of this chapter is dedicated to simulating the response of sandwich composites to blast and impact. A motivation for this research project was to develop simulations of sandwich composites subjected to blast. It was therefore deemed necessary to summarise current progress in this field. Well validated simulations also provide important information on the material properties and responses in order to better understand the responses of the materials to full scale blast tests.

2.2 Blast Resistance of Composite Materials

Blast loading takes the form of a high pressure wave front travelling through a subjected medium such as air or water, and transferring energy to a deformable structure which is situated in the flow of the blast pressure wave. The pressure wave is caused by the rapid overexpansion of explosive gases which travel between 1.1 and 2.0 times the speed of sound in the specific medium. The pressure wave takes the form of an instantaneous increase, followed by an exponential decay, followed by negative pressure due to the momentum of the explosive gases causing a pressure below ambient at the centre of the explosion [15]. In this research project the mediums used for testing were air and water, and a more detailed explanation of the pressure wave travel is provided in Chapter 3 and Chapter 5 respectively.

Air blast loading of composites was performed by Arora et al. [16] in 2011, where glass fibre reinforced polymer (GFRP) face-sheets with styrene acrylonitrile (SAN) foam core sandwich panels were tested using 30 kg Composites 4 (C4) plastic explosives. The use of digital image correlation (DIC) was incorporated to track the out-of-plane displacement and surface strains during the tests. Arora et al. [17] performed further research into the effect of core thickness on panel response, using the same test setup and material constructions. In the same research paper, Arora et al. [17] presented the results of underwater blast testing performed on GFRP tubes and GFRP face-sheet sandwich panels with SAN cores.

The responses of the tube and sandwich panels underwater were recorded using electronic strain gauges adhered to the external GFRP surfaces. This same technique was used in the underwater blast tests presented in this thesis. Further to the air blast and underwater blast tests, Arora et al. [18] performed large scale air blast testing using 100 kg TNT equivalent charges at 14 m stand-off distances on sandwich composite materials. These materials were GFRP and carbon fibre reinforced polymer (CFRP) face-sheet sandwich panels, with SAN foam cores. The different configurations were compared, as well as a steel plate, which was indicative of that used for the hulls of actual warships. A review of the air blast testing performed by Arora et al., and the research into graded density air blast sandwich panels is presented in reference [19], and the air blast research presented in Chapter 3 is published in the same book chapter.

Due to the high expense of blast testing, shock tubes are often used to simulate blast loading on structures. Shukla et al. have performed significant amounts of blast research on fibre composites using a shock tube to compare the dynamic blast response of GFRP and CFRP polymers to their quasi-static properties [20]. This shock tube setup provided input shock pressures of around 0.7 MPa, and reflected pressures on the samples of around 1.7 MPa. The same shock tube set-up was also used to test 3D woven fibre composite materials to characterise the effects of differing areal densities [21], and the effect of using a stitched and unstitch foam core [22]. In the areal density tests the composite panels were subjected to shock loading and then tested using in-plane compression to determine the residual properties of the materials, and therefore determine the extent of damage suffered. The 3D stitched foam core tests compared the results of the shock loading tests to results obtained using a dynamic analysis code, and it was found that with heavier core stitching a better correlation in results was found, due to less shear damage through the sandwich panel thickness. Shock tube tests were also performed on graded sandwich composites and sandwich composites containing polyurea interlayers, in an attempt to mitigate blast energy during core crushing and bending [23]. It was found that by increasing the foam density in the blast direction, the foam incrementally crushed and reduced the bending velocity of the sandwich panel. The polyurea interlayer situated behind the graded core and in front of the rear face-sheet reduced back face-sheet damage. Wang, Gardner and

Shukla [24] also tested the same graded density core with no polyurea interlayer, and found that the incremental crushing of the lower density foam layers reduced the overall deflection speed of the sandwich panel, and thus reduced the amount of damage suffered. The effect of adding polyurea layers to GFRP plies for blast resistance was investigated by Tekalur, Shukla and Shivakumar [25], and it was found that placing a polyurea layer between the GFRP and the blast reduced the central deflection of the composite by 25%. It was found in these tests that placing softer core materials on the blast side of the sandwich composite acted to absorb blast energy early in the deformation, thus reducing back face-sheet deformation. This finding inspired the research conducted into graded density foam cores in this research. Shukla and Wang performed further research into the response of sandwich composites subjected to simultaneous blast loading and edgewise compression [26], and the increased blast deflection due to compressive loading was quantified. This was an important observation for marine structures as the loading generally takes the form of lateral loading due to waves, or in extreme cases blast, but also in the form of edgewise compression due to the top sections of the ship hull being vertical in cross-section. Gardener et al. further quantified the response of sandwich composites to blast loading, with high and low temperatures to quantify the degradation on blast performance [27].

LeBlanc and Shukla performed further shock tube work, using a water filled conical shock tube to simulate underwater blast loading on fibre composite materials, for marine applications [28]. In these tests the GFRP composite plates subjected to blast had electronic strain gauges attached, for comparison to finite element analysis (FEA) simulations, which showed that quasi-static material properties used in the models accurately predicted the responses of the plates, and damage initiation. A conical water filled shock tube was also utilised by Latourte et al. to impulsively load GFRP sandwich panels in underwater scenarios and assess their failure mechanisms [29]. In these tests a monolithic GFRP plate, and symmetric and asymmetric GFRP sandwich panels were subjected to blast, to compare the responses and to evaluate the effects of fluid-structure interaction (FSI) between the water and the composite materials. Mouritz performed underwater shock loading on stitched sandwich composites using 30 g or 50 g plastic explosives, to correlate delamination properties of the GFRP materials with blast

damage [30], considering unstitched, lightly stitched and heavily stitched materials. Ballistic tests were also performed to quantify the effects of stitching.

A blast pendulum was designed by Nurick et al., for performing small scale blast tests within a laboratory, achieving peak pressure of between 60 MPa and 80 MPa. Mild steel plates were tested with failure mechanisms classified into large scale deformation; boundary failure with large deformation; and boundary failure, and the pendulum was attached to a split-Hopkinson pressure bar (SHPB) so that the blast loading could be measured [31]. These tests were also performed on metallic honeycomb sandwich composites with aluminium sheet face-sheets, to compare these to the same face-sheets with air as the core [32]. It was found that crushing of the honeycomb core absorbed a lot of blast energy, and the effect at various impulse values was quantified to design an optimum sandwich panel in terms of core crushing and bending. Reinforced mild steel plates were tested on the pendulum as well in which webs were added to the plates to determine the reduction in blast damage for increased numbers of webs. FEA was also performed for these tests, which highlighted the necessity to include temperature effects for close proximity blasts [33]. Localised bending effects were then considered in FEA for the same tests, modelling tearing in the mild steel, by assuming that 90% of the plastic work done during deformation was converted to heat. Yield stress was then defined at 0 °C; 200 °C; 700 °C; and 1000 °C [34].

Tests were also performed by Langdon et al. on fibre/metal composites [35], and it was concluded that the materials were expected to outperform monolithic metallic plates, from the initial tests performed. Polyvinyl chloride (PVC) foam core sandwich panels with GFRP face-sheets were investigated by Langdon et al. [36] and it was found that increasing the density of the foam core reduced the velocity of the front face-sheet, and as such reduced face-sheet damage. The aim of this research was to compare materials, but to also validate finite element simulations of the constitutive material models. Zhu et al. also tested honeycomb sandwich panels, to assess the effect of core and face-sheet thickness on panel response [37]. The same system was used by Zhu et al. to test metallic sandwich panels containing aluminium foam cores, to compare these to aluminium honeycomb cores also tested [38]. In these tests it was determined that the panel deformation took place in three phases, the front face-sheet accelerated while the core deformed elasti-

cally; the core crushed as the front face-sheet was further deformed; and the back face-sheet al.so began to deform, bending the whole sandwich panel.

The effect of curved metallic sandwich panels to blast loading has been investigated by Shen et al. [39], to characterise the reduced blast deflection suffered when the radius of curvature is increased. These tests also used a pendulum technique, using an SHPB to measure blast loading. The blast pendulum technique was used by Kakogiannis et al. to blast load GFRP tubes, and validate finite element models in which the FSI between the air and the tubes was captured in LS-Dyna, showing good correlation to the experimental results [40].

Another laboratory blast method was utilised by Radford, Deshpande and Fleck, in which aluminium foam projectiles were fired at rigid targets to simulate the pressure versus time response observed in blast loads [41]. This technique was developed further by Deshpande, Heaver and Fleck to simulate underwater blast loading, by firing the foam projectiles at a cylinder of water, which then transmitted the blast load [42]. It was shown in both papers that the pressure profile exerted on the structure was heavily dependent on the ratio of foam projectile mass to the mass of the test structure.

This section has summarised the current published research on the blast loading of structures, and the importance of these tests is highlighted by the inherent inaccuracies in capturing blast responses numerically or analytically. Significant development is in progress into scaling down blast testing to be feasible in a laboratory, to reduce the costs and time involved in performing the tests. This literature provided insight into the deformation mechanisms to be expected during air and underwater blast, and the measurement systems which could be employed to capture the responses of the sandwich composites to blast.

2.3 Strength After Blast

Research was performed by Caprino and Teti in 1994 into the post-impact strength of GFRP face-sheet, PVC foam core sandwich panels. It was found in this research that the residual tensile strength was related to fibre failure, and not correlated to delamination [43]. Caprino, Teti and Iorio then performed further residual strength assessments into GFRP composite materials by fatigue damaging the samples, and

then assessing their acoustic emission response while bringing them to failure [44].

The post-impact residual strength of CFRP face-sheet, PVC foam core sandwich panels was assessed by Bull and Edgren, one construction with thin face-sheets and an intermediate density core; and the other with thick face-sheets and a high density core. The samples were impacted using a drop tower and then loaded in edgewise compression to determine the residual strength reduction of various composites with increased amounts of damage [45]. Zenkert et al. performed edgewise compression tests on CFRP composite materials, to assess their residual strengths after blunt and sharp impacts from a drop tower. The results were recorded using DIC to validate FEA models of the damaged sandwich composites. The intention was to use these FEA models to assess the urgency of repair of a ship hull containing the damaged sandwich panel [46]. Similar tests were also performed by Edgren et al. considering CFRP non-crimp sandwich panels, to assess more closely the failure mechanisms during compression, in the region of impact damage. It was found that there was no correlation between the amount of damage present and the residual compressive strength, as microbuckling occurred at the impact damage location. There was simply a drop in compressive strength from the undamaged state to the impact damaged state [47].

The assessment of post-blast compression strength of GFRP and CFRP sandwich panels was performed by Arora et al., where the sandwich composites subjected to large scale air blast loading were tested in edgewise compression. These sandwich panels were very large in comparison to the small samples generally tested, and they contained a significant amount of damage. The only quantification of damage performed was to inspect the edges, and the deformation of the sandwich panels was recorded using 3D DIC. This provided an indication of subsurface damage due to strain concentrations [48].

Residual strength modelling is something that is also of interest in naval research, as the vessels are required to be in service after suffering damage. Lacy and Hwang developed edgewise compression models of metallic honeycomb sandwich panels which had been subjected to spherical impacts, which were based on numerical results. The FEA models produced considered the individual effects of face-sheet damage and core damage, and the elastic properties of each were degraded by a factor dependent on the size of the damaged region, with failure

controlled by the failure strain of the material [49]. Finite element solutions of honeycomb sandwich panels were also developed by Xie, Vizzini and Yang, to predict compressive strength after low velocity impacts. These models were validated with laboratory experiments, and it was shown that a critical amount of through thickness damage was determined which caused rapid catastrophic failure of the sandwich panels in edgewise compression [50].

The residual tensile strength of Kevlar fibre composites were tested by Reis et al., to assess the effect on impact resistance and residual strength of composites made with nanoclay toughened epoxy. It was found that the nanoclay improved the impact resistance and residual tensile strength of the Kevlar materials [51]. Reis et al. then performed the same tests to determine the effect of varying amounts of nanoclay in the composite material [52]. Post-impact residual tests were also performed on aramid fibre composites and basalt fibre composites by Sarasini et al., but with the residual strength established using four point flexural tests. It was found that the aramid composites showed the best impact resistance, but the basalt composites showed the best residual flexural properties [53].

A polymer and metallic sandwich composite combination was tested by Davies et al., in which CFRP face-sheet, aluminium honeycomb core panels were impacted and then compression tested. Two sets of test were performed with a thick face-sheet and thin core construction, and a thin face-sheet and thick core construction. Finite element models were then created, with the experimental results used to validate the simulations [54].

The majority of this research project considers the ability of sandwich composites to withstand blast, when used as hulls for naval vessels, but it is also important to consider the residual properties of the materials after blast. If a naval vessel survives a blast event, it must be able to withstand continued service, and the research summarised in this section provides the ability to assess residual composite performance. This literature review directly influenced the strength after blast tests presented in Chapter 4, which is an area of research rarely performed. This literature review provided the justification to perform the strength after blast research, to provide an understanding of the continued serviceability of naval vessels after withstanding blast loading. It has been shown that the majority of testing recorded in the literature considers compression properties after impact, which is

informative for this research project which considers edgewise compressive properties after blast loading. Edgewise compression is of interest due to the typical cross-section of a ship hull being vertical at the top, an area which could suffer significant damage in an air blast scenario. The remainder of the hull would be loaded laterally due to the buoyancy of the ship in the water, for which flexural properties after blast were investigated.

2.4 Foam Characterisation

The response of polymeric sandwich composites to blast is largely dictated by the foam polymer used in the core. If large scale damage takes place in the bending stage then the failure is dominated by shear behaviour, and if the core is crushed then the compressive properties of the foam are of high importance. This section summaries current published literature on the material properties of polymeric foams, and of the fracture behaviour of the interfaces between the face-sheets and core.

Due to the compliant nature of foam materials, characterisation is a challenging field. Various American Society for Testing and Materials (ASTM) standards exist, the merits and shortcomings of which are discussed in Chapter 6. A further challenge to testing foam is in correctly establishing strain. Often the grips in the test will slip, resulting in an unusable machine displacement. Wang, Pierron and Thomsen incorporated both DIC and virtual field methods (VFMs) into the shear testing of PVC foam. The shear test was performed in an Arcan fixture, and the combination of DIC and VFM provided the optimum loading configuration to determine the stiffness properties of the materials [55].

The response of foam materials to multiaxial loading is often characterised by an ellipse, as summarised in the Abaqus user manual, with deviatoric and hydrostatic stress components. The hydrostatic response of the foam is plotted along the horizontal axis, with the limits of the ellipse representing hydrostatic tension (positive) and hydrostatic compression (negative). The deviatoric, or Von Mises, response of the foam is represented on the vertical axis, with the limit represented by the pure shear behaviour of the foam. Uniaxial tension and uniaxial compression are then determined on the ellipse surface with a gradient of one

third, in the positive and negative horizontal axis respectively. The data from which the surface of the ellipse is constructed is the yield data of the foam, and the ellipse radius is expected to increase with strain rate, with the hydrostatic tension strength remaining the same [56]. As such, a bounding material property to this curve is hydrostatic compression, as performed by Viot on polypropylene foam samples. The test setup consisted of a pressure chamber containing water or alcohol, with a steel punch to increase the pressure in the vessel. The sample was coated in silicon to avoid excessive edge damage and a flywheel was used to impact the punch [57]. Deshpande and Fleck characterised PVC in hydrostatic, biaxial and uniaxial tension; and hydrostatic and uniaxial compression, to develop a yield curve. The hydrostatic and biaxial tests were performed using a screw driven frame, testing a cube of material with the edges removed to prevent excess strains at the edges. It was found that in tensile tests failure was dominated by cell wall bending, and in compression failure was dominated by elastic buckling of the cell walls [58].

2.4.1 Core and Face-Sheet Interface Properties

When testing the fracture properties of sandwich composites uneven bending moments in the top face-sheet and the foam core and bottom face-sheet cause mixed mode crack tip loading. Ostergaard et al. investigated the effect of mode mixity on the crack growth path in PVC core, GFRP face-sheet sandwich beams. The shear fracture toughness of the interfaces was characterised against the mode mixity, and a transition from fibre bridging to crack growth into the foam was found [59]. The dynamic interface fracture properties were tested by Cantwell and Davies, in which a sliding carriage was used in a dynamic double cantilever beam test, to assess the mode I fracture toughness of honeycomb and CFRP sandwich panels [60]. The improvement on mode I fracture toughness of PVC core and GFRP face-sheet sandwich composites with the use of multi-walled carbon nanotubes was investigated by Patra and Mitra. A double cantilever beam test method was used in this case, with a compliance calibration applied to the results to account for the soft foam core in the tests [61]. The mode III fracture toughness of PVC foam core and steel face-sheet sandwich panels has also been researched by Hernndez-Prez,

Avils and Carlsson. This test was performed by loading the opposite corners of a square specimen, causing the sandwich panel to twist. This was then corrected for the compliance in core compression [62].

The biggest challenge when performing interface fracture assessments on sandwich specimens is maintaining the intended mode mixity at the crack tip. Avils and Carlsson developed an elastic foundation model, to account for the rotation in a double cantilever beam specimen, to correct the values for the case where rotation is not present. The correction factor was achieved using finite element and numerical simulations of the elastic flexural reactions of the top face-sheet with the cross-head load applied, and the core and bottom face-sheet from which the top face-sheet was being debonded [63].

Quispitupa, Bergreen and Carlsson utilised the mode mixity to determine parameters with differing combinations of mode I and mode II loading. This was achieved using a mixed mode bending rig with a debond already present in GFRP face-sheet, PVC foam core sandwich beams. The mode mixity at the crack tip was determined by finite element simulations, and a significant increase in fracture toughness was witnessed with greater mode II loading. With similar density foams as used in the research presented in this theses, it was found that with predominantly mode II loading, the crack propagated into the interfacial layer of the face-sheet, and not into the foam core [64]. Manca et al. also investigated the energy release rate in GFRP face-sheet, PVC foam core sandwich beams using cyclic loading to extend the crack along the interface. The mode mixity at the crack tip was also determined using finite element modelling and it was again found that with mode II dominated loading the crack propagated into the face-sheets, whereas mode I loading encouraged crack propagation into the foam. The use of cyclic loading allowed fewer specimens to be tested and allowed a constant change in fracture energy to be obtained [65]. Mixed mode bending properties were also investigated by Lundsgaard-Larsen et al. in which a double cantilever beam with uneven bending moments was utilised. In this research the bending moments in the face-sheets were reduced by adhering steel bars to them. The test structure allowed the mode mixity at the crack tip to be varied from pure mode I to pure mode II, and the J integral fracture toughness was determined for varying amounts of crack opening [66].

This brief summary shows that limited research has been performed on interfacial properties, and this literature review led to the conclusion that these properties should be omitted from the research project, and merely accounted for in damage propagation in the sandwich panels. This is due to the complexities in characterising interfacial properties, which would have required too large a proportion of the research time available in this project.

2.4.2 Split-Hopkinson Pressure Bar Compression Tests

In underwater blast loading, or close proximity air blast loading, the initial pressure pulse is large enough to cause core crushing in the polymeric sandwich composites. In order to characterise the foams at these strain rates, the use of an SHPB is required, as was performed in this research project. Due to the low impendence of polymeric foams, it is necessary to use pulse shapers in SHPB tests, to slow down the initial loading and prevent the foam from crushing at the incident bar immediately. In order to ensure that stress equilibrium is achieved in SHPB tests, quartz transducers can be placed either side of the test specimen to measure the forces on each face. This system was used by Chen, Lu and Winfree to test polyurethane (PU) foams at strain rates of up to 4,450 s^{-1} [67]. Another issue in performing SHPB tests on foam materials is the low magnitudes of the transmitted pulse, a problem which was overcome by Chen, Zhang and Forrestal with the use of a hollow aluminium transmission bar [68]. Shazly, Bahei-El-Din and Salem also characterised PU at strain rates up to 4,300 s^{-1} using a hollow aluminium transmission bar and copper pulse shapers [69].

The effect of material type on SHPB test design was investigated by Song and Chen, where epoxy syntactic foam was tested using copper disks as pulse shapers. It was also found that copper tubes and copper disks were suitable pulse shapers for low density foam materials [70]. The effects of strain rate on PS foam was tested by Song et al., with rates from 0.001 s^{-1} to 950 s^{-1}, the higher rates achieved with a SHPB. The SHPB tests used a copper pulse shaper, aluminium tubes and a quartz transducer system to accurately determine the stress versus strain response of the PS material [71]. Song, Chen and Jiang also characterised rigid PU foams with densities of 240 kg/m^3 using the same system [72].

The literature presented on SHPB testing, as well as the equations presented by Lifshitz and Leber [73] was used to design the test system, and accurately measure SAN foam responses at very high strain rates.

2.5 Simulating Blast of Composites

Due to the high cost of blast testing, a lot of research is dedicated to simulating the response of sandwich composite materials to blast loading. These simulations take various forms from analytical solutions to numerical solutions and this section provides a summary of significant research to date in the area of blast of composites.

Hoo Fatt and Park developed an analytical solution for the low velocity impact of sandwich composites, in which failure was split into distinct stages. These stages were calculated for face-sheet failure on the impact side, core failure and back face-sheet failure [74]. Hoo Fatt and Palla performed a similar analysis on circular sandwich panels under blast loads, in which the response was split into core crushing, bending and vibration. These analytical predictions were shown to have close correlation to simulations performed using finite element analysis (FEA) in ABAQUS/Explicit [75]. Hoo Fatt and Sirivolu further considered the response of a PVC core sandwich panels by assuming a transversely isotropic behaviour of the foam core, and a rectangular shaped sandwich panel. The core was predicted to yield at the centreline in regions around one quarter of the way in from the edges, and spread in regions in this area. The analytical results were compared to FEA results obtained using ABAQUS/Explicit [76]. Andrews and Moussa also developed analytical solutions for composite sandwich panels under blast loads, where the failure of the sandwich panel took the form of front face-sheet compressive failure, core shear failure or rear face-sheet tensile failure. In this case failure mode maps were created for various sandwich panel dimensions [5]. Li, Kardomateas and Simities developed an analytical solution for the response of sandwich composites to blast loading, by considering the core as a compressible continuous structure and the face-sheets as thin sheets. The transient response of the face-sheets was than calculating using a Fourier transform of the excitation frequency from blast loading [77], [78]. A simplified analytical solution to the blast

loading of sandwich panels was also developed by McConnell and Su, to assess the effect of through thickness fibre reinforcements on the energy absorption of blast energy. The study considered the effect of the reinforcement angle, and was compared to experimental and FEA results [79].

Underwater blast scenarios differ from air blast due to the high pressure pulses and shorter blast durations. Panciroli outlined an analytical approach to determining the transient response of sandwich beams and plates to underwater shock loading, accounting for core compressibility. It is shown that in flat beams and plates the response is dominated by the first mode of vibration, whereas in curved beams and plates the higher order modes dominate [80]. One of the major problems with modelling the blast loading of structures, especially in underwater scenarios, is the FSI experienced on the surface of the structure. In underwater blast the interaction of the water on the sandwich composite causes cavitation, and Schiffer et al. developed analytical and finite element simulations to capture this process which was then validated by experiments. With finite elements the cavitation was modelled in ABAQUS/Explicit using water with a specified cavitation limit. The analytical simulations were split into two phases, the first with the water in contact with the plate, and the second when cavitation began. The first stage was solved with a conservation of energy from the blast wave to the plate, and the cavitation phase was informed by the FEA simulation results. The experimental results, FEA and analytical simulations showed strong correlation [81]. Wei et al. also developed an FSI FEA model in Abaqus/Explicit using an Eularian mesh for the water and a Lagrangian mesh for the sandwich composite. Again a good correlation was observed [82]. The use of FSI in Abaqus was implemented mathematically by McCoy and Sun using the implicit integration function. This was applied to thick walled composite tubes subjected to underwater blast loading [83].

The effect of the curvature of composite panels was investigated experimentally and numerically by Phadnis et al. The FEA material model was user defined, to predict the damage through the thickness of the laminate. The experimental and numerical results were compared in terms of deflection, velocity and in-plane strain, and showed good agreement [84]. Langdon et al. performed full scale, small size air blast tests on GFRP face-sheet, PVC core sandwich panels in order to predict the

responses of the sandwich panels using FEA. The use of a Hashin failure model for the GFRP face-sheets, and a cohesive zone between the face-sheets and foam core was used to predict damage in the composites. The foam core was modelled using the crushable foam material model built into ABAQUS. The damage observed in the FEA results corresponded well to that witnessed in the experimental results [36].

Aluminium graded core sandwich panels have been numerically modelled by Li et al., where the geometry of the panel was hemispherical. The response was modelled using LS-Dyna and used to assess the relative energy absorption of yielding of the face-sheets and interfaces, and crushing of the foam layers [85]. The same material models were then used to compare the responses of graded and uniform aluminium foam core tubes to internal blast loads [86]. An LS-Dyna FEA simulation of curved graded aluminium foam core sandwich panels was compared to experimental results, to show good correlation. In this case the change in performance between a cylindrically curved and spherically curved sandwich panel to blast loading was assessed, to conclude that the cylinder shape outperformed the spherical shape in every case [87]. LS-Dyna was also used by Bahei-El-Din et al. to simulate the blast response of sandwich beams containing a polyurea interlayer between the top face-sheet and core. In this case, the polyurea layer was characterised as a rate sensitive elasto-plastic material, and it was shown to reduce core crushing and to dampen the transient response of the sandwich panel, reducing vibrational damage [88].

By using the basic equations of sandwich plate theory, and applying Hamilton's principle to drive the equations of motion of the sandwich panels, Librescu, Oh and Hohe developed an analytical solution to the response of sandwich panels to air and underwater blast loading [89]. Hause and Librescu then incorporated a Laplace transform into the solution, to provide a closed form of the response, and correctly capture the transient behaviour [90]. These models were then used to determine the effects of core orthotropy, ply thickness and stacking sequence on the accuracy of the solution [91] and then further used to predict the core compressibility and buckling of flat sandwich plates to impulsive loading [92].

The summary of literature into simulating composite materials subjected to blast loading has shown that research is performed using a wide range of tech-

niques. These were considered in full to develop simulations in Abaqus Explicit for this research project.

2.6 Summary

This literature review has been performed to provide a summary of the current published literature in the field of blast of composite materials. This was with the aim of informing the research carried out in this project and to avoid replicating work already published. As has been shown the amount of full scale blast tests published is limited, with a lot of the tests being small in charge size to reduce costs. In these cases, the results are used to validate simulations, or to scale the results to larger charge sizes. The research performed in this project, however, considered much larger charge sizes as these are required for the protection of large ships from threats such as sea mines. Alongside utilising small scale charges, shock tubes are often used to create shock loading on structures using a bursting diaphragm. This is a much more cost effective method of blast loading but has limited energy capabilities. The literature research into full scale blast testing highlighted the current interest into grading the density of the foam cores in order to attenuate the blast energy, to reduce overall damage, more specifically back face-sheet damage. This finding motivated the research into graded density foam cores in this research project. The use of high speed cameras and DIC to track deformation during blast loading formed an important part of the air blast section of this project, and was well informed by the available blast and shock tube literature, as this technique is often used. The use of electronic strain gauges to track deformation is less used, due to the infrequent testing of fully submerged structures.

Strength after blast and impact research literature was investigated as well, as this is of high interest in naval applications. A naval vessel which withstands a blast load must also survive continued service in order to move away from the threat area. The literature review concluded that strength after blast is uncommon due to the small amount of full scale blast research performed, but that residual properties after impact tests are well established. Residual strength and stiffness are the properties generally considered, and these are in bending and edgewise compression with respect to sandwich composites. These are the properties most affect

by damage to the sandwich composite, due to the decoupling of the face-sheets reducing flexural stiffness and promoting face-sheet buckling. The motivation for a lot of strength after impact tests, and the motivation in this research, is to develop residual models in order to calculate or simulate the responses of the composites with damage present. With further development, this could lead to modelling whole ship hulls with localised damage, but this was not within the scope of this project.

Polymer foam characterisation was another research section in this project, and the literature review was imperative in developing test methods for this. Due to the high wave speed in compressing foam in underwater blast, SHPB tests were necessary for material characterisation. The literature review was useful in designing these tests, and led to the decision to use aluminium bars with semi-conductor strain gauges. Further development of pulse shapers was made to the copper shapers used in the literature. Testing polymeric foam in dynamic tension is also difficult due to the weak material at the grips and the challenge in achieving stress equilibrium and the current progress in this area has been summarised. Various tests have also been carried out into hydrostatic tension and compression which provides full characterisation of the foam material in a deviatoric stress and hydrostatic stress yield domain, which is a future work area recommended from this research.

The final section of the literature review considered analytical and numerical modelling of composites subjected to blast and impact. This area of research is fairly vast, so a selection of the different modelling methods have been provided in this chapter. There is a significant amount of progress in the area of mathematical modelling of sandwich composites subjected to blast to develop failure loci for core and face-sheet damage. Some of this literature was used in this research project to select charge sizes and stand-off distances for blast loading. A major motivation of this research project was to document test results which can be used for FEA, either with characterisation or for validation. For this reason, the major accomplishments in the area of simulating composites subjected to blast have been provided. This literature was reviewed in order to educate the research performed to provide the necessary data for these simulations.

Chapter 3

Full Scale Air Blast Testing

3.1 Introduction

This chapter presents full scale air blast testing performed on polymeric sandwich composite panels, with glass fibre reinforced polymer (GFRP) face-sheets. These were performed at a DNV GL explosive testing site situated in RAF Spadeadam, Cumbria, UK. The chapter outlines the tests performed, as well as the digital image correlation (DIC) technique used to capture 3D footage of the out-of-plane panel deflection during the tests, and the strain on the back face-sheet. The explosive charges used were 100 kg nitromethane (100 kg TNT equivalent) and were situated at a distance of 15 m from the sandwich test panel. A 15 m stand-off distance was chosen as this was calculated to be sufficient to cause core and front face-sheet damage in all of the sandwich panels, but to allow for back face-sheet integrity to be maintained in order to protect the high speed camera equipment from blast loading. Failure was required to provide the maximum comparison of the different configurations of sandwich panels. There were three separate air blast studies performed, the first of which considered the effect of core foam polymer type on the damage suffered during blast. Having relatively similar shear moduli, the different foam polymers were expected to behave similarly in elastic loading, but due to dramatically different dynamic material failure properties, it was expected that these would have much different blast loading capacities. The dynamic material property of interest was the strain to failure of the polymer, as the higher stiffness

of the face-sheets resulted in the other foam properties having little effect on the response and the shear strain properties were similar in every case. The three polymers considered were: styrene acrylonitrile (SAN); polyvinyl chloride (PVC); and polymethacrylimid (PMI).

The second blast study used a sandwich construction with a stepwise graded density foam SAN core. This was used by Wang, Gardner and Shukla [24] to mitigate blast energy during blast, and in this case the intention was to reduce the overall panel deflection due to a stiffer back half of the sandwich panel. In the study recorded here, the sandwich panel was compared directly to an equivalent thickness panel with a SAN M130 foam core.

The final blast study used a PVC foam core and GFRP face-sheets, but the front face-sheet incorporated plies of Innegra polypropylene (PP) fibres in order to reduce front face-sheet damage during blast. This blast panel was compared to an equivalent panel which contained no PP fibres, to directly assess the effect of adding these fibres to an otherwise identical GFRP layup.

The blast test cubicles contained two openings of 1.3 m X 1.6 m, with reinforcements around the openings. The sandwich panels were clamped around the edges of the openings between steel plates. If sandwich composite plates were used in a ship hull they would be structurally load bearing, but would be reinforced in a similar manner to the boundary conditions in these tests. However, the hull would be constructed in much larger, curved sections, quite different to the relatively small, flat panels tested in this research. The test panels were sufficiently large to develop an understanding of large scale deformation to blast loadings, and to also be meaningful in verifying analytical and numerical simulations. Once fully validated simulations are achieved these can be extended to be more representative of a ship hull structure.

3.2 Materials

3.2.1 Face-Sheets

The face-sheets chosen in the full scale air blast tests were GFRP. These were chosen over carbon fibre to provide the sandwich panels with greater strain to

failure in the face-sheets, allowing greater strains in the foam cores. The face-sheet construction of the test panels was similar to those tested by Arora [18], containing Gurit QE1200 quadriaxial glass fibre plies. The manufacturing process for the panels was via vacuum consolidation, in which the glass fibres and resin are mixed before applying a vacuum and heat for curing. The panels were made with two different resin systems: SR 8500 epoxy resin with standard hardener, and ST 94 film epoxy resin. The difference was due to availability, but was deemed insignificant due to the failure modes being dictated by the much weaker foam cores in the tests, and the epoxy resins having similar mechanical properties. For both resin systems, the panel was drawn to vacuum and held at room temperature for 24 hours, then heated to 85°C at 1°C/min, and held at this temperature for 12 hours. After this period the sandwich panel was allowed to return to room temperature at approximately 1°C/min. The identification of which resin system was used for the construction of each panel is shown in Table 3.1, as well as the overall panel thickness and areal densities. The ply thickness of a cured QE1200 ply was 1 mm, and that of a cured Innegra PP ply was 0.35 mm. The method of vacuum consolidation on the tooling plate is shown in the schematic in Figure 3.1. A detailed layup schematic of the single core sandwich panels is shown in Figure 3.2, the graded sandwich panel is shown in Figure 3.3 and of the Innegra PP panel in Figure 3.4.

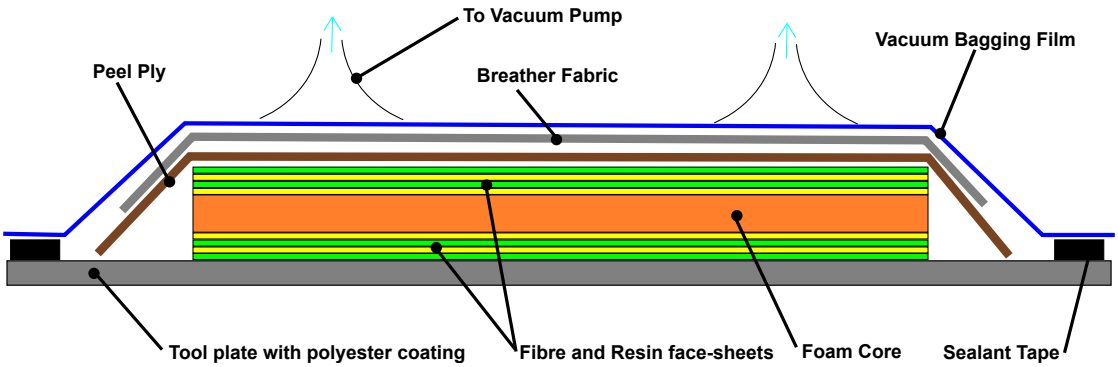


Figure 3.1: Schematic of the layup method of the sandwich panels.

The material properties of the face-sheets were calculated via the rule of mixtures, with the constitutive material properties taken from manufacturer data sheets, as displayed in Table 3.2. As such, it should be stated that the mate-

rial properties are only approximations, as the manufacturing procedures used for these panels vary from those described in the manufacturer data sheets. The fibre volume fraction (v_f) of the QE1200 plies within each resin system was 47%, and the fibre volume fraction of the Innegra PP plies was 62%. The volume fractions were calculated from the glass fibre and PP fibre densities presented in Table 3.2 and the areal densities of the dry fibre plies provided by the manufacturers. By calculating the weight of the fabric used to manufacture each ply and dividing this by the fibre density, the volume of fibres in each ply was calculated. The face-sheet thickness for each panel was measured to determine the volume of each ply including the resin, and from this the fraction of the overall volume occupied by fibres was calculated. The calculation of the bulk density of each ply (ρ) is provided by Equation (3.1), where ρ_f is the fibre density; ρ_m is the matrix density; and v_m is the matrix volume fraction. The Krenchel factor (η) for each ply of quadriaxial glass fibre was 0.375, and for the woven PP plies was 0.5 [93]. The elastic modulus (E) of the plies was then calculated using Equation (3.2), where E_f is the elastic modulus of the fibres; and E_m is the elastic modulus of the matrix. It was assumed that the elastic modulus was identical in tension and compression. Similarly, the bulk tensile and compressive failure strength of each ply (σ_f) is given by Equation (3.3) where σ_{ff} is the failure strength of the fibres; and σ_{fm} is the failure strength of the matrix. The equations to calculate the density, elastic modulus and strength of the plies are detailed in [93]. The calculated values for the glass and PP plies are shown in Table 3.2, and the interlaminar shear strength properties displayed are taken as the values in manufacturer data-sheets for slightly different layup configurations. The density and compressive strength of the PP fibres was unavailable from manufacturer data sheets, so have been given here as properties for bulk PP.

$$\rho = \rho_f v_f + \rho_m v_m \tag{3.1}$$

$$E = \eta v_f E_f + v_m E_m \tag{3.2}$$

$$\sigma_f = \eta v_f \sigma_{ff} + v_m \sigma_{fm} \tag{3.3}$$

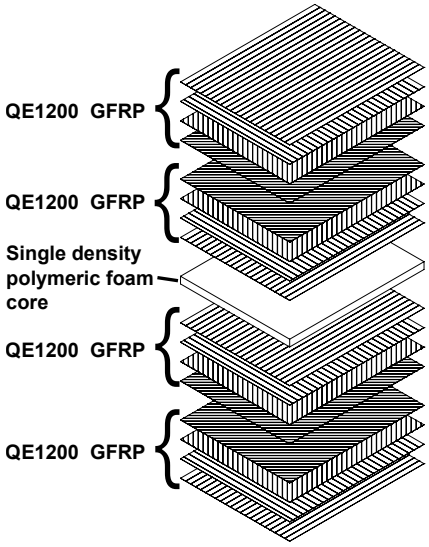


Figure 3.2: Schematic of the layup of the single core sandwich panels, incorporating a 40 mm thick foam core, with two plies of quadriaxial QE1200 GFRP either side.

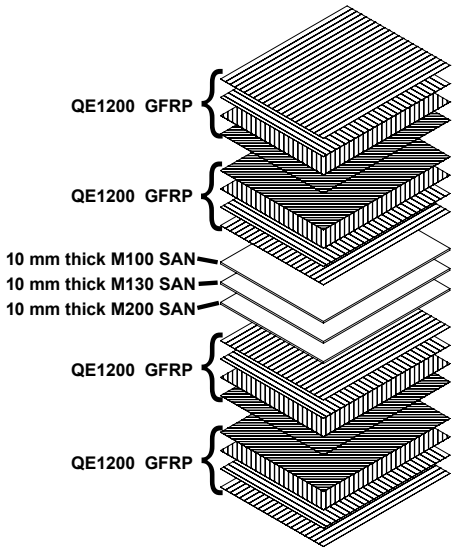


Figure 3.3: Schematic of the layup of the graded core sandwich panel, incorporating three 10 mm thick SAN foam layers, with two plies of quadriaxial QE1200 GFRP either side.

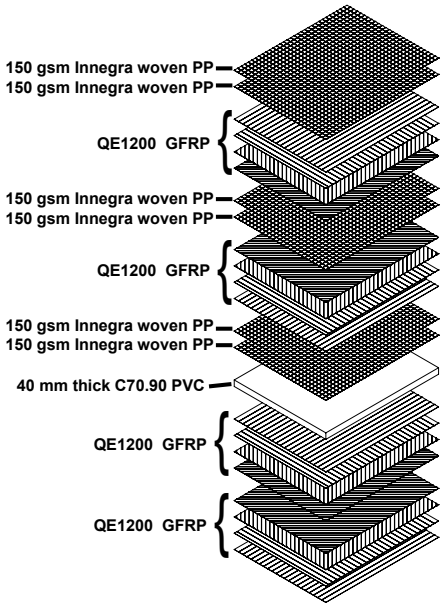


Figure 3.4: Schematic of the layup of the single PVC core sandwich panel, incorporating a 40 mm thick foam core, with two plies of quadriaxial QE1200 GFRP either side and Innegra PP plies interleaved between the glass plies in the front face-sheet.

Table 3.1: Panel construction identification.

Panel Description	Resin System	Overall Panel Thickness (mm)	Areal Density (kg/m^2)
Single M100 SAN Core	ST 94	44.0	10.88
Single C70.90 PVC Core	SR 8500	44.0	10.96
Single 110SL PMI Core	SR 8500	44.0	10.96
Single M130 SAN Core	SR 8500	34.0	10.86
Graded (M100/M130/M200) SAN Core	ST 94	34.3	11.57
Polypropylene Interlayer	SR 8500	46.0	12.84

Table 3.2: Constitutive and bulk face-sheet mechanical properties.

Material	Density (kg/m^3)	Elastic Modulus (GPa)	Tensile Fracture Stress (MPa)	Inter-Laminar Shear Strength (MPa)	Compressive Strength (MPa)
Glass Fibres	2550 [94]	80 [94]	2000 [94]	-	1450 [95]
SR 8500 Resin	984 [96]	3.35 [96]	83 [96]	59 [96]	114 [96]
ST 94 Resin	1021 [97]	3.40 [97]	69 [97]	55 [97]	137 [97]
QE1200/SR 8500 GFRP Ply	1720	15.88	396	59	316
QE1200/ST 94 GFRP Ply	1740	15.90	389	55	328
Innegra IS-940 PP fibres	900 [98]	14.8 [99]	667 [99]	-	39 [98]
Innegra/SR 8500 PP ply	932	5.86	238	59	55

3.2.2 Polymeric Foams

Mechanical testing of the foam materials was performed in order to create material models for finite element analyses (FEA) on blast loading. These mechanical tests are reported in detail in Chapter 6. In this chapter the properties are simply stated. The quasi-static (QS) and dynamic (HR) mechanical properties of the foams are shown in Table 3.3, where the dynamic properties shown are the averages of two dynamic test speeds. This is because the foam showed little rate dependence at dynamic strain rates. It was expected that the important factor in each test would be the fracture strain, as the face-sheets are much stiffer than the foam cores. It can be seen from Table 3.3 that there is a significant difference in tensile fracture strain in each foam. The fracture strains of the SAN Corecell M100 and PVC Airex C70.90 foams are similar when tested at dynamic rates, each failing at about 4.5%, but the fracture strain of the PMI Rohacell 110SL is 2.2%. This explains the increased core cracking witnessed in the PMI Rohacell 110SL core sandwich panel during air blast, as discussed subsequently. The shear failure strains have also been calculated in Table 3.3 using Equation (3.4), where ε_{xy} is the shear strain, τ is the shear stress and G is the shear modulus.

$$\varepsilon_{xy} = 100\,\frac{\tau}{G} \tag{3.4}$$

Table 3.3: Mechanical properties of the foam polymers, including quasi-static (QS) and 180 s^{-1} (HR) rate test results.

Material	Density (kg/m^3)	QS Shear Modulus (MPa)	QS Shear Strength (MPa)	QS Shear Failure Strain (%)*	QS Compressive Modulus (MPa)	QS/HR Compressive Strength (MPa)	QS/HR Tensile Modulus (MPa)	QS/HR Tensile Fracture Stress (MPa)	QS/HR Tensile Fracture Strain (%)
M100 SAN	107.5 [100]	41 [100]	1.45 [100]	3.5	88	1.79/3.4	88/162	2.8/5.7	7.7/4.5
M130 SAN	140 [100]	59 [100]	1.98 [100]	3.4	126	3.03/5.5	133/267	3.8/8.1	7.2/3.8
M200 SAN	200 [100]	98 [100]	2.98 [100]	3.0	239	5.15/10.8	220/436	5.7/7.3	5.6/2.0
C70.90 PVC	100 [101]	30 [101]	1.2 [101]	4.0	88	2.01/ -	71/164	2.8/7.2	9.3/4.4
110SL PMI	110 [102]	55 [102]	2.2 [102]	4.0	76	2.16/ -	139/417	4.1/8.7	5.6/2.2

* Calculated from the quasi-static shear modulus and quasi-static shear strength using Equation (3.4).

3.3 Experimental Methods

3.3.1 Blast Wave Modelling

The blast reflected over-pressure was measured at one location in the centre of the test cubicle underneath the sandwich panels during the blast tests. As such the distribution of loading over the sandwich panel during the test was unknown, as measurements on the surface were not feasible. In order to determine this distribution, the air blast wave computational fluid dynamics (CFD) solver, Air3D, was used to model the blast wave arriving at and travelling over the test cubicle. The CFD solver has no structural capabilities, so there is no deformation of the cubicle or test panels during loading, but it serves to provide an estimate of the distribution over the test panel. The Air3D model utilised 50 mm cube elements, and a time step of 0.002 ms. The element size was determined with the use of a mesh convergence study, the results of which are presented later in this chapter. The timestep of the solution was decided to remain at 0.002 ms, as this correctly predicted the time periods of the blast wave, except for the initial impact on the cubicle front, which would require a timestep which was too small to be computationally efficient. In the CFD model, the floor was perfectly elastic, so 100% of the blast energy was reflected, as was the whole cubicle, which was modelled in full size. The control volume for the analysis was from the centre of the charge to 1 m behind the cubicle, and from the ground to 1 m above the cubicle. The width of the rectangular control volume was 1 m wider than the cubicle, and did not take into account the symmetry of the cubicle in the width direction, so the full cubicle width was modelled. This is because the reflected pressure was to be measured in the centre of the cubicle front, which would cause potential problems if this measurement was on a boundary. All boundaries, except for the floor, were transmissive, so 100% of the blast energy transmitted through them. The reflected overpressure was measured 1 mm in front of the panel, at 476 evenly spaced locations over the location of the test sandwich panels. One more measurement at the location of the reflected pressure gauge was taken. A detailed explanation of the mathematics behind the Air3D solver can be found in Rose [103].

3.3.2 Air Blast Testing

The air blast tests performed used 100 kg nitromethane charges (which had a TNT equivalence of 100 kg), situated at 15 m from the test panel. The stand-off distance from the charge was determined such that core damage, and in some cases front face-sheet compressive damage, would be present in each sandwich panel but no back face-sheet damage. This was due to expensive high speed camera equipment being present in the test cubicle behind the panel, which needed to remain protected from the blast. The charge size and stand-off distance were determined through an analytical solution outlined by Andrews and Moussa [5] for determining the onset of core and face-sheet damage in sandwich composites subjected to blast. Furthermore, the decision was made by considering the damage suffered by similar sandwich panels in research performed by Arora [104], where 25 mm thick SAN Corecell M130 cores, with identical face-sheets as in this research, were subjected to 100 kg TNT equivalent charges at 14 m stand-off distances. It was found that the sandwich panels suffered heavy core and front face-sheet damage, but no back face-sheet damage. In order to decide upon a stand-off distance for the panels tested in this research, the analytical solution by Andrews and Moussa [5] was utilised, with a 100 kg TNT equivalent charge size. This charge size was selected as it would allow a comparison to be made with the research performed by Arora [104], in order to validate and adjust the results from the analytical solution. The boundary conditions in the blast testing are quasi-built-in due to the boundaries being made from steel beams which are flexible. However the analytical solution used here assumes simply supported sandwich panels, so provided an overly conservative result which was corrected by comparison to previous blast test results. The predicted pressure loading (P) with time (t) on the sandwich panel was calculated from the modified Friedlander equation shown in Equation (3.5), where P_s is the peak static overpressure; b is a waveform parameter which is an empirical function of the peak static overpressure; and t^+ is the positive pressure duration of the blast wave. A Friedlander pressure trace is shown in Figure 3.5, with P_r and t^+ highlighted. As outlined by Smith and Hetherington [15], the scaled distance (Z) is generally used when performing blast analyses, which is given in Equation (3.6), where W_{TNT} is the TNT equivalent charge weight; and R is the stand-off

distance. Smith and Hetherington [15] also provide empirical data for the positive pressure time, reflected impulse (I_r), and for the static blast overpressure (P_s) as a function of Z, given by Equation (3.7). This static overpressure was converted into reflected overpressure using Equation (3.8). It was also recommended by Smith and Hetherington [15] that a correction factor of 1.8 be applied to the charge weight for surface bursts, resulting in an effective charge of 180 kg for the 100 kg TNT equivalent charges used in this research. This accounted for the reflections of the blast wave from the floor.

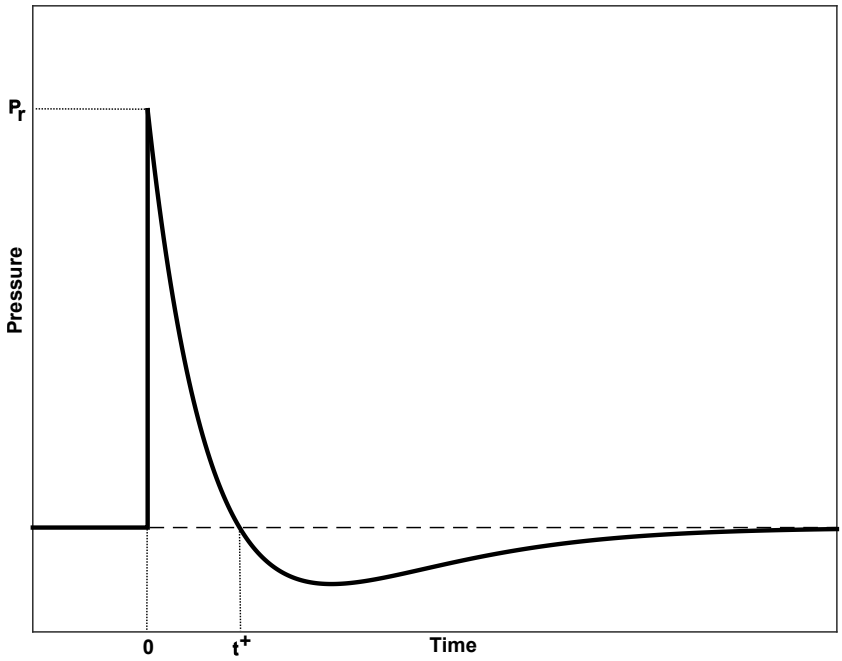


Figure 3.5: Air blast wave loading on a structure.

$$P(t) = P_s \left(1 - \frac{t}{t^+}\right) e^{-b\frac{t}{t^+}} \tag{3.5}$$

$$Z = \frac{R}{W_{TNT}^{\frac{1}{3}}} \tag{3.6}$$

$$P_s = \frac{0.662}{Z} + \frac{4.05}{Z^2} + \frac{3.288}{Z^3}\,[bar] \tag{3.7}$$

$$P_r = 2P_s \left(\frac{7 + 4P_s}{7 + P_s} \right) [bar] \tag{3.8}$$

3.3.2.1 Analytical Prediction

The analytical solution proposed by Andrews and Moussa [5] was first used to calculate the deflection in the sandwich panels required to cause front face-sheet compressive failure, core shear failure and back face-sheet tensile failure. It was assumed in this solution that the failure mechanisms are not coupled, which was inaccurate as core shear failure would clearly lead to stress concentrations in the face-sheets, increasing the likelihood of failure in those locations. However, the solution served to give an indication of the first mechanism of damage to be expected, and how the different materials would behave. The solution was dependent upon a calculation of quasi-static pressure loading to cause damage, and a correction factor based on the natural frequency of the sandwich panel to cause failure under blast. To determine the most suitable stand-off distance for this study, the four single density core sandwich panels tested, as well as the 25 mm thick M130 core sandwich panel and the 40 mm SAN Corecell P800 core sandwich panels tested by Arora [104], were assessed to determine the minimum stand-off distance to protect the back face-sheet. The 40 mm thick P800 sandwich panels were tested with 30 kg Composition-4 (38.3 kg TNT equivalent) charges, at distances of 8 m, 14 m and 16 m. This was of interest in this research due to front face-sheet compressive cracking, and core shear cracking being present in the 8 m case, but not the 14 m and 16 m cases, allowing for minor calibration of the analytical method. The stand-off distances to cause the different modes of failure for each panel are shown in Table 3.4. It can therefore be seen that the method accurately predicts the distance to cause front face-sheet damage, which would in turn cause core cracking which is not predicted by this method, for the lower charge size of 38.4 kg, but for the 25 mm thick M130 sandwich panel, predicts that at any distance below 18.3 m the panel will suffer all three modes of damage. With the fact that the test actually has much stiffer boundary conditions than in this model, and that the blast wave pressure prediction is conservative, a stand-off distance of 15 m was selected, slightly closer than the 16.8 m predicted by the model to cause rear face-

sheet damage. This was chosen to ensure that the maximum amount of damage was witnessed, while still protecting the camera equipment. Also, by choosing a stand-off distance so near to the prediction of the analytical model, it was expected that any rear face-sheet damage would not be catastrophic.

Table 3.4: Damage results according to the analytical solution proposed by Andrews and Moussa [5].

Panel Description	Distance to cause core shear failure (m)	Distance to cause front face-sheet compressive failure (m)	Distance to cause rear face-sheet tensile failure (m)
Single 40 mm M100 SAN Core	28.6	18.4	16.9
Single 40 mm C70.90 PVC Core	26.1	20.0	16.8
Single 40 mm 110SL PMI Core	20.4	15.2	16.8
Single 30 mm M130 SAN Core	27.1	17.3	18.5
Single 25 mm M130 SAN Core	29.5	18.3	19.5
Single 40 mm P800 SAN Core	12.2	8.2	8.9

3.3.2.2 Blast Test Design

The design of the air blast testing was such that the charge was located 15 m horizontally from the sandwich panel, and 1.2 m off the ground, placing it in the vertical centre of the test panel. Two panels were placed side-by-side in the reinforced steel test cubicle, and a reflected pressure gauge was located in the centre, underneath the two panels. The test cubicle consisted of a reinforced steel front, bolted to large concrete culverts, to provide a rigid foundation to the cubicle front. A schematic of the steel front to the cubicle is shown in Figure 3.6, and Figure 3.7 shows the test cubicle from the side, as well as showing the dimensions

of the concrete culverts. The reflected pressure gauge location, as well as the opening for the test panels, can be seen in Figure 3.6, and the fixing method of the steel front to the concrete culverts is shown in Figure 3.7, which consisted of six M24 bolts. The back steel face is also shown, which was similar in construction to the front steel face. In order to securely fix the sandwich panels into the test cubicle, 100 x 6 mm steel strips were attached to the edges of the sandwich panels using Sikaflex 291i marine sealing adhesive. The adhesive was not intended to provide any structural contribution to the boundary conditions during the test, but was simply to aid in assembling the test structure, as it was strong enough to permanently fix the steel strip to the panel. These steel strips were attached to both sides of the sandwich panel. The bolt holes for attaching in the test panel to the cubicle went through both the steel strips and the composite sandwich structure. In order to prevent the core from crushing upon tightening of the bolts, steel tubes were placed inside the holes in the sandwich panel such that the ends were against the steel strips. These were inserted before the steel strips were attached. A schematic of the front of the test cubicle with the panel in place, and of the clamping arrangement is shown in Figure 3.8. A schematic of the whole blast test layout is shown in Figure 3.9. A thick steel plate was placed under the charge to create an elastic foundation for the very high energy initial blast wave from the detonation, but after that the reflecting surface was simply the concrete floor. The height of the charge was set using polystyrene foam, which offered negligible blast energy absorption. The reflected pressure gauge used in the test was a PCB 102A06 and was housed inside a steel box for measuring the pressure. The box contained a Nylon disk at the front, which acted to distribute the load evenly to the pressure sensor, to avoid the effect of the highly pressurised air particles from wrapping around the front of the pressure sensor making the reading inaccurate. The Nylon disk was supported on three brass pins inside the pressure transducer housing. Figure 3.10 shows a schematic of the reflected pressure sensor housing, which was bolted to the front of the test cubicle. In order to validate blast calculations a side-on pressure gauge was situated at 15 m from the centre of the charge, at the same height. The reflected pressure sensor was situated normal to the blast wave direction, measuring the pressure as the air particles came to rest against the surface. The side-on pressure gauge was parallel to the blast wave, so measured

the static pressure as the air particles moved over the face of the pressure sensor. To reduce the disruption of the flow over the surface of the side-on pressure sensor, a thin steel plate was used, with a PCB 102A06 sensor in the centre, as shown in Figure 3.11.

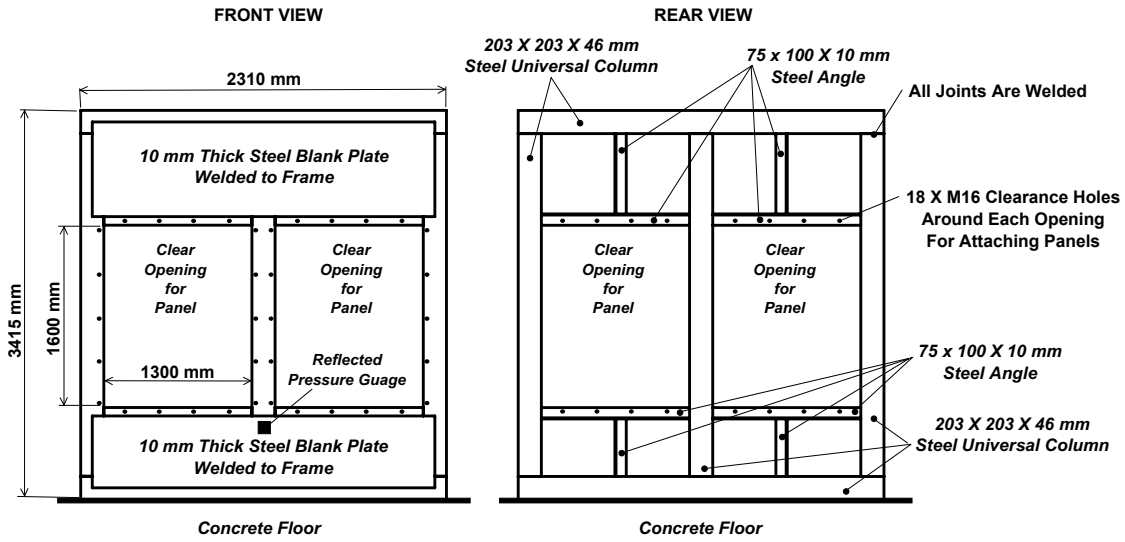


Figure 3.6: Schematic of the steel front of the test cubicle.

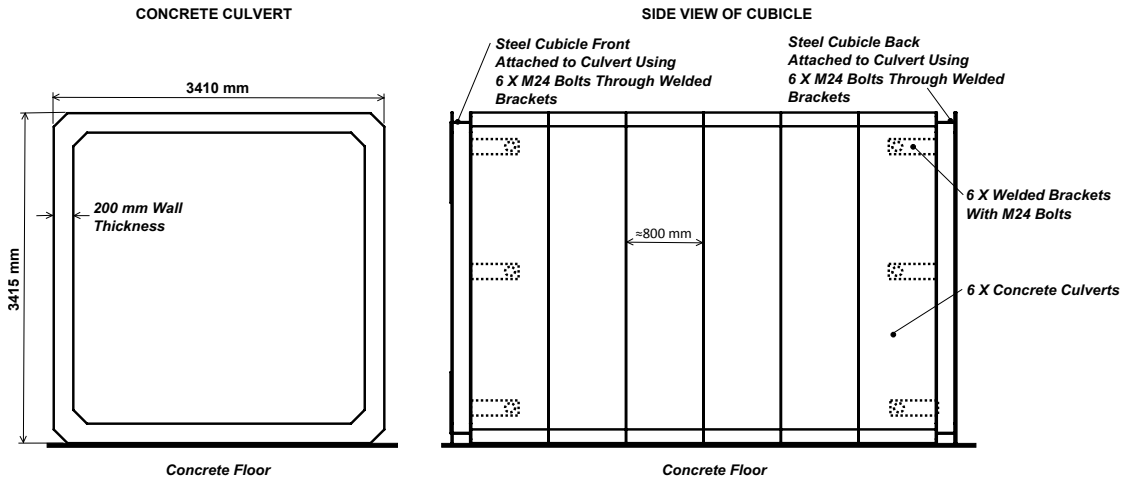


Figure 3.7: Schematic of the test cubicle, showing the concrete culverts.

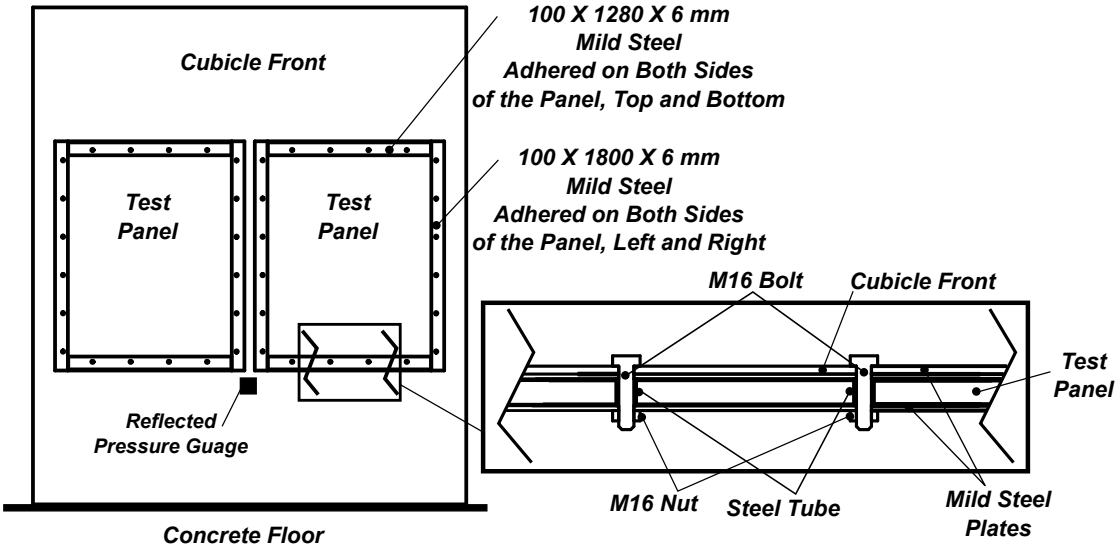


Figure 3.8: Schematic of the front of the test cubicle and the test panels. Also shown is the clamping arrangement of the sandwich panels onto the cubicle front.

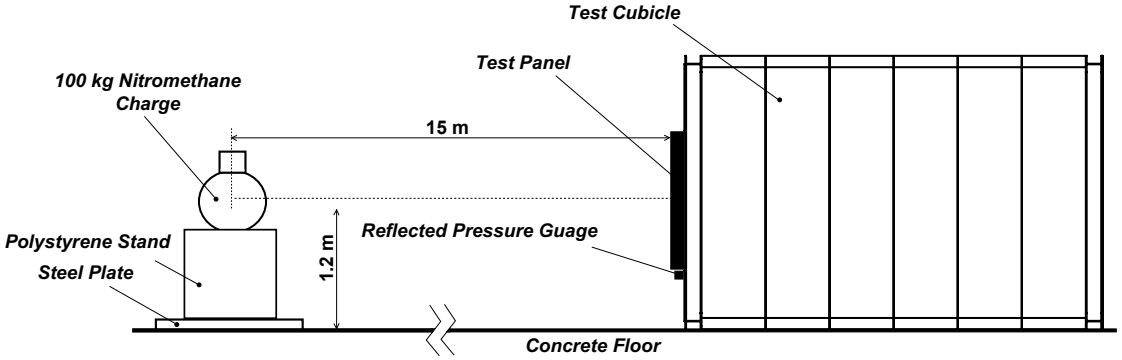


Figure 3.9: Schematic of the blast test layout.

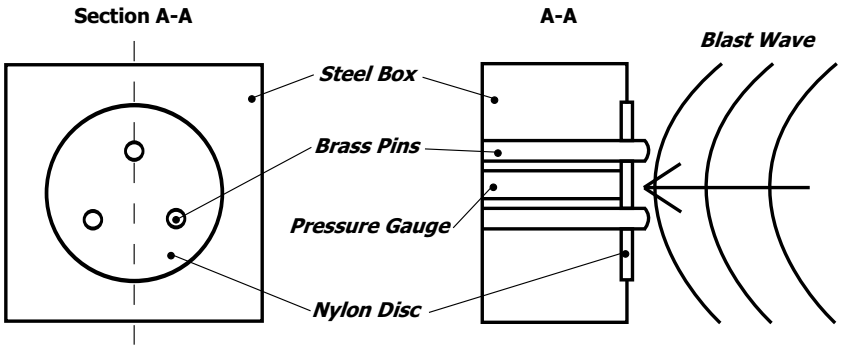


Figure 3.10: Schematic of the reflected pressure gauge.

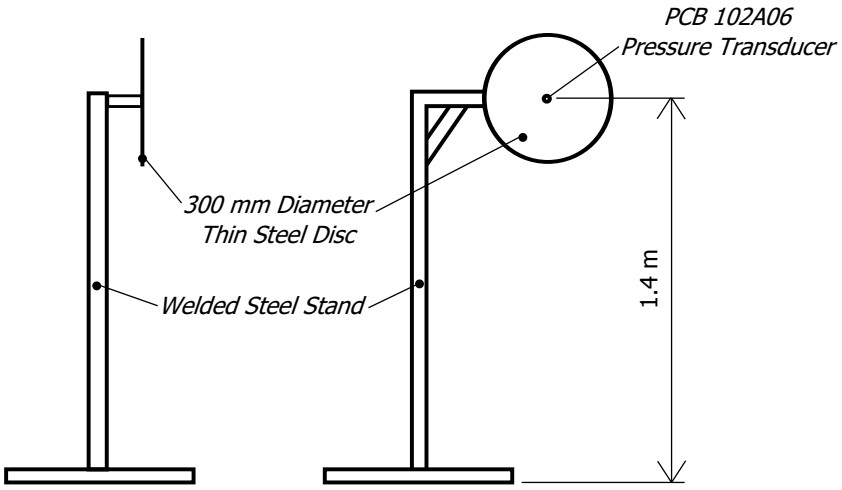


Figure 3.11: Schematic of the static pressure gauge.

3.3.3 Digital Image Correlation

The main measurement technique used in the blast tests was high speed 3D digital image correlation (DIC). This technique used two identical high speed cameras located such that their angles of incidence to the surface being measured were approximately 25°. The high speed cameras were triggered by a transistor-transistor-logic (TTL) signal produced by one camera but received by both, to ensure they were both triggered at the same time. This signal circuit was open before detonation as the other ends of the electrical cables were not connected. These open ends were taped to the side of the charge, and the TTL circuit was completed by the ionising of air around the charge upon detonation. The two cameras were synchronised using a TTL signal between the two cameras, with the signal generated by one camera and received by the other. The 5 V TTL signal was sent every time the shutter opened, to ensure that the two shutters operated at the same time.

Calibration of the two high speed cameras was achieved by taking numerous images of a calibration object known to the GOM Aramis software, so the location of the two cameras in 3D space was determined. The test panel was covered in a random black speckle pattern on a white painted background, which was then tracked by the Aramis DIC software as the surface deformed. As the deformation was recorded by both cameras, and with the 3D space mapping, it was possible to track the speckled surface in 3D. Full details of this technique are provided

in Sutton et al. [105]. The calibration cross used was supplied by GOM UK, and was a "CC20" pattern. Calibration images of two of the cameras are shown in Figure 3.12, and also shown in these images are a speckled test panel, and the inside of the cubicle front. It can be noted from these images that the two universal columns either side of the test panel were speckled, and this was so that rigid body movement of the cubicle front during blast loading could be removed, so that the data collected was of the test panel relative to the boundaries. Two pairs of identical high speed cameras were used in the blast tests, each with Nikon 50 mm fixed focal length lenses. The high speed cameras were Photron SA1.1's and Photron SA5's. The camera specifications used for the tests are shown in Table 3.5. The Photron SA1.1 camera had a Bayer colour sensor which worked by applying a filter to each pixel, allowing only red, green or blue wavelengths of light through. The pixel filters were arranged in rows, such that a row either contained red and green, or blue and green filters in a pattern as shown in Figure 3.13. As with most digital sensors, the photons of light were then quantised into one of 4096 intensity levels, as the sensors were 12-bit, through the analogue to digital converter (ADC). With the Bayer filters 50% of the pixels received green light, 25% received blue light and 25% received red light. The camera then took the value from each overlapping block of four pixels, to determine the RGB level in that location, resulting in images which were missing information on the outer most edges of the images (1022 x 1022 in this case). However, for commercial suitability the outer pixel values were extrapolated, which was unimportant here due to the data at the edges being lost. It should be noted that the images from the greyscale Photron SA5 camera were saved in 16-bit, so some smoothing of the data took place in converting from 12-bit to 16-bit. In the case of a single greyscale sensor, the information at each pixel was simply saved as a greyscale value. The Photron SA1.1 RGB images were kept at 12-bit, which was the same as captured by the sensor. For the DIC technique employed by the Aramis software to work, it was necessary for the images to be in 8-bit greyscale format, an operation performed by Aramis in the later versions, as used in this research. The algorithm used to convert the RGB images to greyscale is shown in Equation (3.9), and the formula to convert each pixel from 12-bit or 16-bit to 8-bit is given in Equation (3.10), where the bit depth of a 12-bit image is 4,096, and the bit-depth of a 16-bit image

is 65,536. The factor is multiplied by the 8-bit bit depth minus one, as for an image the 8-bit greyscale range is 0-255, not 1-256 as implied by 8-bit. The conversion of the 12-bit greyscale images from the sensor to the 16-bit image saved in the camera use the same form of equation as in Equation (3.10). While it is difficult to quantify the effect of these factors on the error experienced by the system, it is worth considering them to develop an understanding of the limitations of the technique for this application, especially when colour high speed cameras are used. In order to do this the noise present using DIC from before the blast wave arrived at the sandwich panels was measured, to account for measurement inaccuracies as well as external factors such as wind loading the test structure. This error analysis is detailed in Appendix B and uncertainty values for out-of-plane displacement and the core shear strain are presented.

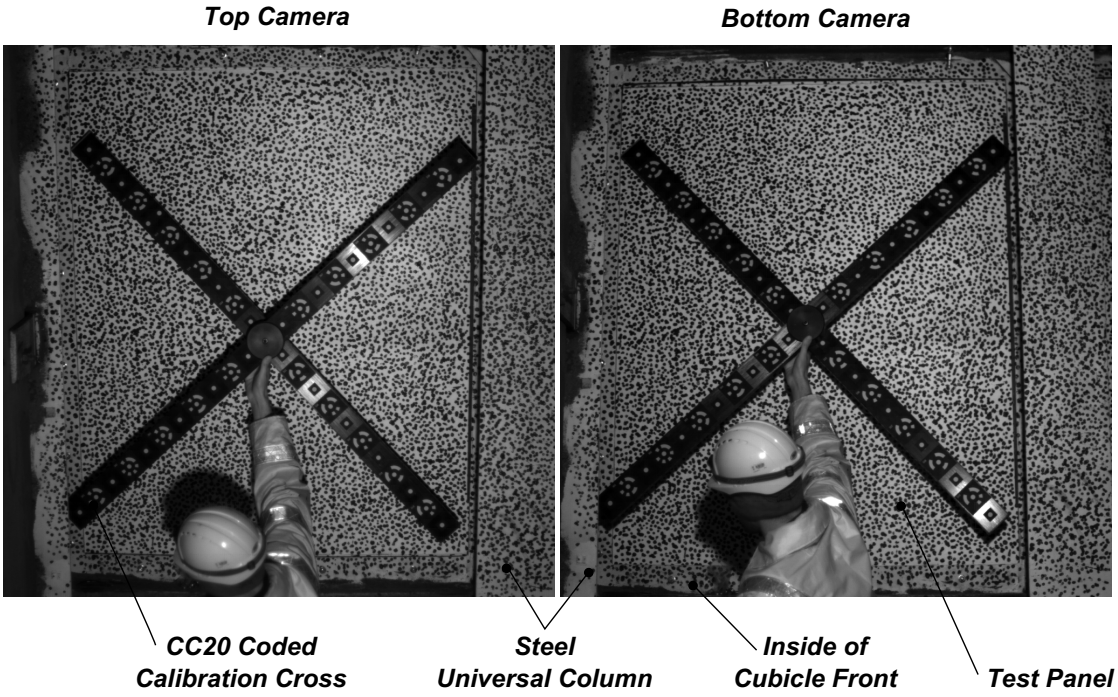


Figure 3.12: Top and bottom camera images of the CC20 calibration cross.

$$Greyscale = 0.25Red + 0.50Green + 0.25Blue \tag{3.9}$$

Table 3.5: Specifications for the high speed cameras used to record the panel responses to blast loading [6] [7].

	Photron SA1.1	Photron SA5
Resolution (pixels)	1024 x 1024	1024 x 1024
Frame Rate (frames/s)	5400	7000
Pixel Size (μm/pixel)	20	20
Sensor Description	12-bit ADC Bayer colour	12-bit ADC single
Record Duration (s)	1.56	2.02
Shutter Exposure Time (μs)	0.5	0.16

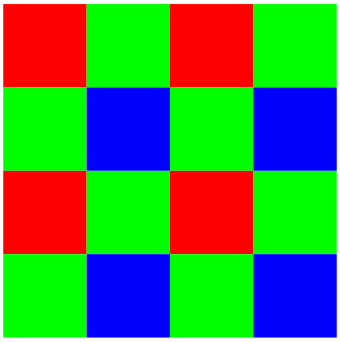


Figure 3.13: Pixel filter order in a Bayer sensor.

$$8\ Bit\ Pixel\ Value = \frac{12\ bit\ or\ 16\ bit\ pixel\ value}{12\ bit\ or\ 16\ bit\ depth}\,(8\ bit\ depth) - 1 \tag{3.10}$$

The angle between the incidence of the two cameras during DIC was recommended by the Aramis manual as 25° [106], and due to the large size of the test panels 50 mm focal length lenses were used on each camera. As the high speed cameras contained the same size sensors, the calculation of setup parameters was identical in each case. The overall camera setup of the high speed camera equipment for blast testing is shown in Figure 3.14. A diagram to aid in explaining the calculation procedure for the camera positions is shown in Figure 3.15, where D_C is the distance from the centre of the panel to the centre of the camera sensor; D_1 is the distance of the centre of the sandwich panel to the camera beam; and D_2 is the distance between the high speed cameras on the camera beam. The formula for calculating the distance from the centre of the panel to the centre of the camera sensor is given in Equation (3.11), and Equation (3.12) provides the distance of the line of the two camera sensors to the speckled panel surface. The distance between the cameras is given by Equation (3.13). It was recommended by the Aramis user manual that each speckle is 3-5 pixels in diameter [106], and that there is roughly a 50% coverage of speckles on the surface. The largest dimension of interest was 1.7 m, and the sensor had 1024 pixels across, meaning that each pixel represented 1.66 mm on the sandwich panel surface. Therefore each speckle was made to be between 5 mm and 10 mm in diameter. An example of the speckle pattern can be seen behind the calibration cross in Figure 3.12.

$$D_c = \frac{0.85\ sin\,(91.2°)}{sin\,(11.3°)} \tag{3.11}$$

$$D_1 = D_c\ cos\,(12.5°) \tag{3.12}$$

$$D_2 = 2D_c\ sin\,(12.5°) \tag{3.13}$$

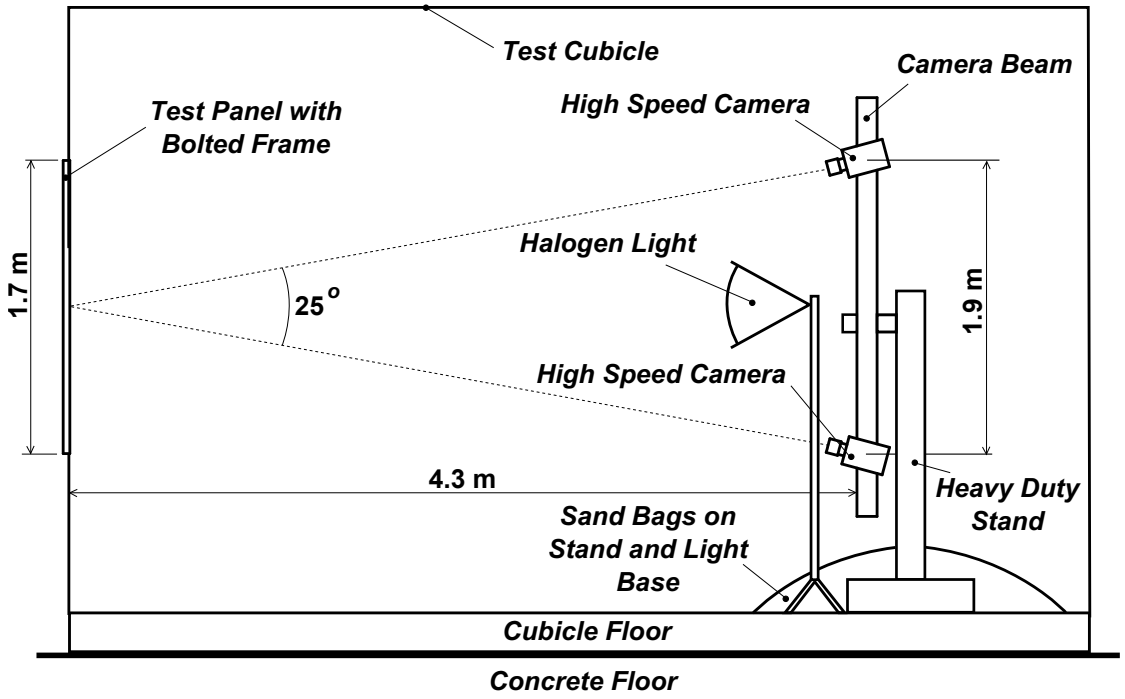


Figure 3.14: Schematic of the high speed camera equipment inside the test cubicle.

3.3.3.1 Digital Image Correlation Data Processing

The high speed images recorded during blast were processed with the 3D DIC software, Aramis, and all of the raw data was exported for post-processing in MATLAB. The data exported from Aramis was taken at coordinate points approximately 1 mm apart, and linearly interpolated into a grid pattern of exactly 1 mm spacing in MATLAB, to provide a more usable data set. As these coordinates were points in 3D space and time, it was possible to calculate shear strain, displacement and velocity in all three directions. The raw out-of-plane displacement and maximum principal strain data exported from Aramis is shown in Appendix A, for the five air blast panels for which DIC data was obtained. The initial data to be drawn from the DIC results was the out-of-plane displacement of each panel, as this provided an understanding of the resistance of the construction to blast. As will be shown in the DIC results, the failure mechanisms during blast loading were firstly core cracking and debonding between the core and face-sheet, and then front face-sheet failure. Until failure took place, it was assumed that

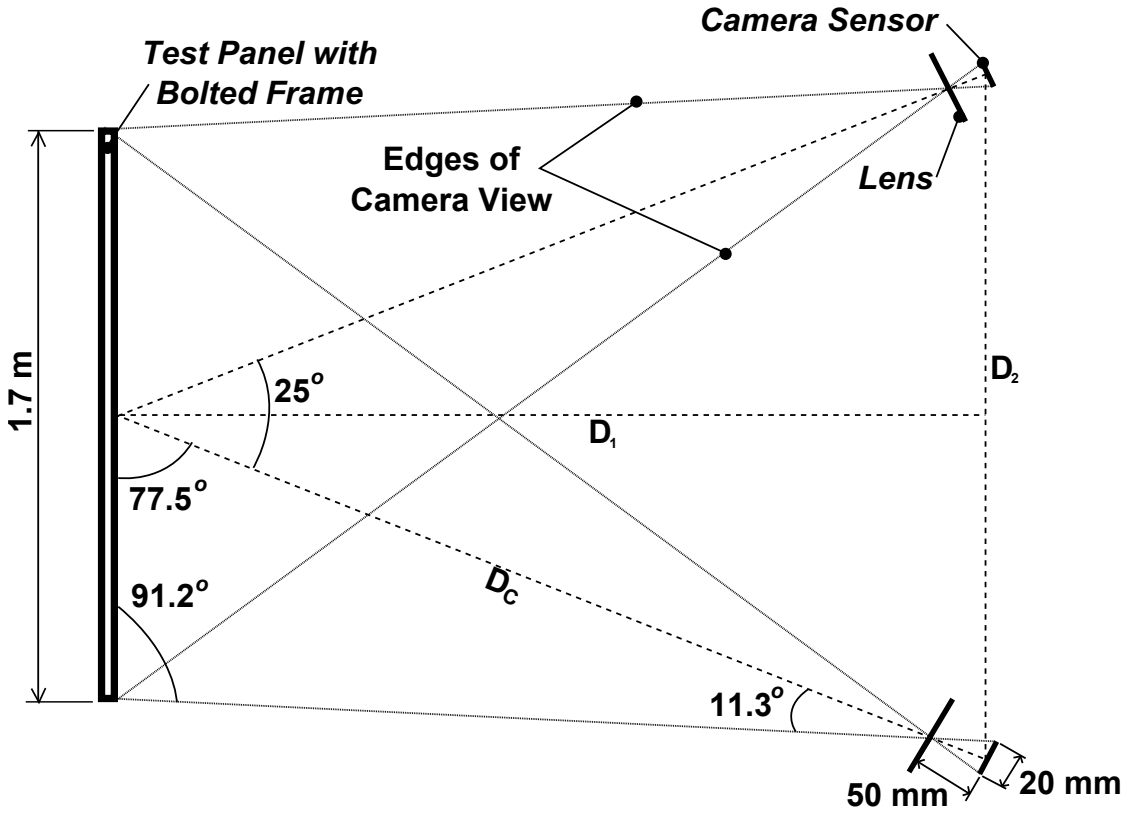


Figure 3.15: Calculation of the camera locations for 3D DIC.

the in-plane displacements of the two face-sheets were identical in magnitude and opposite in direction, and that the out-of-plane displacement of both face-sheets were completely identical. The assumptions rely upon there being no membrane effects in the sandwich panel, so that the centreline strain is zero throughout deformation. This allows the shear strain in the foam core (γ) to be calculated. In order to calculate the core shear strain, the deformed shape of each 1 mm by 1 mm DIC facet was considered, as shown in Figure 3.16. This method was only performed across the horizontal centre of the panel, as this is where the shear strain was greatest. The shear strain was calculated using Equation (3.14), where α was calculated using Equation (3.15), and β was calculated using Equation (3.16). In Figure 3.16, Equation (3.15) and Equation (3.16), Δx is the in-plane horizontal displacement calculated from the back face-sheet strain; d is the out-of-plane displacement of each facet; x is the size of the facet (1 mm); h is the thickness of the foam core; and the subscript n refers to the facet number. It should be noted that an assumption of a zero centreline strain resulting in no membrane effects is unrealistic, as under such large deformations membrane effects will take place. However, without strain measurements on the front face-sheet it was not possible to measure the membrane strain in the sandwich panel. As such the core shear strain values are an approximation and provide comparative values only.

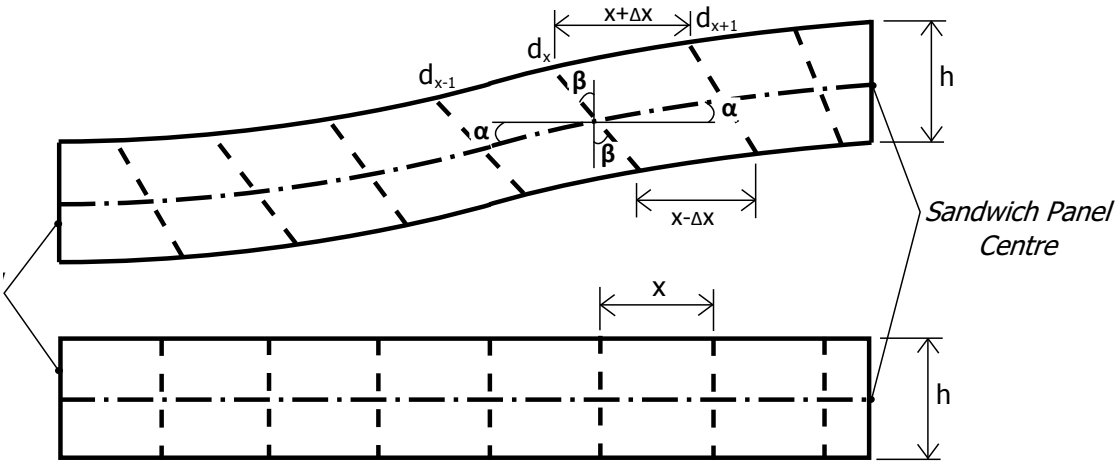


Figure 3.16: Diagram showing the definition of α and β in calculating the core shear strain.

$$\gamma = \alpha + \beta \tag{3.14}$$

$$\alpha = \frac{1}{2}\, tan^{-1}\left(\frac{d_{n+1} - d_{n-1}}{2x}\right) \tag{3.15}$$

$$\beta = tan^{-1}\left(\frac{2\Delta x}{h}\right) \tag{3.16}$$

The final stage of the DIC processing was to use the out-of-plane displacement to calculate the velocity (v) of each facet, and thus the kinetic energy (KE), using Equation (3.17), where M is the mass of the facet. Using the method described previously for predicting the pressure distribution across the sandwich panel surface, the work done (WD) was calculated using Equation (3.18), where P_r is reflected pressure on the facet, A is the facet area and d is the out-of-plane displacement of that facet. By using Equation (3.19), where SE is the strain energy and PE is the plastic energy is permanently deforming the material, it was possible inspect the drop in strain energy in the structure when fracture took place. It was assumed that the plastic energy dissipated was negligible as all damage was brittle in behaviour.

$$KE = \frac{1}{2}Mv^2 \tag{3.17}$$

$$WD = P_r\, A\, d \tag{3.18}$$

$$WD = KE + SE + PE \tag{3.19}$$

3.3.4 Post-Blast Damage Assessment

The second set of measurements taken from the blast tested panels was from post-blast damage inspection. This technique involved sectioning the test panels, photographing each edge of each section, and mapping the core shear cracks and debonding between the face-sheets and core in each. Each sandwich panel was sectioned such that post-blast flexural and compression testing could be performed,

meaning that the sections were of different sizes. The results of these tests are presented in Chapter 4, and the key to the sections cut out of the blast panels is shown in Figure 4.1 in Chapter 4. The section edge photographs were taken in line with a steel rule, to allow for size calibration of the images, and a MATLAB script created which loaded each image to the screen for the user to click on each corner of each straight section of core crack, as well as each corner of each length of face-sheet to core debond. An example of a damaged PVC Airex C70.90 core sandwich panel sample is shown in Figure 3.17, and the edges of the core cracks and debond are shown, as would be selected in the MATLAB script. These selections are then connected with straight lines. This MATLAB script allowed the location of every type of damage to be recorded, to produce damage maps highlighting where most damage took place during blast. The percentage of damage and the magnitude of damage were also recorded, the latter being possible with calibration from the steel rule present in the photographs. With a full coordinate system of damage on the section edge, it was possible to find the full length of cracks and debonds, and as such estimate the total amount of damage for the section. For each of the front and rear face-sheet to core interfaces, the percentage of the section edges containing debond was found, to provide an overall percentage debond for the section. The estimates of the cracks travelling through the core were a little more difficult to obtain, due to the paths of the cracks inside the sections being unknown. Three measurement estimates were taken from tracking core cracks: the total number of through thickness cracks; the total cracked surface area; and the total percentage of each section edge containing any cracks. The total number of through thickness cracks for the section (N_C) was calculated from the sum of the cracks over one face of the section, multiplied by the length of the face (L or W), and then divided by the total of the four face lengths. This is described in Equation (3.20), where W and L are defined in Figure 3.18, and the subscripts refer to the two length and two width faces. N_{CL} and N_{CW} refer to the number of cracks across the length face and width face respectively. The total cracked surface area (A_C) was calculated by taking the average total crack distances of two opposing faces, multiplying them by the distance between the two faces, and taking the sum of this and the other two faces. This is shown in Equation (3.21), where L_C and W_C are the lengths of each crack along the length and width faces respectively, referred to by the subscript.

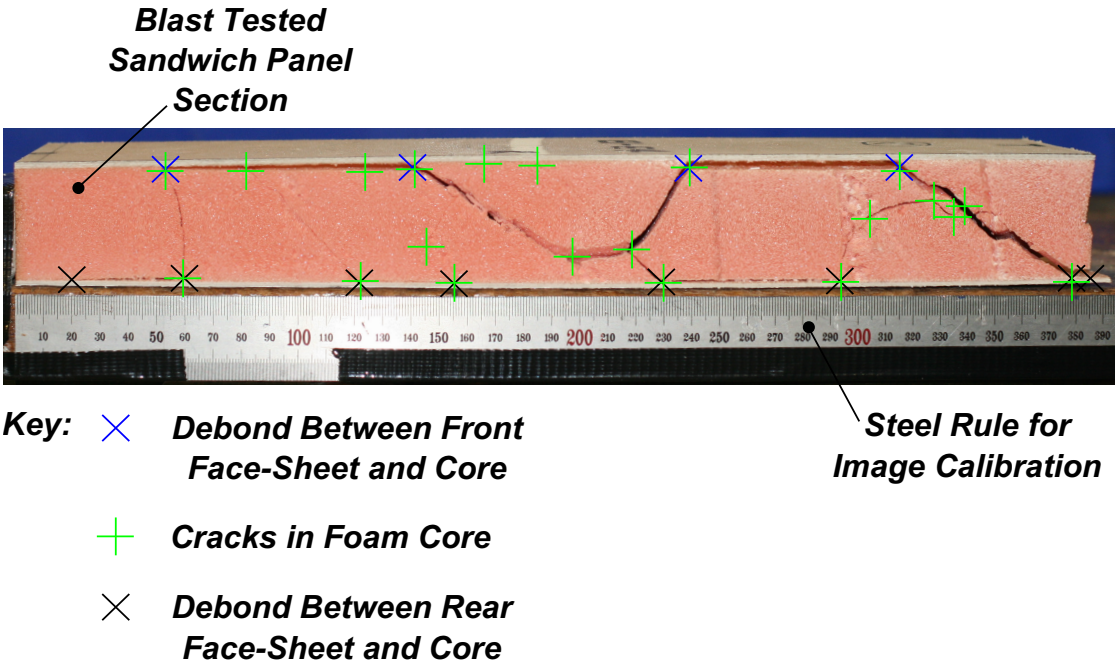


Figure 3.17: Damage mapping of a section of the PVC Airex C70.90 blast panel.

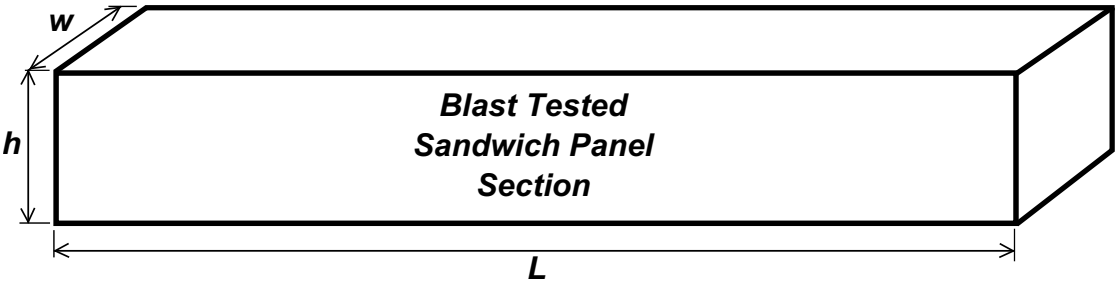


Figure 3.18: Post-blast section dimension key.

$$N_C = \frac{N_{CL_1} L_1 + N_{CL_2} L_2 + N_{CW_1} W_1 + N_{CW_2} W_2}{L_1 + L_2 + W_1 + W_2} \tag{3.20}$$

$$A_C = \frac{\sum L_{L_1} + \sum L_{L_2}}{2} W + \frac{\sum L_{W_1} + \sum L_{W_2}}{2} L \tag{3.21}$$

3.4 Results

3.4.1 Blast Pressure

As the full cubicle was modelled in the Air3D simulations, a mesh convergence study was necessary to understand the effect of element size on the results. For this convergence study element sizes of 150 mm, 100 mm, 75 mm, 50 mm and 25 mm were used. The pressure traces predicted by the simulations at the location of the reflected pressure gauge are shown in Figure 3.19. The convergence study shows that reducing the mesh size acts to increase the accuracy of the initial pressure spike, and to model this spike more accurately would require an inefficient amount of computational time. The 25 mm mesh study took 28 hours to process 10 ms of loading data, resulting in the 50 mm mesh being used for further simulations, due to unjustifiable computational expense. A comparison of the Air3D results using a 50 mm mesh to the pressure measured in the first blast test and to the pressure trace calculated using the Friedlander equation is shown in Figure 3.20. This comparison shows very close agreement between the pressure trace predicted using Air3D and that measured during the test, and the pressure traces measured in the other two tests were consistent with test one and as such the Air3D pressure trace. The pressure trace predicted using the Friedlander equation has a much greater decay time, and this is likely to be faster in reality due to clearing of the air particles around the sides of the test cubicle, whereas the reflected pressure calculated using the Friedlander equation assumes an infinitely large reflecting surface. In order to account for the small variation in the simulation and test results, however, the distribution of pressure over the surfaces of the sandwich panels was recorded from the simulations as a percentage of the pressure recorded at the gauge location at each time increment, to provide a non-dimensional pressure

distribution over the surface. The pressure distribution is shown for the left hand sandwich panel in Figure 3.21. This distribution is used in the energy balance equations for each sandwich panel, by multiplying the percentage by the pressure value measured during the test at the gauge location. The frames from an external camera are also shown for the blast test performed on the 110SL PMI sandwich panel, and the PP fibre Innegra sandwich panel, in Figure 3.22.

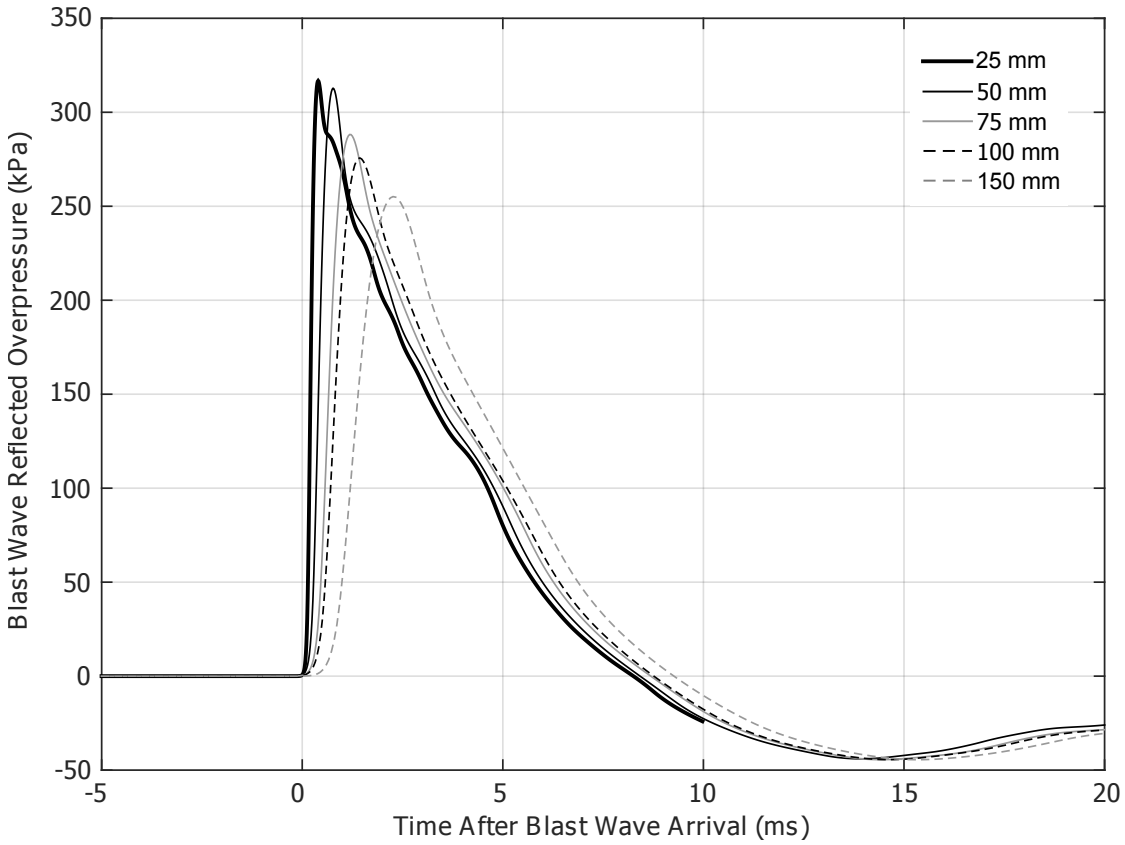


Figure 3.19: Mesh convergence study using element sizes of 25 mm, 50 mm, 75 mm, 100 mm and 150 mm, for the Air3D blast wave simulation.

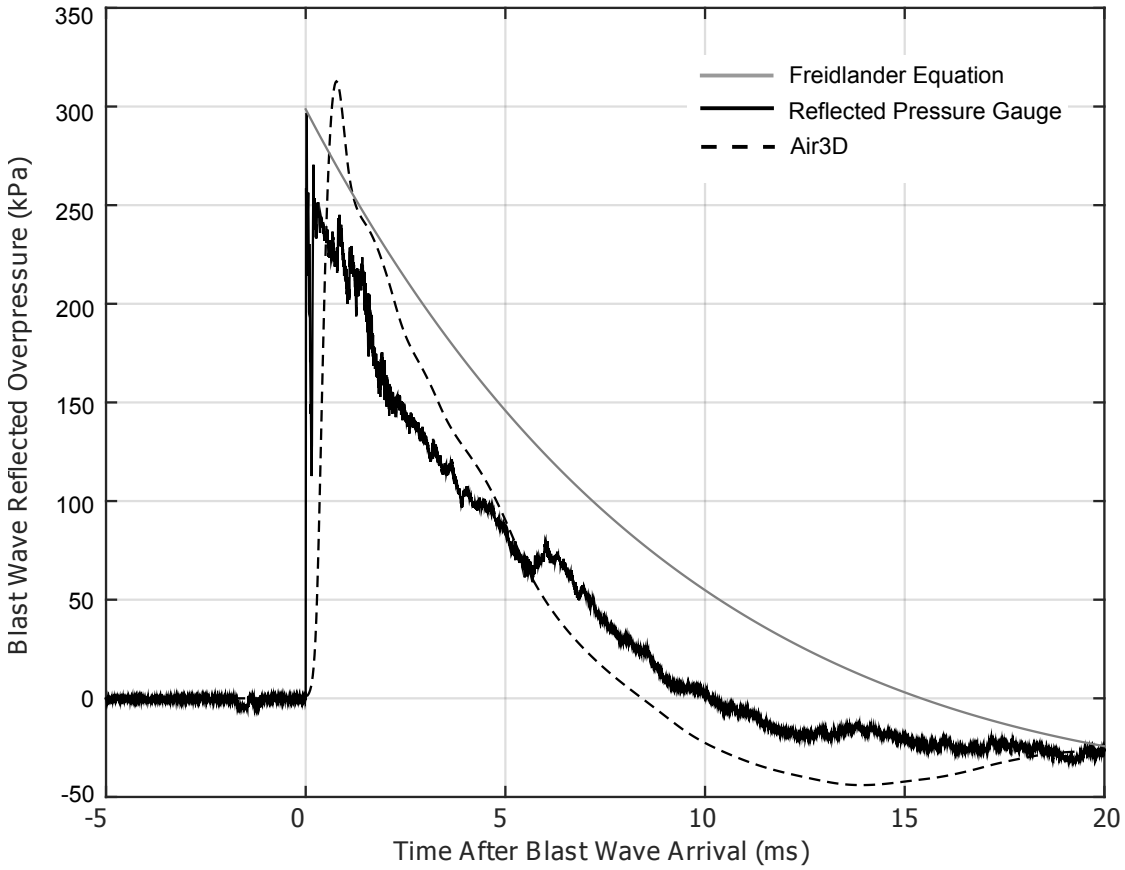


Figure 3.20: Comparison of the pressure calculated at the gauge location using the Friedlander equation and using Air3D, and the pressure measured during the first blast test.

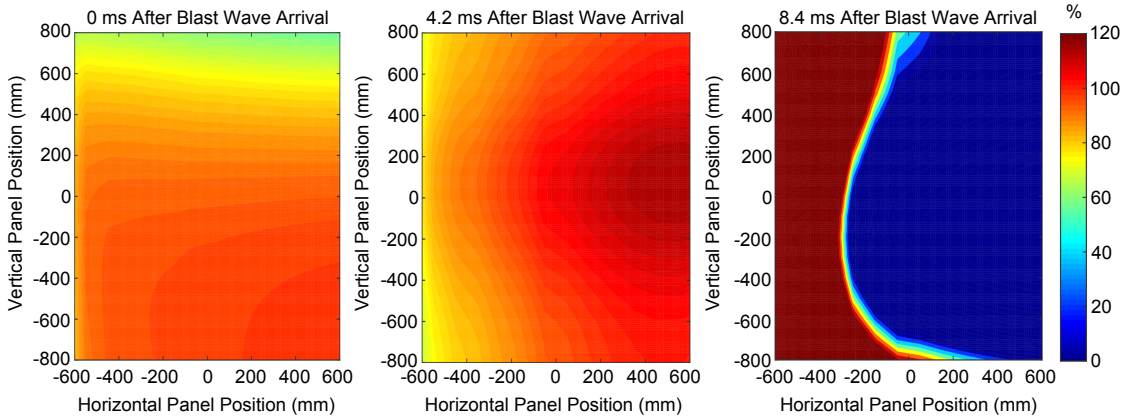


Figure 3.21: Pressure distribution across the front face of the sandwich panel as a percentage of the pressure at the reflected gauge location.

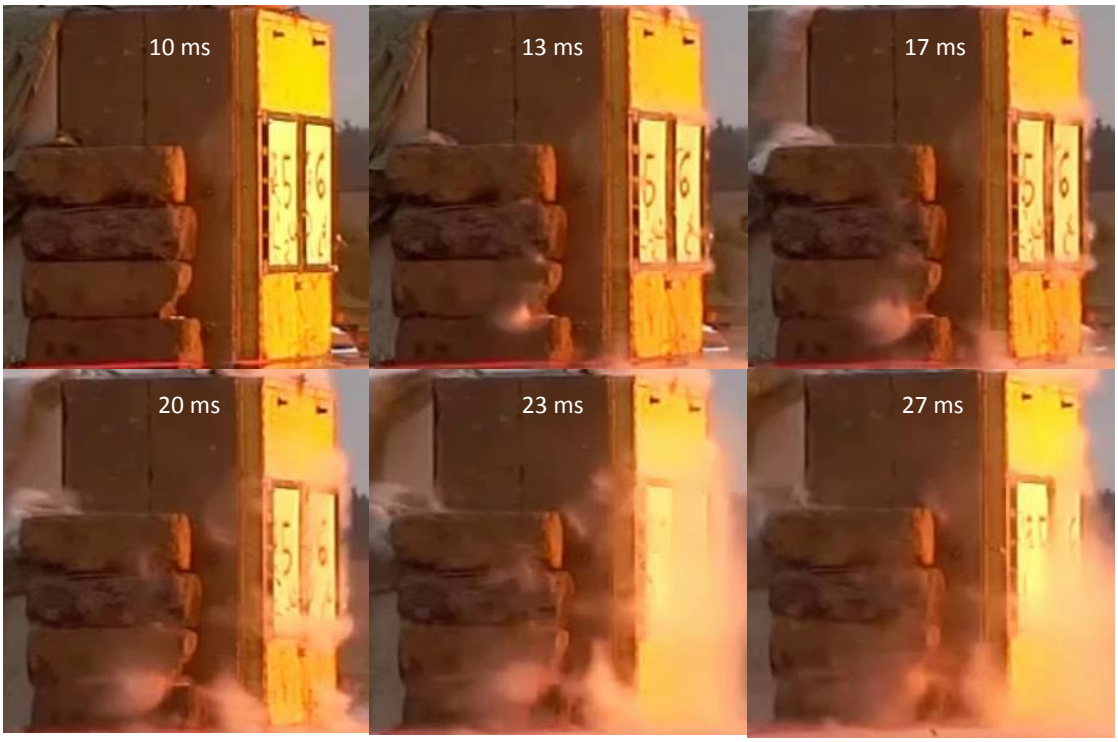


Figure 3.22: Frames taken from an external camera during blast testing of the PMI Rohacell 110SL sandwich panel and the PP fibre Innegra front face-sheet sandwich panel. Also shown is the time from detonation, at the top of each frame.

3.4.2 Out-of-Plane Displacement

3.4.2.1 Foam Polymer Comparison

The out-of-plane displacement contour plots of the 40 mm thick PVC Airex C70.90 foam core sandwich panel are shown in Figure 3.23. This figure shows the DIC results for every high speed camera image captured, from the time of arrival of the blast wave through to the first maximum pull-out of the panel and on to the peak out-of-plane deflection on the second oscillation, at 26.6 ms after blast wave arrival. Beyond this point the panel oscillates at a natural frequency until coming to rest, but due to dust and water it was not possible to capture DIC results past the points shown in Figure 3.23. The contour plots clearly show the "bathtub" shaped loading in the sandwich panel, caused by large amounts of bending one quarter into the panel. These contour plots are shown as an example of the results of DIC, but as the maximum bending takes place across the horizontal centre of the sandwich panels, it is more suitable to display the results as edge contour plots, as shown for the PVC Airex C70.90 sandwich panel in Figure 3.24. The initial, positive out-of-plane displacement of the PVC Airex C70.90 foam core sandwich panel is shown in Figure 3.24a, up until the centre of the panel reaches the maximum displacement, and the return of the panel to zero and then the pull-out is shown in Figure 3.24b. The horizontal contour plots for the 40 mm thick SAN Corecell M100 foam core sandwich panel are shown in Figure 3.25, with the initial deflection shown in Figure 3.25a and the rebound and pull-out shown in Figure 3.25b. Figure 3.26 shows the horizontal section profiles of the 40 mm thick PMI Rohacell 110SL sandwich panel, with Figure 3.26a and Figure 3.26b showing the deflection and rebound phases respectively. From the three sets of deflection contour plots it is clear that there is little difference between the initial displacement shapes, and that in all cases the foam cracks at around one quarter and three quarters across the width of the panel, causing high displacement gradients in these locations. However, the pull-out in the PMI and PVC cases shown in Figure 3.24b and Figure 3.26b respectively, are much greater than the pull-out in the SAN case shown in Figure 3.25b. This is due to much less core damage in the SAN case than in the PVC and PMI cases, meaning that it is more resistant to the momentum and negative pressure bending which causes the pull-out. The difference in core

damage does not change the initial deflection shape, as at the point of damage the velocity of the panel is almost at rest, however, this is not the case on rebound, as the damage is present throughout.

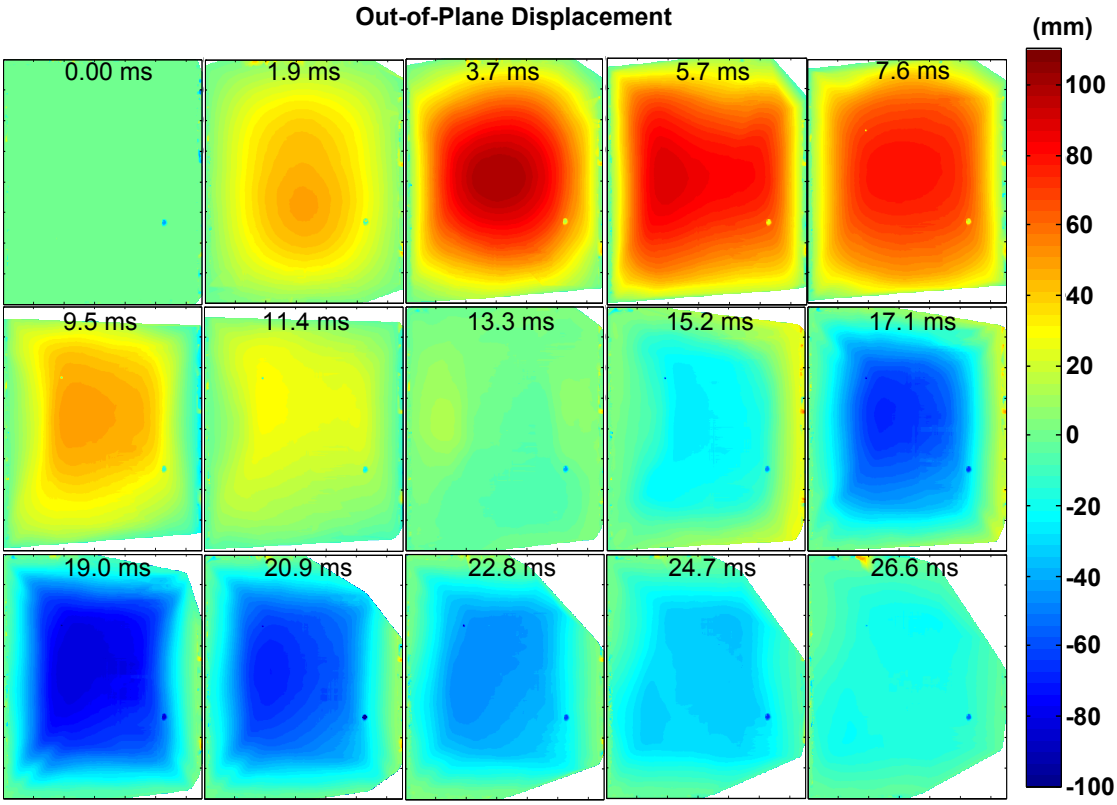


Figure 3.23: Contour plots of out-of-plane displacement of the 40 mm thick PVC Airex C70.90 foam core sandwich panel.

The horizontal deflection shapes show that the maximum displacement of the sandwich panels take place at the centre and at the two quarter points across the centre of the sandwich panel. It is, therefore, possible to assess the strength of the sandwich panel by considering these three points over time, as with more damage present the maximum deflection and pull-out are greater, as well as the rebound time to reach the maximum pull-out, due to reduced stiffness of the damaged sandwich panel. The central deflection, and left and right quarter deflections for the 40 mm thick PVC Airex C70.90 core sandwich panel are shown in Figure 3.27, and Figure 3.28 shows the same traces for the 40 mm thick M100 SAN core sandwich panel. The quarter and central point deflections of the 40 mm thick PMI Rohacell

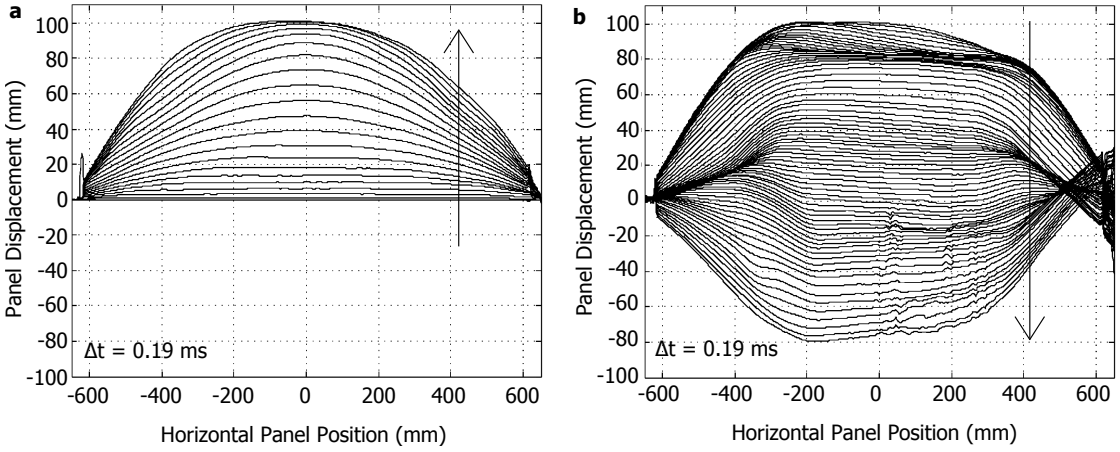


Figure 3.24: Out-of-plane displacement of the horizontal centre section of the 40 mm thick PVC Airex C70.90 foam core sandwich panel for a) the initial displacement; and b) the rebound.

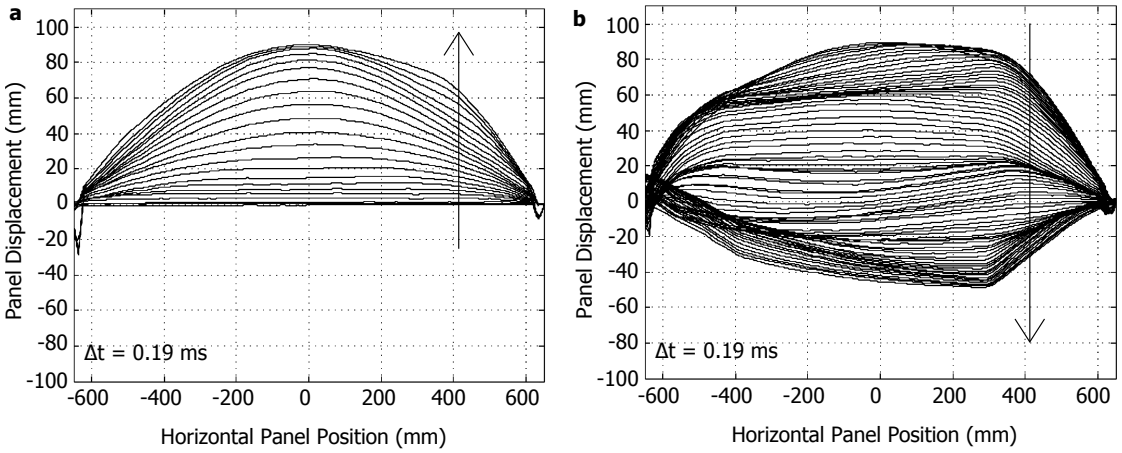


Figure 3.25: Out-of-plane displacement of the horizontal centre section of the 40 mm thick SAN Corecell M100 foam core sandwich panel for a) the initial displacement; and b) the rebound.

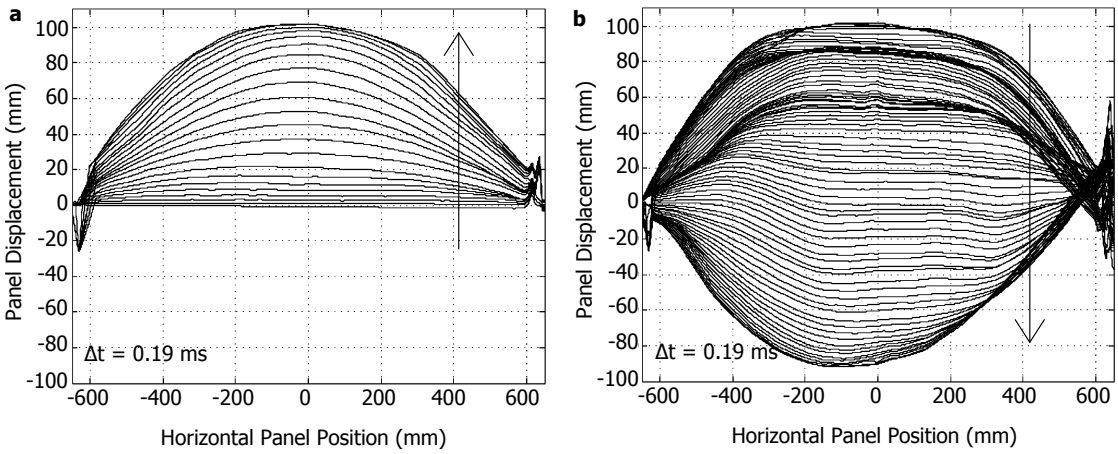


Figure 3.26: Out-of-plane displacement of the horizontal centre section of the 40 mm thick PMI Rohacell SL110 foam core sandwich panel for a) the initial displacement; and b) the rebound.

110SL core sandwich panel are shown in Figure 3.29 and it can be seen that all three peaks are greater than the SAN case due to largely increased damage, but similar to the PVC case. This is due to the initial deflection being predominantly elastic with damage taking place quite late in the deflection, so the initial responses of the sandwich panels are similar. The pull-out displacements clearly show that the PMI Rohacell 110SL sandwich panel deflects towards the blast the most, then the PVC Airex C70.90 case and then the SAN Corecell M100 case. This is due to the damage being present during the whole pull-out deflections so the effects of damage are more pronounced.

3.4.2.2 Graded Density Core

The horizontal centre section profiles of out-of-plane displacement of the graded density core are shown in Figure 3.30, and this provides a direct comparison to the 40 mm thick SAN Corecell M100 foam core profiles shown in Figure 3.25. This comparison shows that the back face-sheet deflection of the graded density panel is much smoother than in the single core case, and this is due to cracking first occurring in the low density foam layer facing the blast, and then in the medium density core in the centre, resulting in less overall cracking in the high density foam at the back. The central and quarter point displacements of the graded density

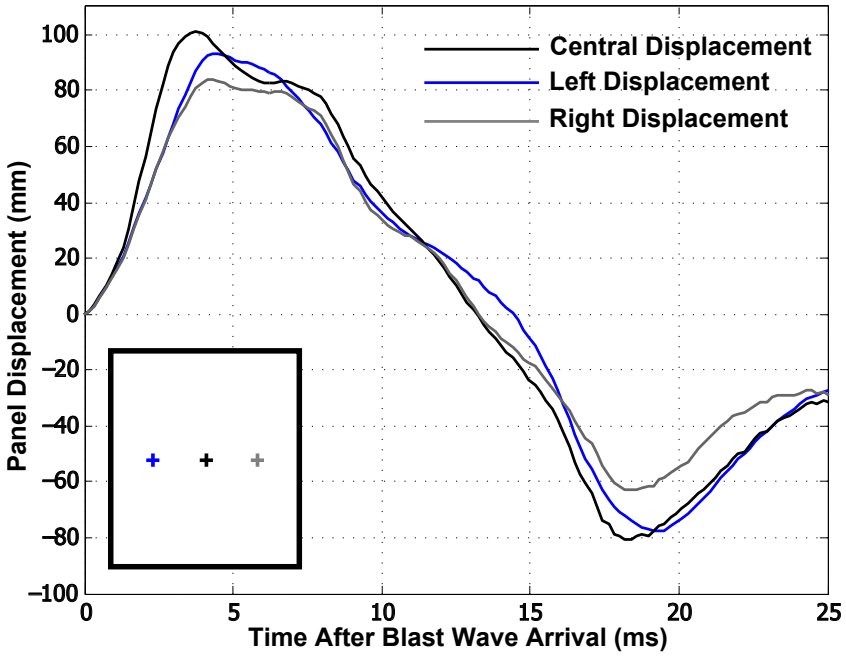


Figure 3.27: Out-of-plane displacement of the centre, and left and right quarters of the 40 mm thick PVC Airex C70.90 foam core sandwich panel.

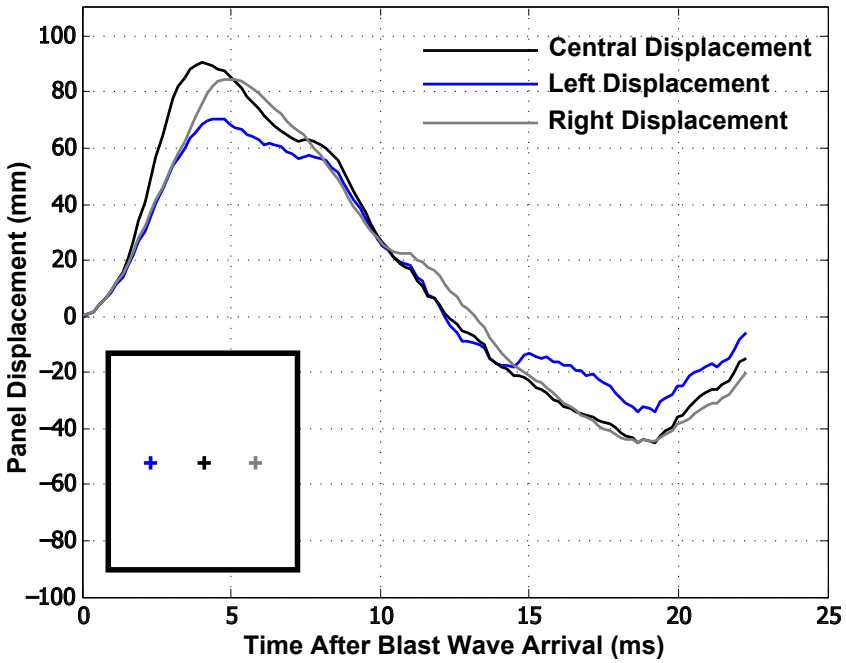


Figure 3.28: Out-of-plane displacement of the centre, and left and right quarters of the 40 mm thick SAN Corecell M100 foam core sandwich panel.

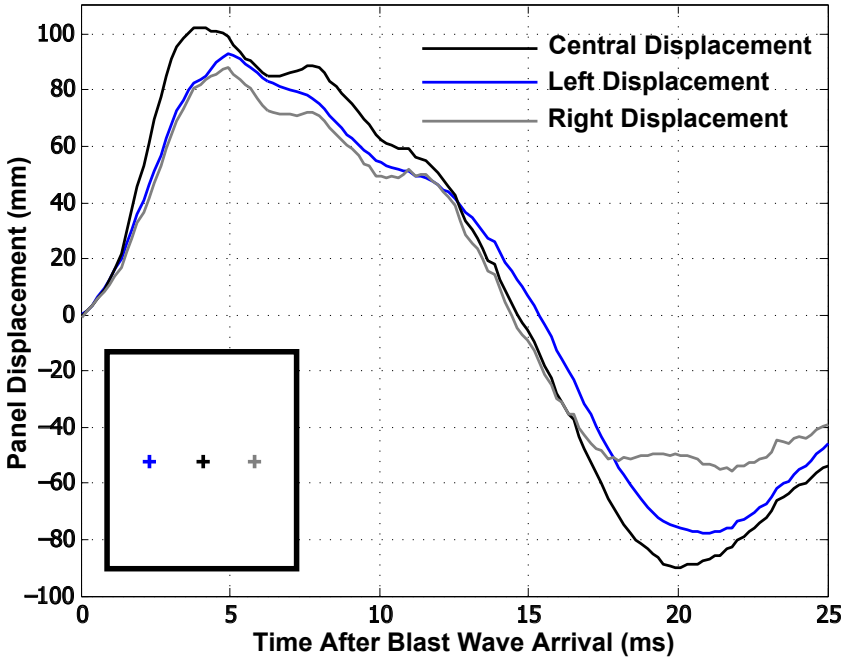


Figure 3.29: Out-of-plane displacement of the centre, and left and right quarters of the 40 mm thick PMI Rohacell SL110 foam core sandwich panel.

sandwich panel are shown in Figure 3.31, which provides a comparison to the central and quarter point displacements of the single density core case shown in Figure 3.28. The central displacement of the graded core sandwich panel is greater than the M100 core case, but this is simply due to the graded core being 30 mm thick where the M100 core was 40 mm thick. The quarter point displacements however, are fairly symmetrical for the graded case, but in the M100 case the right displacement is very high. This is due to heavy damage occurring on this side due of the asymmetry of the boundary conditions caused by the cubicle.

3.4.2.3 Compliant Face-Sheet

The central and two quarter point out-of-plane displacements are shown for the 40 mm thick PVC Airex C70.90 core sandwich panel, containing compliant PP plies in the front face-sheet, in Figure 3.32. The horizontal contour plots for the central section of the same sandwich panel are shown in Figure 3.33, where Figure 3.33a shows the initial displacement and Figure 3.33b shows the rebound

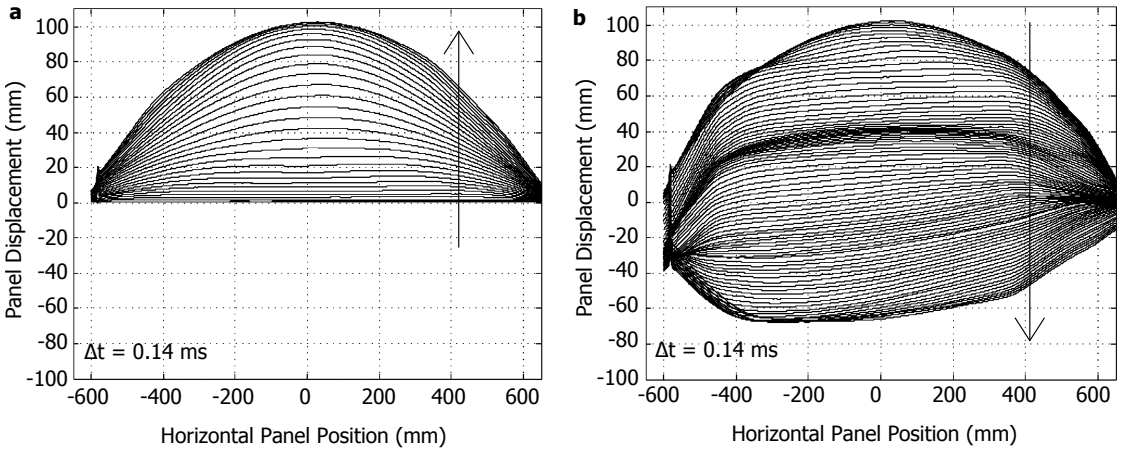


Figure 3.30: Out-of-plane displacement of the horizontal centre section of the 30 mm thick SAN graded density foam core sandwich panel for a) the initial displacement; and b) the rebound.

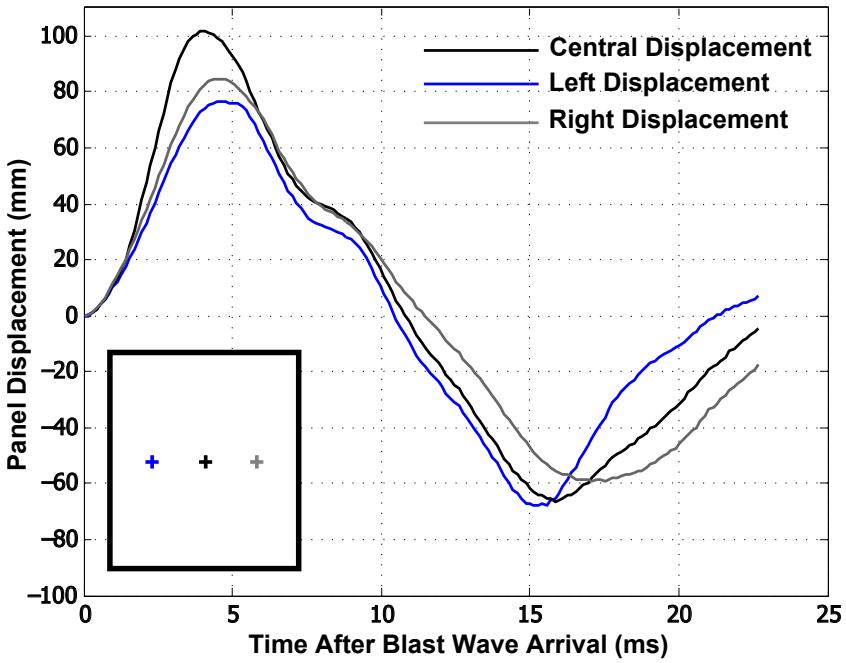


Figure 3.31: Out-of-plane displacement of the centre, and left and right quarters of the 30 mm thick SAN graded density foam core sandwich panel.

of the deflection. These two figures provide a direct comparison to the 40 mm thick PVC Airex C70.90 sandwich panel, which contained only GFRP plies, and the central and quarter point displacements for this are shown in Figure 3.27. The horizontal deflection shapes are provided in Figure 3.24. From the central and quarter point plots it can be seen that the panel with the PP plies deflected less, which was expected due to the thicker front face-sheets. It can also be seen that the damage implied by the deflection profiles is similar, and this was also found in the post-blast sectioning presented subsequently. However with similar amounts of core damage present, the PP ply sandwich panel suffered no front face-sheet damage due to the presence of the PP plies, unlike the solely GFRP face-sheet comparison.

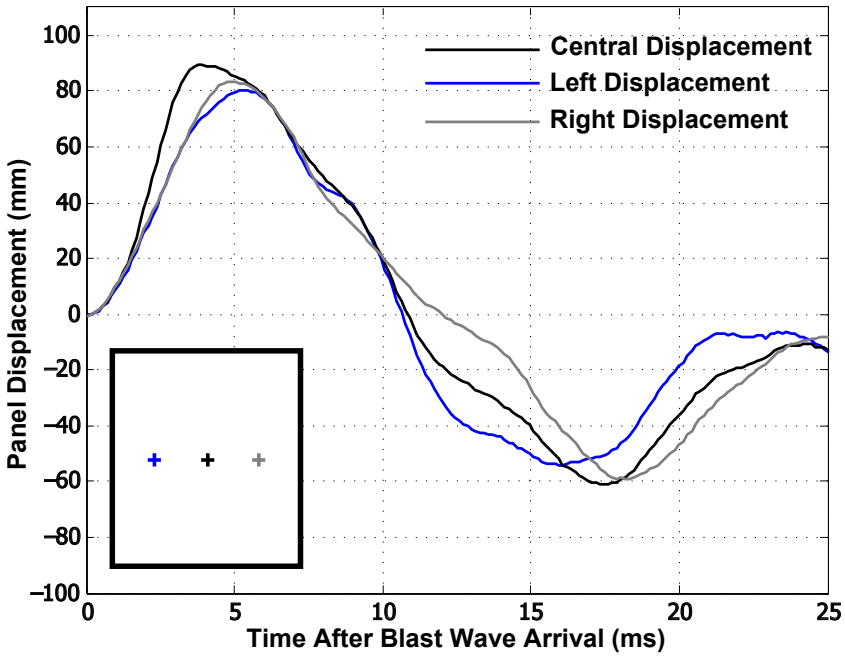


Figure 3.32: Out-of-plane displacement of the centre, and left and right quarters of the 40 mm thick PVC Airex C70.90 core sandwich panel, with compliant PP plies in the front face-sheet.

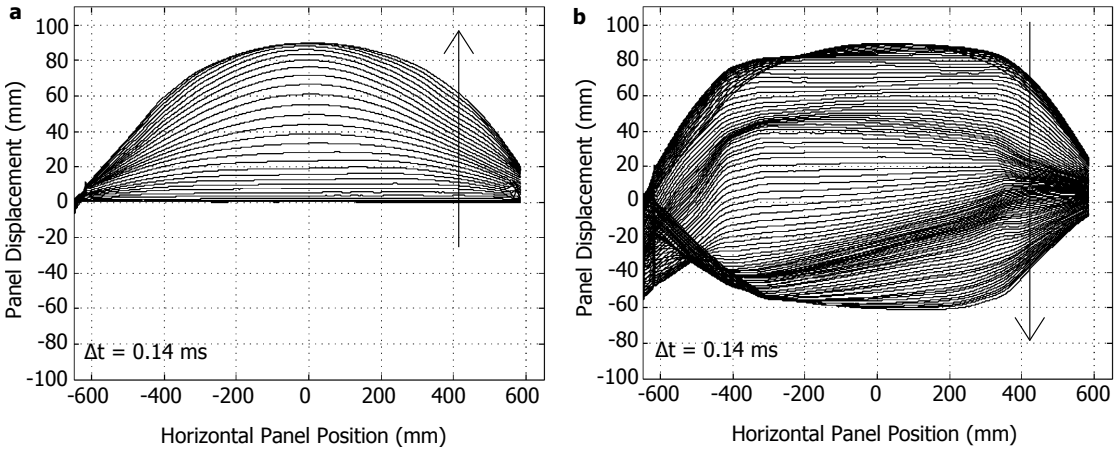


Figure 3.33: Out-of-plane displacement of the horizontal centre section of the 40 mm thick PVC Airex C70.90 core sandwich panel, with compliant PP plies in the front face-sheet for a) the initial displacement; and b) the rebound.

3.4.3 Core Shear Strain

During air blast deflection it is assumed that there is no strain in the through thickness direction of the panel, allowing the shear strain in the core to be calculated from the in-plane strain of the face-sheets, and the out-of-plane displacement of the panel. The calculation for the core shear strain was shown previously, and the plots presented here are simply to illustrate the mechanisms of shear strain across the central section of the panel during failure. The results can, however, be used to influence modelling techniques and provide failure parameters for the foam, as dynamic shear tests of foam are very difficult to perform.

3.4.3.1 Foam Polymer Comparison

The distribution of shear strain across the horizontal centre section of the 40 mm thick PVC Airex C70.90 sandwich panel is shown in Figure 3.34, where the black lines are approximately up to failure and the red lines are post-failure. It can be seen that the failure shear strain of the core is at around 7.5°. The same information is provided for the 40 mm thick SAN Corecell M100 sandwich panel in Figure 3.35, and in this case the ultimate shear strain is at around 5° on the left and 6° on the right, due to the asymmetric boundary conditions. The final panel in

the foam polymer comparison was the 40 mm thick PMI 110SL Rohacell sandwich panel which is shown in Figure 3.36. In this case the ultimate shear strain was around 6°. It is worth noting that the ultimate strains highlighted in the plots are merely the onset of cracking, and when cracking begins near the edges the cracks propagate inwards as the nearby foam is subjected to greater shear strains. This region is shown by the red lines in the plots as the sections of high strain near the edges. The drop in shear strain in the centre is the undamaged foam which is not strained, due to damage at the edges. It can be seen in the M100 and C70.90 cases that the central drop is quite significant, but in the 110SL case it is not, due to damage being present across the entire width.

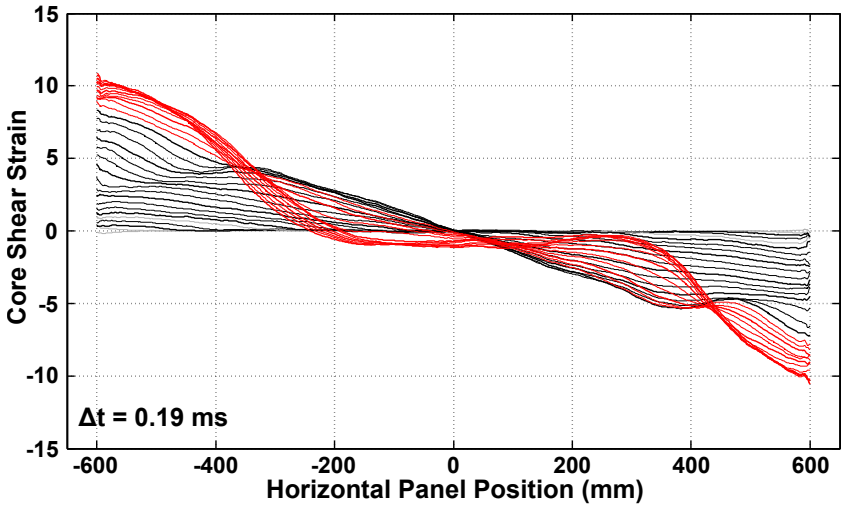


Figure 3.34: Shear strain in the core of the 40 mm thick PVC Airex C70.90 core sandwich panel, where the black lines are up until failure, and the red lines are post-failure.

3.4.3.2 Graded Density Core

The core shear strains for the graded density foam core sandwich panel are shown in Figure 3.37, and an ultimate shear strain of around 6° is visible. When compared to the single M100 SAN core sandwich panel results shown in Figure 3.35, is can be seen the shear strain plot is much more symmetric due to more complicated crack paths providing a smoother displacement, and a similar region of lower shear strain

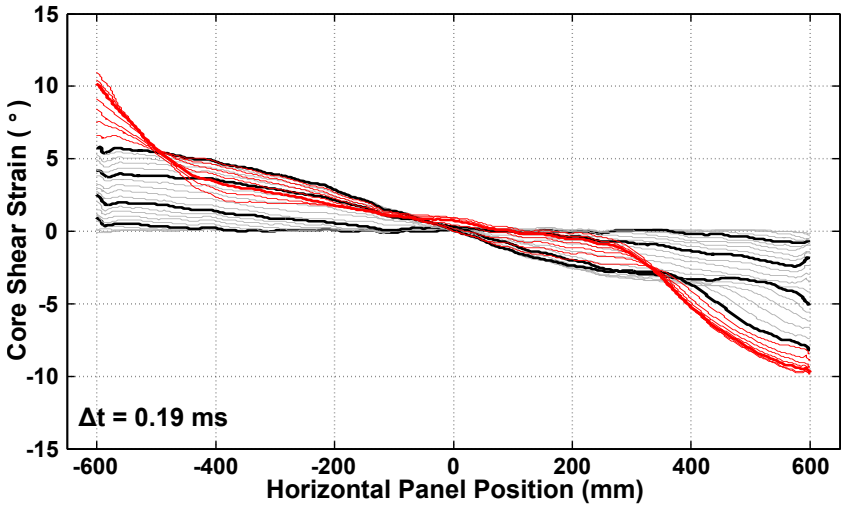


Figure 3.35: Shear strain in the core of the 40 mm thick SAN Corecell M100 core sandwich panel, where the black lines are up until failure, and the red lines are post-failure.

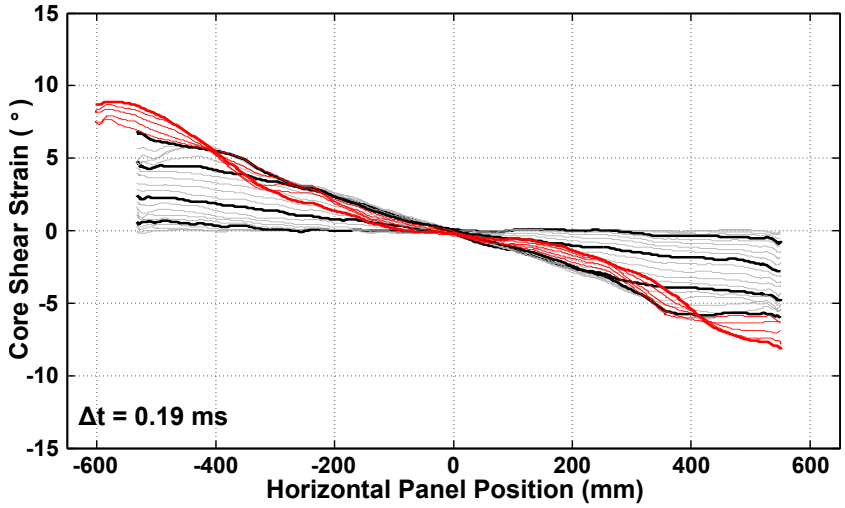


Figure 3.36: Shear strain in the core of the 40 mm thick PMI Rohacell 110SL core sandwich panel, where the black lines are up until failure, and the red lines are post-failure.

in the centre. This region of shear strain shows that the extent of damage into the panel is similar in both panels, which is validated in the subsequent section.

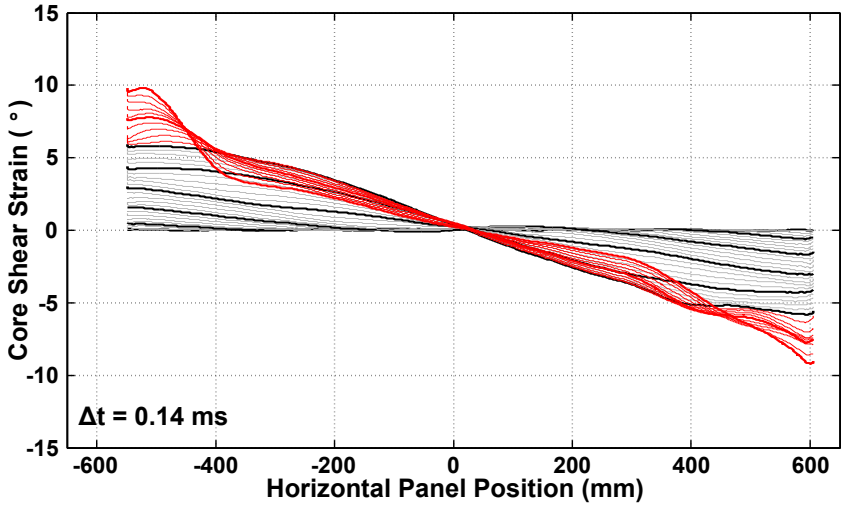


Figure 3.37: Shear strain in the core of the 30 mm thick SAN Corecell graded core sandwich panel, where the black lines are up until failure, and the red lines are post-failure.

3.4.3.3 Compliant Face-Sheet

The compliant face-sheet sandwich panel provided a direct comparison to the single PVC Airex C70.90 core sandwich panel, and it was expected that the amount of core damage would be similar in each case. The compliant face-sheet results are shown in Figure 3.38, to be compared to the PVC Airex C70.90 core sandwich results in Figure 3.34. It can be seen in the Innegra case that the ultimate shear strain is around 6° on the left and 7° on the right, and that the central region is similar in size to the C70.90 case, showing a similar amount of damage.

3.4.4 Energy Balance

The final set of information ascertained from the air blast DIC results was the work done during blast, the kinetic energy of the sandwich panel and the resulting strain energy in the panel. These results provide a comparison of the amount of damage suffered in the sandwich panels during blast, from the strain energy, but this value

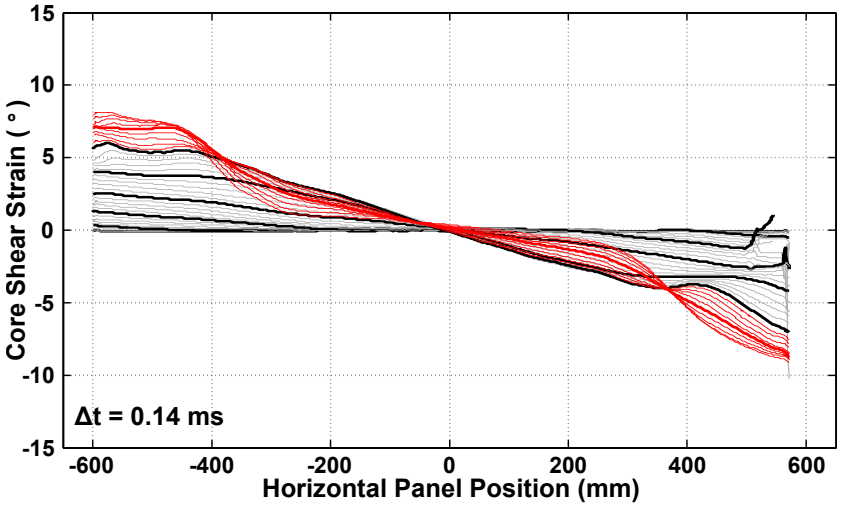


Figure 3.38: Shear strain in the core of the 40 mm thick PVC Airex C70.90 core sandwich panel, containing compliant PP plies in the front face-sheet, where the black lines are up until failure, and the red lines are post-failure.

is merely intended as a comparative figure due to the uncertainties generated by the calculation methods for work done and kinetic energy. The important value obtained from this study is the maximum strain energy in the sandwich panel, which is the point at which fracture took place. The maximum strain energy values calculated in the sandwich panels during blast loading are tabulated in Table 3.8. The energy balance information for the response of each sandwich panel to blast loading can also be used to compare the DIC results with simulation results, as it is very simple to extract energy values from FEA simulations.

3.4.4.1 Foam Polymer Comparison

Figure 3.39 shows the cumulative sum of work done, kinetic energy and strain energy for the C70.90 sandwich panel. The strain energy provides an estimate of the energy stored up as strain due to elastic deformation, which can be seen to suddenly drop when fracture takes place. The same plots for the M100 and 110SL cases are shown in Figure 3.40 and Figure 3.41 respectively. As the work done is calculated from the blast force and the panel displacement, it is greater for the C70.90 and 110SL cases, due to the greater out-of-plane displacement of the panels. The kinetic energy is fairly linear in all cases, but is greatest for the

110SL case and least for the M100 case, due to these containing the most and least core cracking respectively. As the panel cracks it offers less resistance to the blast force, so the velocity increases, thus increasing the kinetic energy and decreasing the strain energy. It can be seen that the smallest drop in strain energy is in the M100 case, then the C70.90 case and the most in the 100SL case, which corresponds to the amount of damage witnessed.

3.4.4.2 Graded Density Core

The energy balance for the graded core sandwich panel is shown in Figure 3.42, which can be directly compared to the M100 results shown in Figure 3.40. It can be seen that the work done in the graded case was greater, due to the out-of-plane displacement being higher, but the strain energy decreases much less, implying that the panel retained more stiffness during deflection. In the case of the graded panel this does not necessarily mean there is less overall damage, but shows that bending stiffness is retained more than in the M100 case.

3.4.4.3 Compliant Face-Sheet

Figure 3.43 shows the energy balance for the compliant face-sheet sandwich panel, which was to be compared to the C70.90 core sandwich panel results shown in Figure 3.39. The energy values are similar in the two cases, showing that the damage suffered is similar.

3.4.5 Post-Blast Damage Assessment

Alongside DIC results obtained during blast deformation, the sandwich panels were also sectioned to record the damage suffered during blast. Figure 3.18 shows the pattern used to section each sandwich panel, which was chosen to allow the post-blast test specimens detailed in Chapter 4 to be produced. This section provides maps of both debonding and foam cracking failure modes, and also provides total values of areas of debond and cracked surface areas in each case.

In the damage maps presented subsequently, the location of damage is highlighted by red lines, where the outline of the sections cut out of the sandwich panel

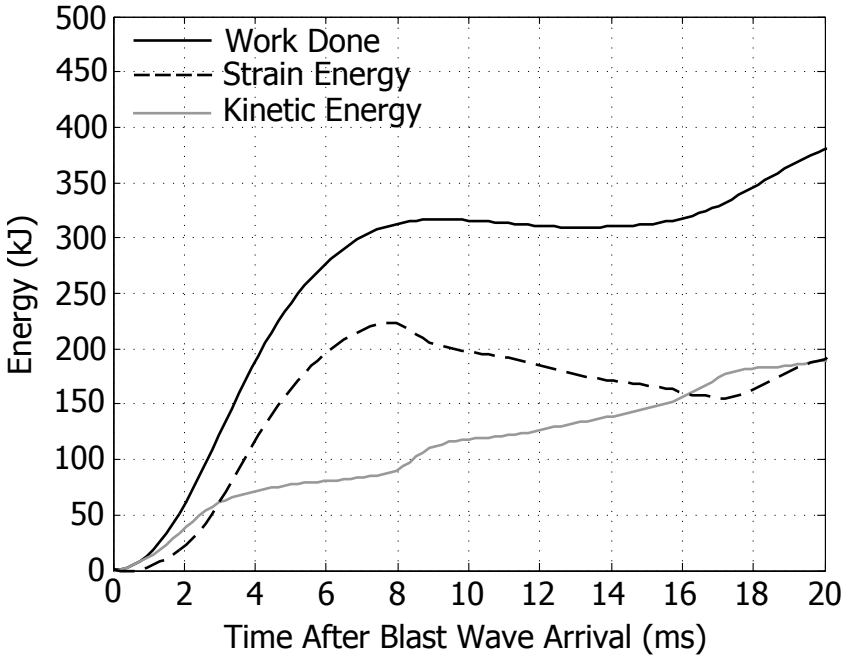


Figure 3.39: Cumulative work done, kinetic energy and strain energy in the 40 mm thick PVC Airex C70.90 core sandwich panel.

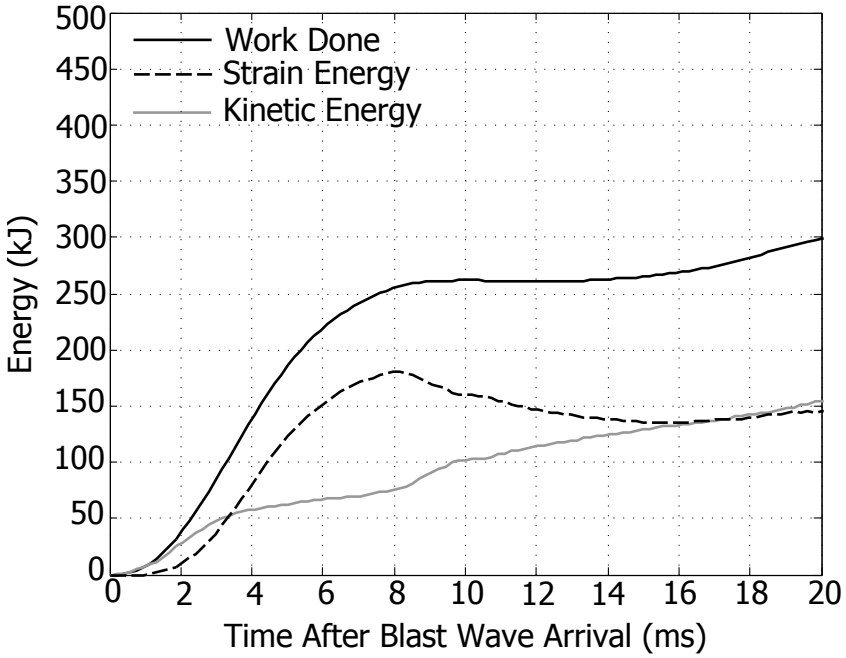


Figure 3.40: Cumulative work done, kinetic energy and strain energy in the 40 mm thick SAN Corecell M100 core sandwich panel.

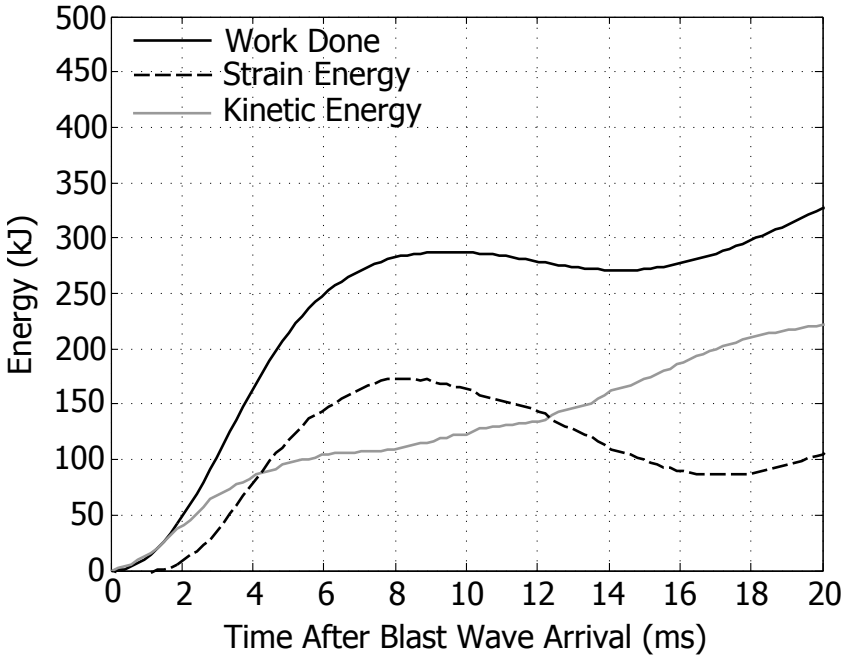


Figure 3.41: Cumulative work done, kinetic energy and strain energy in the 40 mm thick PMI Rohacell 110SL core sandwich panel.

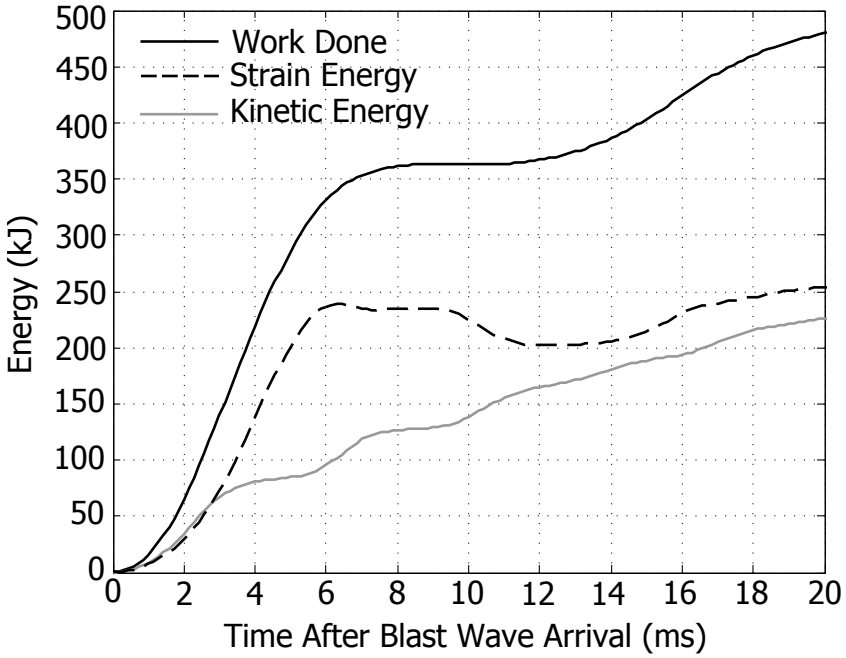


Figure 3.42: Cumulative work done, kinetic energy and strain energy in the 30 mm thick SAN Corecell graded core sandwich panel.

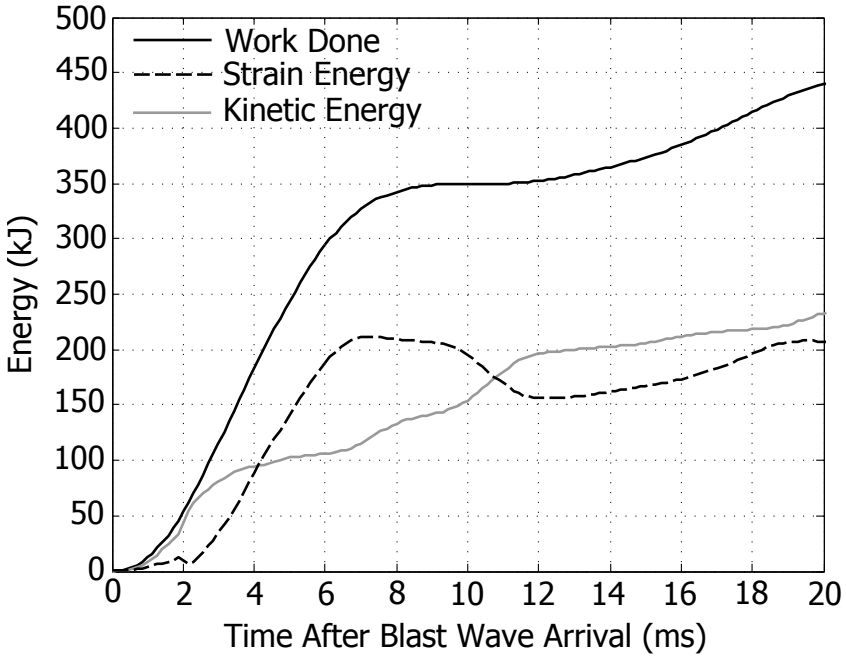


Figure 3.43: Cumulative work done, kinetic energy and strain energy in the 40 mm thick PVC Airex C70.90 core sandwich panel, containing compliant PP plies in the face-sheet.

are shown by the grey lines. Three different maps are shown for each panel to show the locations of any debonds between the front face-sheet and the foam core; the locations of any cracks in the foam core; and the locations of any debonds between the rear face-sheet and the foam core. In the graded density case an extra four maps are provided to show the locations of debonds between each of the foam layers, as well as between the face-sheets and the foam; and individual maps of the cracking present in each of the foam layers.

3.4.5.1 Foam Polymer Comparison

A map of damage in the 40 mm thick PVC Airex C70.90 sandwich panel is shown in Figure 3.44, with Figure 3.44a showing the locations of debonding between the back face-sheet and core, Figure 3.44b showing the locations of cracks in the foam core and Figure 3.44c showing the locations of debonding between the front face-sheet and foam core. It can be seen from Figure 3.44 that the majority of debonding took place between the front face-sheet and core, and that very little damage took place in the centre of the sandwich panel. The damage map of the 40 mm thick SAN Corecell M100 foam core sandwich panel is shown in Figure 3.45, where Figure 3.45a shows debonding between the back face-sheet and core; Figure 3.45b shows cracks in the foam core; and Figure 3.45c shows debonding between the front face-sheet and foam core. It was not possible to section the 40 mm thick PMI 110SL Rohacell panel due to the damage being too substantial for use in a circular saw. A summary of the amounts of debond and cracks for the M100 and C70.90 cases are shown in Table 3.7 and Table 3.6 respectively.

3.4.5.2 Graded Density Core

It was not possible to collect DIC data for the 30 mm thick SAN Corecell M130 core sandwich panel due to problems in triggering the high speed cameras during the test, but the panel was sectioned after blast testing, and a damage map is provided in Figure 3.46. This map provides a direct comparison to the 30 mm thick SAN Corecell graded core sandwich panel damage map, as shown in Figure 3.47. It can be seen from the two damage maps that there is more damage overall in the graded case, but the majority of this damage takes the form of debonding between

the layers and not foam cracking. This is due to the crack propagation through the foams being arrested at the boundaries, and then travelling along the interface due to this being the path of least resistance. Another comparison to be made is between the graded density and M130 cases, presented here, and the M100 case presented in Figure 3.45. These three panels have very similar areal densities, and in terms of damage it is clear that the M130 sandwich panel performs the best. The graded case suffers significant damage but low core cracking, protecting the rear face-sheet from damage due to a smoother deflection, as shown in the DIC results. The results of the damage map are summarised in Table 3.6 and Table 3.7.

3.4.5.3 Compliant Face-Sheet

The post-blast damage map of the 40 mm thick PVC Airex C70.90 sandwich panel with compliant PP plies in the front face-sheet is shown in Figure 3.48, and this provides a direct comparison to the PVC Airex C70.90 core sandwich panel with just GFRP plies in the face-sheets, shown in Figure 3.44. As shown in the figures, and in the summarised results in Table 3.6 and Table 3.7, there is a similar amount of damage present in the two tests, in terms of core cracking and debond. However, the front face-sheet in the compliant face-sheet sandwich panel, suffered no cracking, unlike the purely GFRP front face-sheet in the polymer comparison case. This lack of front face-sheet cracking was due to the compliant PP plies, and provides a useful result for naval vessels as this front face-sheet integrity would prevent water ingress into the sandwich panel.

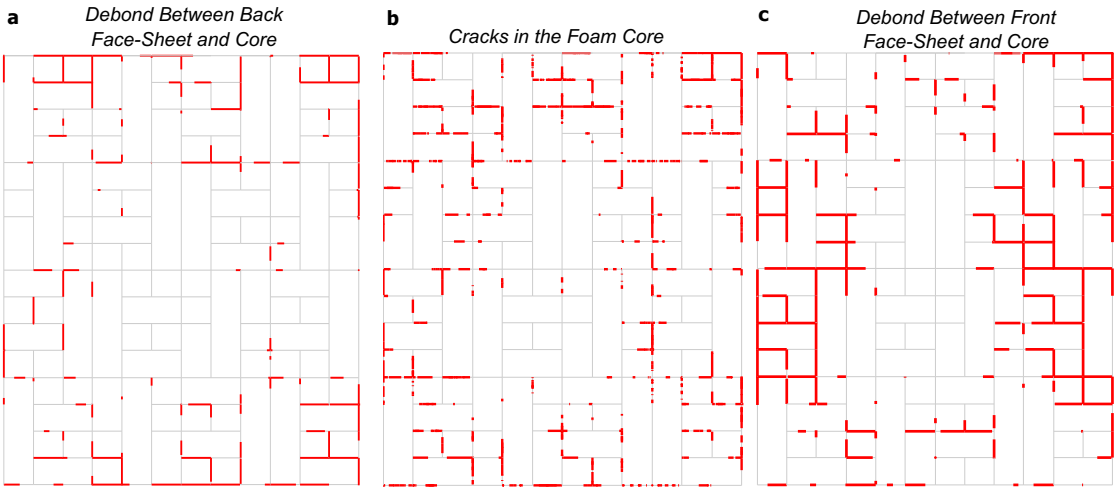


Figure 3.44: Damage map of the 40 mm thick PVC Airex C70.90 foam core sandwich panel, showing a) debonding between the back face-sheet and core; b) cracks in the foam core and c) debonding between the front face-sheet and core.

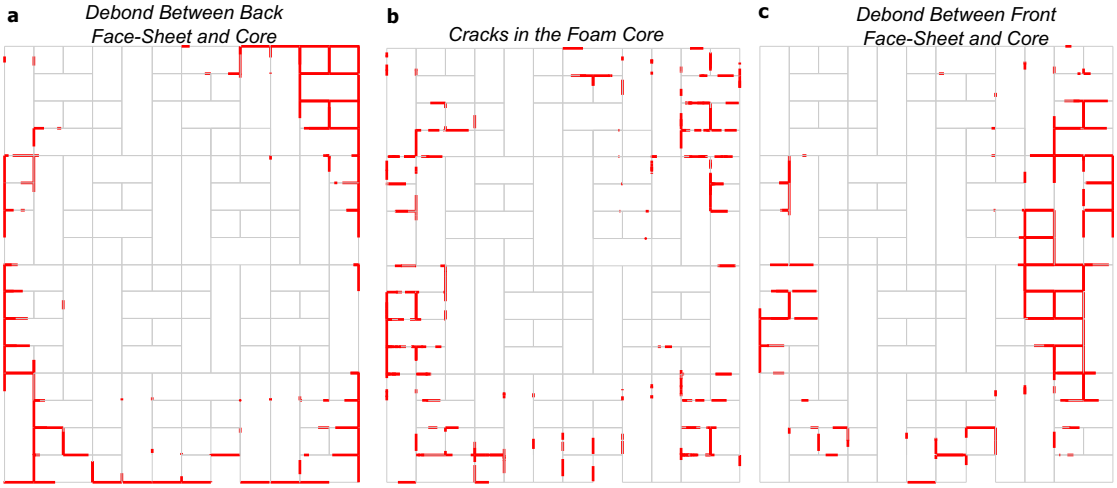


Figure 3.45: Damage map of the 40 mm thick SAN Corecell M100 foam core sandwich panel, showing a) debonding between the back face-sheet and core; b) cracks in the foam core and c) debonding between the front face-sheet and core.

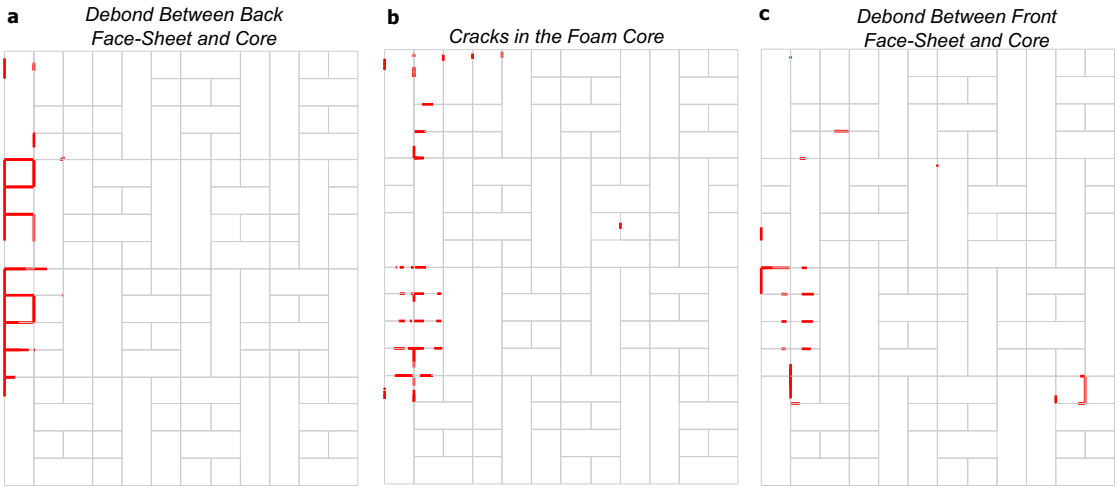


Figure 3.46: Damage map of the 30 mm thick SAN Corecell M130 foam core sandwich panel, showing a) debonding between the back face-sheet and core; b) cracks in the foam core and c) debonding between the front face-sheet and core.

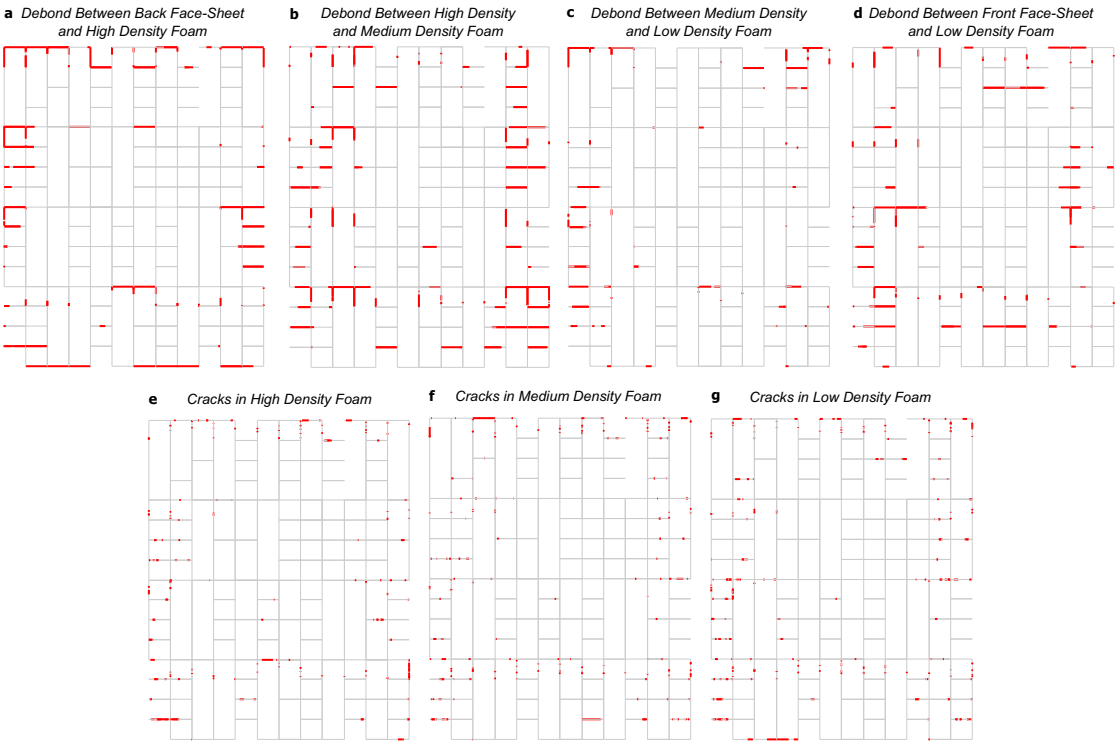


Figure 3.47: Damage map of the 30 mm thick SAN Corecell graded foam core sandwich panel, showing a) debonding between the back face-sheet and core; b) cracks in the foam core and c) debonding between the front face-sheet and core.

Table 3.6: Summary of core cracks caused by blast testing.

Panel Description	Total Number of Through Thickness Cracks	Total Crack Area (m^2)	Fraction of Panel Containing Cracks (%)
Single 40 mm M100 SAN Core	38	0.81	17
Single 30 mm M130 SAN Core	11	0.18	3.3
Graded 30 mm SAN Core	33*	0.23*	4.6*
Graded: High Density Foam	30	0.19	3.7
Graded: Medium Density Foam	34	0.21	3.9
Graded: Low Density Foam	35	0.29	6.1
Single 40 mm C70.90 PVC Core	121	2.45	41
Single 40 mm C70.90 PVC Core with Innegra Face-Sheets	135	2.72	50

* Average of the three foam layers.

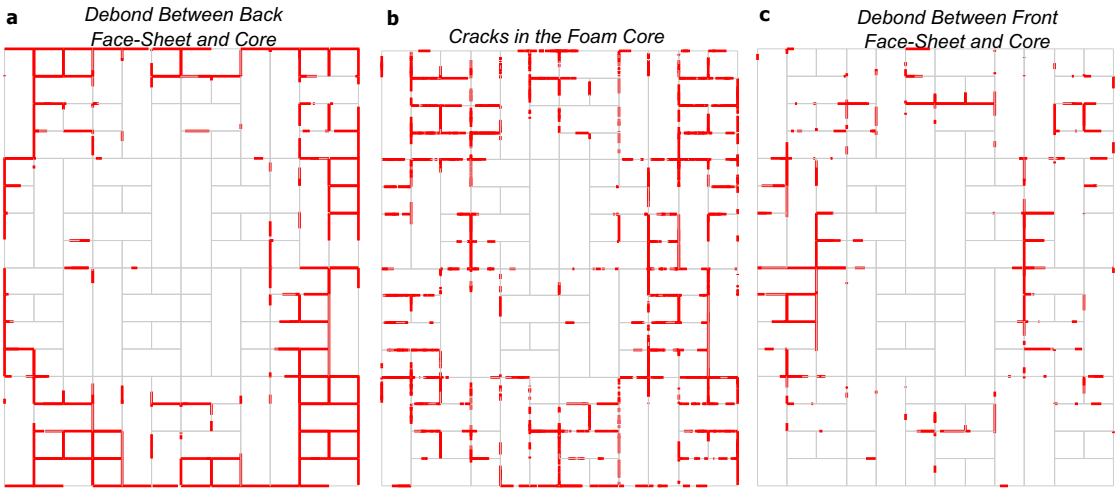


Figure 3.48: Damage map of the 40 mm thick PVC Airex C70.90 foam core sandwich panel, with compliant PP plies in the front face-sheet, showing a) debonding between the back face-sheet and core; b) cracks in the foam core and c) debonding between the front face-sheet and core.

Table 3.7: Summary of debonding caused by blast testing.

Panel Description	Fraction of the panel with front face-sheet and core debond (%)	Total front face-sheet and core debond area (m^2)	Fraction of the panel with back face-sheet and core debond (%)	Total front face-sheet and core debond area (m^2)
Single 40 mm M100 SAN Core	21	0.37	19	0.38
Single 30 mm M130 SAN Core	2.2	0.05	6.3	0.16
Graded 30 mm SAN Core	12*	0.27*	25†	0.63†
Graded: Rear Face-Sheet and High Density Foam	-	-	26	0.63
Graded: High and Medium Density Foam	-	-	24	0.64
Graded: Medium and Low Density Foam	8.9	0.21	-	-
Graded: Front Face-Sheet and Low Density Foam	16	0.33	-	-
Single 40 mm C70.90 PVC Core	48	0.89	30	0.55
Single 40 mm C70.90 PVC Core with Innegra Face-Sheets	18	0.31	41	0.70

* Average of the front face-sheet and low density foam interface, and the low and medium density foam interface.

† Average of the back face-sheet and high density foam interface, and the high and medium density foam interface.

3.5 Discussion

3.5.1 Air3D and Digital Image Correlation

The response of the sandwich panels to air blast loading was recorded using high speed cameras and DIC, to track the out-of-plane displacement and in-plane strain of the back face-sheet. The high speed cameras used were 1 megapixel in resolution, which equated to each pixel having an area of around 1.5 mm^2. The facet spacing used in Aramis, the DIC software used to analyse the images, was approximately 1 mm on the speckle pattern. By exporting the data into MATLAB, and using grid interpolation for each high speed camera frame captured, the data was regularised across the sandwich panel surface. This process allowed more flexibility with the data, as the exported data from Aramis had points which moved in-plane, due to the displacement of the sandwich panel, so the MATLAB processing preserves the correct data in the original, regular facet locations. This process is achievable within Aramis, but importing into MATLAB enables much more data processing functionality to be used. The raw out-of-plane displacement and maximum principal strain data for the five air blast tests are shown in Appendix A.

The use of Air3D was used to predict blast loading on the sandwich panel, but to also provide the loading on each individual facet. Over the 15 m stand-off distance, the prediction of the actual blast pressure magnitude on the sandwich panel was difficult to achieve accurately, due to the assumption of a perfectly elastic floor and of a perfectly spherical 100 kg TNT equivalent charge size. However, by placing a reflected pressure gauge on the front of the test cubicle, and recording the pressure at this location in the Air3D simulations, it was possible to calculate a dimensionless pressure distribution across the sandwich panel by assuming the same relation to the reflected pressure gauge. With the pressure loading and the displacement of each facet obtained it was possible to perform an energy balance of work done and kinetic energy, to provide a more quantitative comparison of the sandwich panels. Furthermore, the individual facet pressure profiles could be incorporated into finite element simulations to provide more accurate loading conditions, and the simulation results compared using grid interpolation in MATLAB

to provide an exact comparison to DIC. This study, however, was out of the scope of the work reported in this thesis.

3.5.2 Out-of-Plane Displacement

The most simple and robust comparison of results drawn from the DIC of air blast responses was of out-of-plane displacement. From the out-of-plane displacement, failure of the sandwich panel was clearly visible in the form of sharp changes in gradient where the foam core and face-sheets have failed, caused by a local drop in bending stiffness. Also by using high speed cameras with frame rates of 5,400 s^{-1} and 7,000 s^{-1} it was possible to capture the deceleration of the sandwich panel due to the unloading wave reaching the low stiffness area of damaged panel, around one quarter of the distance into the panel on the horizontal dimension. It was also possible to remove rigid body motion of the cubicle front in the tests by speckling the I-beam in the centre of the front of the test cubicle. Using Aramis the movement of this beam was then removed from the results, to allow only the panel deflection to be assessed relative to the boundaries.

The central and quarter point out-of-plane displacements of the sandwich panels were compared in this study and the central displacements of the five sandwich panels for which DIC data was available are plotted in Figure 3.49 for comparison. The central displacement provided an overall quantification of the sandwich panel bending stiffness, and in the foam polymer comparison it was found that the M100 SAN core deflected the least. The C70.90 PVC core deflected less than the 110SL PMI foam core, and these results correlated with the damage suffered in each case. The difference in maximum out-of-plane displacement between the quarter points and the panel centre provided a comparison of the damage suffered, as with more core cracking and debonding the maximum panel deflection took a square shape, meaning that the quarter point displacements were closer to the centre displacement. The lack of symmetry observed between the quarter points was due to a lack of symmetry in the test cubicle.

The amount the sandwich panel pulls back out of the test cubicle, as shown by the negative displacement in the plots, is another useful indicator of the damage suffered. The pull-out was caused by the momentum of the sandwich panel

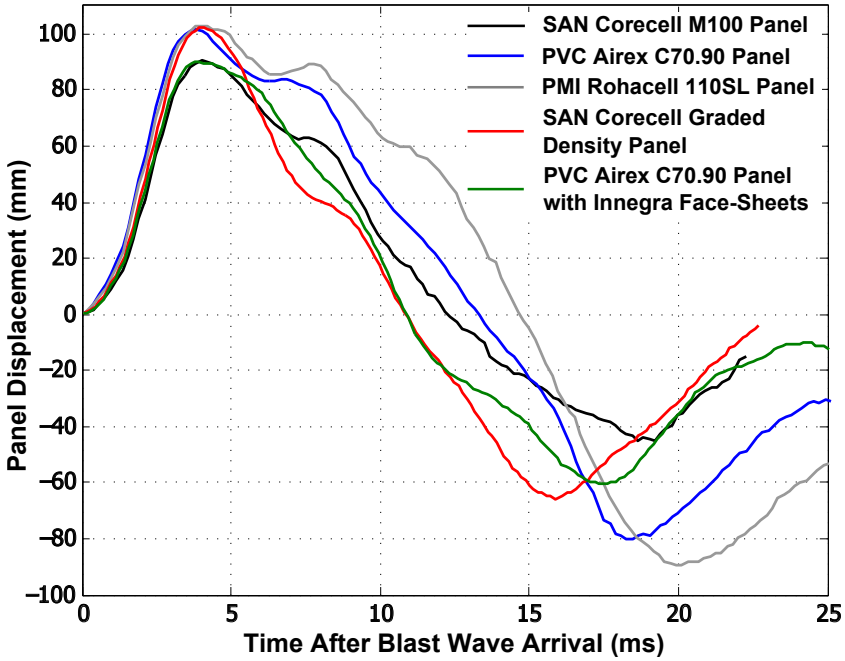


Figure 3.49: Central out-of-plane displacement of the five air blast tested sandwich panels for which DIC data was available.

returning from the maximum displacement, as well as the negative blast pressure caused by the rapid overexpansion of explosive gas causing a pressure reduction at the charge location. At the point of pull-out the sandwich panel had suffered all of the damage it was likely to suffer, and the negative blast pressure was not great enough to cause further failures. Therefore the extent of pull-out is dictated purely by the residual bending stiffness in the sandwich panel. As shown in Table 3.8 the pull-out of the M100 SAN case was the least in the polymer comparisons, followed by the C70.90 PVC sandwich panel, and then the 110SL PMI sandwich panel.

The graded density sandwich panel suffered a maximum out-of-plane displacement of 102 mm and a maximum pull-out of 66 mm, as shown in Table 3.8. This was much greater than the M100 SAN case to which it was compared, but this was expected due to the graded foam core being 30 mm thick, compared to the 40 mm thick M100 foam core. However, the graded SAN core had a very similar out-of-plane displacement to the C70.90 PVC and the 110SL PMI cases, and suffered less pull-out, implying it suffered less damage. This finding was verified by the damage mapping technique discussed subsequently.

The displacement shape of the graded sandwich panel was also much smoother than all of the other sandwich panels, which indicates less damage suffered near the rear face-sheet during blast. Furthermore, the comparison of the central point and the quarter points shows a large difference in out-of-plane displacement indicating less core cracking and debonding. An interesting result in the graded case is that the pull-out displacement shape has fairly large gradient changes, and this is due to the majority of core cracking taking place in the low and medium density foam cores, and few cracks in the high density foam. This caused the initial displacement to be smooth as the high density foam at the back was relatively undamaged, and then as the cracks in the low density core were pulled apart on the rebound the localised stiffness was reduced.

The out-of-plane displacement of the compliant Innegra PP front face-sheet sandwich panel was greatly reduced by the thicker front face-sheet, as compared to the C70.90 PVC core case in the polymer comparison. The initial out-of-plane displacement was reduced by 10% by implementing the PP plies in the front face-sheet, and the pull-out was reduced by 25%. The areal density increase from implementing the PP plies was 14%. The benefits of implementing these PP layers, however, are in the increased compressive strain to failure of the PP plies compared to glass fibre or carbon fibre plies. While offering a negligible structural contribution once the interleaved glass plies have failed, the PP plies provide a seal to the water which would otherwise flow into the cracked foam core if the front face-sheet fractured.

3.5.3 Core Shear Strain

The core shear strain in the sandwich panels was calculated from the out-of-plane displacement and in-plane back face-sheet strain of the sandwich panel, measured using DIC. The system is limited in accuracy due to the assumption that there is no in-plane centreline strain membrane effect present during deformation, which is not true due to the large deflections witnessed in response to air blast. However it was not possible to account for centreline strain without measurements on the front face-sheet, so this system was used to provide a qualitative evaluation of the shear strains in the various sandwich panel constructions. As shown in Table 3.8

the shear strain was very similar in every case. The shear strain was converted to a percentage value using Equation (3.22), which provided the shear strains at failure presented in Table 3.8. Considering the quasi-static shear failure strains in Table 3.3 (which assumed a perfectly elastic response), all of the foams are shown to possess very similar shear strains to failure in quasi-static loading conditions. With this information, it can be concluded that the technique is somewhat useful in a comparative sense, to calculate an approximation of the shear strain in the sandwich panels upon failure. The different responses of the sandwich panels are therefore related to the point at which this failure strain is reached in the loading cycle, the energy dissipated during fracture, the tensile properties of the foam, and the adhesion properties of the resin to the foam polymer. As will be shown in Chapter 6, the dynamic tensile strain to failure of the 110SL PMI foam is much lower than the M100 SAN and the C70.90 PVC cases which helps to explain the earlier fracture in this case.

$$\varepsilon_{xy} = 100\, tan\,(\gamma) \tag{3.22}$$

3.5.4 Energy Balance

By utilising the individual facet system with DIC results and Air3D simulations, as discussed earlier in this section, it was possible to calculate the work done on and the kinetic energy of each facet. This provided a comparative study of the amount of strain energy in each sandwich panel at the time of failure. The drop in strain energy at fracture was indicative of the reduced bending stiffness caused by damage. This study built on from the core shear strain findings, where the shear strain to failure was the same in every case. It was concluded that the dominant failure mode in the foam was therefore due to the tensile component of loading, which enables an explanation of the different behaviour of each panel. A greater strain energy at failure denotes more deformation of the panel at the point of failure, and is identified in the energy damage plots as a peak in the strain energy curves. This is because the kinetic energy of the sandwich panel increased when the foam fractured, due to reduced stiffness.

The graded density foam core sandwich panel failed with the most strain energy

due to the slower propagation of cracks through the foam thickness, as shown in Table 3.8. Also visible in the energy balance plot for the graded core, shown in Figure 3.42, is an extended period after failure of high strain energy, and this is due to the higher density foam still being relatively undamaged, so the kinetic energy did not increase as quickly after initial fracture. The M100 SAN core sandwich panel showed low strain energy at fracture, lower than the C70.90 PVC case and similar to the 110SL PMI case. This is due to the low out-of-plane displacement of the sandwich panel compared to the other two, which resulted in less work done. This is important to consider when comparing the strain energy in this way, and ideally the work done in every case would be the same, for a more useful comparison.

Another benefit of this method of comparing the energies during blast is the ability to compare the results with finite element simulations. Retrieving work done, kinetic energy and strain energy from simulations is a robust method of comparison, and alongside the ability to compare DIC facet data to element data, and Air3D facet loading with element loading, the blast tests can be fully utilised to validate FEA. However, this was out of the scope of this research project.

3.5.5 Post-Blast Damage Assessment

As shown in Table 3.6 and Figure 3.7 the damage suffered in the single core sandwich panels was fairly evenly split across debonding in the two interfaces and cracking in the foam core. The 30 mm thick M130 SAN core sandwich panel showed the least damage by far, with the M100 SAN core showing the next least, then the C70.90 PVC core panel, and the 110SL PMI sandwich panel showing the most damage. The overall fraction of each panel containing any form of damage is shown in Table 3.8 and these figures are an average of the percentage of each type of damage: front face-sheet and core debonding; core cracking; and rear face-sheet and core debonding.

The compliant PP front face-sheet sandwich panel, containing a 40 mm thick PVC foam core, suffered a similar amount of core cracking and rear face-sheet debonding to the C70.90 PVC sandwich panel to which it was compared, as shown in Table 3.8. However, the PP impregnated front face-sheet suffered no compressive

fracture, and there was much less front face-sheet debonding observed. These are both positive for underwater environments to prevent water from entering the heavily cracked core.

As shown by Figure 3.47 the graded density core sandwich panel suffered a significant amount of core cracking and debonding at all of the interfaces, but they were heavily distributed and small in crack length. This was due to the number of interfaces present preventing crack propagation through the panel. As expected, the cracking in the lower density foam was greater than in the higher density foam. However, debonding was more severe between the rear face-sheet and high density foam, and this was due to the high degree of bending present due to the lower density foam at the front.

3.6 Conclusion

Six full scale air blast tests were performed on polymeric foam core, GFRP face-sheet sandwich panels to compare the blast resistance of different constructions. The polymeric foam used in the core was studied, comparing SAN, PVC and PMI, to assess how their different mechanical properties affected the blast resistance of the sandwich panels. Also, a graded density foam core sandwich panel was tested, to assess if the core damage suffered during blast could be mitigated with the use of a graded core. Finally, PP Innegra fibre plies were interleaved between glass fibre plies in the front face-sheet of a PVC core sandwich panel, to assess the reduced displacement witnessed by using a slightly stiffer front face-sheet, and the reduced front face-sheet damage. The main results of the air blast tests are presented in Table 3.8 for comparison. It can be seen that the M130 SAN core sandwich panel suffered the least amount of damage in the blast tests, but due to problems in triggering the high speed cameras it was not possible to obtain DIC results for this test panel. It was found that all three sandwich panels containing SAN foam cores suffered significantly less damage than the other foam polymers, and this was due to their higher strain to failure than the PVC and PMI foams. The dynamic material properties of the foam materials are detailed in Chapter 6.

The use of paired high speed cameras, and a speckle pattern on the rear face-sheet of the sandwich panels allowed 3D DIC to be used to track the out-of-plane

displacement and in-plane strain of the sandwich panels. The main benefit of this was to assess the out-of-plane displacement and compare the ability of each sandwich panel to resist deformation from the blast wave. In the foam comparison study if was found that the M100 SAN core sandwich panel deflected and rebounded the least, followed by the C70.90 PVC foam core panel and then the 110SL PMI sandwich panel. The initial deflection of the panel is controlled by the shear modulus of the foam core to increase bending stiffness, and the amount of damage suffered by the core to reduce the bending stiffness. The rebound, or pull-out, suffered is also directly related to the amount of damage suffered, as the negative pressure wave is insufficient to damage the panel itself. Therefore the pull-out is greater for more damaged sandwich panels. The DIC results also allowed the shear strain in the form core to be estimated by assuming that there was no shear in the face-sheet, and that there was no through thickness strain during bending. It was found that the shear strain at failure of each foam core was the same, which agreed with the manufacturer data sheet shear properties. It was concluded from this that the difference in the response of each foam was caused by differing levels of fracture toughness, and different amounts of strain to failure in tension. It is expected that the fracture toughness of the 110SL PMI foam is the lowest out of those studied, followed by the C70.90 PVC foam, and this is an area of recommended future research.

The final set of results obtained from DIC was the strain energy at failure in the sandwich panel and the reduction in strain energy after damage took place. This was achieved by calculating the work done from an Air3D CFD simulation on each facet location over the sandwich panel surface, and the kinetic energy from the corresponding facet using DIC. This provided an energy balance in which the strain energy present at failure was determined. The reduction in strain energy is indicative of damage suffered as the bending stiffness was reduced when damage took place. This is intended for future use in FEA validation.

The use of a graded density foam core acted to arrest crack propagation during blast loading, and reduce the amount of cracks present in the high density foam layer at the back. This created a much smoother deflection shape, protecting the rear face-sheet from damage. The lower density foams at the front suffered much more damage, but the cracks were highly distributed due to the adhered interfaces

in the sandwich panel.

By incorporating PP fibre plies within the front face-sheet of a PVC foam core sandwich panel, debonding between the front face-sheet and core was reduced and front face-sheet compressive failure was prevented. This was achieved whilst still witnessing the same level of core cracking and rear face-sheet to core interface debonding. This is an important finding for naval applications, as it would prevent water from entering the cracked foam core of the ship hull structure. The out-of-plane displacement and pull-out of the sandwich panel was also significantly reduced with only a small increase in areal density.

Table 3.8: Summary of the air blast test results.

Panel Description	Maximum Central Out-of-Plane Displacement (mm)	Maximum Central Pull-Out (mm)	Approximate Core Shear Strain at Break (%)	Maximum Strain Energy (kJ)	Fraction of Panel Containing damage (%)
Single 40 mm M100 SAN Core	90 ± 3	46 ± 3	9.6 ± 1.9	179	19
Single 30 mm M130 SAN Core	-	-	-	-	3.9
Graded 30 mm SAN Core	102 ± 3.0	66 ± 3	10.5 ± 1.9	239	14
Single 40 mm C70.90 PVC Core	101 ± 3	81 ± 3	13.2 ± 1.9	223	40
Single 40 mm 110SL PMI Core	102 ± 3	90 ± 3	10.5 ± 1.9	173	-
Single 40 mm C70.90 PVC Core with Innegra Face-Sheets	90 ± 3	61 ± 3	10.5 ± 1.9	212	36

Chapter 4

Strength After Blast Testing

4.1 Introduction

The previous chapter described the response of various sandwich composite structures to blast loading, and this chapter quantifies the residual strength of the different constructions after blast. The motivation for this work was to ensure that marine architects can design a marine vessel such that after successfully withstanding a blast, it could continue with reduced service. This service may include staying afloat until a repair vessel arrives, or simply moving away from the threat area. The post-blast damage mapping of the sandwich panels was presented in Chapter 3, and the panels were sectioned such that they would produce suitable test specimens for the tests presented in this chapter. The most crucial loading criteria to a marine hull in service is lateral loading due to wave slamming, and in-plane loading due to the weight of the ship in the water. The structural rigidity of sandwich composites is caused via shear loading in the foam core, separating the high stiffness fibre composite face-sheets, thus increasing their second moment of area and increasing bending stiffness. Therefore, it is clear to see that with damage present in the core, and in the interfaces between the core and face-sheets, shear loads will not be transferred so the bending stiffness will reduce. Also, sandwich composites possess substantial in-plane compressive properties, due to the high stiffness of the face-sheets, and the foam acts to prevent buckling in the face-sheets. As with bending, it is intuitive to see that with core and interface damage,

the onset of buckling will take place sooner, so the damaged sandwich panels will withstand a lesser compressive load. This chapter quantifies the reduction in stiffness and load bearing capacity with varying amounts of damage, and considers the effect of loading rate on these strength reductions. This is achieved using three point flexural testing, which results in a constant shear load across the specimen, and edgewise compression tests. Flatwise compression samples were also cut from the blast panels, but these were not tested due to time constraints.

4.2 Materials

The test specimens were identical to those presented in Chapter 3, with the exception that the 40 mm thick Polymethacrylimid (PMI) Rohacell 110SL was not tested, as the damage sustained during blast was too great to cut the sandwich panel into sections, or to perform any meaningful tests. As such, the specimens presented in this section all contained 2 mm thick glass fibre reinforced polymer (GFRP) face-sheets either side of a 30 mm or 40 mm thick polymeric foam core. The cores contained either styrene acrylonitrile (SAN) or polyvinyl chloride (PVC) foam. The sandwich panels were a 30 mm thick SAN Corecell M130 core sandwich panel; a 30 mm thick SAN graded foam core sandwich panel; a 40 mm thick SAN Corecell M100 core sandwich panel; a 40 mm thick PVC Airex C70.90 core sandwich panel; and a 40 mm thick PVC Airex C70.90 core sandwich panel with polypropylene (PP) Innegra plies interleaved in the GFRP front face-sheet. Two resin systems were used in the construction of the sandwich panels, either SR 8500 epoxy resin with a standard hardener; or ST 94 film resin. A key of resin systems used in each panel, alongside overall test panel thickness and areal density is shown in Table 3.1. Constitutive and bulk face-sheet mechanical properties are shown in Table 3.2, and of the foam polymers used in the sandwich panel cores are shown in Table 3.3. The test samples were cut with a circular saw blade containing teeth with a negative hook angle to prevent fibre snagging, and the pattern is shown in Figure 4.1. The cutting pattern shows flatwise compression samples which were omitted from the tests as they were deemed to be the least informative of the three experiments. The presence of damage in the flatwise specimens would affect the through-thickness compressive properties due to disconnected foam pieces inside

the sandwich specimen sliding over each other. In a large ship hull section the cracked foam sections would remain held in place by the surrounding foam, so the tests would not be a realistic representation of the residual properties of a real ship hull. This is also true for the flexural and edgewise compression tests, however it was possible to determine generic residual properties from these tests such as the damaged shear modulus and damaged shear strength of the sandwich panels in flexural loading, and the buckling strength of the face-sheets in edgewise compressive loading.

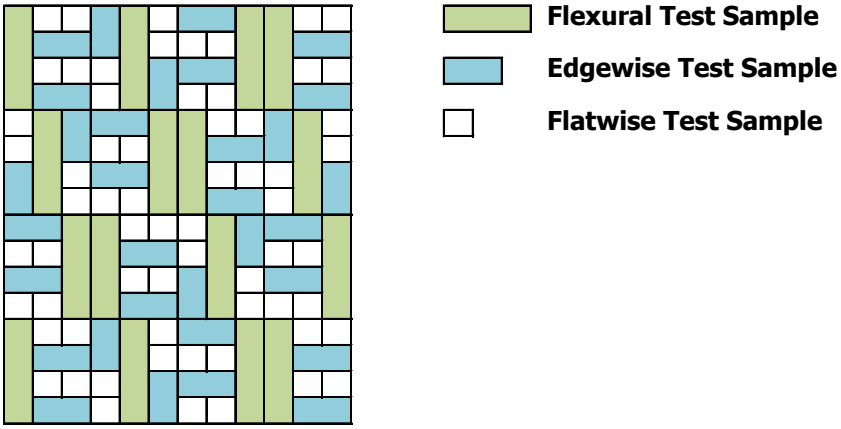


Figure 4.1: Locations of the flexural; edgewise compression; and flatwise compression test samples, cut from the air blast tested sandwich panels.

4.3 Experimental Methods

4.3.1 Flexural Testing

In order to develop an understanding of how the flexural rigidity of the sandwich panels varies with differing amounts of damage, three point bending tests were performed. This method was chosen as it would cause constant shear strain across the whole sandwich beam in the undamaged cases, allowing a comparison to a bulk shear modulus in the damaged cases. In all tests the side edge of the sandwich panel was speckled, to allow digital image correlation (DIC) to be performed during loading. As the damaged specimens underwent complex loading due to uneven stress distributions, the average shear strain across the whole sandwich beam was

measured in each case, to plot shear stress versus shear strain. Therefore, an effective shear modulus for the beam was determined, as well as the ultimate shear stress as calculated from the load. The tests were performed at one of three machine displacement speeds: 0.154 mm/s; 20 mm/s; and 56.4 mm/s. This was performed to check for rate effects, but the lower speeds were not tested in all specimens. The lower speeds were omitted in most sets due to limited amounts of available samples, and wave slamming being a dynamic event. Also the rate sensitivity tests showed little dependence on test speed. These speeds were selected based on test machine availability. A schematic of the three point bending test method is shown in Figure 4.2, and this test design was developed in line with the ASTM C393 [107] testing standard for flexural testing of sandwich composites. The tests were performed on either a biaxial 250 kN ESH hydraulic testing machine, or an Instron 8872 fatigue testing machine. The test samples either failed in top face-sheet (the front face-sheet in the blast tests) compressive failure, or in core shear failure during the three point bending tests. The core shear failure took the form of either core cracking, or debonding between the core and face-sheets. In some cases the top 12 mm diameter roller indented to top face-sheet, and these test results were disqualified from the analysis. As shown in Figure 4.2, rollers of 25 mm diameter were used on the base in line with the testing standard, and the span length between these was 350 mm. This span was the maximum possible from the sandwich composites, as the original blast panels had already been cut into 16 sections of 400 x 325 mm for transportation and storage. The test samples were all cut to a width of between 100 mm and 110 mm.

4.3.1.1 Data Processing

The measurements taken during the three point bending tests were cross-head displacement of the machine, load applied by the top roller and photographs of one long edge at set time intervals for DIC processing. Due to the 10 mm thick rubber pad between the top roller and the top face-sheet, it was not possible to use the cross-head displacement to calculate any properties of the test specimens. Therefore, the displacement of the centre of the test sample was measured by processing the DIC images in Aramis. The size of the pixels was calibrated against the edge

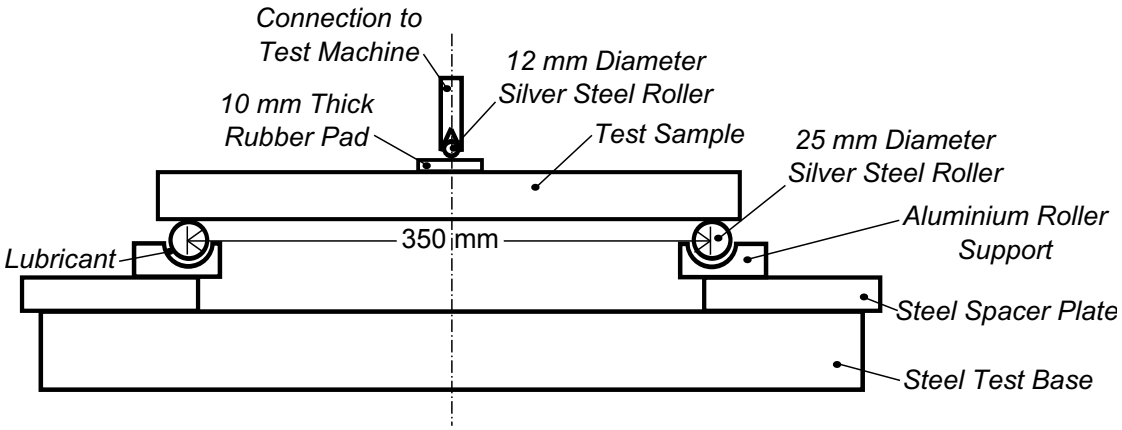


Figure 4.2: Schematic of the three point bending test method.

images of the rollers in the tests as these were manufactured with sharp edges, reflected a lot of light and were photographed perpendicular to the face against a dark background. The load and central displacement were used to calculate the effective stiffness of each sandwich specimen using Equation (4.1), where $\frac{dP}{d\delta}$ is the gradient of the load (P_c) versus central displacement (δ). Also shown in Equation (4.1) is the equation to compare the effective stiffness (K_{eff}) with the bending stiffness (D) and the panel shear rigidity (U), where S is the span of the test sample (350 mm) [107]. The load and central displacement were determined from the machine load cell and from DIC respectively. To prevent frame alignment errors from the DIC, Equation (4.2) was used to calculate the effective stiffness from the test results, where t is time. The equation for calculating the panel bending stiffness for all specimens except for the complaint face-sheet case, is shown in Equation (4.3), where E is the face-sheet modulus; c is the sandwich specimen thickness; h is the foam core thickness; and W is the sandwich specimen width. In the case of the compliant face-sheet specimens, the bending stiffness was calculated using Equation (4.4), where T is the face-sheet thickness; and the subscripts 1 and 2 refer to the front and back face-sheet respectively. The shear rigidity (U) of the panel was calculated using Equation (4.5), where G is the shear modulus of the foam core. This equation was then used for the damaged cases, to provide a value of "damaged shear modulus", which can be used for modelling the post-blast behaviour of sandwich panels. Equation (4.6) was used to calculate the

maximum shear stress (τ) during the test, and Equation (4.7) was used to calculate the maximum direct stress(σ) in the face-sheets in each test. The maximum shear and direct stresses provided the strength of the sandwich panels in bending, with varying amounts of damage.

$$K_{eff} = \frac{dP_c}{d\delta} = \left[\frac{S^3}{48D} + \frac{S}{4U}\right]^{-1} \tag{4.1}$$

$$\frac{dP_c}{d\delta} = \frac{\partial P_c}{\partial t} \cdot \frac{\partial t}{\partial \delta} \tag{4.2}$$

$$D = \frac{Eb\left(c^3 - h^3\right)}{12} \tag{4.3}$$

$$D = \frac{E_1 T_1 E_2 T_2 W \left(d + c\right)^2}{4\left(E_1 T_1 + E_2 T_2\right)} \tag{4.4}$$

$$U = \frac{GW\left(c + h\right)^2}{4h} \tag{4.5}$$

$$\tau = \frac{P_c}{W\left(c + h\right)} \tag{4.6}$$

$$\sigma = \frac{P_c L}{2TW\left(c + h\right)} \tag{4.7}$$

4.3.2 Edgewise Compression Testing

The second set of strength after blast testing considered the edgewise loading of sandwich specimens with varying amounts of blast damage present. When in service the ship hull is required to support the weight of the vessel in the water, causing significant quasi-static and intermediate rate edgewise loading. Testing was performed on an Instron 5985 universal testing machine, with a Canon EOS 350D digital single-lens reflex (DSLR) camera and Phantom Miro M310 high speed camera used to measure the axial DIC strain in the quasi-static and dynamic tests respectively. Similar to the flexural tests, the strain across the surface of the damaged specimens was irregular, so an average strain was measured to determine

an effective compressive modulus of the damaged sandwich specimens. The tests were performed in accordance with ASTM C364 [108]. In order to ensure even loading on both face-sheets, a 10 mm thick rubber spacer was placed between 10 mm thick steel plates, and the compression platens. This accounted for any inconsistency in the cut along the specimen edge. The full compression test setup is shown in Figure 4.3.

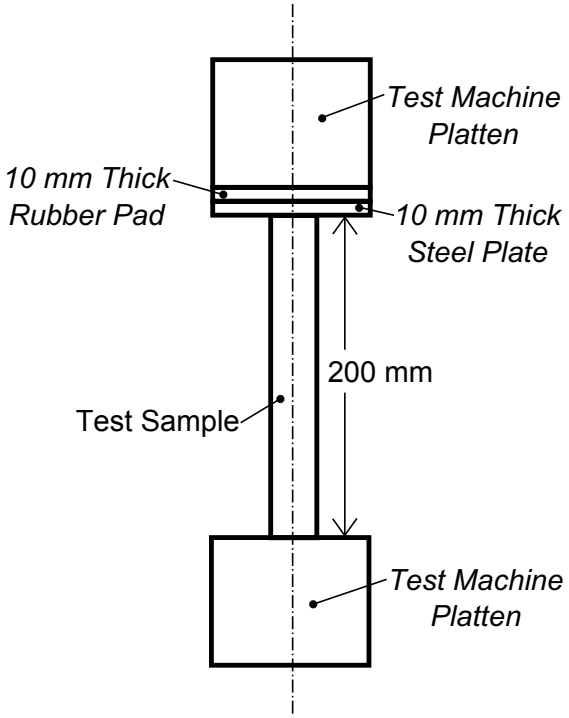


Figure 4.3: Schematic of the edgewise compression test method.

4.3.2.1 Data Processing

Due to slippage at the platens and the strain of the rubber sheet, it was not possible to use machine displacement for the test results. Instead DIC images of the tests were captured with a DSLR or high speed camera. The DIC images were processed for in-plane strain using Aramis. In order to avoid the necessity of aligning the camera frame with the load, the stiffness of the sandwich panel was calculated using Equation (4.8), where E_{eff} is the effective edgewise compression stiffness; σ_y is the in-plane engineering stress; and ε_y is the in-plane engineering strain. The

engineering stress was calculated using Equation (4.9), where F is the applied force; and W and T are the specimen width and face-sheet thickness respectively. The engineering stress was calculated using this method due to the negligible stress in the foam core compared to the GFRP face-sheets. This calculation method is detailed in ASTM C364 [108].

$$E_{eff} = \frac{\partial \sigma_y}{\partial t} \cdot \frac{\partial t}{\partial \varepsilon_y} \tag{4.8}$$

$$\sigma_y = \frac{F}{2\,W\,T} \tag{4.9}$$

4.3.3 Damage Quantification

The method for tracking damage locations was described in Chapter 3. This method resulted in estimated foam core crack surface areas and areas of debond at interfaces. The prediction of the crack surface areas was by interpolating the crack length on two opposing faces, through the perpendicular distance between the cracks. For the estimation of debond surface areas, the fraction of each face debonded was recorded, and an average fraction of all four faces calculated. In order to show how mechanical properties of the test samples varied with damage, it was necessary to determine a non-dimensionalised quantity, to provide an overall severity of damage in each specimen. As the maximum theoretical core crack surface area is a diagonal crack across the entire length of the longest face of the test sample, the core cracks were non-dimensionalised against this. The debond damage was non-dimensionalised against the maximum possible area of debond on each interface, by simply multiplying the specimen width and length. Core crack damage and debond damage were combined by summing the non-dimensionalised values. This resulted in damage levels which were greater than 100% and is expressed at "Total Damage (%)" in this chapter.

4.4 Results

4.4.1 Flexural Testing

4.4.1.1 Rate Effects

This section will present the effect of test speed on the response of the blast tested sandwich beams. It was only possible to acquire enough test samples containing no visible damage from the 30 mm thick SAN Corecell M130 core sandwich panel, to perform a study at three different test rates: 0.154 mm/s; 20 mm/s; and 56.4 mm/s. A total of 13 samples were tested from this sandwich panel, 11 of which contained no visible damage. Four samples were tested at 0.154 mm/s, three samples were tested at 20 mm/s, and two at 56.4 mm/s. Figure 4.4 shows the measured effective stiffness values of the test samples, and it can be seen that at quasi-static rates the effective stiffness is greater. The medium and high rate effective stiffness values are around 1.1 MN/m, and for the quasi-static tests are around 1.55 MN/m, corresponding to core shear moduli of 71 MPa and 264 MPa respectively, using Equation (4.5). The SAN M130 foam has a shear modulus of 59 MPa [100], so closer to the medium and high rate values, but still slightly less. This is due to the DIC method measuring an average central displacement of the beam but not accounting for indentation. This results in a greater effective stiffness as the load increases but the overall central displacement is reduced due to indentation. This effect is only witnessed in the undamaged specimens, as indentation does not occur in the damaged specimens.

The direct stress in the face-sheets and shear stress in the foam core at failure is consistent across all tests, as shown in Figure 4.5, where Figure 4.5a shows the core shear stress at compressive failure of the top face-sheet; and Figure 4.5b shows the direct face-sheet stress at compressive failure of the top face-sheet. Figure 4.6 shows DIC results of compressive strain in the through thickness direction at the point of failure of the top face-sheets, and it can be seen that failure of this type is encouraged by the weak foam core allowing buckling of the front face-sheet in compression, at a critical stress.

The undamaged specimens exhibit rate sensitivity between quasi-static and medium to high rates, and it is expected that should the test rate be increased to

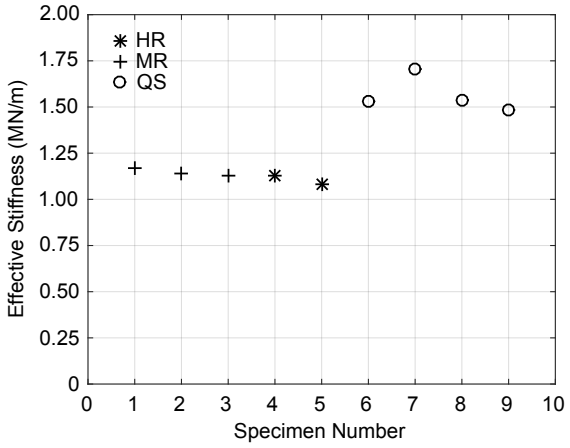


Figure 4.4: Effective stiffness of 30 mm thick SAN Corecell M130 core sandwich beams, tested at high, medium and quasi-static speeds. All of the test samples contained no visible damage prior to flexural testing.

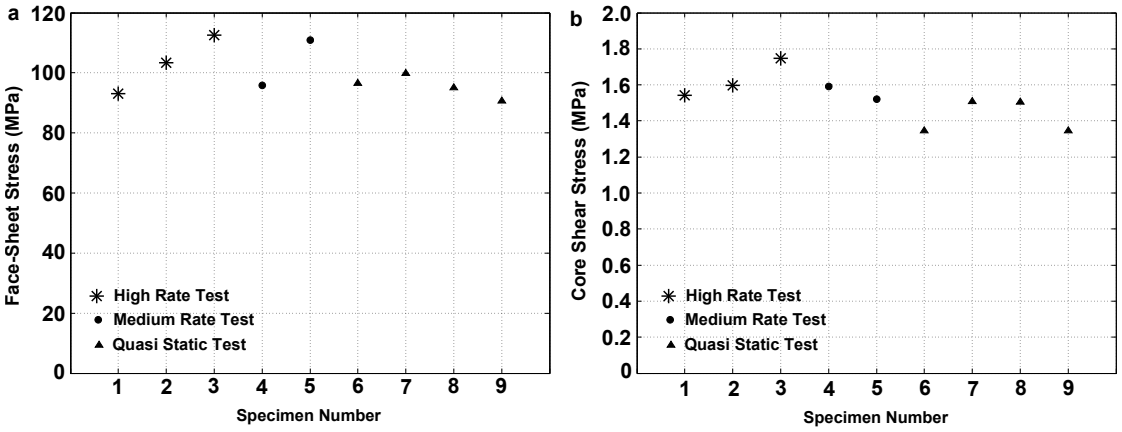


Figure 4.5: a) Direct face-sheet stress and b) core shear stress at failure of 30 mm thick SAN Corecell M130 core sandwich beams, tested at high, medium and quasi-static speeds. All of the test samples contained no visible damage prior to flexural testing.

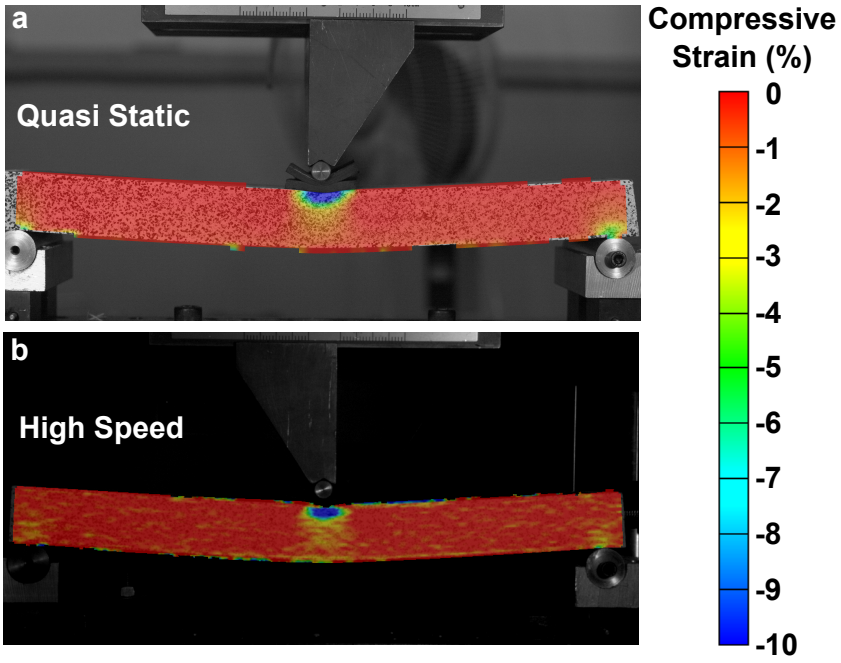


Figure 4.6: a) Quasi-static and b) high speed compressive strain of two 30 mm thick SAN Corecell M130 core sandwich beams. These test samples contained no visible damage prior to flexural testing.

impact speed this effect would be magnified, due to localised crushing of the foam core. The medium to high rates of testing were of interest in this study, as the aim of the research was to assess resistance to loading from waves of the hull of naval vessels. For this reason, the subsequent three test panels were tested at medium and high rates only, due to a limited number of test samples available.

4.4.1.2 Stiffness

The two types of gross damage present in the blast tested sandwich panels were core cracking and debonding between the face-sheets and foam core. In the case of the graded density foam core debonding was also present between the foam layers. The damage in each test specimen was recorded using a MATLAB script, as described in Chapter 3, and this section considers the effect of the amount and type of damage present on the effective stiffness of the test sample in three point bending. In the results presented here the central deflection of the sandwich panel during loading was measured using DIC, and the load recorded using the load cell in the test machine. The specimens taken from the 30 mm thick SAN Corecell M130 foam core sandwich panel had only two out of 11 containing visible damage. It was, therefore, unrealistic to draw any conclusions from these tests on the effect of damage on this construction of sandwich panel. However in the case of the 30 mm thick SAN graded density sandwich panel, damage was present in varying amounts, to provide an overall plot of effective stiffness versus damage suffered. The visible damage present is as described earlier in this chapter, and the results of the graded density sandwich specimens are shown in Figure 4.7. The graded sandwich specimen results show that there is a clear drop in effective stiffness as the amount of damage increases, as is expected, and that at the onset of minor damage the effective stiffness drops dramatically. The outlying point in Figure 4.7 is caused by highly distributed damage across the specimen, with no full debonding of interfaces. A DIC contour plot of maximum principal strain (MPS) is shown in Figure 4.7 for this point, and if compared to the other DIC contour plot shown, it can be seen that the lower effective stiffness case has much more severe damage. In the case of the graded density foam core, it is found that the effective stiffness reduced to an average value of 0.07 MN/m. By using Equation (4.1) this implies a

specimen shear rigidity of 6133 N, or a specimen shear modulus of 1.6 MPa. This damaged shear modulus could then be used to calculate the response of moderately to heavily damaged graded blast panels to subsequent loading scenarios.

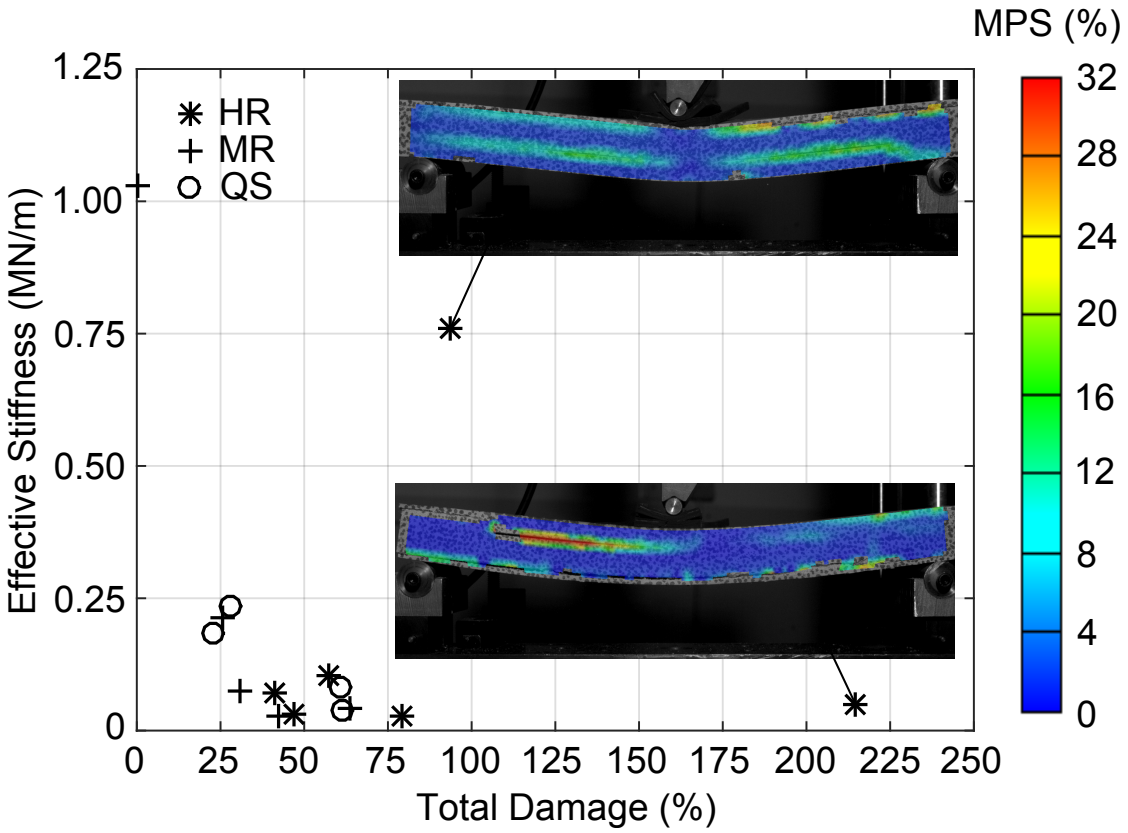


Figure 4.7: Effective stiffness versus visible damage for the 30 mm thick SAN Corecell graded core sandwich panel, tested at three different rates.

As the 40 mm thick PMI Rohacell 110SL sandwich panel was too damaged during blast to be sectioned into smaller samples, it was not included in these tests. However the 40 mm thick SAN Corecell M100 sandwich panel, and the 40 mm thick PVC Airex C70.90 sandwich panel were tested, allowing a comparison of the residual stiffness capabilities of the two foam cores. The effective stiffness versus damage plot of the M100 sandwich panel is shown in Figure 4.8, and for the C70.90 panel is shown in Figure 4.9. The outlying points in the M100 case of Figure 4.8 are caused by there only being debonding present between one face-sheet and core, and very small amounts of core cracking. Also shown in Figure 4.8

are DIC maximum principal strain plots, where the highly damaged specimen which exhibited low effective stiffness is shown to have mixed damage across the whole panel. These results imply that the critical factor in retaining bending stiffness in the sandwich beams is to prevent debonding of the face-sheets from the foam core, as preventing debonding in both face-sheets results in high bending stiffness. This is an intuitive conclusion, as the foam core is present in the sandwich panel to transmit shear between the stiff face-sheets, which are loaded in tension and compression. With core cracks present and no debonding, the face-sheets will remain coupled, but the shear stiffness of the foam core is reduced, thus reducing the bending stiffness. However, with the presence of debonding the face-sheets become decoupled, so shear is not transmitted between the face-sheets, dramatically reducing the bending stiffness of the sandwich beam. The results of the C70.90 cases presented in Figure 4.9 have one outlying result. In this case, the sandwich panel contained no bottom face-sheet debonding and 23% top sheet debonding, with 60% of the specimen length containing cracks. This further supports the hypothesis that bending stiffness is retained with lower debonding. The DIC contour plot shown indicates that failure took place when debonding initiated at a crack, emphasising even more strongly that the damage mechanisms in loading a pre-damaged specimen are complex. The results of these two tests show that the two sandwich beams have similar effective stiffness values without the presence of damage, and the effective stiffness values reduce similarly in each case. From the two sets of tests, it was found that with moderate to high damage present (above 100% using the quantification method outlined previously), the effective stiffness values of the M100 and C70.90 sandwich panels were likely to reduce to 0.09 MN/m and 0.11 MN/m respectively. These values imply shear rigidities of 7885 N and 9641 N for the two panels respectively. The damaged shear moduli of the M100 and C70.90 panels were 1.6 MPa and 2.0 MPa respectively.

The final blast test panel to be tested for residual strength was the 40 mm thick PVC Airex C70.90 core sandwich panel, which contained compliant PP fibres in the front face-sheet, designed to mitigate front face-sheet compressive failure during blast. The purpose of the blast tests performed on the compliant face-sheet sandwich panel was to assess if the front face-sheet survived with similar amounts of core damage suffered as in the identical case without the PP plies, and it was found

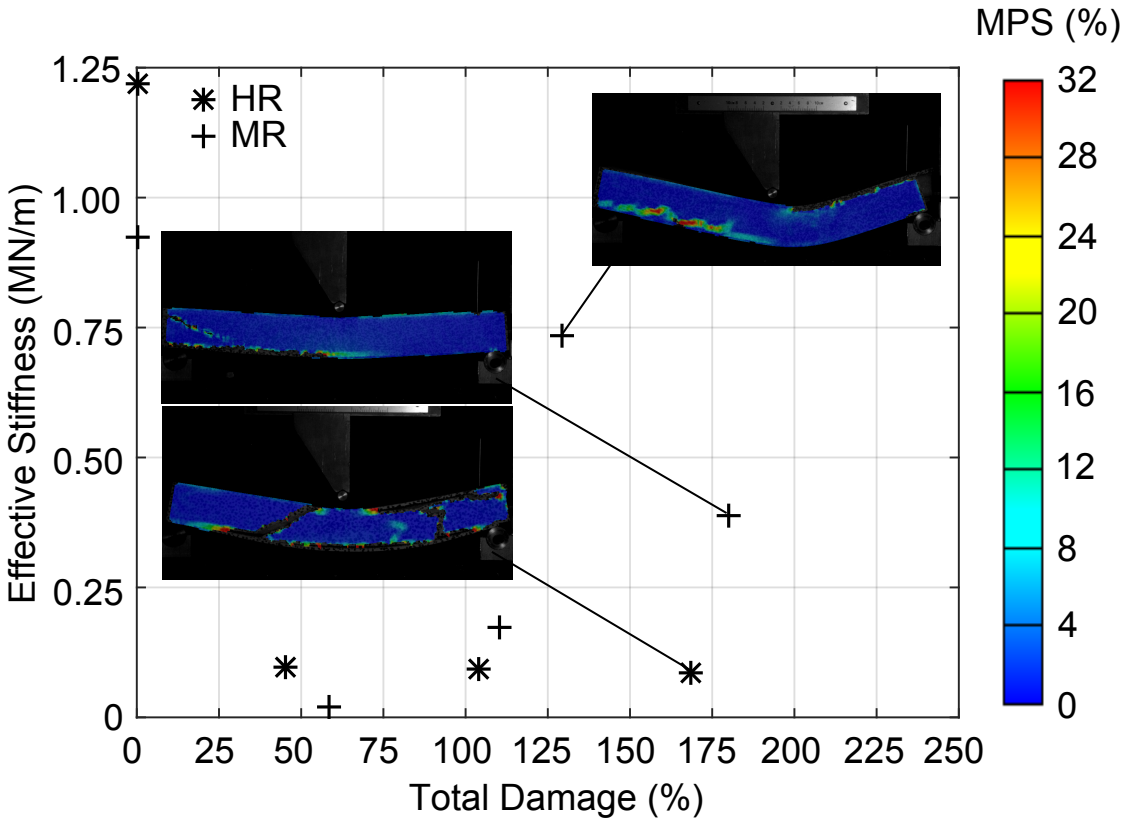


Figure 4.8: Effective Stiffness versus visible damage for the 40 mm thick SAN Corecell M100 core sandwich panel, tested at two different rates.

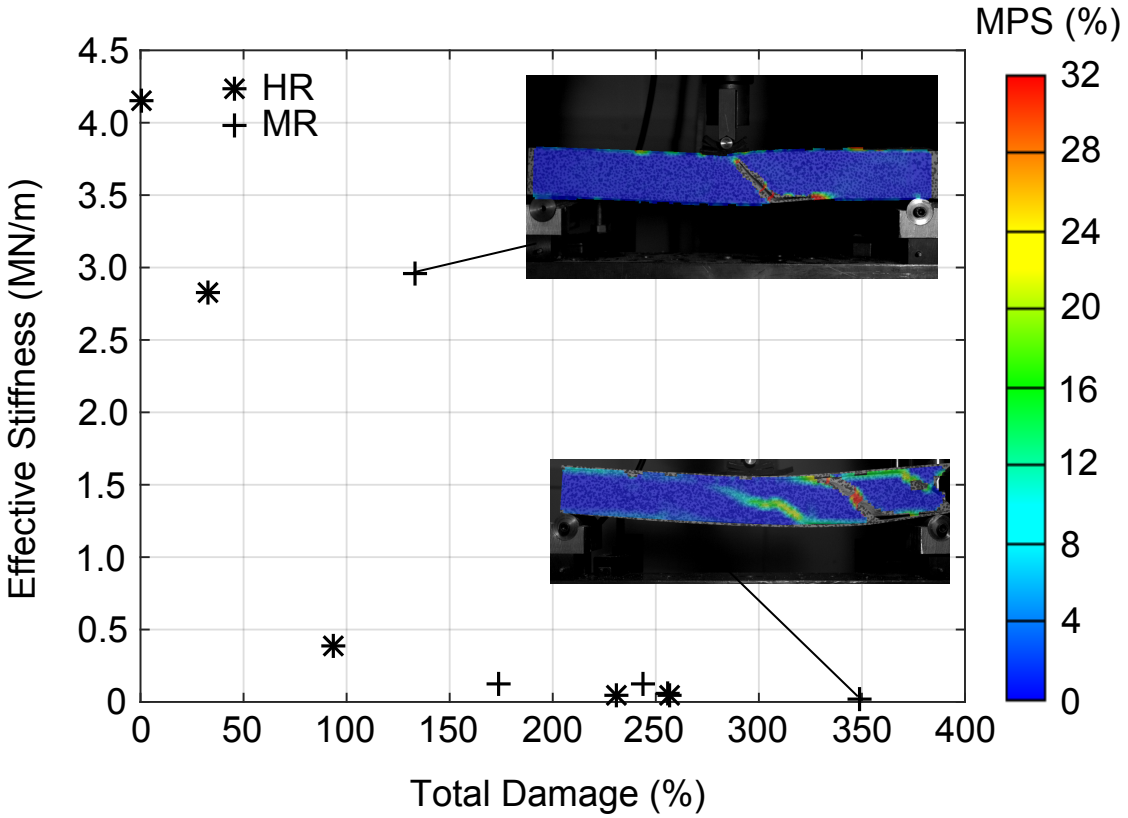


Figure 4.9: Effective stiffness versus visible damage for the 40 mm thick PVC Airex C70.90 core sandwich panel, tested at two different rates.

that front face-sheet damage was mitigated. As the core crack and debond levels were similar to the case without the PP plies, it was expected that the reduction in bending stiffness was similar, and the results of the effective stiffness versus visible damage for this sandwich panel are shown in Figure 4.10. In these results the one slightly outlying point contains a small amount of debond, as witnessed in the outlying points presented previously. As with the polymer comparison cases, the effective stiffness of the sandwich panel with moderate damage drops to around 0.1 MN/m. This value of effective stiffness was used to calculate a panel shear rigidity of 8,966 N, and a damaged core shear modulus of 1.8 MPa.

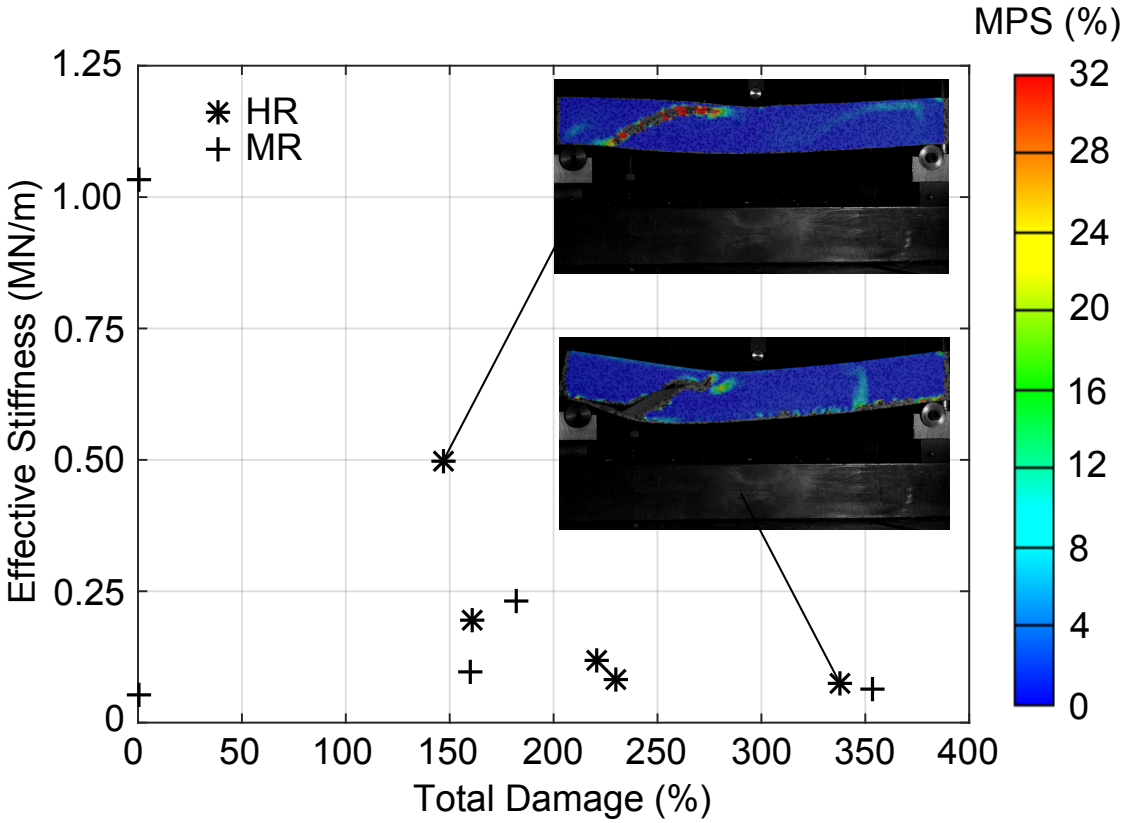


Figure 4.10: Effective stiffness versus visible damage for the 40 mm thick PVC Airex C70.90 sandwich panel with PP front face-sheet fibres, tested at two different rates.

4.4.1.3 Strength

The second important parameter in the post-blast behaviour of the sandwich composites is the maximum load carrying capacity. This section presents the maximum shear stresses in the foam core and the maximum direct stresses in the face-sheets at failure for each case. As with the effective stiffness data, there were not enough damaged M130 specimens to perform a study on residual strength for this panel. The results of the graded density sandwich panel, however, are shown in Figure 4.11, where Figure 4.11a shows the core shear stress with varying amounts of damage, and Figure 4.11b shows the direct stress in the face-sheets versus visible damage. As with the effective stiffness results for the graded density core, there is an outlying data point in Figure 4.11, caused by high dispersion of damage across the beam. From these results it can be seen that the shear and direct stress limits of the graded density sandwich panel reduce to around 0.2 MPa and 10 MPa respectively upon the onset of damage.

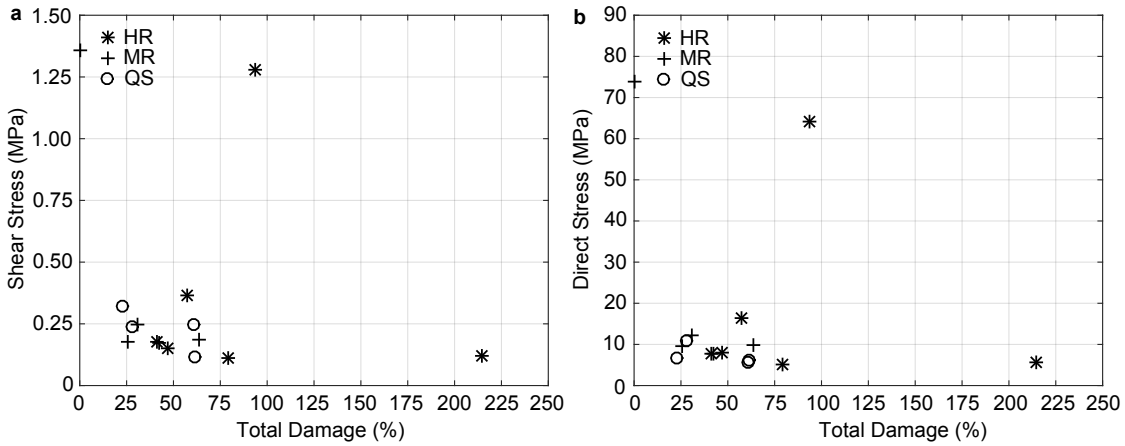


Figure 4.11: a) Maximum shear stress and b) maximum direct face-sheet stress versus visible damage for the 30 mm thick SAN Corecell graded core sandwich panel, tested at three different rates.

The maximum core shear and direct face-sheet stress for the 40 mm thick SAN Corecell M100 foam core sandwich beams are shown in Figure 4.12a and Figure 4.12b respectively. As with the graded density panel, the M100 test specimen strength reduces to a constant value when damage is present. These reduced values are approximately 0.2 MPa for core shear and 10 MPa for direct face-sheet stress.

The 40 mm thick PVC Airex C70.90 core sandwich specimens, however, show a clear linear decrease in shear and direct failure stress with increased amounts of damage, as shown in Figure 4.13a and Figure 4.13b respectively. The difference in the two responses is likely to be caused by the smaller amounts of damage in the C70.90 samples being dominated by core cracks, and not by debond, unlike the M100 samples where the smaller damage contained debonding. As with the effective stiffness results, debonding is the key factor in deteriorating the bending properties of the sandwich beams as the two face-sheets are decoupled. The C70.90 specimen shear and face-sheet failure stresses reduce to around 0.1 MPa and 10 MPa respectively for moderate to high damage, when both debonding and core cracking is present.

The shear strength and face-sheet failure stress in the compliant face-sheet sandwich specimens reduced to around 0.2 MPa and 10 MPa respectively when damage was present. Aside from the outlying result, as discussed in the effective stiffness section, the failure stresses reduce to constant values with moderate damage present. The results of the shear strength and face-sheet strength versus damage are shown in Figure 4.14a and Figure 4.14b respectively.

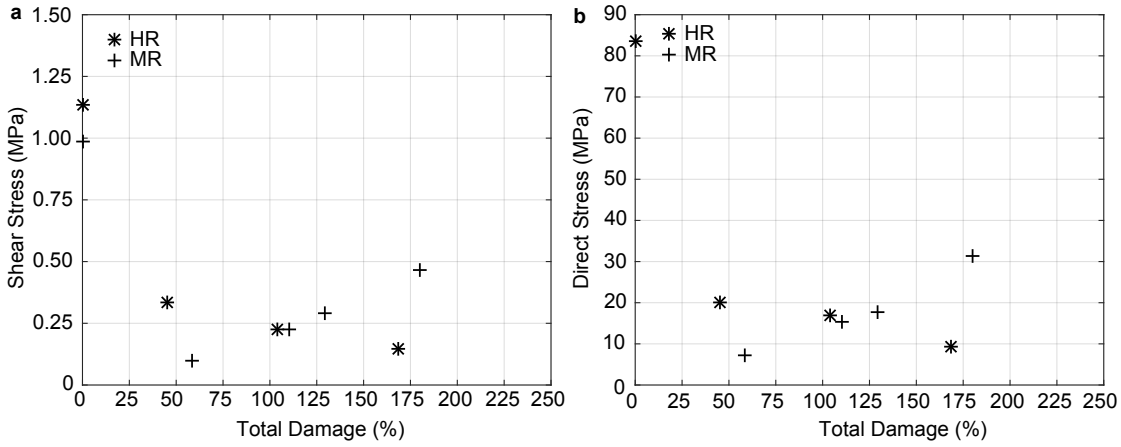


Figure 4.12: a) Maximum shear stress and b) maximum direct face-sheet stress versus visible damage for the 40 mm thick SAN Corecell M100 core sandwich panel, tested at two different rates.

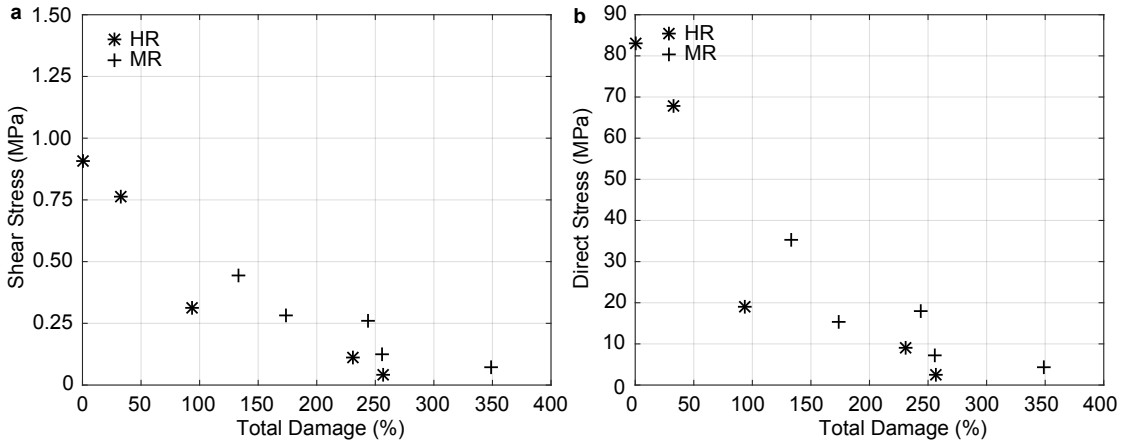


Figure 4.13: a) Maximum shear stress and b) maximum direct face-sheet stress versus visible damage for the 40 mm thick PVC Airex C70.90 core sandwich panel, tested at two different rates.

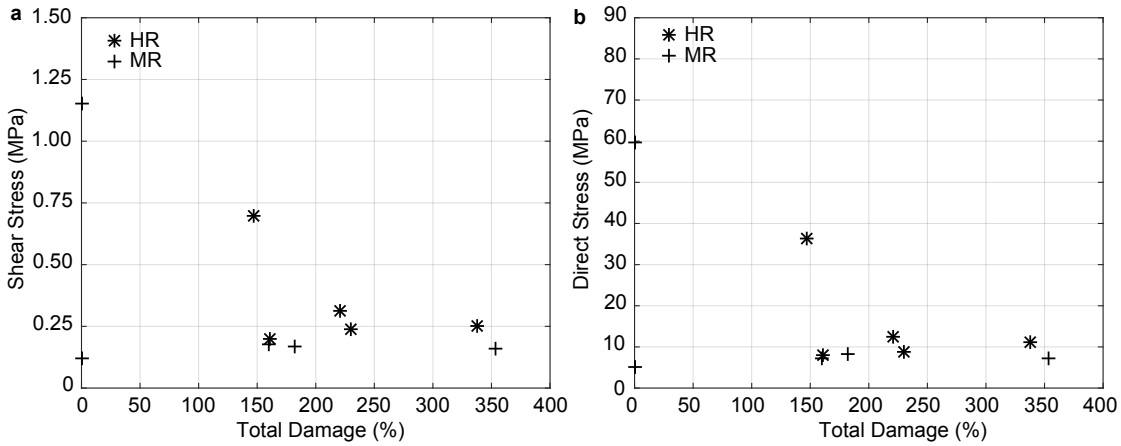


Figure 4.14: a) Maximum shear stress and b) maximum direct face-sheet stress versus visible damage for the 40 mm thick PVC Airex C70.90 sandwich panel with PP front face-sheet fibres, tested at two different rates.

4.4.2 Edgewise Compression Testing

4.4.2.1 Rate Effects

The edgewise compression strength of GFRP face-sheet sandwich panels is much greater than their flexural effective stiffness. For this reason, it was not possible to use a test machine with a great enough load capacity to test the specimens at 56.4 mm/s. However, the in-plane loading of the ship hull is caused by static loading of the ship weight and reasonably low frequency oscillations due to the buoyancy of the ship. The maximum possible test speed in these tests was 5 mm/s, which was used for the medium rate tests, and 0.03 mm/s was used for the quasi-static tests. As with the flexural tests, the 30 mm thick SAN Corecell M130 core sandwich panel was used to assess the effect of loading rate on response, as this was the only sandwich panel which produced enough specimens with no visible damage. A plot of compressive modulus for samples tested at the two different speeds is shown in Figure 4.15 for M130 samples with no visible damage. It can be seen that the compressive modulus appears to decrease on average as the testing rate is increased, but that there is significant variation in the results obtained. The most likely cause of this variation in compressive modulus was bending in the face-sheets, meaning that the load was not transmitted along the glass fibres. This could be caused by local defects which were not visible in the damage inspections, or by uneven loading not accounted for by the rubber pads used for testing. It is expected that the reduction in modulus with higher loading rates was caused by greater instabilities in the face-sheets, caused by uneven loading. At greater test rates the rubber pads were more stiff, so offered less correction to evenly distribute the load across the two face-sheets. The results of the edgewise compression testing of the graded density foam core, at the medium and high rates, are shown in Figure 4.16, for cases with no visible damage present. In the graded case there was a clear reduction in compressive modulus with loading rate, and the DIC images shown alongside data points in Figure 4.16 show that this was caused by localised bending in the face-sheets.

The maximum in-plane stress measured during the 30 mm thick SAN Corecell M130 core sandwich panel is shown in Figure 4.17, and it can be seen that there was no correlation between test speed and strength of the sandwich panels. Similarly

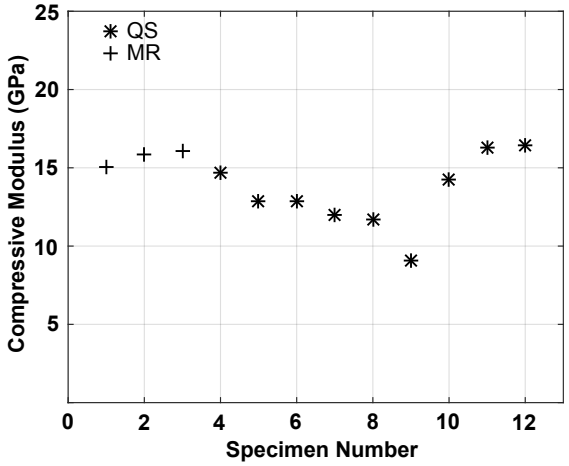


Figure 4.15: Compressive modulus of 30 mm thick SAN Corecell M130 core sandwich beams, tested at medium and quasi-static speeds. All of the test samples contained no visible damage prior to edgewise compression testing.

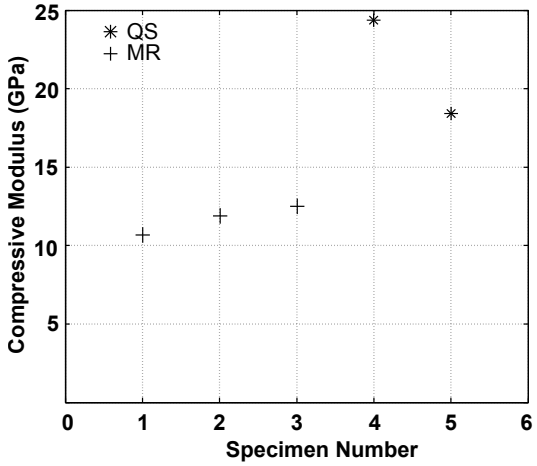


Figure 4.16: Compressive modulus of 30 mm thick SAN graded core sandwich beams, tested at medium and quasi-static speeds. All of the test samples contained no visible damage prior to edgewise compression testing.

to the compressive modulus results, there is a fair amount of spread in the medium speed results, and this was caused by bending instabilities in the face-sheets being more pronounced at higher rates. The average strength of the specimens was 144 MPa. The in-plane compressive strengths of the 30 mm thick SAN graded density core sandwich specimens are shown in Figure 4.18, for cases with no visible damage. As with the M130 specimens, the graded density specimens showed no dependence on loading rate, and the average strength of the undamaged specimens was 152 MPa.

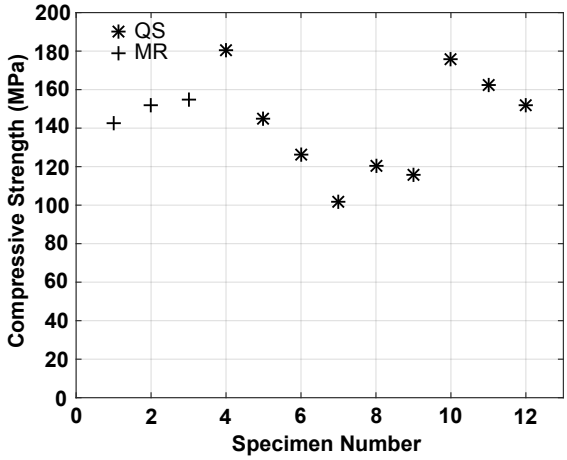


Figure 4.17: Maximum in-plane stress of 30 mm thick SAN Corecell M130 core sandwich beams, tested at medium and quasi-static speeds. All of the test samples contained no visible damage prior to edgewise compression testing.

4.4.2.2 Stiffness

The variation in compressive modulus versus visible damage present for the 30 mm thick SAN Corecell M130 sandwich panel, and the 30 mm thick SAN graded density sandwich panel are shown in Figure 4.19 and Figure 4.20 respectively. The outlying medium rate data point in the M130 case, at around 75% damage, was caused by the damage taking the form of core cracks, and not debonding, which was discussed in the flexural test results. In edgewise compression, the core does not offer much stiffness to load, but acts to prevent bending in the face-sheets, meaning they buckle at a greater load. Therefore, debonding will remove this advantage, reducing the load at which buckling happens. Core cracking has

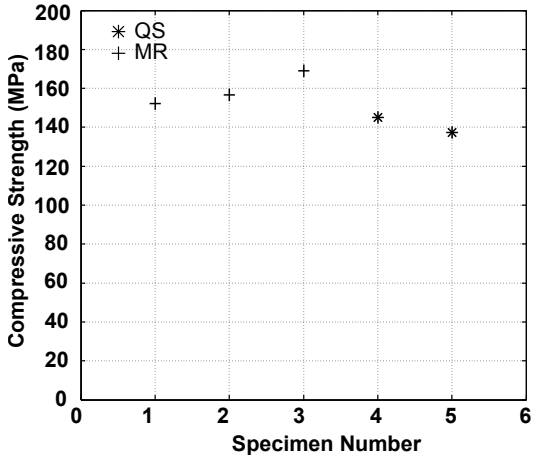


Figure 4.18: Compressive strength of 30 mm thick SAN Corecell graded core sandwich beams, tested at medium and quasi-static speeds. All of the test samples contained no visible damage prior to edgewise compression testing.

a similar effect, except that much more cracking is required to allow bending in the face-sheets, as a large area of foam will still be in contact with the face-sheets with minor cracks. For the graded density core case, it can be seen that there was no trend between the amount of damage present and stiffness, and this was due to the complexity of damage modes in the test samples. As there were four interfaces and three foam layers in the sandwich panels, it was not possible to witness a trend. For example, debonding between the foam layers, with no cracking and face-sheet debonding, was fairly common in the sandwich panel, and in these cases the compressive modulus remained almost unaffected by damage. This was because the face-sheets were still prevented from buckling by remaining adhered to a layer of foam. This is shown in some of the DIC strain contour plots in Figure 4.20.

The results of the residual edgewise compressive modulus tests on the 40 mm SAN Corecell M100 sandwich panel, and the 40 mm thick PVC Airex C70.90 sandwich panel are shown in Figure 4.21 and Figure 4.22 respectively. In the M100 case, the compressive modulus is shown to decrease to around 2 GPa with moderate to heavy damage present. In the C70.90 case the outlying results of modulus at damage levels of 160% and 110% were caused by complete debonding of one face-sheet but not the other. This caused the load to stay similar to the

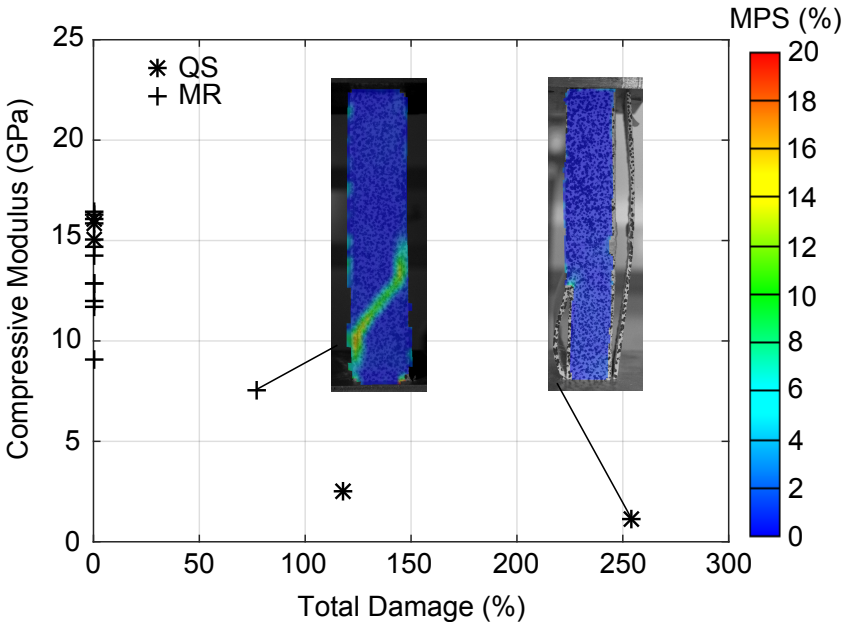


Figure 4.19: Compressive modulus versus visible damage for the 30 mm thick SAN Corecell M130 core sandwich panel, tested at two different rates.

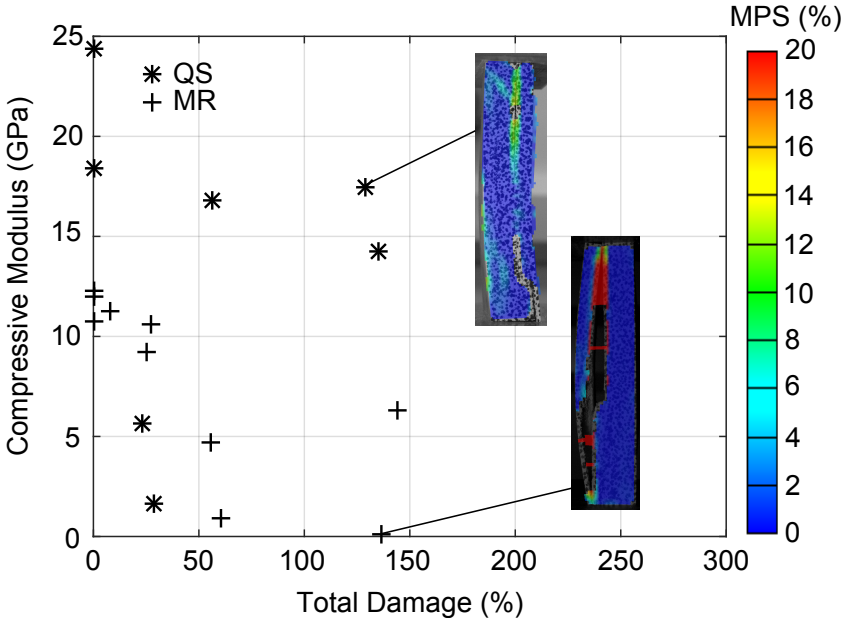


Figure 4.20: Compressive modulus versus visible damage for the 30 mm thick SAN graded density core sandwich panel, tested at two different rates.

undamaged case. The rest of the results showed a decrease in modulus to an average of around 0.5 MPa with moderate to heavy damage.

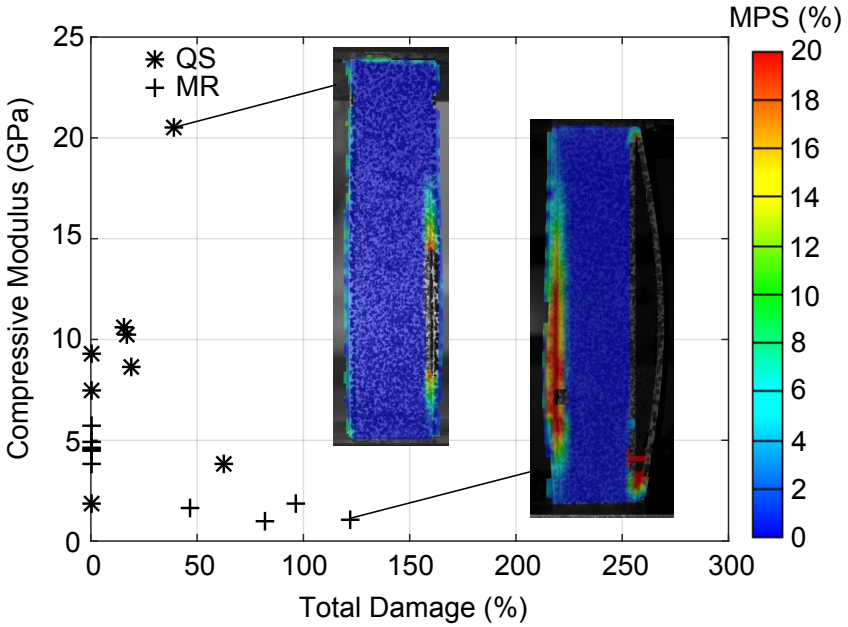


Figure 4.21: Compressive modulus versus visible damage for the 40 mm thick SAN Corecell M100 core sandwich panel, tested at two different rates.

Figure 4.23 provides the compressive moduli of the compliant PP test specimens with varying amounts of visible damage prior to testing. In the tests on this sandwich panel, the outlying results were in specimens where the back face-sheet had debonded, but the front, thicker face-sheet was still connected to the foam core. With heavy damage present the edgewise compressive modulus of the compliant face-sheet sandwich specimens reduced to around 2 GPa.

4.4.2.3 Strength

Figure 4.24 and Figure 4.25 show the relationship between in-plane compressive strength and visible damage prior to testing of the 30 mm thick SAN Corecell M130 core sandwich panel and the 30 mm thick SAN graded density core sandwich panel respectively. Unlike the compressive moduli of these specimens, the compressive strength shows a clear trend with damage present. The M130 specimen strength reduced to a constant strength of around 10 MPa with moderate to heavy damage,

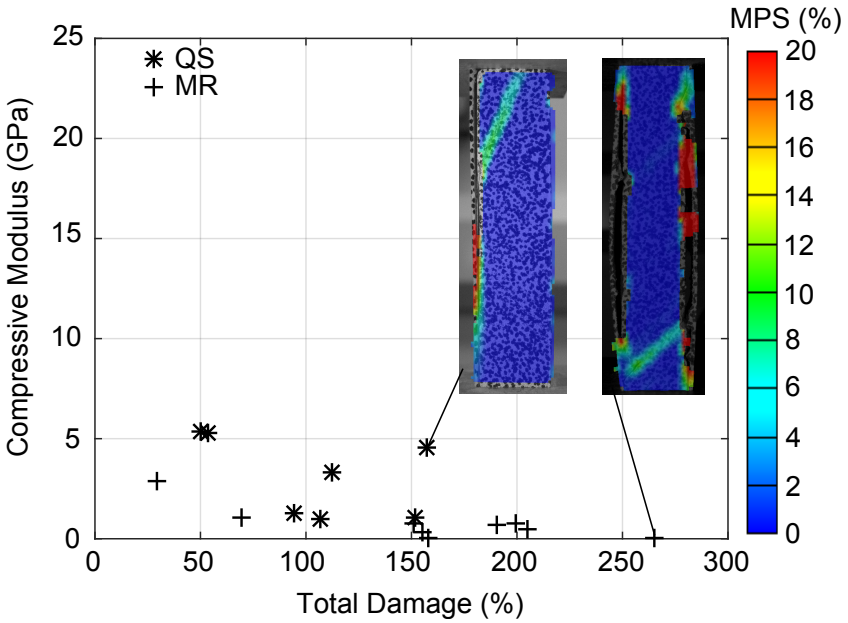


Figure 4.22: Compressive modulus versus visible damage for the 40 mm thick PVC Airex C70.90 core sandwich panel, tested at two different rates.

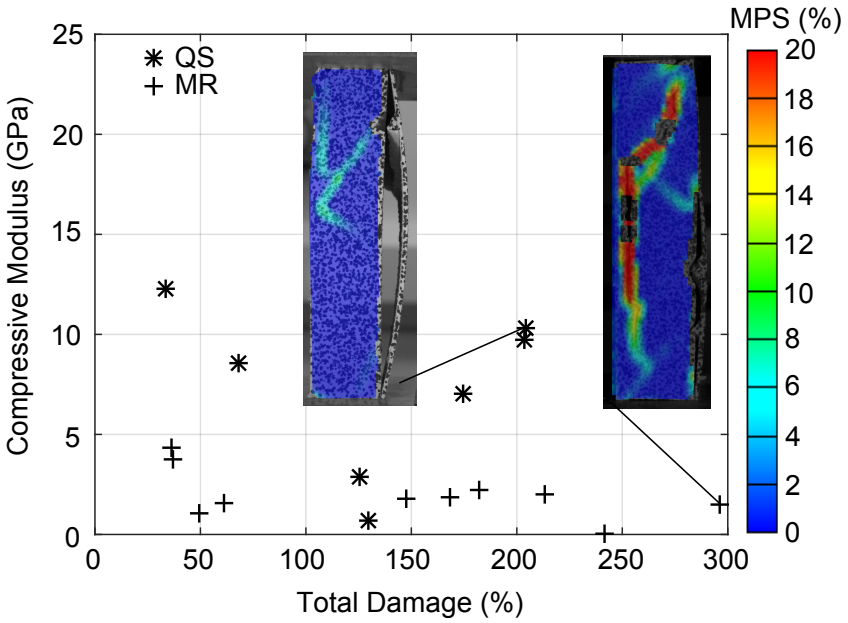


Figure 4.23: Compressive modulus versus visible damage for the 40 mm thick PVC Airex C70.90 core sandwich panel with Innegra PP plies in the front face-sheet, tested at two different rates.

whereas the graded density specimens reduced to around 20 MPa on average. The graded residual strength was greater due to damage being more distributed through the sandwich panel, and debonding between the face-sheets and core being less than the debonding between the foam layers. This meant that the face-sheets were prevented from buckling by the foam layers they remained adhered to.

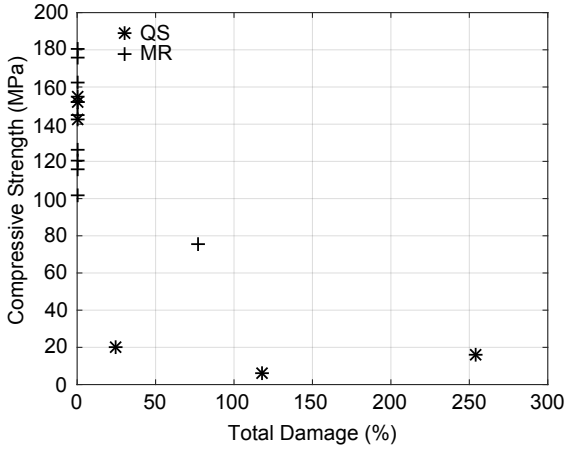


Figure 4.24: Compressive strength versus visible damage for the 30 mm thick SAN Corecell M130 core sandwich panel, tested at two different rates.

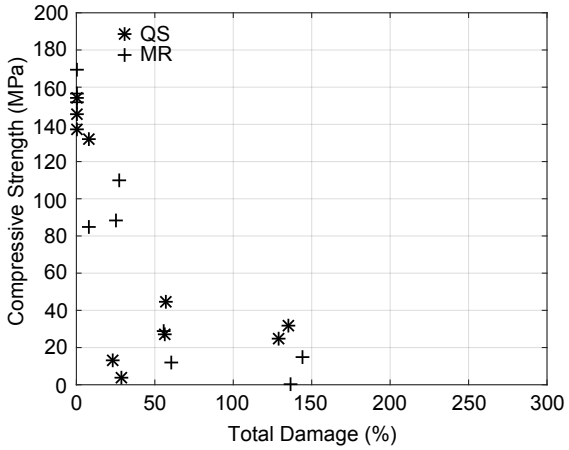


Figure 4.25: Compressive strength versus visible damage for the 30 mm thick SAN Corecell graded density core sandwich panel, tested at two different rates.

The results of the 40 mm thick SAN Corecell M100 core, and the 40 mm thick PVC Airex C70.90 core sandwich panels are shown in Figure 4.26 and Figure 4.27

respectively. In the M100 case there is a clear linear reduction in sandwich panel strength with increasing damage, and this was also present in the C70.90 specimens. In the C70.90 cases, there was an outlying result, caused by debonding on only one side. The C70.90 panel strength reduced to around 3 MPa with moderate to heavy damage, but the M100 specimens did not contain enough damage to fully define a constant reduced strength. However, visual extrapolation of the data implied that this strength reduced to around 10 MPa.

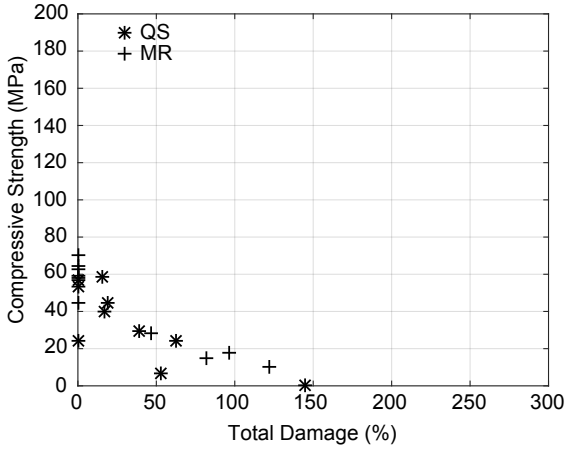


Figure 4.26: Compressive strength versus visible damage for the 40 mm thick SAN Corecell M100 core sandwich panel, tested at two different rates.

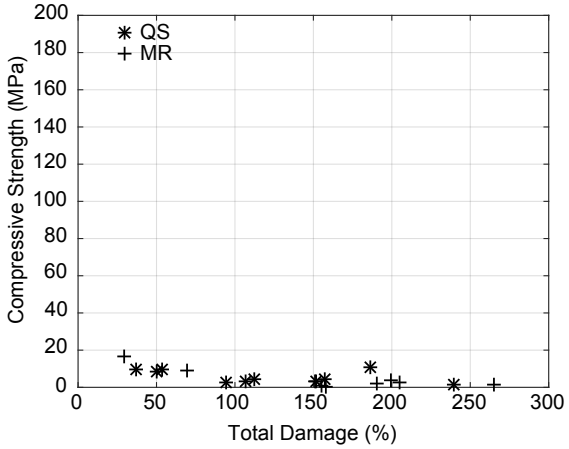


Figure 4.27: Compressive strength versus visible damage for the 40 mm thick PVC Airex C70.90 core sandwich panel, tested at two different rates.

Figure 4.28 provides the strength versus visible damage plots of the 40 mm thick PVC Airex C70.90 foam core sandwich panel, containing compliant Innegra PP plies within the front face-sheet. Due to most specimens not suffering debonding between the core and the thick front face-sheet, a trend in damage with strength was less pronounced. It appears that with moderate to heavy damage, the strength reduced to an average of 10 MPa, but there was a large deviation associated with this value, depending on the types of damage.

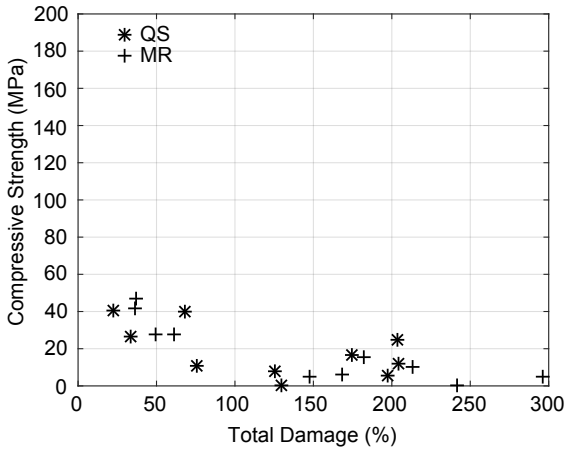


Figure 4.28: Compressive strength versus visible damage for the 40 mm thick PVC Airex C70.90 core sandwich panel with Innegra PP plies in the front face-sheet, tested at two different rates.

4.5 Discussion

4.5.1 Flexural Tests

The post-blast flexural tests recorded in this chapter were performed according to the test standard ASTM C393 [107]. In order to prevent core crushing at the indentor it was necessary to use thick rubber pads to spread the load. Bending stiffness was calculated with the use of DIC to track the central displacement of the test samples, as machine displacement could not be used due to the rubber pads. The DIC could also be used to measure shear strain during the tests in order to calculate the shear modulus from the calculated shear stress. However, it was found

to be more robust to calculate the effective shear modulus from the effective beam stiffness using Equation (4.1). When calculating the effective shear modulus the direct face-sheet stiffness was assumed to be unaffected by damage, an assumption which is invalidated for areas where front face-sheet cracking took place. However, this system is sufficient for comparing the foam cores, as the intended use for this assessment is in FEA, where damage would not be included in the face-sheets in the elastic material models. A summary of the test results obtained for the flexural tests are shown in Table 4.1, where the damaged properties are provided as an average of the damaged test results performed at both medium rates and high rates. These values were calculated from the point at which the property had reached a plateau, and outlying results were omitted. The undamaged properties were calculated from an average of results with zero visible damage, omitting any very low values where it was clear that damage was present which had not been identified with the inspection method.

The data in Table 4.1 show good correlation between the calculated bending stiffness and the undamaged bending stiffness measured from the tests. The stiffness values are similar in every case due to the in-plane stiffness of the face-sheets being much higher than the shear modulus of the foam core, but it can be seen that in the M100 case the bending stiffness is increased due to the higher shear modulus of the SAN core. The results also show that the bending stiffness values all reduce to around 0.1 MN/m when damage is present. From this the shear moduli shown in Table 4.1 were calculated and could be used as foam shear properties in an FEA study. The damaged specimen foam shear strengths were similar in every case, as were the damaged face-sheet strengths.

From the flexural test results it is clear that with damage present in the sandwich composites, the specimens have the same bending properties. This is due to the decoupling of the two face-sheets with core damage, meaning that all of the stiffness is caused by the in-plane stiffness of the face-sheets. The DIC results also show that the amount of core cracking present in the specimens has much less of an effect on the bending properties than debonding between the face-sheets. Using a graded density foam core does not alter this observation, as the foam layers simply move over each other when debonded.

Table 4.1: Post-blast flexural test results summary for the five air blasted sandwich panels.

Panel Description	Calculated Effective Stiffness (MN/m)	Undamaged Effective Stiffness (MN/m)	Damaged Effective Stiffness (MN/m)	Effective Damaged Shear Modulus (MPa)	Undamaged Shear Strength (MPa)	Damaged Shear Strength (MPa)	Undamaged Face-sheet Strength (MPa)	Damaged Face-sheet Strength (MPa)
M100 SAN	1.25	1.07 ± 0.21	0.09 ± 0.05	1.6	1.13	0.21 ± 0.09	83.45	13.78 ± 5.34
M130 SAN	1.02	1.38 ± 0.24	-	-	1.51 ± 0.10	-	98.83 ± 6.35	-
Graded SAN	1.08	1.03	0.05 ± 0.03	1.6	1.36	0.19 ± 0.08	73.98	8.45 ± 3.5
C70.90 PVC	1.02	4.15	0.07 ± 0.04	2.0	0.91	0.15 ± 0.10	82.94	9.39 ± 6.07
C70.90 PVC with PP Interlayers	1.12	1.03	0.12 ± 0.07	1.8	1.15	0.19 ± 0.06	59.58	8.07 ± 2.48

4.5.2 Edgewise Compression Tests

Edgewise compressive loading of ship hulls is caused by the static weight of the ship in the water, and the up and down movement of the ship caused by buoyancy. For this reason, low and medium rates were tested and this allowed easily accessible testing equipment to be used. The rate dependence of the undamaged specimens was tested first, and it was found that the strength was independent of test rate, but that the compressive modulus was greater at medium test rates. This could either be due to the rate sensitivity of the rubber pad used for evenly distributing the load, by inaccuracies in measuring the elastic modulus using DIC, or by the dynamic buckling of the face-sheets.

As with the flexural test specimens, the edgewise compression specimens showed similar plateau levels with heavy damage, except for the PVC C70.90 sample with was much lower. In the case of edgewise compression the undamaged compressive moduli were discounted, as DIC is too inaccurate at low strains to provide usable results. The points were shown in the plots for illustration of the stiffness reduction only.

The edgewise compression test results are summarised in Table 4.2 and it can be seen that all of the results are similar, with the compression strength reducing to around 10 MPa in every case except for the C70.90 samples. The results presented in Table 4.2 with damage present are calculated from an average of the results where a clear plateau was visible, with any outlying results omitted. The undamaged strength was calculated from the results with zero damage present, removing any unexpectedly low values as it was clear that existent damage had not been picked up in the damage mapping process. In the SAN M100 case, the undamaged compressive strength result is omitted, as the measured values were found to be unexpectedly low. The cause of this anomaly is likely due to unidentified damage in the specimens or sample failure at the compression platens which was not highlighted by DIC. The low residual strength of the C70.90 test samples is caused by much greater core cracking than the SAN cases, in which the majority of damage was debonding. Debonding is not as problematic as the foam still acts to prevent buckling in the face-sheets, unless they bow away from the foam, whereas a high crack density causes a less integral anti-buckling mechanism.

Furthermore, with more core cracks the foam slips outwards when loaded in edgewise compression, thus pushing the face-sheet out and causing buckling to happen earlier. This observation is highlighted by the greater compressive strength of the damaged graded density foam core samples, as the crack distribution was much greater in this sandwich panel. This resulted in small pieces of cracked foam, which were not large enough to displace the face-sheets outwards.

Table 4.2: Post-blast edgewise compression test result summary for the five air blasted sandwich panels.

Panel Description	Damaged Compressive Modulus (GPa)	Undamaged Compressive Strength (MPa)	Damaged Compressive Strength (MPa)
M100 SAN	1.93 ± 1.33	-	16.69 ± 5.89
M130 SAN	3.72 ± 3.38	144.11 ± 24.03	14.00 ± 7.28
Graded SAN	-	152.39 ± 10.70	20.14 ± 13.76
C70.90 PVC	1.81 ± 1.85	-	4.67 ± 4.22
C70.90 PVC with PP Interlayers	2.15 ± 1.10	-	17.66 ± 16.06

4.6 Conclusion

Characterisation of the air blast tested sandwich panels showed that the different constructions had a negligible effect on the post-blast flexural properties. It was found that the bending stiffness and strength were very dependent on debonding, but that cracking had less of an effect. This is due to debonding causing the two face-sheets to decouple, so shear load is not transmitted across. It was found that the bending stiffness reduced to around 1% of the undamaged specimens, and the shear strength reduced to approximately 10%. By calculating an effective shear modulus from the bending stiffness results, it is possible to develop simulations which behave in an elastic manner using the residual effective shear properties. However, this was out of the scope of this research project.

The edgewise compression results showed that the residual properties are affected by core cracks more than debonding. This is due to the cracked foam pieces moving outwards when loaded in edgewise compression, causing the face-sheets to buckle earlier. This is highlighted by the much lower compressive strength of the damaged PVC C70.90 sandwich panel, which contained many more core cracks than the SAN samples. Furthermore, the graded density sandwich panel had a much greater residual edgewise compressive strength than the other samples, due to greater crack distribution. As with the residual flexural properties, the edgewise compression properties can be used to model a ship hull elastically, after a blast event, to assess whether the ship could operate in reduced service after surviving blast loading.

It was clear from the experiments that once the face-sheets in the sandwich specimens are decoupled the properties reduce to represent the in-plane properties of the face-sheets only. For this reason, the various foam core materials have very little influence on the post-blast flexural and edgewise compression properties of the materials.

Chapter 5

Full Scale Underwater Blast Testing

5.1 Introduction

This chapter presents the results of full scale underwater blast tests performed on glass fibre reinforced polymer (GFRP) and carbon fibre reinforced polymer (CFRP) face-sheet, styrene acrylonitrile (SAN) core sandwich panels. The foam cores of these panels were either a single 30 mm thick SAN Corecell M130 foam layer, or three 10 mm thick SAN foam layers, forming a stepwise graded density core as tested in Chapter 3. The intention of utilising a graded density core was to dissipate blast wave energy as it travelled through and crushed the three foam layers, due to incremental crushing. This was expected to create a more even deflection of the sandwich panel and to reduce the overall out-of-plane displacement at failure due to energy absorption. These tests are similar to those performed by Gardner, Wang and Shukla [109], where a shock tube was used to test the blast resistance of a stepwise graded foam core. It was shown in this research that incrementally increasing the foam density in the direction of the blast wave reduced the deflection of the back face due to energy absorption during crushing. This study also considered the effect of using GFRP or CFRP face-sheets on underwater blast resistance. A comparison between GFRP and CFRP to air blast loading has been performed by Arora et al. [18], where it was found that the

CFRP sandwich panel outperformed the GFRP case. It was expected in this case that the high CFRP stiffness would cause boundary failure due to high bending moments at the edges, where the GFRP panels were expected to deflect with a more rounded shape, creating less of a bending moment at the boundaries. In each case the response of the sandwich panel to blast loading was recorded using 14 electronic strain gauges on the front face-sheet and 16 electronic strain gauges on the back face-sheet. The panels were clamped into large, sealed, steel boxes, creating quasi-built-in boundary conditions and air backing. The locations of the strain gauges allowed strain mapping across the panel surfaces to be completed, and for the out-of-plane displacement of the panels to be calculated. Both the side-on pressure and the reflected pressure were measured during blast, to check for the consistency of the four tests.

5.2 Materials

The construction of the sandwich panels for underwater blast testing was similar to the sandwich panels used for air blast testing, as presented in Chapter 3. The layup of the sandwich panel faces were symmetrical about the foam core, with eight plies of fibres on either side. The sandwich panels were constructed using vacuum consolidation, where the fibres and core were coated in resin, before being consolidated under vacuum and held at vacuum for 24 hours. The sandwich panels were then heated to 85°C at 1°C/min, and held at this temperature for 12 hours. After this period the sandwich panels were allowed to return to room temperature at approximately 1°C/min. The layup of the single core GFRP and CFRP sandwich panels are shown schematically in Figure 5.1, and for the graded core in Figure 5.2. The glass fibres used were plies of quadriaxial QE1200, the carbon fibres were biaxial XC411 and the resin system was SR8500/SD8601 Sicomin epoxy. The GFRP and CFRP face-sheets were designed such that they would both have a cured thickness of approximately 2 mm. As in Chapter 3 the material properties of the face-sheets were calculated using the rule of mixtures, and these properties for the fibres and the fibre and epoxy systems are shown in Table 5.1.

The polymeric foam cores used in these underwater blast tests were made from SAN, and were identical to the SAN cores used in the air blast tests presented in

Chapter 3. As shown in Chapter 6 the foams were tested at quasi-static (QS) and dynamic (HR) rates, and a summary of the material properties of these foams is presented in Table 5.2.

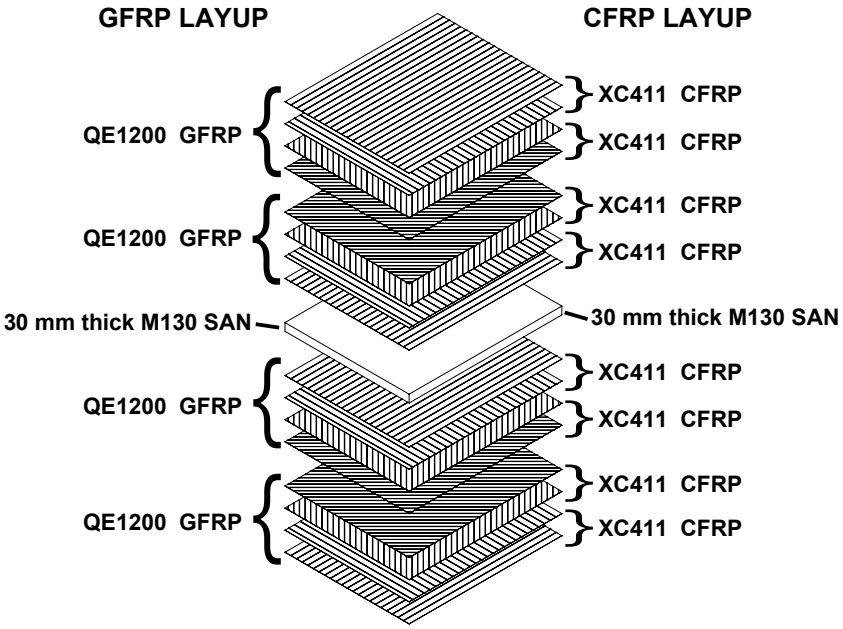


Figure 5.1: Schematic of the layup of the single core sandwich panels.

Table 5.1: Constitutive and bulk face-sheet mechanical properties.

Material	Density (kg/m^3)	Elastic Modulus (GPa)	Tensile Fracture Stress (MPa)	Inter-Laminar Shear Strength (MPa)	Compressive Strength (MPa)
Glass Fibres	2550 [94]	80 [94]	2000 [94]	-	1450 [95]
Carbon Fibres	1790 [110]	225 [95]	3350 [95]	-	2500 [95]
SR 8500 Resin	984 [96]	3.35 [96]	83 [96]	59 [96]	114 [96]
QE1200/SR 8500 GFRP Ply	1720	15.88	396	59	316
XC411/SR 8500 CFRP Ply	1355	40.62	623	59	493

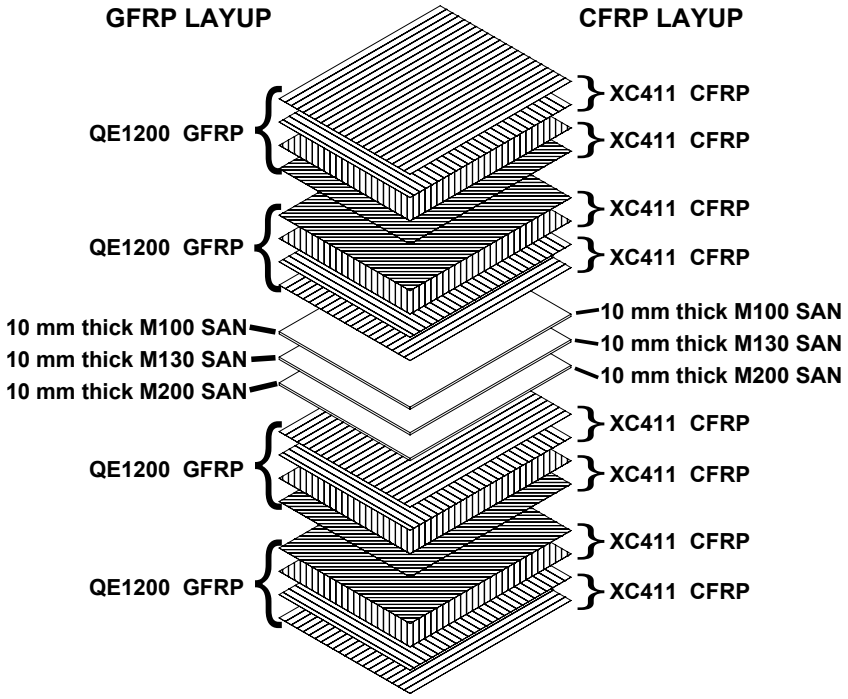


Figure 5.2: Schematic of the layup of the graded core sandwich panels.

Table 5.2: Mechanical properties of the foam polymers, including quasi-static (QS) and 180 s^{-1} (HR) rate test results.

Material	Density (kg/m^3)	QS Shear Modulus (MPa)	QS Shear Strength (MPa)	QS Compressive Modulus (MPa)	QS/HR Compressive Strength (MPa)	QS/HR Tensile Modulus (MPa)	QS/HR Tensile Fracture Stress (MPa)	QS/HR Tensile Fracture Strain (%)
M100 SAN	107 [100]	41 [100]	1.45 [100]	88	1.79/3.4	88/162	2.8/5.7	7.7/4.5
M130 SAN	140 [100]	59 [100]	1.98 [100]	126	3.03/5.5	133/267	3.8/8.1	7.2/3.8
M200 SAN	200 [100]	98 [100]	2.98 [100]	239	5.15/10.8	220/436	5.7/7.3	5.6/2.0

5.3 Experimental Methods

5.3.1 Underwater Blast Testing

The test structure consisted of a welded steel channel box, constructed from 150 x 75 x 10 mm channel butt welded together with the flanges outwards, with a 10 mm thick steel plate sealed and bolted onto the back. The 800 mm square sandwich panel was then sealed and bolted onto the front of the channel box, with 10 mm thick steel strips sealed and bolted around the perimeter of the front face, to create quasi-built-in boundary conditions. This setup is shown in Figure 5.3. The explosive sources used for the tests were 1 kg plastic explosive 4 (PE4) spherical charges, situated at 1 m from the front face of the sandwich panel to the centre of the charge. These charges had an equivalent weight of 1.28 kg TNT. The charge was held in place for testing using a pine frame, bolted onto the front of the steel box. The shape and material selection for this frame was such that it would not load the sandwich panel upon detonation, and would simply break apart. In order to hold the test frame vertical in the water, a large steel bar was strapped to the bottom of the steel box, at a distance of around 1.5 m, weighing approximately 40 kg. Two lifting eyes were attached to the top of the steel box, and a crane was used to lower the whole structure into the water to a charge depth of 3 m. This was measured by marking the chains on which the test structure was hanging. The pressure during blast was measured using two Neptune Sonar T11 gauges, one to measure the side-on blast pressure, and another to measure the reflected blast pressure. The side-on gauge was attached to a 10 mm diameter steel bar, such that it was protruding from the end and measured the hydrostatic pressure in the water as the wave passed over. The steel bar was welded to the back of the steel box and deformed such that the gauge was at the same height as the charge but 1 m away. The reflected gauge was attached to the top of the steel box, on a section of 150x75x10 mm channel. The charge frame, pressure gauge assembly and lifting assembly are shown in Figure 5.4.

The loading expected from the 1 kg PE4 charge was approximated using empirical data found in Smith and Hetherington [15], with Equation (5.1), where P_H is the hydrostatic side-on pressure in the water, P_m is the peak pressure, t is

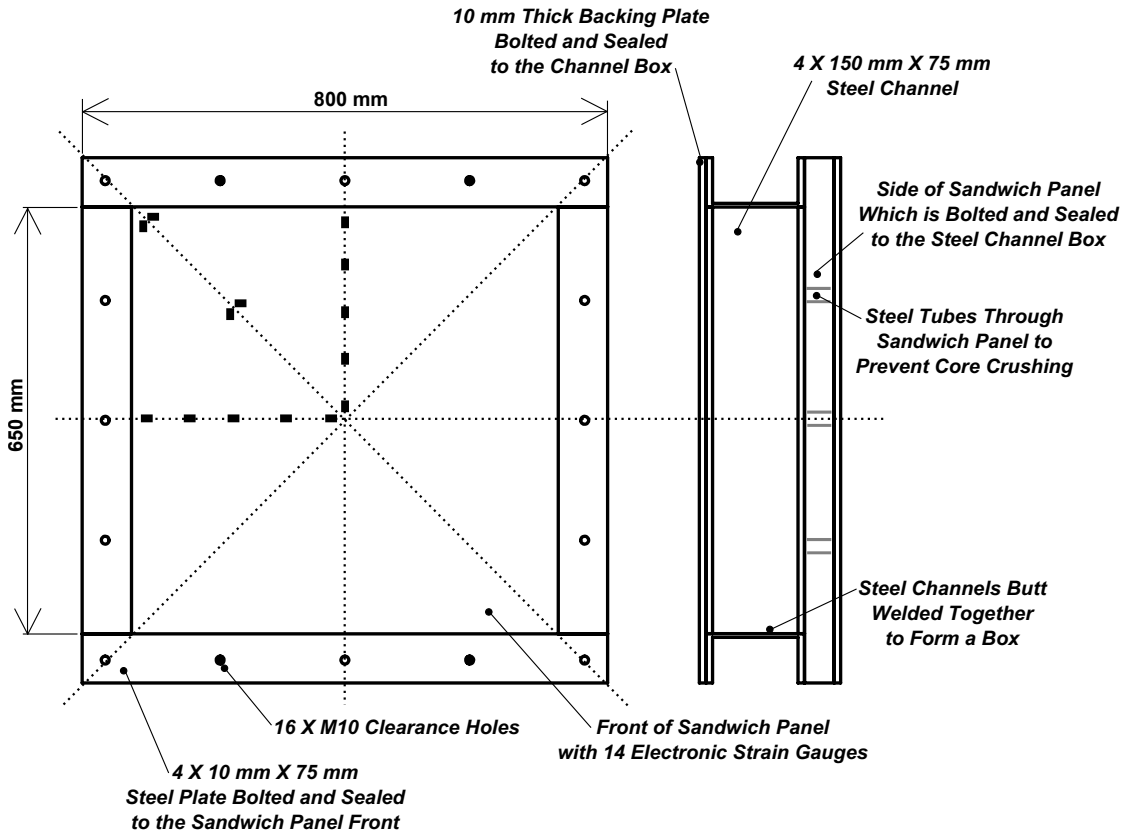


Figure 5.3: Schematic of the underwater blast test frame.

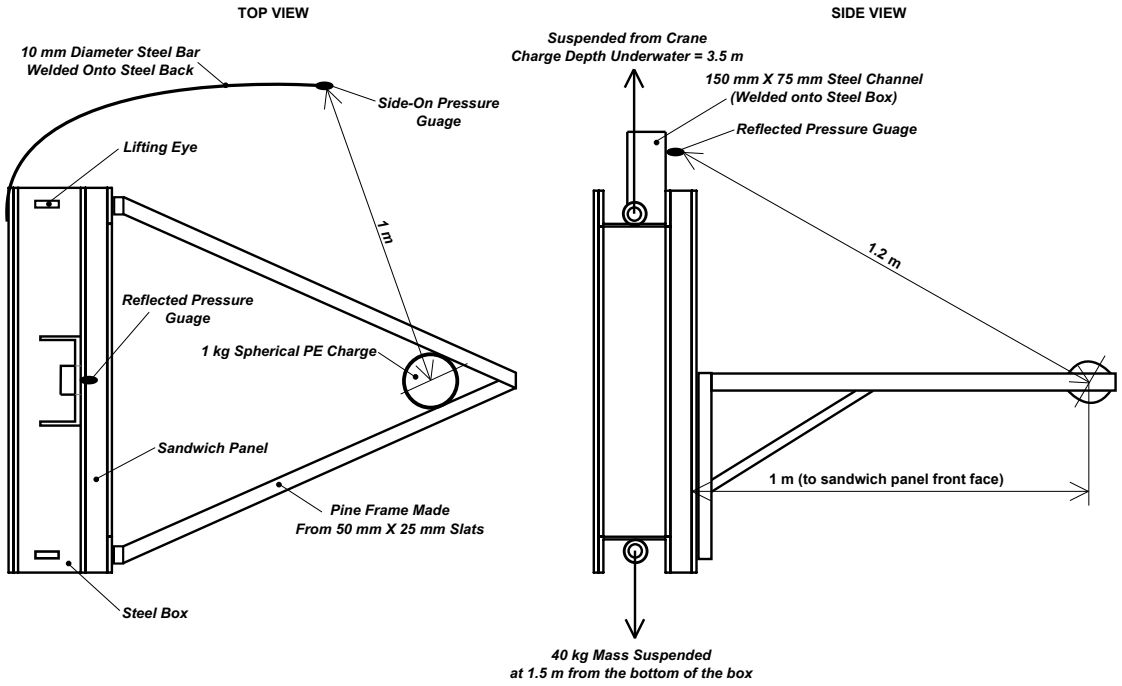


Figure 5.4: Schematic of the underwater blast test charge and pressure gauge layout.

the time after blast wave arrival, and θ is a wave parameter found empirically. In the case of 1 kg PE4 at 1 m stand-off, P_m and θ are 50.1 MPa and 0.08 ms respectively. This loading was chosen as it would cause full compressive failure of the foam cores, and complete failure of the face-sheets.

$$P_H(t) = P_m e^{-\frac{t}{\theta}} \tag{5.1}$$

5.3.2 Pressure Gauges

To record the pressure traces during blast, two Neptune Sonar T11 pressure gauges were used. The gauges measured the hydrostatic pressure in the water as the blast wave passed over them. The side-on gauge measured the unimpeded blast wave pressure as it passed over it. This meant the water particles did not lose momentum as they travelled past the gauge. The side-on pressure gauge was attached to a thin steel arm out to the side of the structure, as shown in Figure 5.4. The reflected pressure gauge measured the blast wave pressure as the particles came

to rest against the surface of the test structure, therefore measuring the actual loading on the structure. A schematic of the reflected pressure sensor fixed into the test frame is shown in Figure 5.5, and this was connected via a Bayonet Neill-Concelman (BNC) cable to a charge amplifier and data acquisition system. As the pressure sensors were piezo-electric, they returned to zero under constant quasi-static pressure. Therefore the pressure measured during the test was the pressure generated by the blast plus the hydrostatic pressure caused by the water depth.

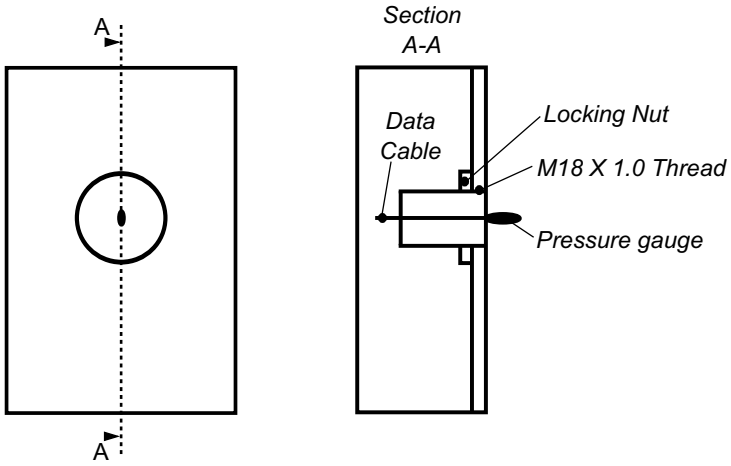


Figure 5.5: Schematic of the reflected pressure gauge.

5.3.3 Electronic Strain Gauges

To measure the response of the composite sandwich panels, electronic foil strain gauges were adhered to the front and rear face-sheets. The sandwich panels were square in shape, so only one quarter of each panel had strain gauges attached. A total of 30 gauges were adhered to each panel, with 14 on the front face, closest to the explosive charge, and 16 on the rear face, in contact with air. The number of strain gauges was limited to the number of data acquisition channels available. The strain gauges were located as shown in Figure 5.6. All of the strain gauges were TML FLA-2-350-11 350 Ω foil gauges, adhered with TML CN adhesive. The surface treatment to attach the gauges was to roughen the epoxy surface with fine emery cloth, and to clean it with isopropanol alcohol before applying the adhesive. The strain gauges were supplied with leads attached, so solder terminal pads were

adhered close to the gauges, with the strain gauge leads and data wires attached to the terminal. The gauges, lead wires and solder connections were then covered in a liberal coating of wax to make them waterproof, with tape then covering the wax and data cables for extra protection. Some slack was left in the lead wires to prevent damage when applying the wax. The lead wires used were 8 core 15 m length category 5 ethernet cables, and the strain gauges were in quarter Wheatstone bridge formation. The connections to the amplifiers were via crimped RJ45 connections, to allow simple changing of the test panels. The calculation for converting strain to voltage out of the Wheatstone bridge is shown in Equation (5.2), where BV is the bridge voltage (5V), GF is the gauge factor (2.1) and ε is the strain. The ethernet cables were clamped securely to the steel frame before transportation, to ensure the connections to the gauges were not broken, and were checked regularly for integrity. The ethernet cables attached to the back face passed through slots cut into the steel channel of the box, before sealing and bolting the sandwich panel on. The steel backing plate was sealed and bolted last, to allow access to all of the connections until the last stage. During blast, the data cables lay against the steel to prevent them from moving and tearing away from the panel and were secured to the chains holding the test panel in the water. This meant that the wiring would only fail when the composite panel failed, and not due to the connections being damaged. The data cables were passed out of the water and into a control room next to the test pond where high frequency oscilloscopes and amplifiers were located to record the test data.

Photographs of the underwater blast test setup are shown in Figure 5.7, where Figure 5.7a shows the single core CFRP sandwich panel before the charge is placed in the pine charge holder; Figure 5.7b shows the same sandwich panel after the charge is installed; and Figure 5.7c shows the whole test setup, including the crane, of the single core GFRP sandwich panel test.

$$V_0 = \frac{BV\ GF\ \varepsilon}{4} \tag{5.2}$$

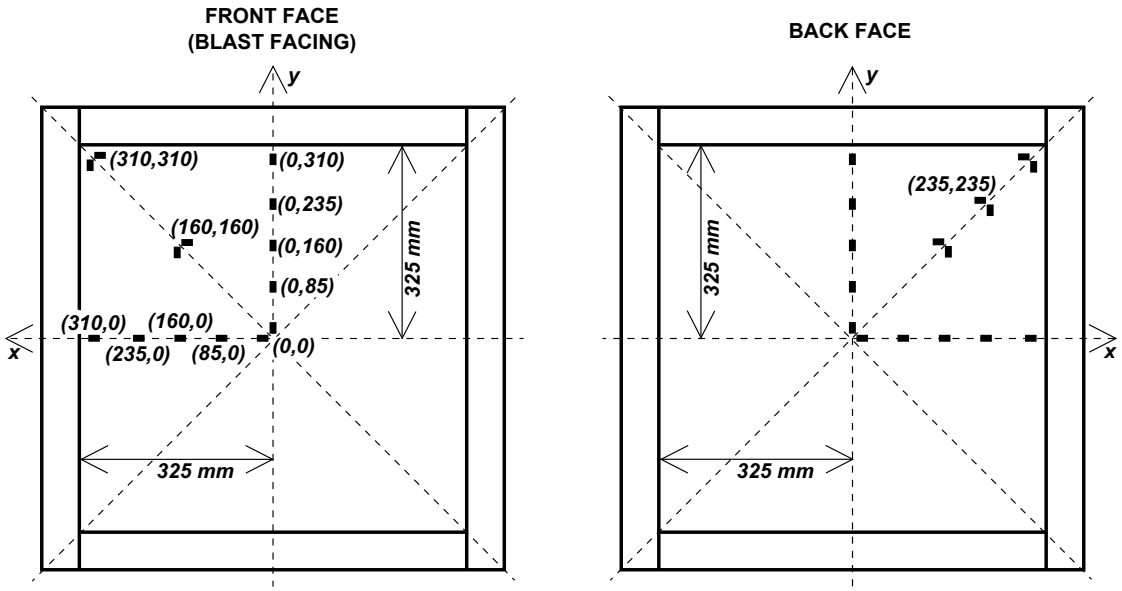


Figure 5.6: Locations of the 30 electronic strain gauges attached to the sandwich panels.

5.3.4 Data Processing

The first stage of processing the electronic strain gauge readings was to filter out noise in the data, which was completed using a moving average method, to remove high frequency noise. Furthermore, the time of the data points were zeroed at the point of detonation, which was possible due to a spike in the voltage readings caused by thermal radiation from the explosion. Once a set of usable, filtered strain versus time curves were acquired, the strain along each line of gauges was interpolated between the gauge locations. This provided an indication of the areas of compressive and tensile strain in the panel along the horizontal, vertical and diagonal lines of strain gauges which are shown in Figure 5.6.

The next stage was to use an iterative method along each of these three lines of strain, starting from the boundary, to estimate the out-of-plane displacement of the panel. The centreline strain of the sandwich panel was first calculated based on an average of the front and back face strain in that location, and it was assumed that the centreline nodes would not move in-plane during deformation. This method of averaging the front and rear face-sheet strains ensured that the membrane effects were captured as the in-plane strain was calculated. With the

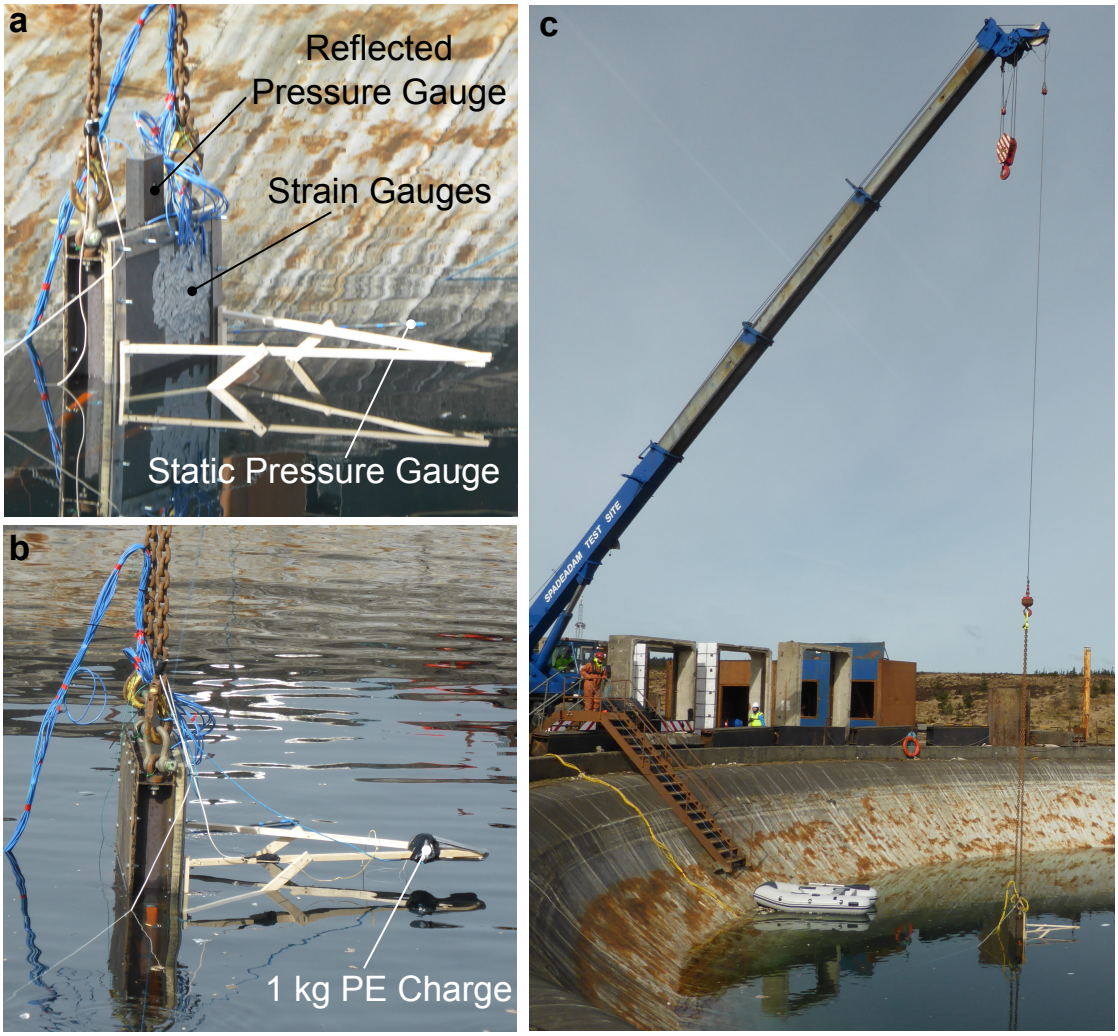


Figure 5.7: Photographs of the underwater blast test setup showing a) the single core CFRP test panel before the charge was assembled; b) the single core CFRP sandwich panel with the charge assembled; and c) the whole test setup of the single core GFRP sandwich panel test, before the charge was assembled.

original length of the section, and the new length due to the strain, it was possible to calculate the out-of-plane deflection using Pythagoras Theorem. This method is shown in Figure 5.8, where e_n is the centreline strain in that particular location, X is the distance between interpolated points; d is the incremental out-of-plane displacement; and y is the overall out-of-plane displacement. Using this iterative approach for each time increment of strain measured, it was possible to work out the relative displacement of the two nodes on one cell, d_n, using Equation (5.3), which in turn was used to calculate the overall displacement of the node, y_n using Equation (5.4). As this method relied upon the face-sheet strains only, and an assumption that the in-plane strain was distributed linearly through the sandwich panel thickness, the calculations were unaffected by the large reduction in thickness of the sandwich panels due to core crushing.

$$d_n = \sqrt{(X + Xe_n)^2 - X^2} \tag{5.3}$$

$$y_n = y_{n-1} + d_n \tag{5.4}$$

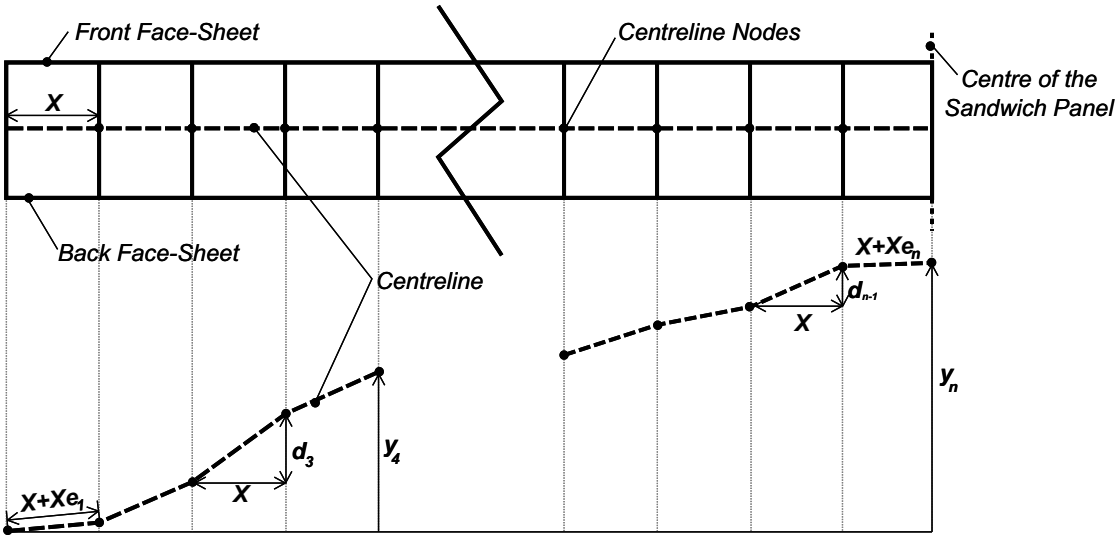


Figure 5.8: Schematic of the iterative method for calculating out-of-plane displacement.

5.4 Results

5.4.1 Selecting and Filtering Raw Data

The raw strain gauge data obtained during the test had clear strain patterns with high frequency noise at varying frequencies. As the noise frequencies were much greater than the frequency of the strain response, a simple low-pass filter was applied to the data, with a span selected to encompass the lowest frequency of the high frequency noise. The lowest of the high frequency noise was found to be 50 kHz, 10% of the 500 kHz sampling frequency, so the span was set to 10 data points. This resulted in an average strain value calculated across every section of 10 data points. An example of raw and filtered strain data, taken from a back face strain gauge on the single core GFRP sandwich panel, is shown in Figure 5.9, where the detonation spike is also visible in the raw data. The time shown in this plot has not been zeroed against the detonation time. This spike is caused by thermal radiation from the charge, and is the point at which the time is zeroed in each set of test data.

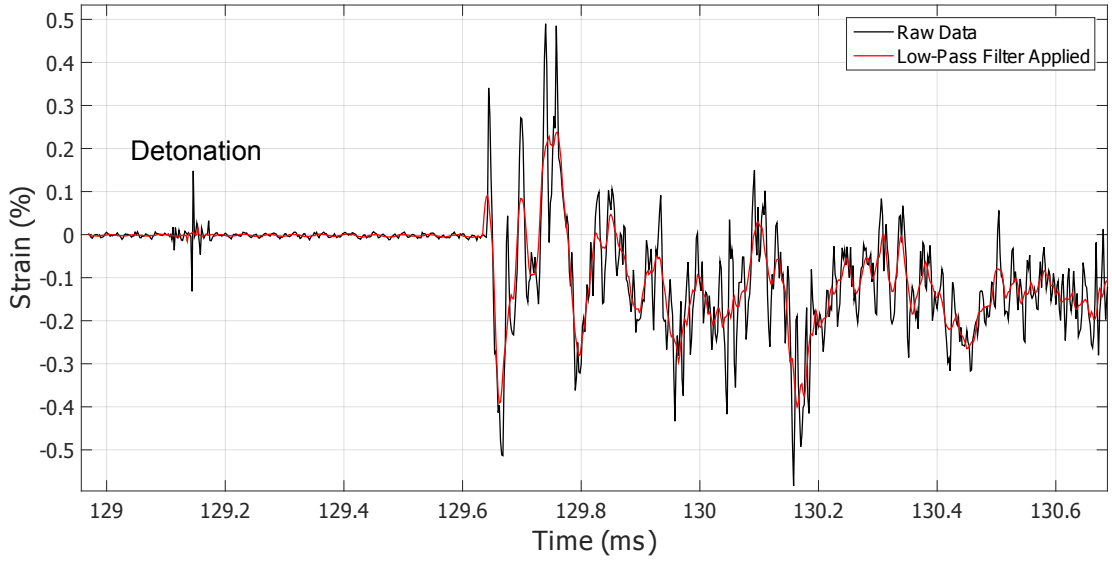


Figure 5.9: Raw strain gauge data versus time, and a moving average filter applied. Detonation is shown as a spike in the data, due to radiation from the charge.

5.4.2 Pressure Traces

As shown by Figure 5.4 two pressure gauges were used in the blast tests, one to measure the side-on pressure as the blast waves passed over it, and one to measure the reflected pressure as the water particles transmitting the blast wave came to rest on the surface of the test structure. Due to limitations in design capabilities, the reflected pressure gauge was situated at 1.2 m from the centre of the charge. However the reflected pressure on the sandwich panels were corrected using this measured value combined with the measured side-on pressure. The reflected gauge actually measured the overpressure, meaning that the total pressure on the sandwich panel was the hydrostatic pressure of the water in addition to the pressure from the blast wave as measured by the pressure gauge. The pressure traces measured in each test are shown in Figure 5.10, where Figure 5.10a shows the trace for the single core GFRP test; Figure 5.10b for the graded core GFRP test; Figure 5.10c shows the single core CFRP test; and Figure 5.10d shows the graded core CFRP test. The reflected pressure gauge is 0.2 m further away from the charge than the side-on pressure gauge, which explains the delayed arrival of the pressure wave in Figure 5.10b and Figure 5.10c. In the single core GFRP case, a reflected pressure trace was not obtained and for the graded core CFRP case a side-on pressure trace was not obtained. By comparison of the measured reflected pressure with the predicted side-on pressure at 1.2 m stand-off, it was possible to correct the measured side-on pressure to an estimate of the reflected pressure. This was achieved by increasing the peak side-on overpressure by the same percentage as in the 1.2 m stand-off case, and retaining the same positive pressure duration of the blast wave, and this is visible as "adjusted" in Figure 5.10a, Figure 5.10b and Figure 5.10c. The cumulative impulses delivered to the test structures are shown in Figure 5.11, where the single core GFRP case is shown in Figure 5.11a; the graded core GFRP case is shown in Figure 5.11b; the single core CFRP case is shown in Figure 5.11c; and the graded core CFRP case is shown in Figure 5.11d. From Figure 5.10 and Figure 5.11 it is clear that there is strong repeatability across the four tests, in terms of the energy delivered to the test structures.

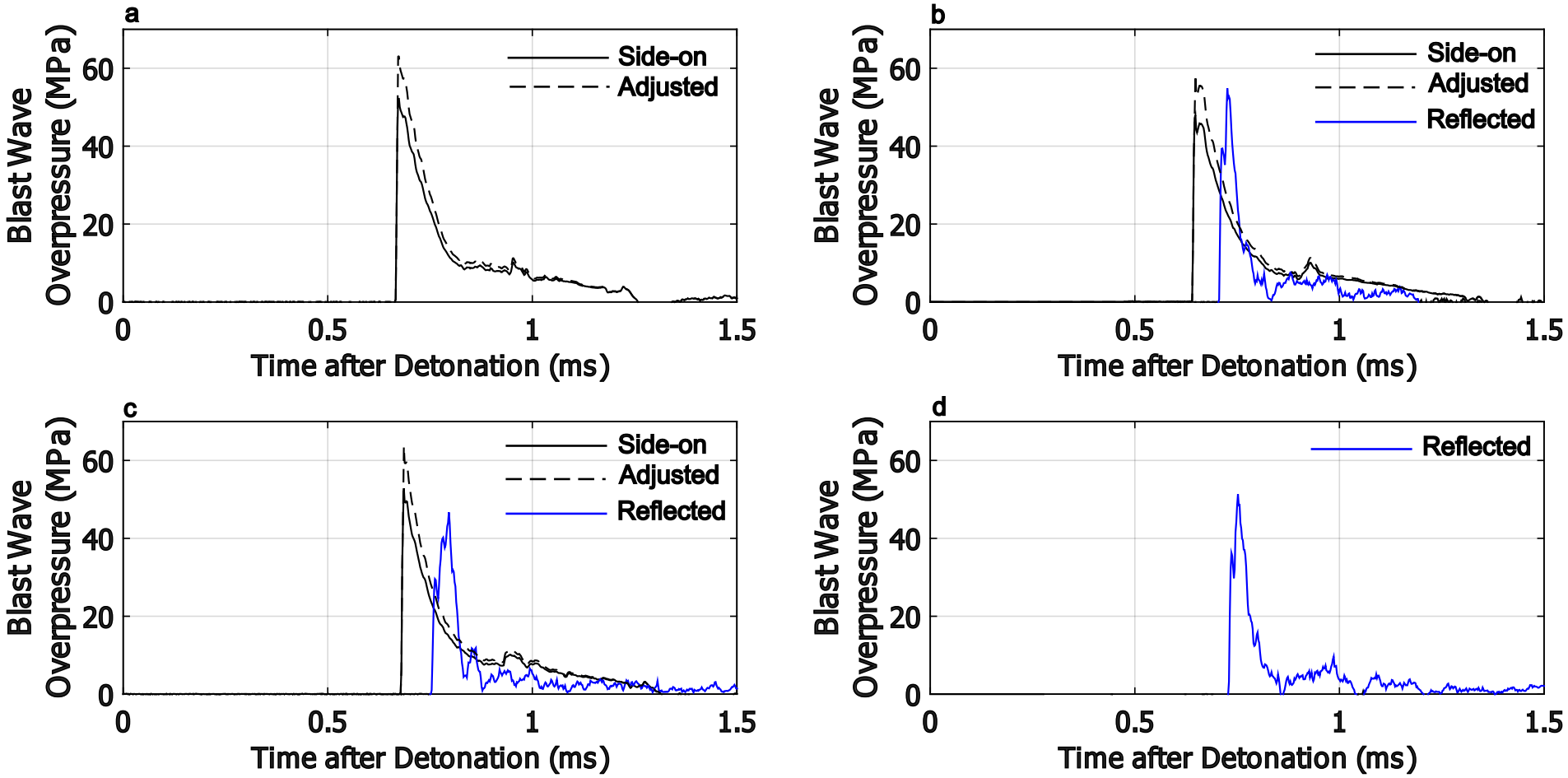


Figure 5.10: Side-on, reflected and adjusted pressure traces recorded for a) the single core GFRP test; b) the graded core GFRP test; c) the single core CFRP test; and d) the graded core CFRP test.

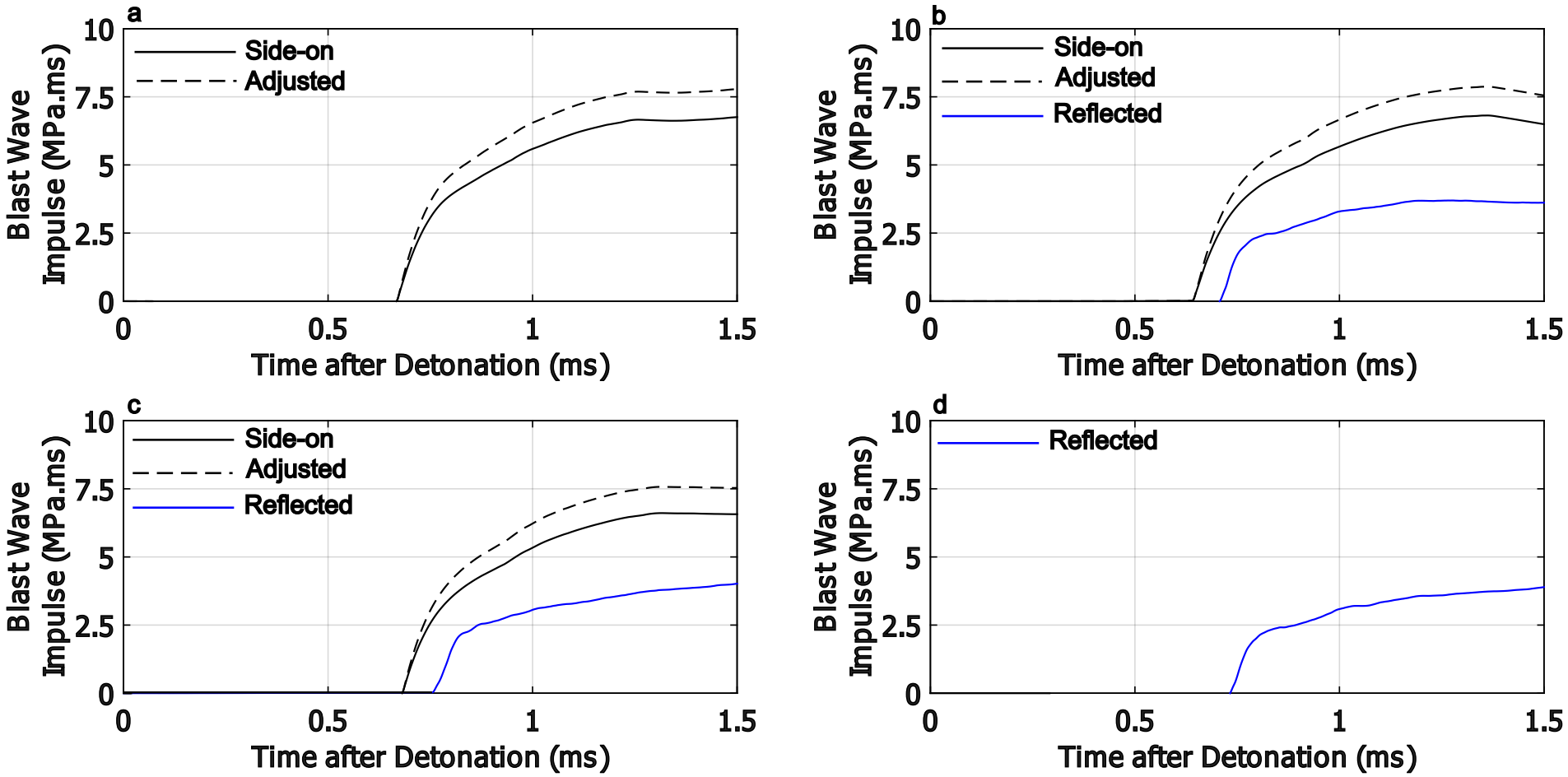


Figure 5.11: Side-on, reflected and adjusted impulse traces recorded for a) the single core GFRP test; b) the graded core GFRP test; c) the single core CFRP test; and d) the graded core CFRP test.

5.4.3 Strain Measurements

To display the strain across the quarter of the sandwich panels, each line of gauges, as shown in Figure 5.6 were linearly interpolated, to show the maximum or minimum principal strain (MPS) across the diagonal section, the horizontal strain (ε_X) across the horizontal section and the vertical strain (ε_Y) across the vertical section. This section provides the contour plots and will highlight key features of this. Finally, the time after which the panel failed is extracted from the data, and the deflection shape of each face-sheet implied by the strain data.

5.4.3.1 Single Core GFRP Sandwich Panel

The filtered strain gauge data for the front and rear face-sheet strain gauges, for the single core GFRP sandwich panel, are shown in Figure 5.12 for the horizontal gauges, Figure 5.13 for the vertical gauges and Figure 5.14 for the diagonal gauges. The figures on the left hand side of each plot show the location of the strain gauge for the corresponding raw data. The strains were then interpolated across each direction, where there were enough data present to permit this.

The strain contour plots for the single core GFRP sandwich panel are shown in Figure 5.15, where Figure 5.15a and Figure 5.15b illustrate the horizontal centre section strain across the front and back face-sheets respectively; Figure 5.15c and Figure 5.15d show the vertical centre section strains across the front and back face-sheets respectively, and Figure 5.15e and Figure 5.15f show the maximum principal front and back face-sheet strains from the diagonal strain gauges respectively. In each case, a schematic of the direction of the strain line is provided on the left hand side. It can be seen from the strain contour plots that the blast wave arrives at the sandwich panel approximately 0.7 ms after detonation. The back face-sheet centre vertical and diagonal strain switches between tension and compression up until failure, and this is expected to be due to an oscillation of the steel box, periodically loading the back face-sheet in compression. Complete failure of the sandwich panel occurs at around 0.9 ms, where the sandwich panel becomes debonded from the steel frame on all edges on both faces. Upon arrival of the blast wave, the front face-sheet strain is tensile, due to crushing of the foam core, and the back face-sheet is compressive, due to the elastic deformation of the steel box. At the end

of this crushing phase, the back face-sheet enters into tension and stays in tension until failure. During this period the front face-sheet strain is approximately zero, due to a mixture of bending and membrane loading. During the deflection phase of the test, the outer corners of the back face-sheets are in compression, as shown by Figure 5.15f. After failure of the sandwich panel boundary, at around 0.9 ms, the back face-sheet remains in tension and the front face-sheet in compression, due to the panel being pushed inside the steel box. It is at this stage that front face-sheet failure of the sandwich panel takes place, and not during the deflection while the boundaries are still intact. The sandwich panels, upon removal from the steel box, are shown in Figure 5.16 and it can be seen that the boundaries failed by shearing of the polyurethane sealant and the bolts tearing out of the edges of the sandwich panel. Furthermore, compressive cracks are present in the corners of the back face-sheet. In all four blast tests the boundaries completely failed, so the sandwich panels were completely detached from the steel boxes at the ends of the tests.

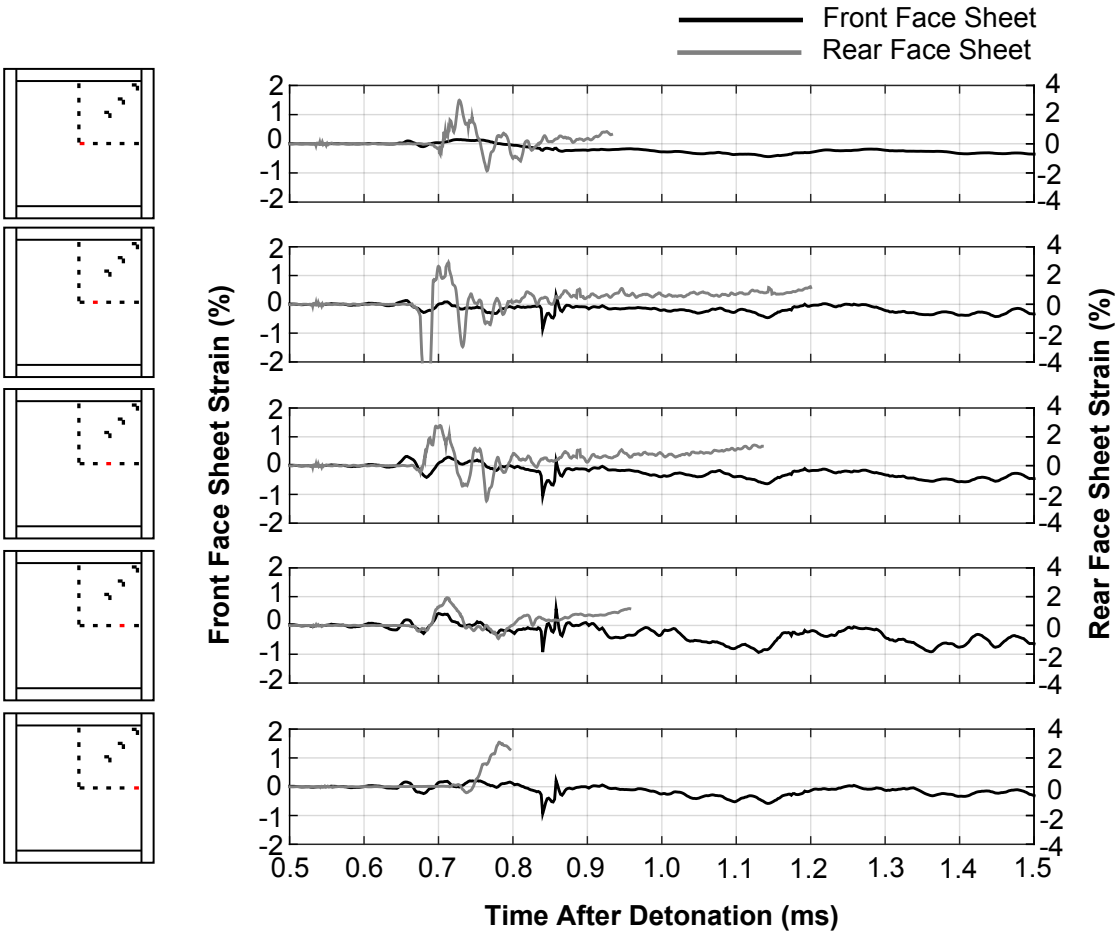


Figure 5.12: Raw strain gauge data for the horizontal strain gauges on the single core GFRP sandwich panel.

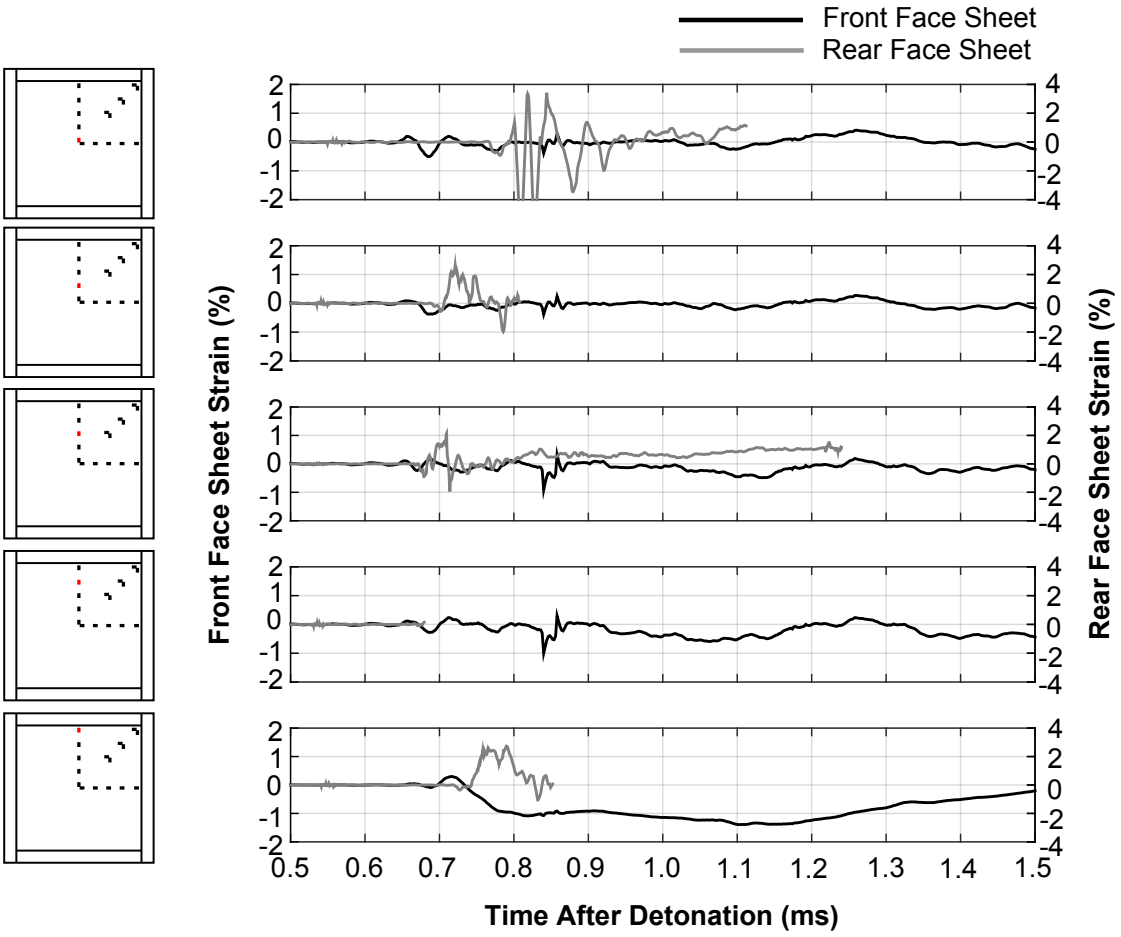


Figure 5.13: Raw strain gauge data for the vertical strain gauges on the single core GFRP sandwich panel.

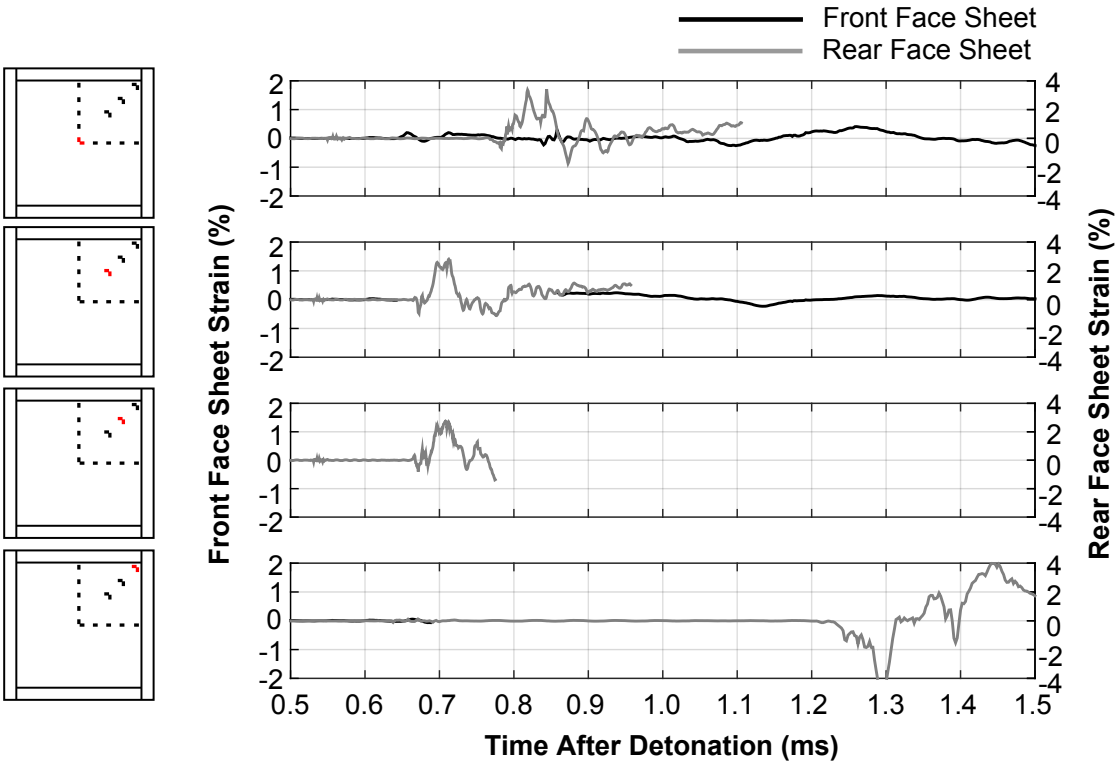


Figure 5.14: Raw maximum principal strain gauge data for the diagonal strain gauges on the single core GFRP sandwich panel.

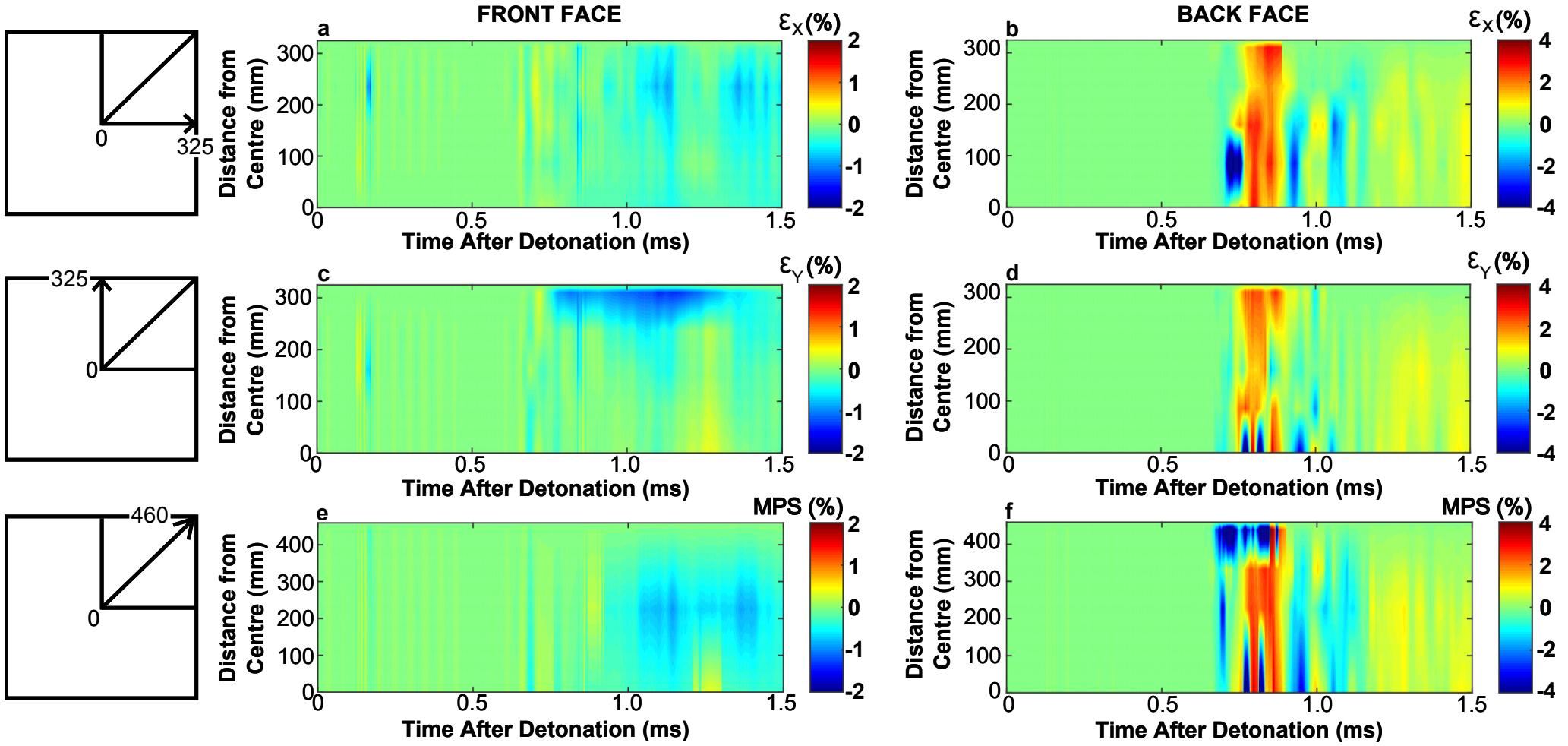


Figure 5.15: Variation of strain with time for a) the horizontal section of the front face; b) the horizontal section of the back face; c) the vertical section of the front face; d) the vertical section of the back face; e) the diagonal section of the front face; and f) the diagonal section of the back face, for the single core GFRP sandwich panel.

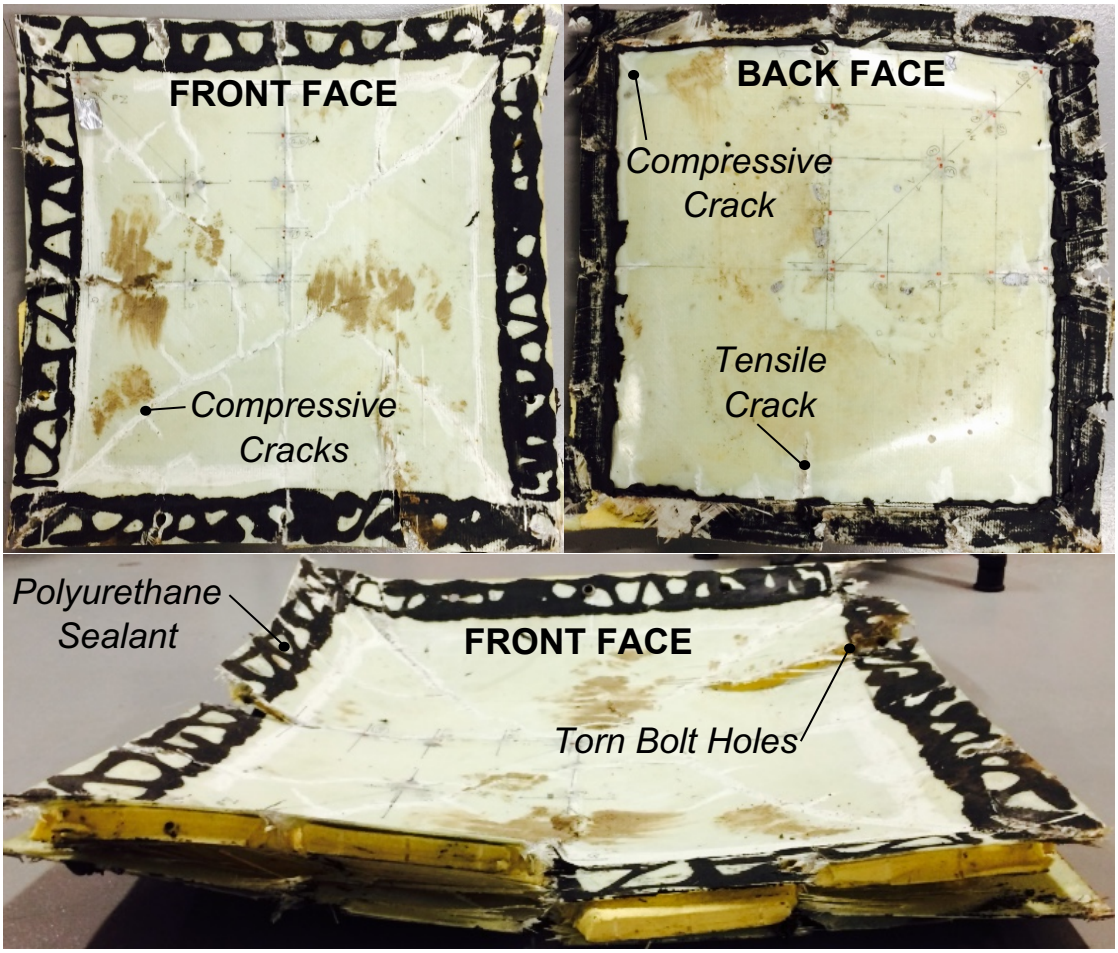


Figure 5.16: Photographs of the single core GFRP sandwich panel after blast testing.

5.4.3.2 Graded Core GFRP Sandwich Panel

Figure 5.17, Figure 5.18 and Figure 5.19 show the horizontal, vertical and diagonal strains respectively for the front and rear face-sheet strain gauges on the graded core GFRP sandwich panel. The strain gauge position in each plot is shown in the key on the left. Figure 5.20 provides the linearly interpolated strain contour plots of the graded core GFRP sandwich panel, with Figure 5.20a and Figure 5.20b showing the horizontal centre strain of the front and back face-sheet respectively. Figure 5.20c and Figure 5.20d show the vertical centre section strains of the front

and back face-sheets respectively and Figure 5.20e and Figure 5.20f show the front and back face-sheet maximum principal strains respectively for the diagonal section strain. The response of the back face-sheet of the graded GFRP sandwich panel is different from the single GFRP sandwich panel in that the strain builds up to critical failure strain much later, which is highlighted by the strip of high strain in Figure 5.20d. As with the single core case, an oscillation of strain is visible up until failure, which is expected to be caused by elastic loading and unloading of the steel box. The failure of the sandwich panel is also in the form of the sealant shearing at the boundaries, and this takes place at 0.85 ms. Photographs of the graded GFRP sandwich panel after removal from the steel box are shown in Figure 5.21, with similar damage patterns as seen in the single core GFRP case.

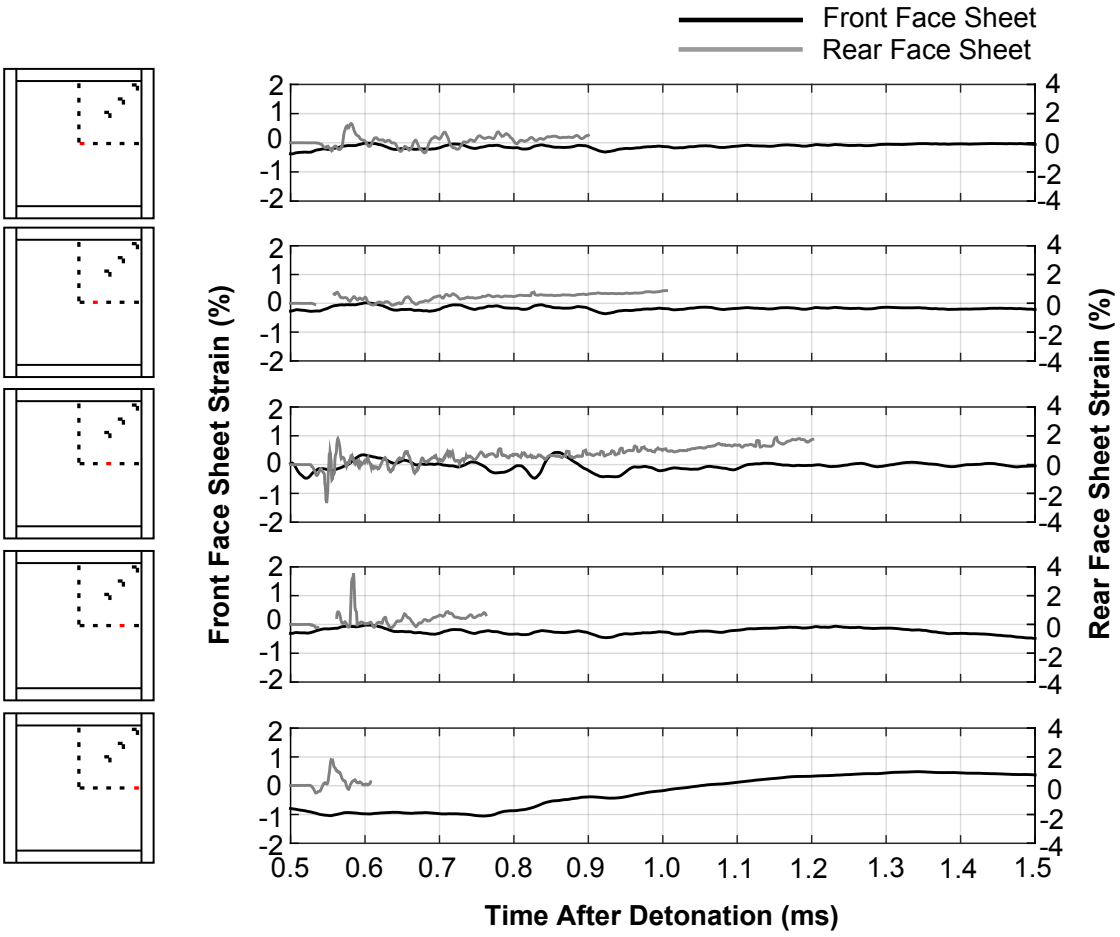


Figure 5.17: Raw strain gauge data for the horizontal strain gauges on the graded core GFRP sandwich panel.

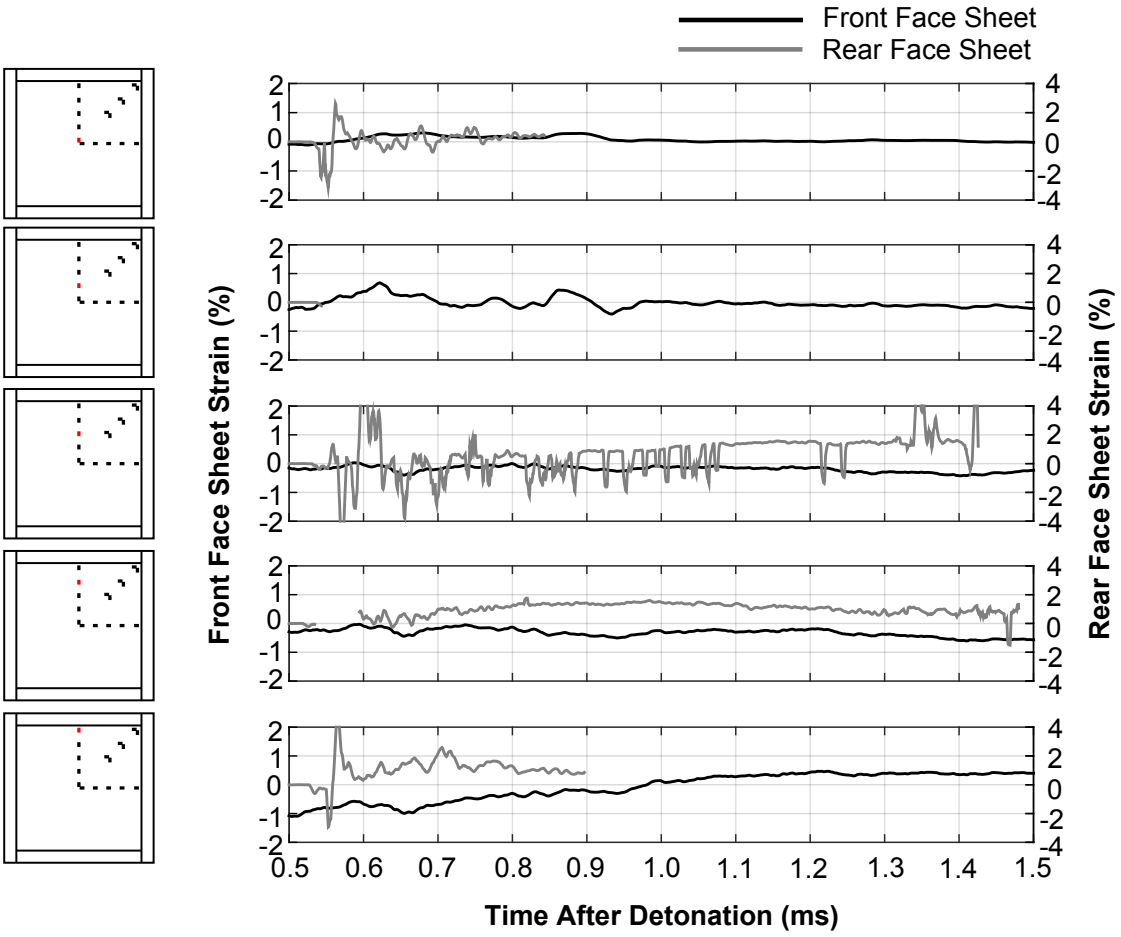


Figure 5.18: Raw strain gauge data for the vertical strain gauges on the graded core GFRP sandwich panel.

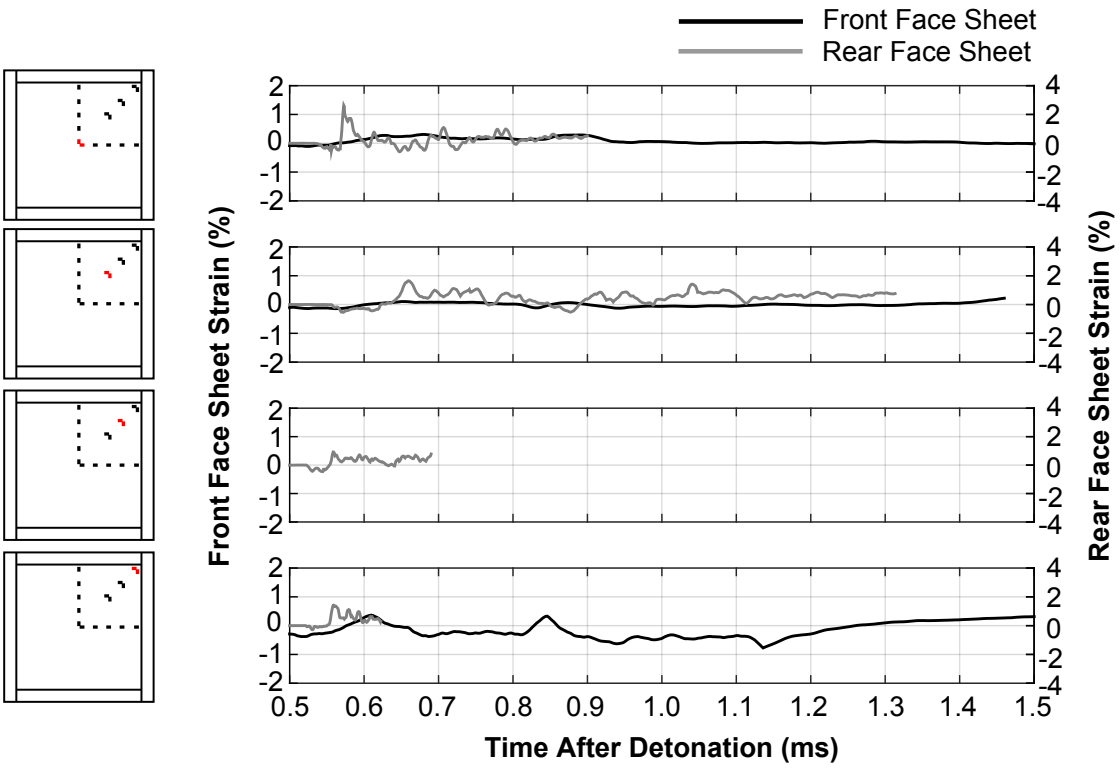


Figure 5.19: Raw maximum principal strain gauge data for the diagonal strain gauges on the graded core GFRP sandwich panel.

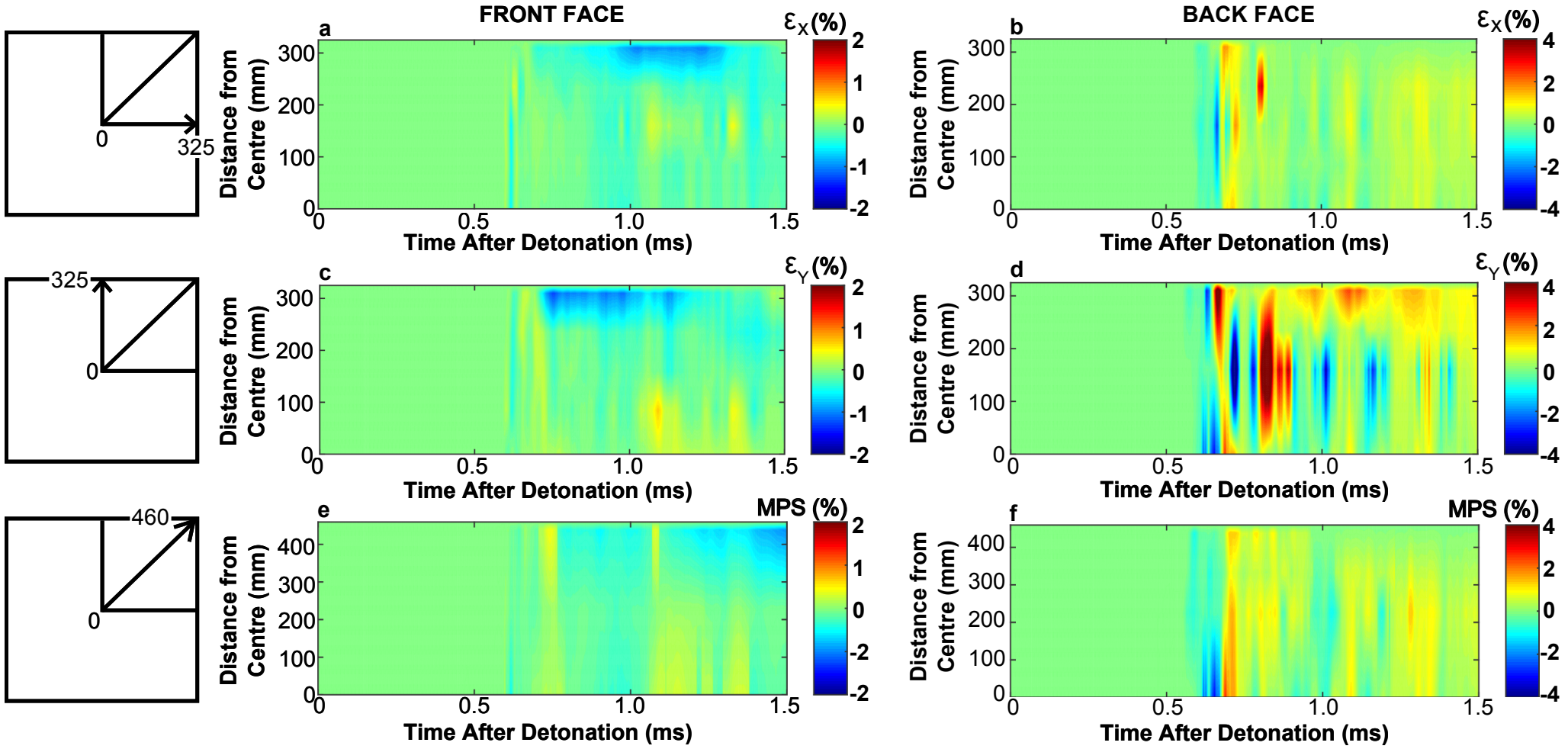


Figure 5.20: Variation of strain with time for a) the horizontal section of the front face; b) the horizontal section of the back face; c) the vertical section of the front face; d) the vertical section of the back face; e) the diagonal section of the front face; and f) the diagonal section of the back face, for the graded core GFRP sandwich panel.

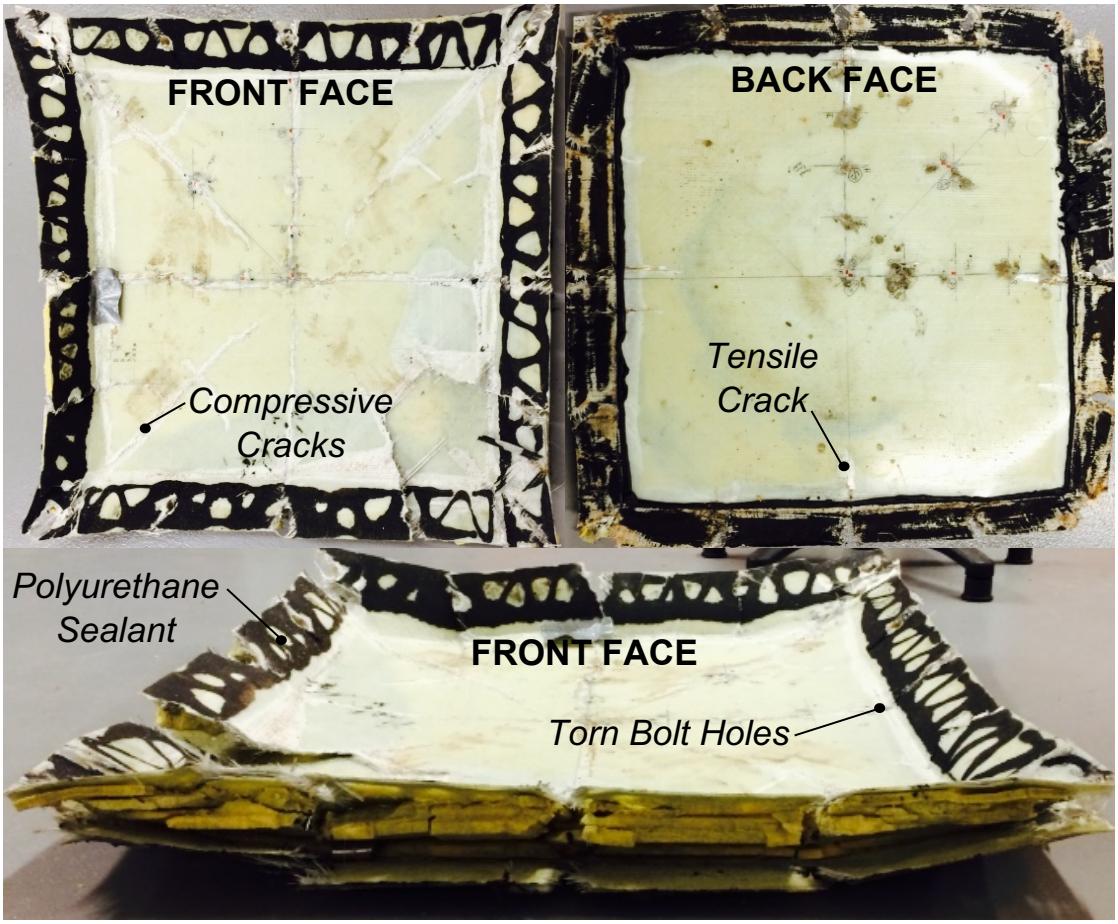


Figure 5.21: Photographs of the graded core GFRP sandwich panel after blast testing.

5.4.3.3 Single Core CFRP Sandwich Panel

The filtered horizontal strain gauge data for the front and rear face-sheets are shown in Figure 5.22; for the vertical gauges in Figure 5.23; and for the diagonal gauges in Figure 5.24. The strain contour plots for the single core CFRP sandwich panel are shown in Figure 5.25 with the front and back face horizontal centre section strains shown in Figure 5.25a and Figure 5.25b respectively, and the front and back face-sheet strains for the vertical centre section shown in Figure 5.25c and Figure 5.25d respectively. For the diagonal section, the maximum principal strain in the front and back face-sheets are shown in Figure 5.25e and Figure 5.25f

respectively. Failure of the sandwich panel took place at 0.93 ms, and the strain took a similar form to the GFRP cases, with oscillations of the strain levels caused by the elastic deformation of the steel box. However, in the case of the single core CFRP sandwich panel, the failure takes the form of fracture of the back face-sheet, as is visible in the post-blast photographs in Figure 5.26.

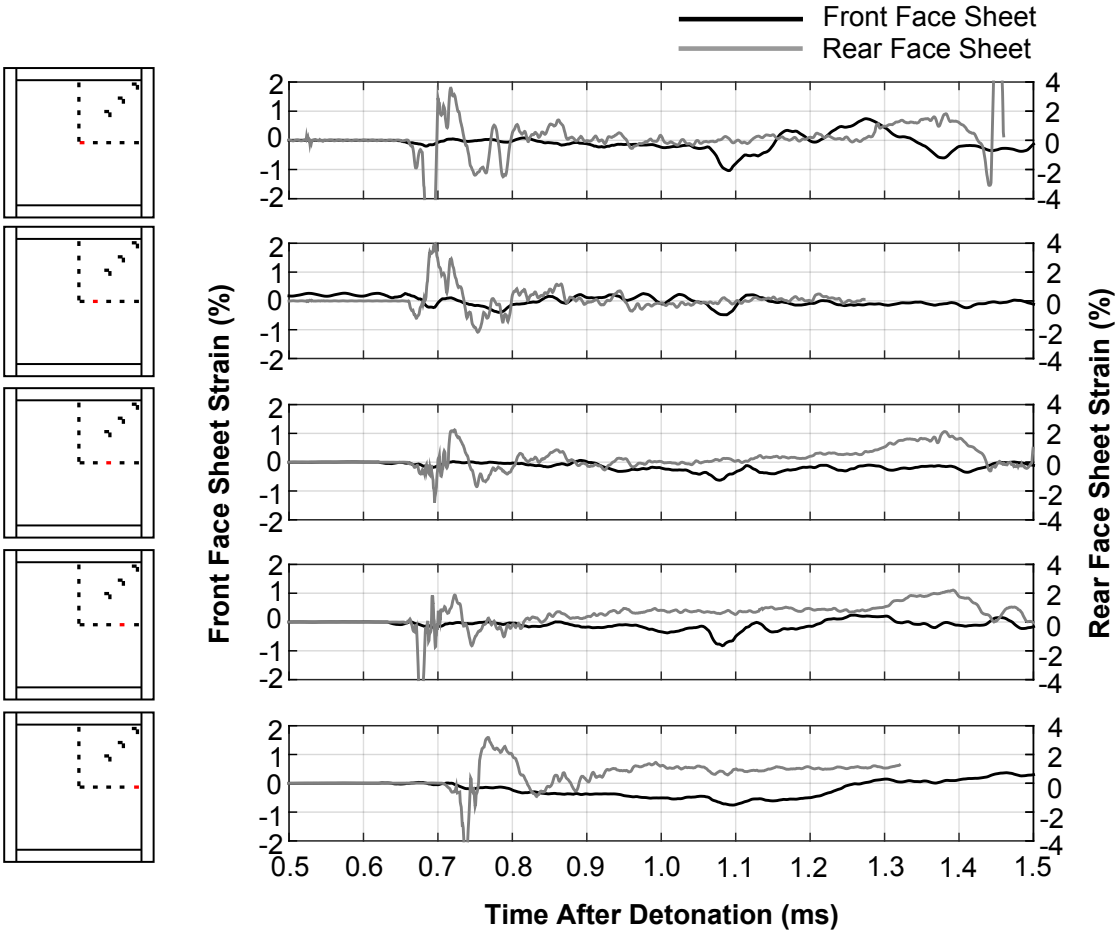


Figure 5.22: Raw strain gauge data for the horizontal strain gauges on the single core CFRP sandwich panel.

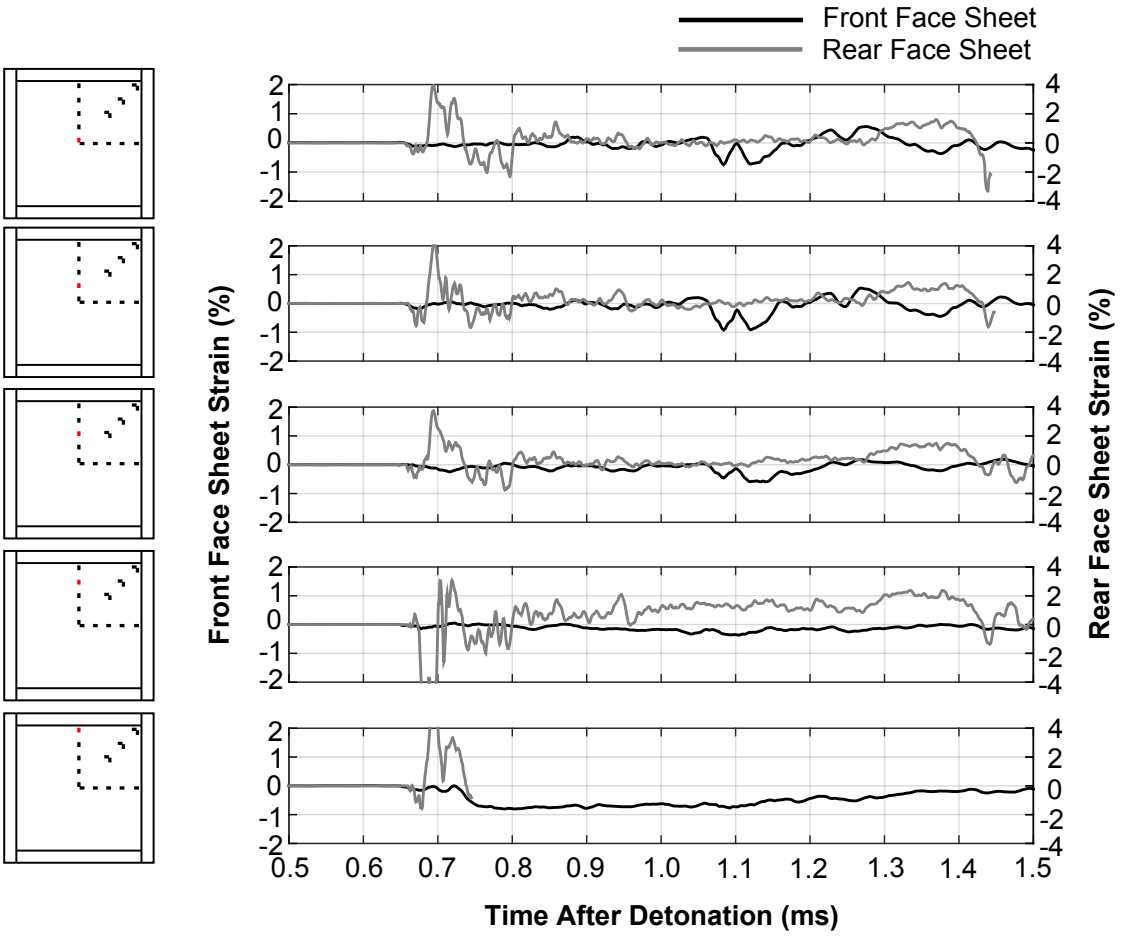


Figure 5.23: Raw strain gauge data for the vertical strain gauges on the single core CFRP sandwich panel.

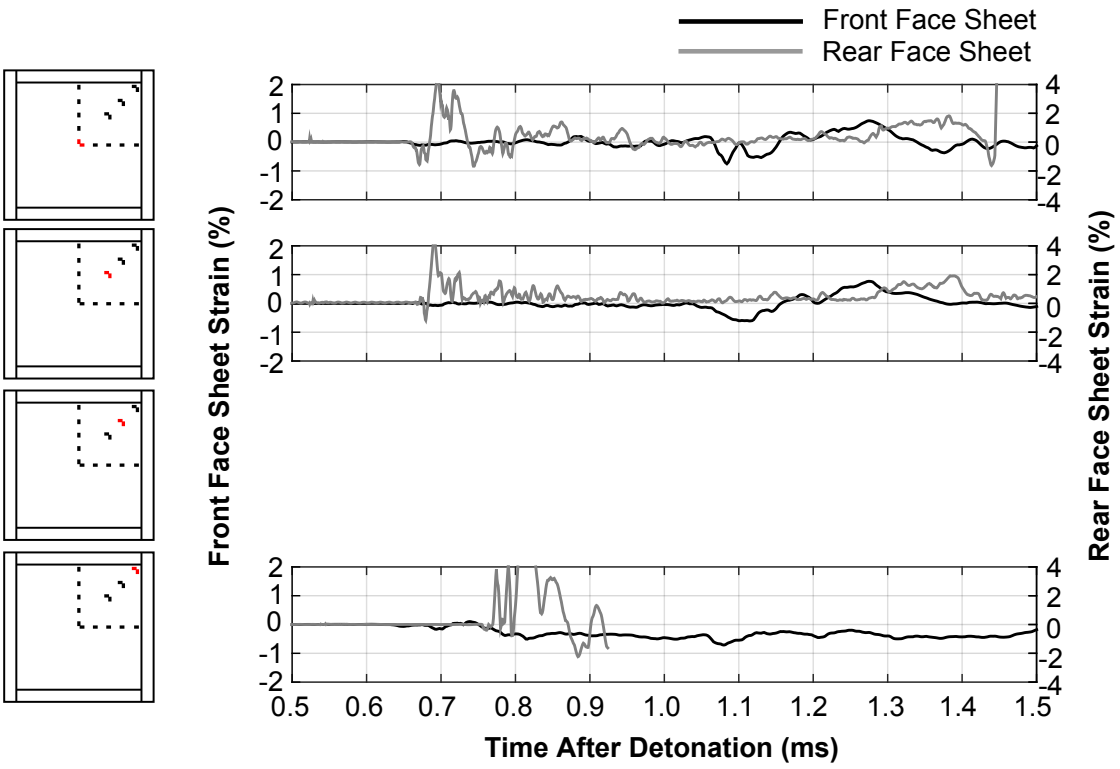


Figure 5.24: Raw maximum principal strain gauge data for the diagonal strain gauges on the single core CFRP sandwich panel.

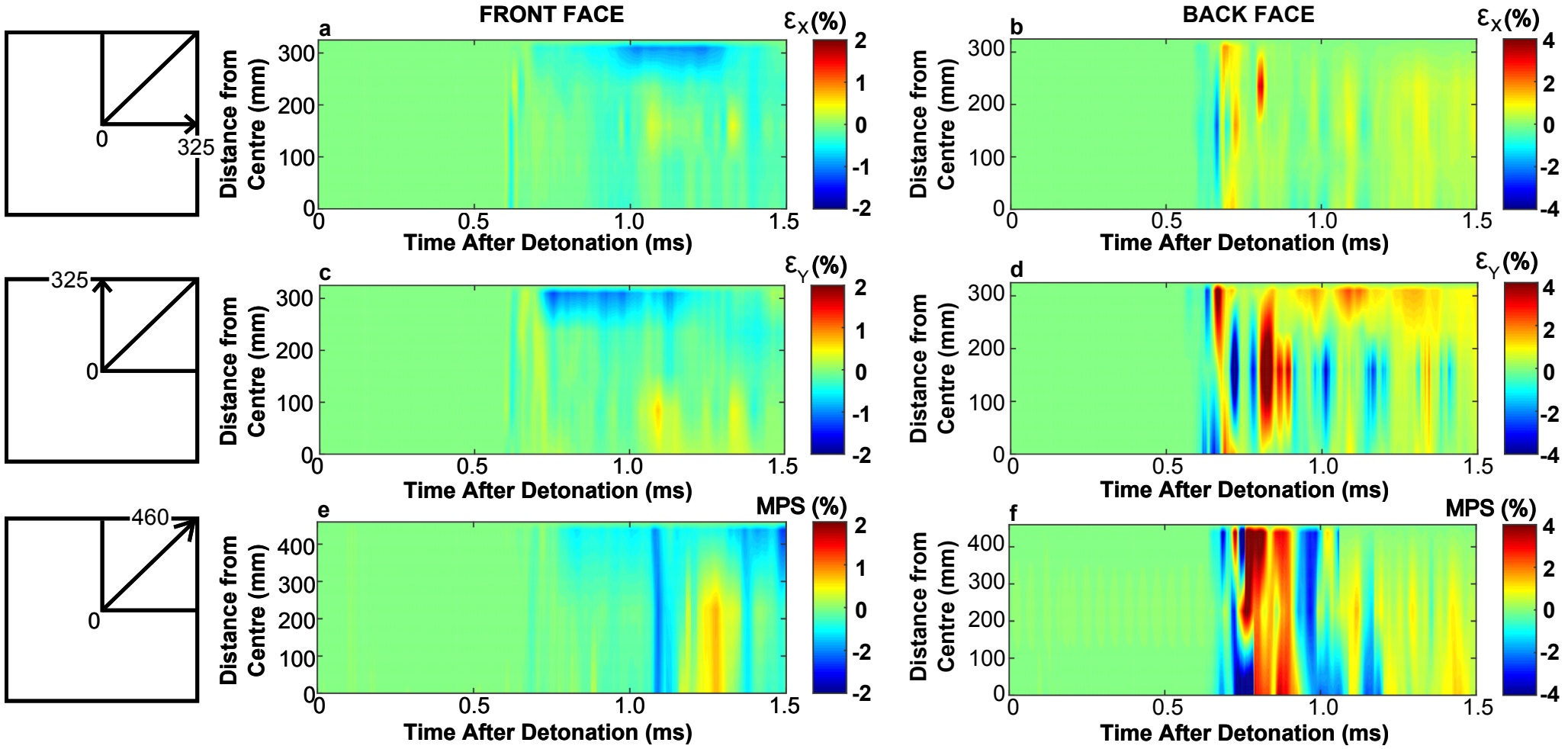


Figure 5.25: Variation of strain with time for a) the horizontal section of the front face; b) the horizontal section of the back face; c) the vertical section of the front face; d) the vertical section of the back face; e) the diagonal section of the front face; and f) the diagonal section of the back face, for the single core CFRP sandwich panel.

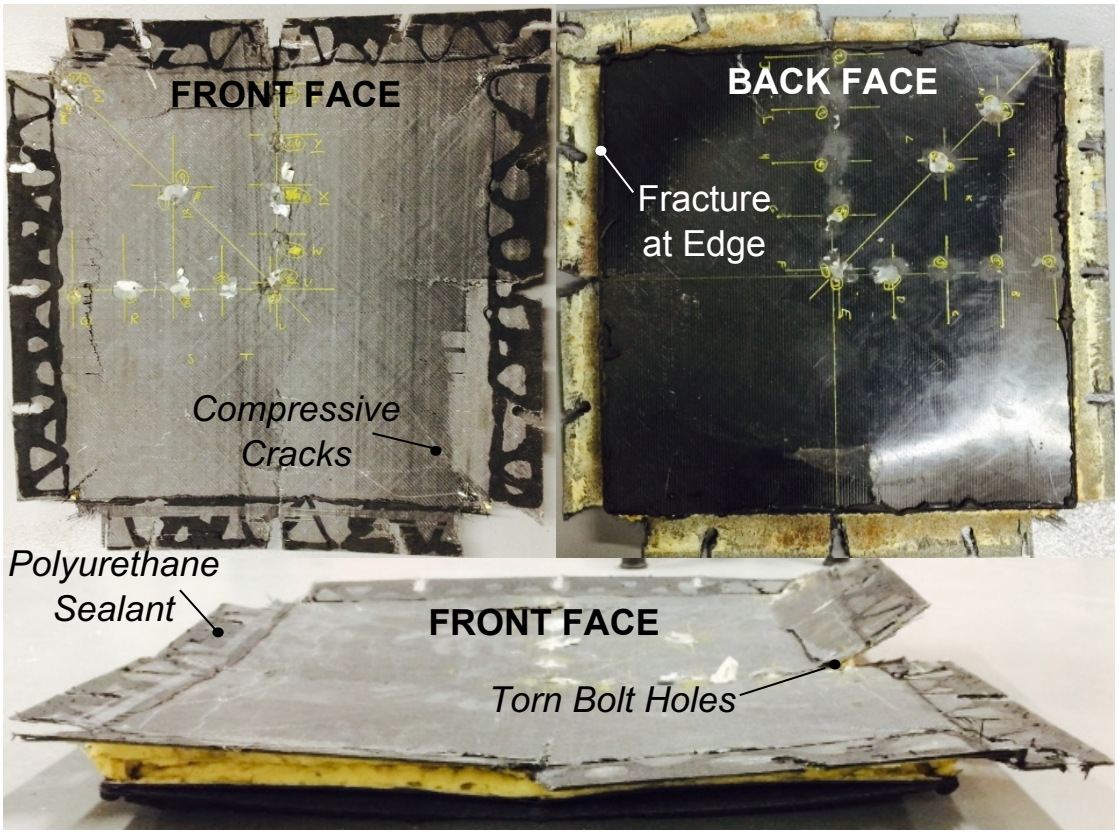


Figure 5.26: Photographs of the single core CFRP sandwich panel after blast testing.

5.4.3.4 Graded Core CFRP Sandwich Panel

The horizontal, vertical and diagonal strain gauges for the graded core CFRP sandwich panels are shown in Figure 5.27, Figure 5.28 and Figure 5.29 respectively. These are for the front and rear face-sheet strain gauges. The strain contour plots of the graded core CFRP sandwich panel are shown in Figure 5.30, with the front and back face-sheet strains of the horizontal centre section shown in Figure 5.30a and Figure 5.30b respectively. The front and back face-sheet strains of the vertical centre section are shown in Figure 5.30c and Figure 5.30d respectively, and for the diagonal section front and back face-sheet maximum principal strains in Figure 5.30e and Figure 5.30f respectively. The strain traces for the graded case differ significantly from the single core case, in that the deflection is much

flatter in shape, causing very high strain at the boundary, which ultimately fails in tension. This flat deflection shape is expected to be due to the graded foam layers absorbing energy, so creating a more uniform deflection of the back face-sheet. As with the single core CFRP case, the panel fails due to back face-sheet fracture around the boundaries, as shown in Figure 5.31.

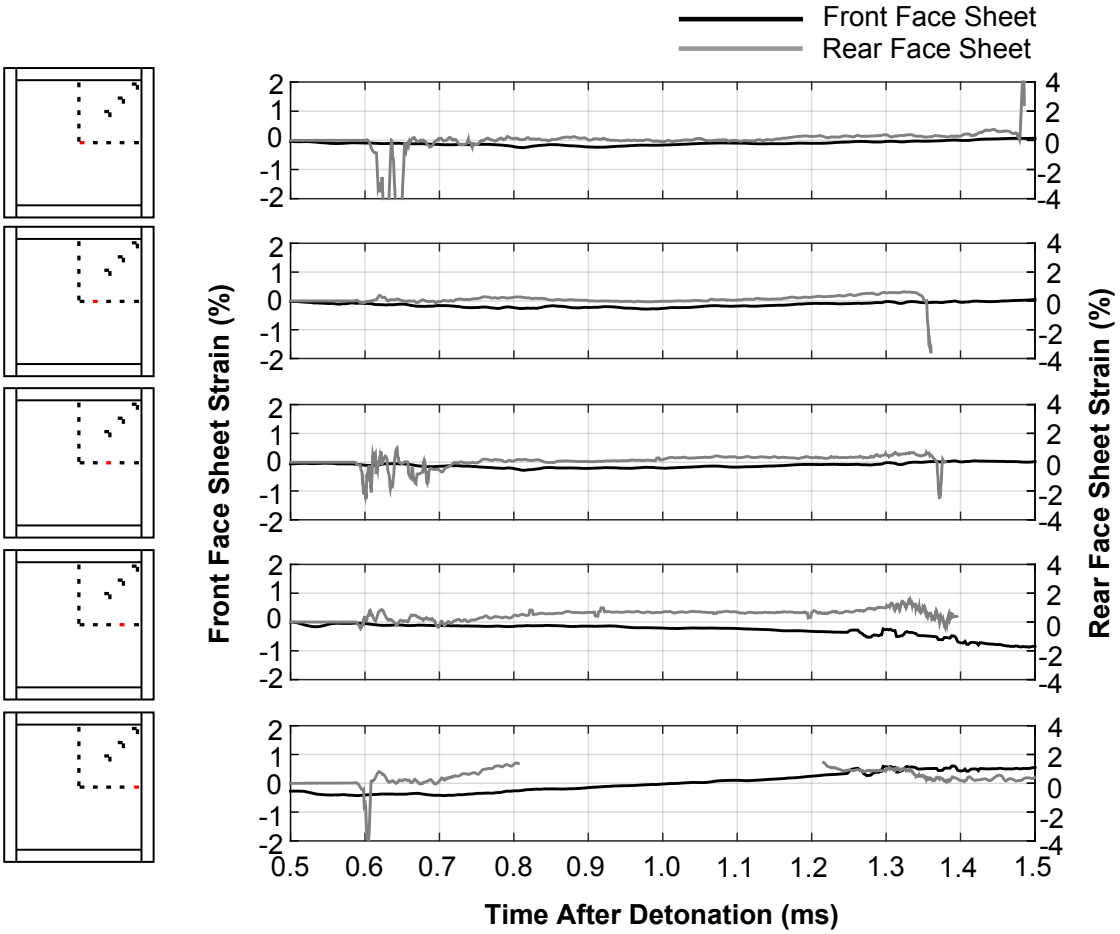


Figure 5.27: Raw strain gauge data for the horizontal strain gauges on the graded core CFRP sandwich panel.

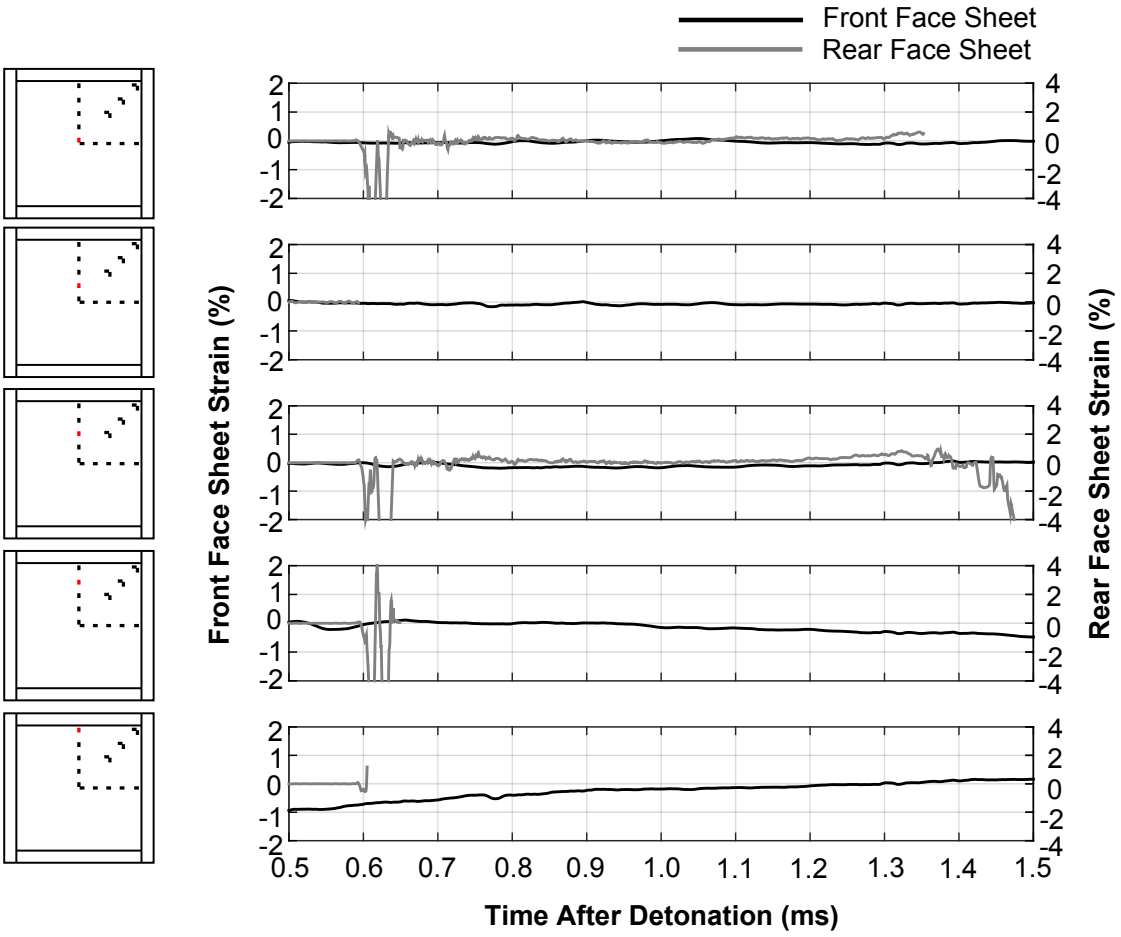


Figure 5.28: Raw strain gauge data for the vertical strain gauges on the graded core CFRP sandwich panel.

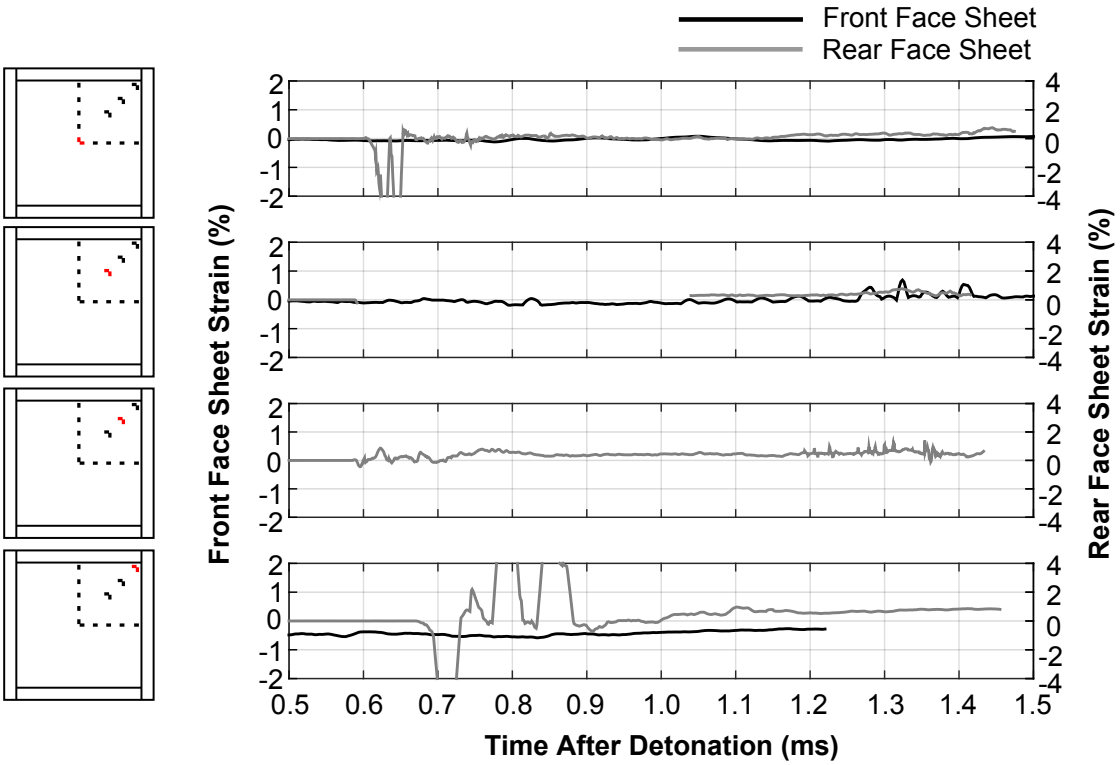


Figure 5.29: Raw maximum principal strain gauge data for the diagonal strain gauges on the graded core CFRP sandwich panel.

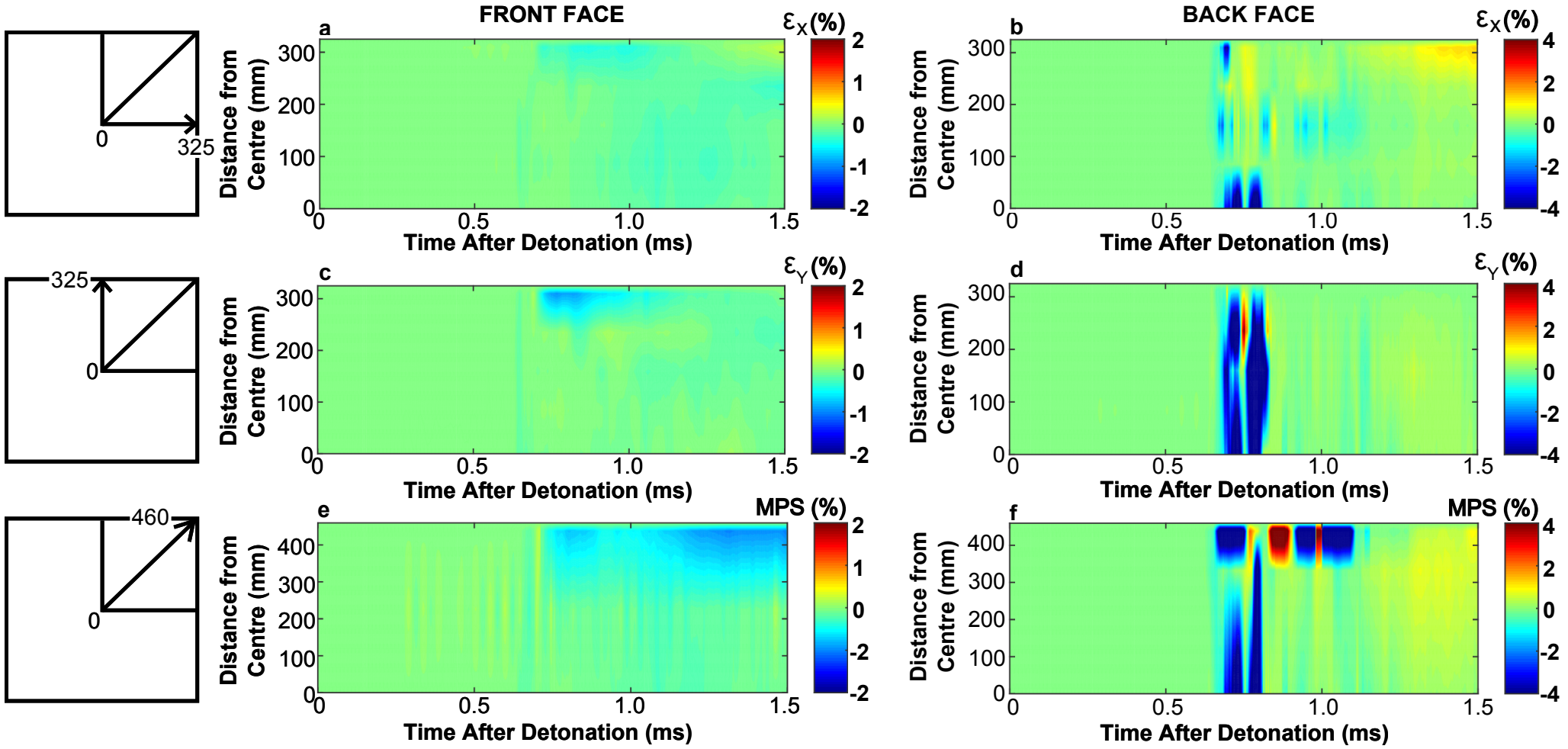


Figure 5.30: Variation of strain with time for a) the horizontal section of the front face; b) the horizontal section of the back face; c) the vertical section of the front face; d) the vertical section of the back face; e) the diagonal section of the front face; and f) the diagonal section of the back face, for the graded core CFRP sandwich panel.

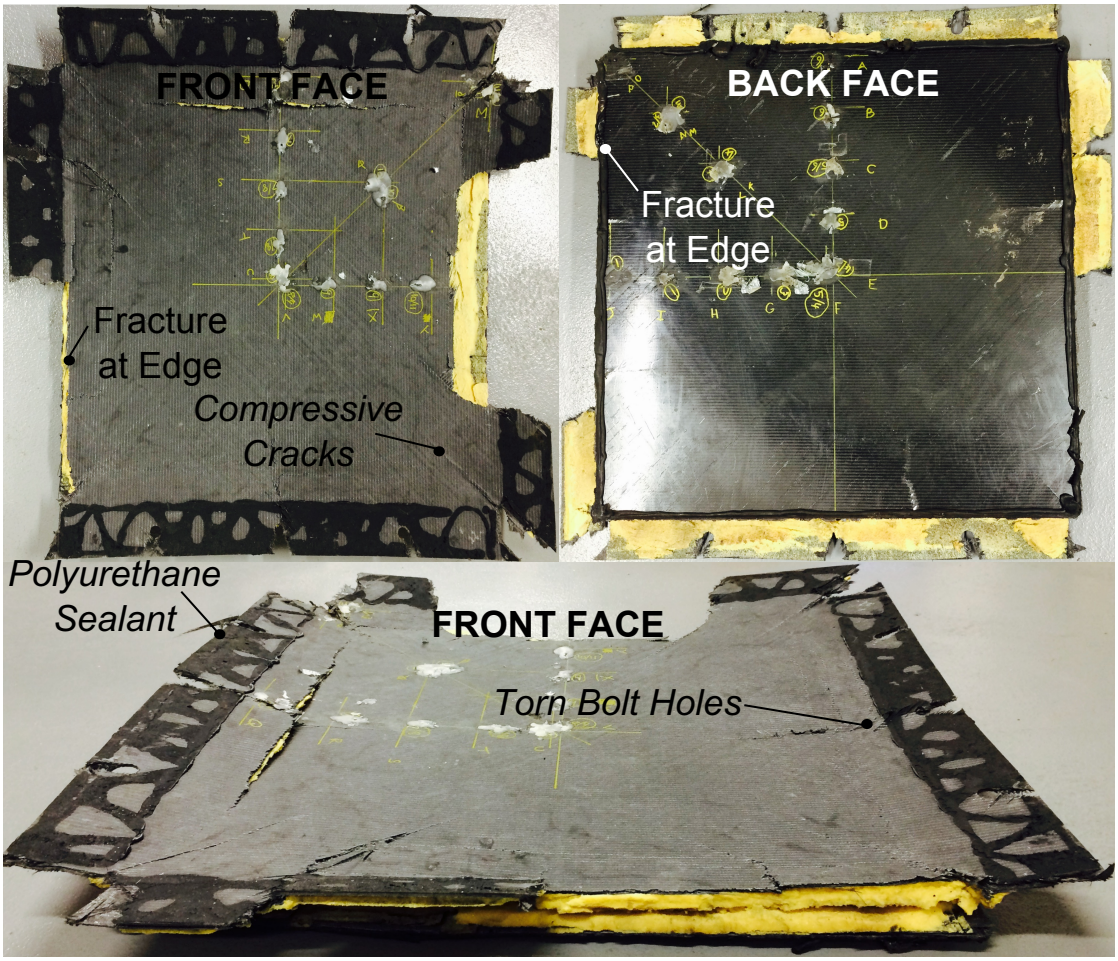


Figure 5.31: Photographs of the graded core CFRP sandwich panel after blast testing.

5.4.4 Out-Of-Plane Displacement Calculations

From the linearly interpolated strains measured across the horizontal, vertical and diagonal sections of the sandwich panel, it was possible to determine an approximation of the out-of-plane displacement across these lines. This method was described previously in this chapter, and the results are presented in this section. The out-of-plane displacements are for the centreline of the sandwich panels, as they are calculated using an average of the two face-sheet strains.

5.4.4.1 Single Core GFRP Sandwich Panel

The out-of-plane displacement of the single core GFRP sandwich panel is shown in Figure 5.32, with the deflection shape of the horizontal centre section shown in Figure 5.32a, the vertical centre section shown in Figure 5.32b and the diagonal section shown in Figure 5.32c. The out-of-plane deflection of the centre of the sandwich panel is shown in Figure 5.32d, along with the side-on blast pressure measured during the test. From the edge displacement plots, its is clear to see that the sandwich panel deflects in a "bathtub" shape, due to the transmission of the wave through the panel causing high bending moments at the edges, which progressively move towards the centre of the sandwich panel. As the calculation of out-of-plane displacement relies upon the interpolation of strain from five gauges over a large distance, loss of data causes poor definition of the deflection shape, as can be seen in Figure 5.32c. In Figure 5.32c this is caused by missing data from the front face-sheet strain gauges, causing the displacement to be linearly interpolated from the panel edge to the panel centre. The deflection shown is relative to the edge of the sandwich panel, thus accounting for the deflection of the steel box. The peak deflection measured during the test was 48 mm at 0.86 ms after detonation and this is an average of the central displacements calculated from the horizontal, vertical and diagonal gauges.

5.4.4.2 Graded Core GFRP Sandwich Panel

Figure 5.33 provides the out-of-plane displacements calculated for the graded core GFRP sandwich panel, where Figure 5.33a and Figure 5.33b show the deflection shapes for the horizontal and vertical centre sections respectively. Figure 5.33c shows the deflection shape for the diagonal centre and Figure 5.33d provides the central displacement of the sandwich panel with time, as well as the side-on pressure measured during the test. This displacement at failure was 34 mm at 0.81 ms after detonation measured from an average of the central displacement calculations along the horizontal, vertical and diagonal lines of strain gauges. The deflection shape of the edge contour lines is also fairly smooth, with the deflection being a "bathtub" shape for a longer duration. This sandwich panel showed the most expected deflection shapes and this is due to very few gauge failures during de-

formation. The diagonal line deflection in Figure 5.33c is as expected, due to the square deflection shape witnessed when deforming a square panel under uniform loading. The vertical deflection shape in Figure 5.33b transitions from a "bathtub" shape to straight lines, and this is due to the bending wave reaching the centre of the sandwich panel so removing the "bathtub" loading. However, due to missing rear face-sheet strain gauge data near maximum deflection, the curved shape of the panel is not captured fully and instead straight line contours are observed.

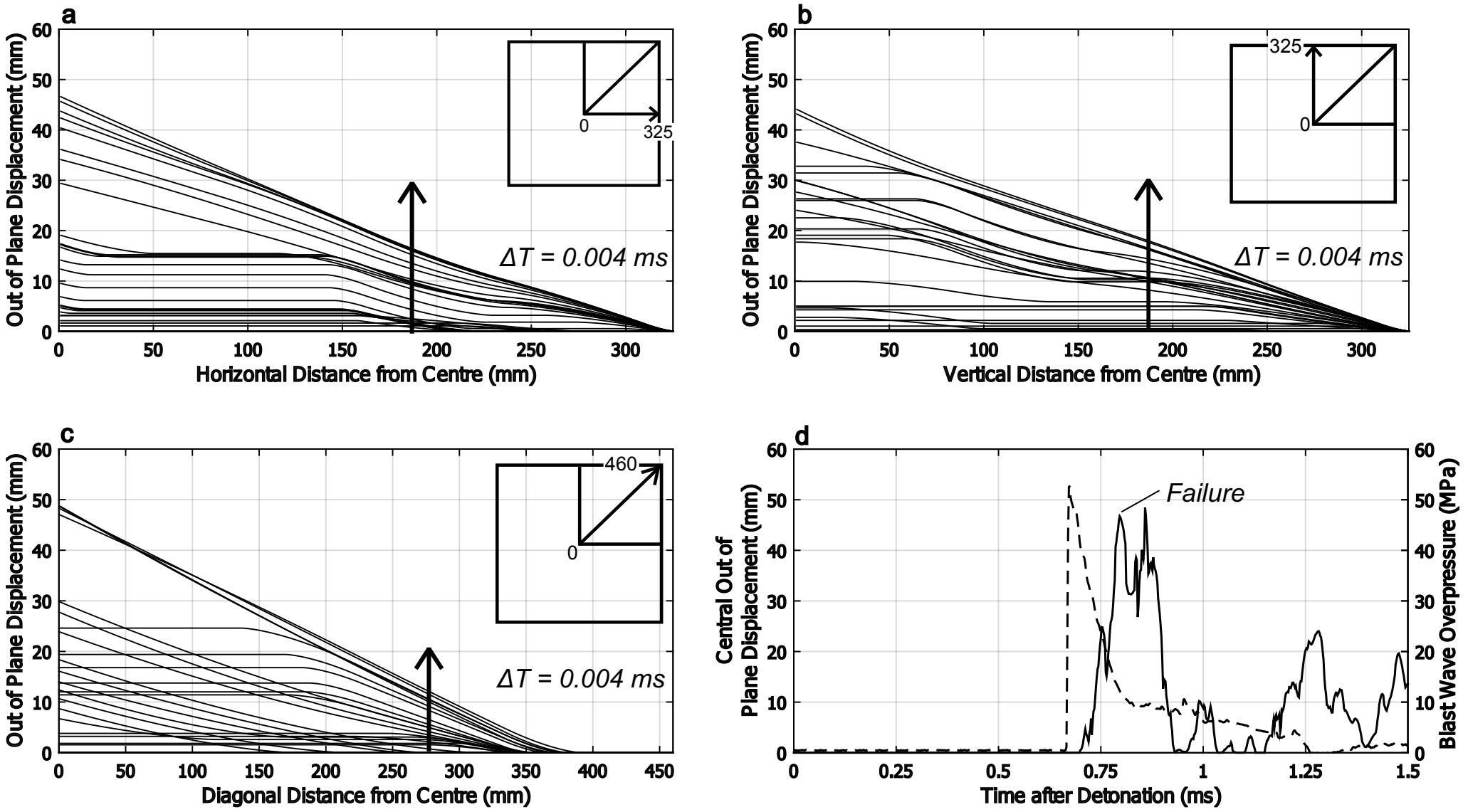


Figure 5.32: a) The horizontal centre section displacement; b) the vertical centre section displacement; c) the diagonal section displacement; and d) the central deflection and the measured side-on blast pressure, of the single core GFRP sandwich panel. The time step between the section displacement plots is 0.01 ms.

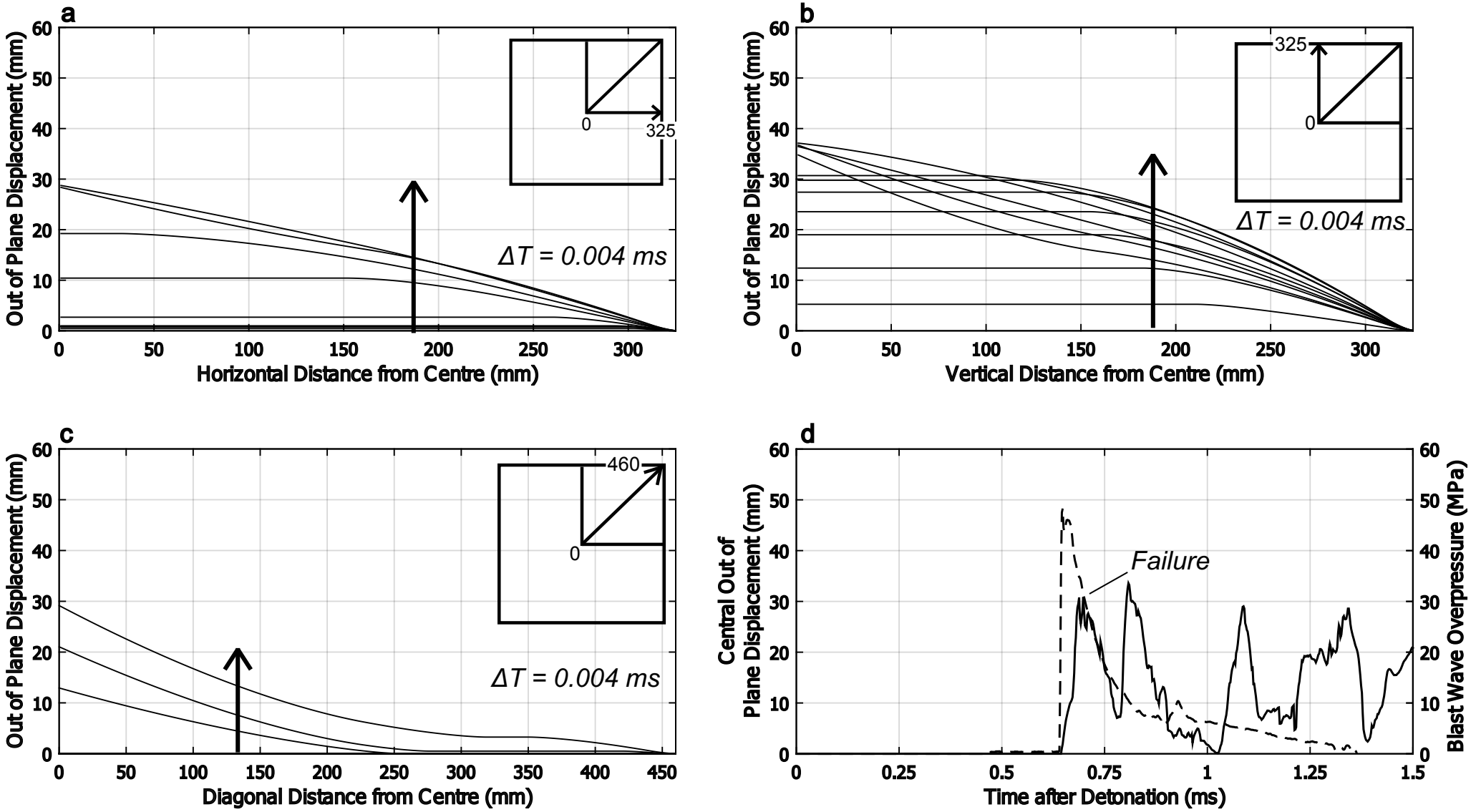


Figure 5.33: a) The horizontal centre section displacement; b) the vertical centre section displacement; c) the diagonal section displacement; and d) the central deflection and the measured side-on blast pressure of the graded core GFRP sandwich panel.

5.4.4.3 Single Core CFRP Sandwich Panel

The single core CFRP sandwich panel deflection plots are shown in Figure 5.34, with the horizontal and vertical sections shown in Figure 5.34a and Figure 5.34b respectively, and the diagonal section shown in Figure 5.34c. The central deflection versus time, and the measured side-on blast pressure wave are shown in Figure 5.34d, with failure taking place at 0.89 ms, with a deflection of 50 mm. The central deflection with time is calculated as an average of the central deflection from the horizontal, vertical and diagonal strain gauges. The deflection shape is significantly different to the GFRP cases, with a "bathtub" shape near the edges, but then a smooth deflection in the centre. This is expected to be due to a concentrated load effect in the centre of the sandwich panel, witnessed in the single core CFRP panel because the face-sheets are much stiffer and the single layer foam core crushes quickly. This causes the deflection shape witnessed in Figure 5.34a and Figure 5.34b.

5.4.4.4 Graded Core CFRP Sandwich Panel

Figure 5.35 provides the deflection plots of the graded core CFRP sandwich panel. Figure 5.35a and Figure 5.35b show the horizontal and vertical section plots respectively, and Figure 5.35c shows the diagonal section plot. In all of these deflection shapes, the "bathtub" shape witnessed in both GFRP cases is demonstrated. Figure 5.35d shows the central displacement with time, with a failure displacement of 13 mm at 0.85 ms, and this was calculated from an average of the central displacements at failure when measured along the horizontal, vertical and diagonal gauges. The low deflection and the smooth deflection shape of this graded density panel show that the graded core acted to smooth out the deflection shape, unlike in the single core case. The pressure plot shown here is calculated and was not obtained during the test.

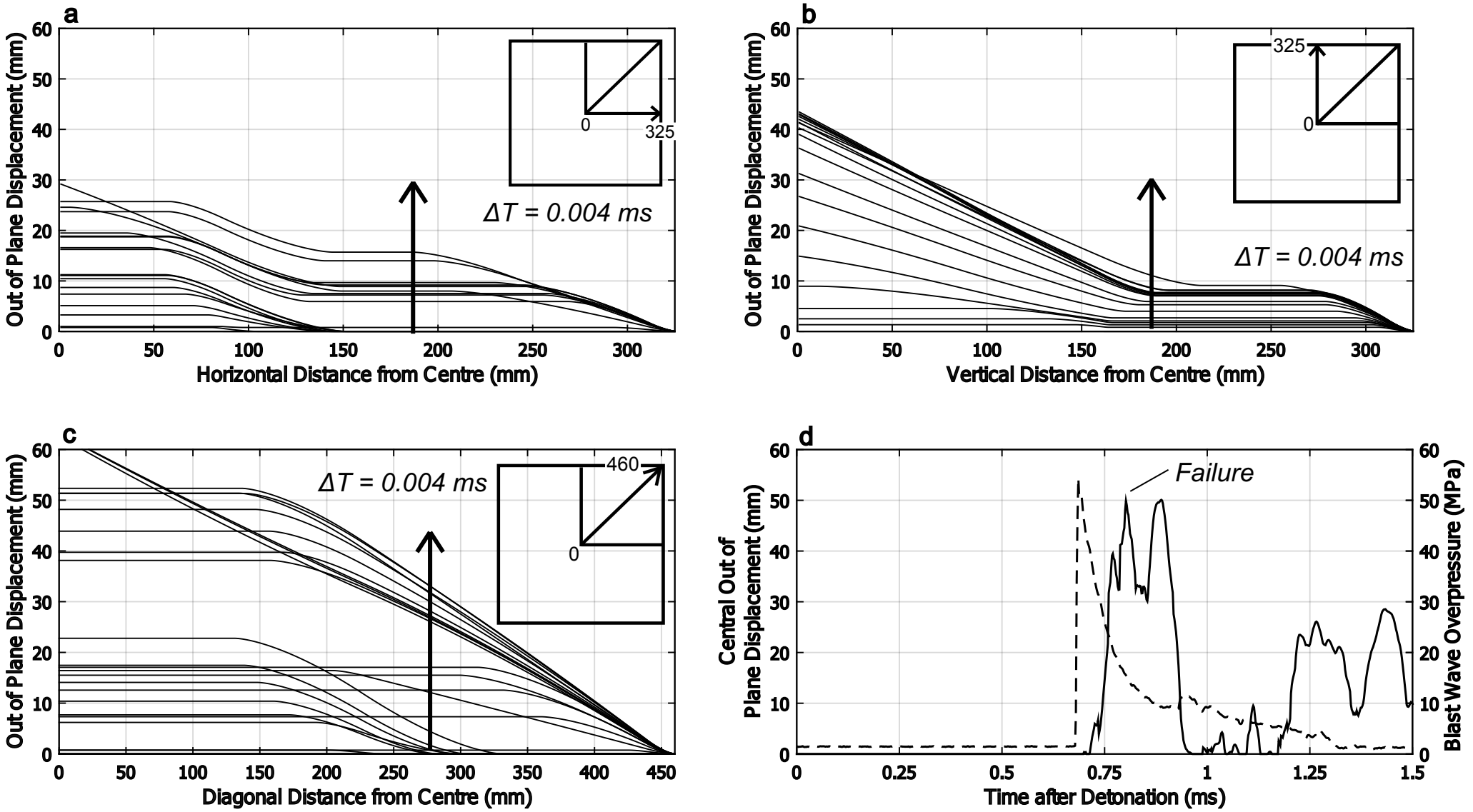


Figure 5.34: a) The horizontal centre section displacement; b) the vertical centre section displacement; c) the diagonal section displacement; and d) the central deflection and the measured side-on blast pressure of the single core CFRP sandwich panel.

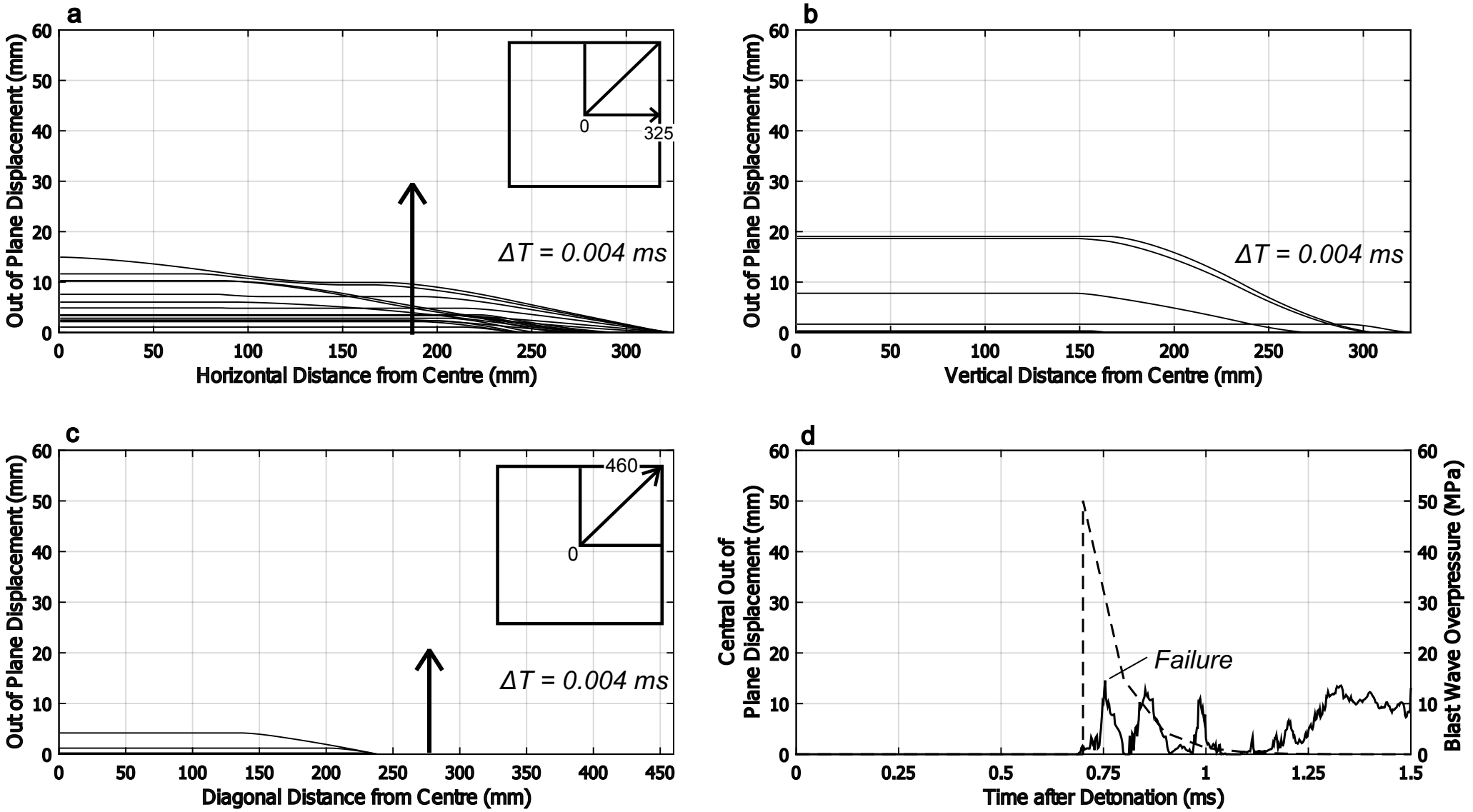


Figure 5.35: a) The horizontal centre section displacement; b) the vertical centre section displacement; c) the diagonal section displacement; and d) the central deflection and the calculated side-on blast pressure of the graded core CFRP sandwich panel.

5.5 Discussion

The motivation behind this set of underwater blast tests was to validate the hypothesis that with a graded density foam core in a polymeric foam sandwich panel, the blast wave energy can be absorbed such that the deflection of the sandwich panel is reduced compared with a single density core. Furthermore, it was expected that in a comparison between sandwich panels with GFRP and CFRP face-sheets, the CFRP sandwich panel would suffer catastrophic boundary failure, due to the higher stiffness panels causing greater bending moments at the edges. The results from all four tests are summarised in Table 5.3. Also shown in Table 5.3 is the displacement velocity, calculated as the average gradient of the initial deflection of the sandwich panel upon arrival of the blast wave.

5.5.1 Effect of Using a Graded Density Core

The results, summarised in Table 5.3 show clearly that the central displacement at failure is reduced by using a graded density foam core. The time to failure is also lower in the graded cases, but by a much less significant amount, so it is difficult to draw any conclusions from this. From the out-of-plane displacement plots, it has been shown that the use of a graded density foam core creates a much smoother displacement profile across the sandwich panel, a result which was also found in the air blast results presented in Chapter 3. The smoother displacement, in this case, is due to both a higher energy absorption, but also the higher density foam at the back which is stronger in tension, meaning fewer cracks propagate through the layer. The tensile properties of the foam are very different once crushed, but it is intuitive that the high density SAN M200 foam is more resistant to cracking than the low density M100 foam at the front of the panel, encouraging cracking in the front foam and allowing a smoother back face-sheet displacement.

The results of high strain rate compression tests of the M100, M130 and M200 SAN foams are shown in Chapter 6, and these allowed a comparison to be made in the energy absorbed in crushing the single density cores and the graded density cores. Dynamic stress versus strain curves were constructed from a combination of quasi-static and dynamic tests (the plots for which are shown in Figure 6.33

in 6), up to a pressure of 60 MPa, which was the peak pressure measured in the underwater blast tests. By applying Equation (5.5) to the constructed stress versus strain curves, where E_c is the crushing energy; z is the crushing displacement and A is the cross sectional area, for the 10 mm thick foam layers in the graded core and the 30 mm layer in the single core, a comparison of the energy absorbed during blast was made. In each test the boundaries were fixed from in-plane displacement, so the cross sectional area was assumed to be the exposed 650 mm squared area of the sandwich panel, resulting in a constant area of 0.4225 m^2. Using this method the energies absorbed in crushing the 10 mm thick M100, M130 and M200 layers were found to be 32.6 kJ; 39.2 kJ and 50.1 kJ respectively. The total absorption was therefore 123.0 kJ compared to the 118.0 kJ absorbed by the 30 mm thick M130 SAN foam core. This 5 kJ increase in absorbed energy alongside the blast wave energy dissipated inside the core due to foam interfaces, and the extra energy to crack the higher density foams compared to the low density foam, aid in explaining the reduced deflection of the graded density sandwich panels.

$$E_c = \int_0^z \sigma\left(z\right) A\left(z\right) dz \tag{5.5}$$

5.5.2 The Effect of Glass Versus Carbon Fibre Face-Sheets

The final column in Table 5.3 shows the initial displacement velocity of the centre of the sandwich panel, which is significantly slower for the graded core CFRP case than for the single core CFRP case. However, in the GFRP tests it was found that the graded core responded more quickly upon arrival of the blast wave. It is expected that the reason for this is that the front CFRP face-sheet offered more resistance to core crushing than the GFRP front face-sheet, as during the crushing stage the front face-sheet will act as a membrane so will be loaded in tension, as is visible in the strain contour plots. This would cause the core crushing to happen over a longer period of time, thus reducing the time that the panel was in the bending phase. In the GFRP case, the face-sheet offered much less resistance to core crushing, but the graded core acted to increase the time before the panel entered into the bending phase. It would appear from the results that this then caused the panel to reach the initial peak displacement quicker as it responded

over a shorter space of time. From both the velocity and the displacement at failure, it is clear that the CFRP sandwich panel benefitted more from the use of a graded density core. Another interesting result from Table 5.3 is that the central displacements to failure of both the single core GFRP and the single core CFRP sandwich panels are similar, despite the CFRP panel being much stiffer than the GFRP panel. By assessing Table 5.3 it can be seen that the time to failure in every sandwich panel was the same, and it is understood that the failure location is always at the boundary, either in the form of rear face-sheet failure in the CFRP panels, or the GFRP panels pulling out and shearing the sealant. The graded cores dampen the out-of-plane displacement, thus reducing the central deflection at failure, but it appears that this is not the case in the single density cores. It is expected that with a larger panel, or smaller blast impulse, the central deflection of the GFRP sandwich panel would be greater than the CFRP sandwich panel, as observed in the graded density cases.

5.6 Conclusion

The underwater blast tests documented in this chapter were performed to test novel material constructions, as well as to develop the test techniques and data processing methods. The results from this research form a qualitative comparison of CFRP face-sheets versus GFRP face-sheets, and graded density cores versus single density cores. The comparative study showed that the use of a graded density foam core reduced the central deflection of both the GFRP and CFRP sandwich panels at failure, and the effect was more so in the CFRP case than the GFRP case. This result was due to the crushing of the graded density core absorbing more blast energy than the single density core as well as greater dissipation of the blast wave moving through the sandwich panel due to the foam layer interfaces. Furthermore, the deflection of the graded density sandwich panel was smoother than the single core case, and it is expected that this is due to core cracks during bending being encouraged in the lower density foam at the front of the panel, thus reducing the crack density in the rear of the sandwich panel. This was also observed in the air blast test results. The findings from this research into using a graded density core for energy absorption and blast wave attenuation agree well

with the research performed by Gardner, Wang and Shukla, where SAN Corecell foams were graded in GFRP sandwich beams and shock loaded. It was found that the acoustic attenuation due to the mismatch of the foam layers resulted in a lower energy shock wave reaching the rear face-sheet. This reduced the deflection and velocity of the rear face-sheet, and was due to both incremental core crushing of the foams absorbing more blast energy, and scattering of the shock wave at the foam interfaces [109].

The effect of using CFRP face-sheets instead of GFRP face-sheets was to cause the sandwich panel to fail by tearing the rear face-sheet, instead of pulling out of the frame in the GFRP case. This was due to the much greater stiffness of the CFRP face-sheets. The central deflection at failure of the CFRP graded sandwich panel was less than the GFRP graded sandwich panel, due to the increased stiffness of the face-sheets.

The underwater blast tests also provided developments in the area of underwater blast testing. By using square panels it was possible to isolate one quarter of the sandwich panel, so utilise more electronic strain gauges to record the response of the sandwich panel. The higher density of strain gauges then allowed the out-of-plane displacement of the centreline of the sandwich panel to be calculated, as the gauges were placed on the opposing face-sheets. This led to out-of-plane contour plots, which were coarse due to the spacing of the strain gauges, but which allowed the expected "bathtub" shape to be observed. Also, by finding the cumulative out-of-plane displacement along each line of gauges to the centre, a fairly robust value of central displacement was calculated, which provided a useful comparison of the sandwich panel constructions. This technique would be greatly improved by more densely spaced strain gauges, reducing the distance over which the strain is interpolated, but the results provide a positive finding.

Due to the close proximity of the charges none of the sandwich panels survived the blast. The charges were detonated close to the sandwich panels to ensure full core crushing and full boundary failure took place. This was done to investigate the effect of using a graded density core to absorb energy in core crushing, and to investigate the effect of face-sheet stiffness on boundary failure. A recommended area of future work would be to performed tests with increasing panel sizes, to study the effect of panel size on the boundary loading, and to increase the distance

of the charge away from the panel, to assess the differing survivability of the panels when boundary failure does not occur. This could be achieved by developing a finite element model of the test and validating it against the work presented in this project, to then change the panel size and charge parameters numerically.

Table 5.3: Summary of the underwater blast test results from the graded density and single density GFRP and CFRP sandwich panels.

Test	Peak Adjusted Reflected Pressure (MPa)	Adjusted Reflected Impulse at Failure (MPa.ms)	Displacement at Failure (mm)	Time to failure (ms)	Displacement Velocity (m/s)
Single Core GFRP	63	5.2	48	0.86	507
Graded Core GFRP	58	5.1	34	0.81	699
Single Core CFRP	64	5.2	50	0.89	554
Graded Core CFRP	-	-	13	0.85	221

Chapter 6

Foam Characterisation

6.1 Introduction

To understand the difference in the behaviour of the polymeric foams used as cores in the sandwich composite materials, characterisation tests were performed in tension and compression at quasi-static and dynamic rates. By carrying out these tests it was possible to determine different failure properties at increased loading rates, and correlate these to the results observed in the full scale blast tests. As shown in Chapter 3, during air blast loading the foam fractures near the edges. This was caused by a combination of shear and tensile load. Due to the complexity of performing dynamic shear tests, they were not performed in this research, and a proportional relationship between shear and tension was assumed, for comparing the various foams. Dynamic compression tests were performed on a split Hopkinson pressure bar (SHPB), to test strain rates in the region of those witnessed in the foam crushing stage of underwater blast tests. Digital image correlation (DIC) was utilised to measure the strain in test samples in all tests, as gripping soft materials such as foam causes problems in measuring strain from grip displacement on the test machine. DIC was also used to check for strain equilibrium across the test samples.

The tests performed in the characterisation were quasi-static compression; dynamic compression; quasi-static tension; and dynamic tension. The dynamic compressive characterisation was to assess the behaviour of the SAN foams in under-

water blast scenarios, to explain the improved performance of the graded density cores to the single density cores. Quasi-static tests were performed to gain the full stress versus strain responses of the foams in tension and compression, as opposed to the individual properties provided by manufacturers. Dynamic tension tests were carried out as the foam shear strain plots in Chapter 3 showed that the differing failure points across the foam cores were caused by a combination of tensile and shear loading. As the shear strain to failure of the foams was expected to be the same, it was expected that different tensile failure properties were the cause of the different responses.

In the foam characterisation research, material properties of the polymeric foams were determined as bulk properties, not accounting for the heterogeneity of the materials. As will be shown in the subsequent sections of this chapter, cell collapse in compression and fracture in tension takes place at local instabilities due to cell wall buckling or cell wall fracture. Furthermore, compressive material properties were determined in the through-thickness direction of the foam materials, and tensile properties were determined in the in-plane direction. The foams were expected to be isotropic in-plane, but anisotropic in all three dimensions. The compressive properties were applicable to underwater blast loading, in which through-thickness crushing of the foam occurs, so measuring through-thickness properties was deemed as suitable. Any tensile fracture of the foam during bending would take place in-plane, so it was deemed acceptable to measure tensile specimens in-plane.

6.2 Quasi-Static Compression

6.2.1 Experimental Methods

Quasi-static mechanical properties of the foam materials are provided by the manufacturers [100], [101], [102], but it was deemed necessary to perform tests to ascertain the full stress versus strain response of elastic and post-elastic deformation, as well as to validate the properties presented in the literature. Quasi-static compression was performed on all of the foams used in air blast testing: SAN M100; SAN M130; SAN M200; PVC C70.90; and PMI 110SL. The test setup was

influenced by the ASTM C365/C265M test standard [111], and the tests were performed using a 150 kN Instron 5984 universal testing machine. The test samples were cut using a fine bandsaw blade with a guide, and checked for squareness before testing. The sample size was 30 mm x 30 mm, with the thickness of the foam sheets available. The thickness was not changed, as the foam production process results in very flat sheets so it was deemed unnecessary to process them further. A self aligning platen was used in the test to ensure any deviation in the load train was accounted for in the test. A schematic of the load train is shown in Figure 6.1. Square samples were used for these tests to allow the use of 2D DIC to measure elastic strain in the test samples. This is stated as acceptable in the test standard [111], and the Poisson's ratio after foam crushing is approximately zero. DIC was performed using a Canon 350D digital single lens reflex (DSLR) camera, which was triggered using the mobile telephone application "Triggertrap" with an image captured every 3 seconds. The elastic modulus of compression (E) was then calculated from the stress (σ), as calculated from the load cell and cross sectional area of the specimen, and strain from DIC (ε), using Equation (6.1), where t is time. This removed the possibility of misalignment of the data from DIC and the load cell. The ASTM standard on which the test was based suggests using the chord of the central section of linear elasticity for the compressive modulus, to avoid the calculation being distorted by the bedding in of the sample and the initial yield behaviour before crushing begins. This method was used in practice, when selecting the load data and DIC data for which to apply Equation (6.1). Prior to testing the load train was loaded to 50 kN without the specimen present, to ensure that the equipment was properly bedded and that the self aligning platen was flat in the test machine. It was also not necessary to account for compliance in the load train as the elastic modulus of the foam was so low.

The elastic modulus, crushing stress, crushing strain and plateau stress values recorded from each test were calculated from the DIC strain and load cell, and the densification was recorded as the strain at which the stress began to increase exponentially with strain. Once past the elastic section, the strain was recorded using the machine displacement, as DIC was not possible once cells began to collapse. An exponential equation was fitted to this increase using Equation (6.2), where σ_p is the plateau stress, Q and λ are densification constants, ε_D is the strain

at which densification began as measured using the test machine displacement and ε_M is the strain measured using the test machine displacement. DIC was not possible once cells began to crush due to excessive distortion of the speckle pattern, which is why the machine displacement was used for the strain values in Equation (6.2). The densification constants were estimated from plotting the natural log of stress against strain for the data beyond the densification strain, and finding the gradient of the line to fit to Equation (6.3).

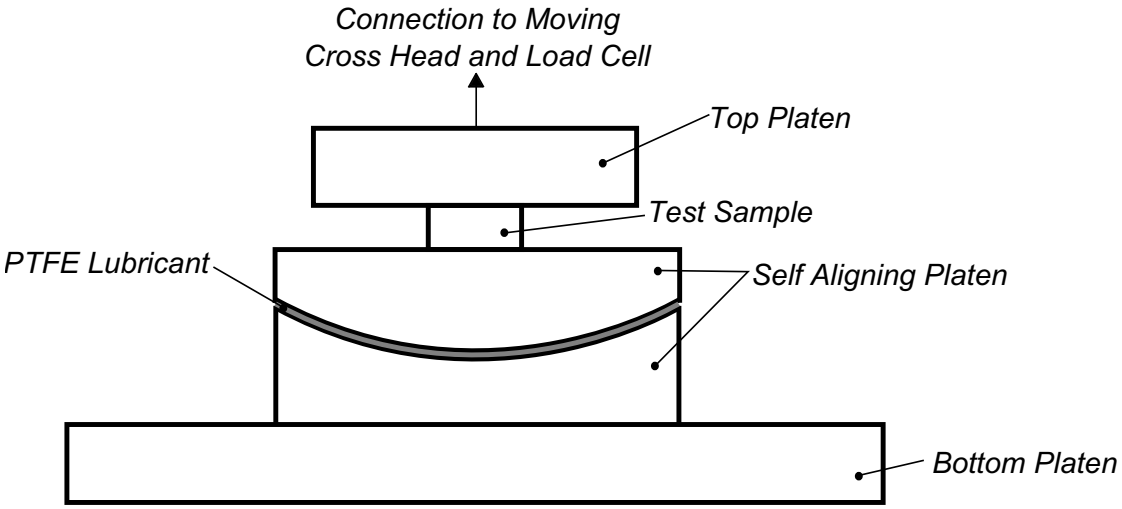


Figure 6.1: Schematic of the quasi-static compression test setup used to characterise SAN, PVC and PMI foams.

$$E = \frac{\partial \sigma}{\partial t} \cdot \frac{\partial t}{\partial \varepsilon} \tag{6.1}$$

$$\sigma = \sigma_p + Q e^{\lambda(\varepsilon_M - \varepsilon_D)} \tag{6.2}$$

$$ln\left(\sigma - \sigma_p\right) = ln\left(Q\right) + \lambda\left(\varepsilon_M - \varepsilon_D\right) \tag{6.3}$$

6.2.2 Results

6.2.2.1 SAN Foam

Due to the high repeatability of the SAN compression tests, and the large times taken per test, only three of the M100 and M200 foams were tested, and a fourth M130 sample was tested due to greater spread in the results. The thickness of foam sheets available for the M100; M130; and M200 materials were 40 mm; 30 mm; and 10 mm respectively. In order to achieve the same quasi-static strain rate of 0.025 s^{-1}, the test speeds were 1 mm/min; 0.75 mm/min; and 0.25 mm/min for the M100, M130 and M200 foams respectively.

The results of the three M100 samples are shown in Figure 6.2, in which engineering strain is calculated using the displacement of the machine crosshead. As can be seen from Figure 6.2, crushing took place at a strain of 3.6%, which was the average DIC strain in the samples at the peak in the load measured by the load cell immediately after the linear elastic section of the response. Densification began at about 40%, as measured using the machine displacement. Two DIC contour plots of compressive strain for one of the SAN M100 test samples are shown in Figure 6.3, with the average DIC compressive strain shown above the contour plots. The image at 3.6% corresponded to the maximum stress calculated immediately after the linear elastic section of the response, and the 5.0% plot shows how the two bands of cell collapse spread with increased loading. At this point DIC analysis was stopped as the cell collapse was too great for image correlation to take place.

The stress versus strain responses of the M130 foam core specimens are shown in Figure 6.4, where four samples were tested instead of three, due to the greater spread in data. It can be seen that crushing of the foam happened at around 4.4%, as measured using DIC, and densification began at about 40%, as with the M100 foam.

Finally, the SAN M200 specimen stress versus strain responses are shown in Figure 6.5, where crushing took place at 6.6%, as measured using DIC, and densification at around 40%, measured using machine displacement.

Table 6.1 summarises the properties of the M100, M130 and M200 foams, also showing the plateau stress which is important for calculating energy absorbing

characteristics during underwater blast, as presented in Chapter 5. It should be noted that in Table 6.1 the compressive modulus values are calculated from strain measured with DIC, and the load measured using data from the test machine load cell, using Equation (6.1). The crushing strain is also measured using DIC and the densification strain is measured using the test machine displacement. Table 6.1 also highlights the importance of independently measuring the material properties, as the compressive moduli measured with DIC are much lower for the three SAN foams than stated by the manufacturer. The measured crushing strengths are greater as this is the stress at which cell collapse began, whereas the compressive strength specified by the manufacturer is the stress at which yielding of the cell walls is expected to begin. The standard deviation values for the compressive modulus, crushing strength and crushing strain are provided, based on the spread in the data across the tests. They are not provided for the plateau stress as these were determined by visual inspection of the graphs, and the densification constants were fitted to all of the exponentially increasing data. The densification strain was determined from the point at which the exponential fit line crossed the plateau stress.

6.2.2.2 PVC Foam

The only PVC foam to be tested in this research was Airex C70.90, used in air blast testing both in the core polymer type comparison and in the compliant face-sheet research. Three samples of this foam were tested, as the results were very repeatable, and each foam was 40 mm thick, which was the thickness of the foam sheets available. The engineering stress versus engineering strain results of the C70.90 foam compression tests are shown in Figure 6.6, and a summary of the crushing strength and strain, plateau stress and densification strain is shown in Table 6.1. Also shown is the compressive modulus of the PVC foam. As with the SAN foams, the compressive modulus was calculated using DIC for the strain and the load cell to measure stress in the samples, and the crushing strain was measured using DIC. As shown in Table 6.1 the compressive modulus measured using DIC is much lower than that specified by the manufacturer and the crushing strength is the same as the compressive strength specified.

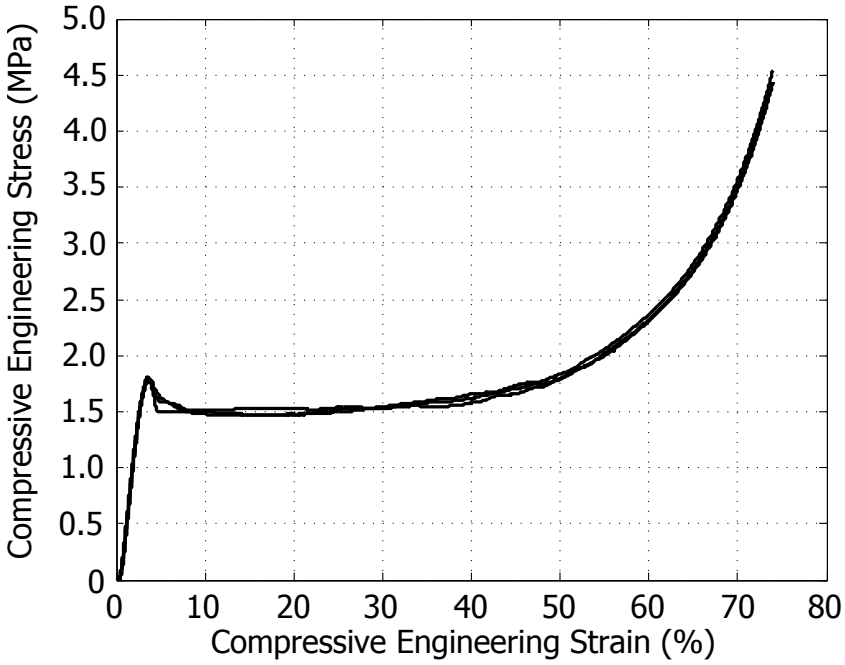


Figure 6.2: Engineering stress versus engineering strain for the three SAN Corecell M100 test samples.

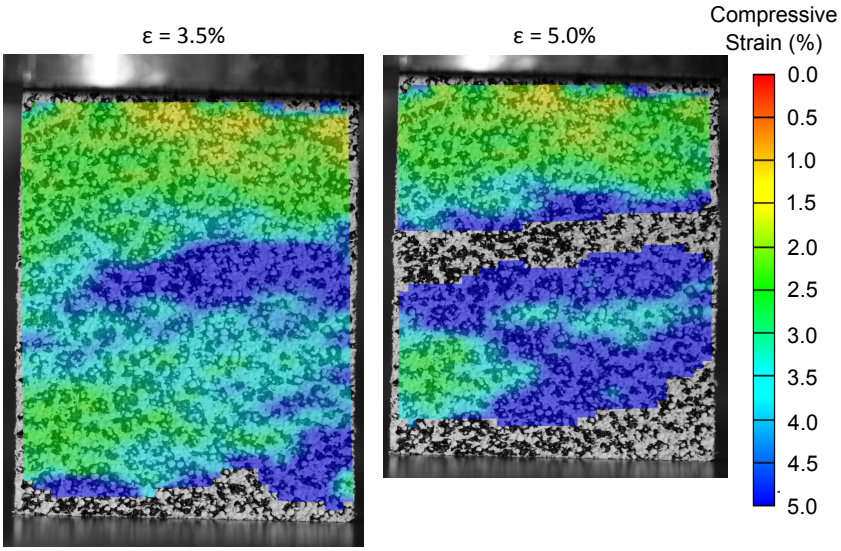


Figure 6.3: DIC contour plots of engineering compressive strain for one of the SAN Corecell M100 test samples. The image on the left shows the strain captured at the peak stress following the linear elastic compression of the sample, and the image on the right shows the strain when cell collapse has fully developed. The strain value above each image is the average strain in the specimen, measured using DIC.

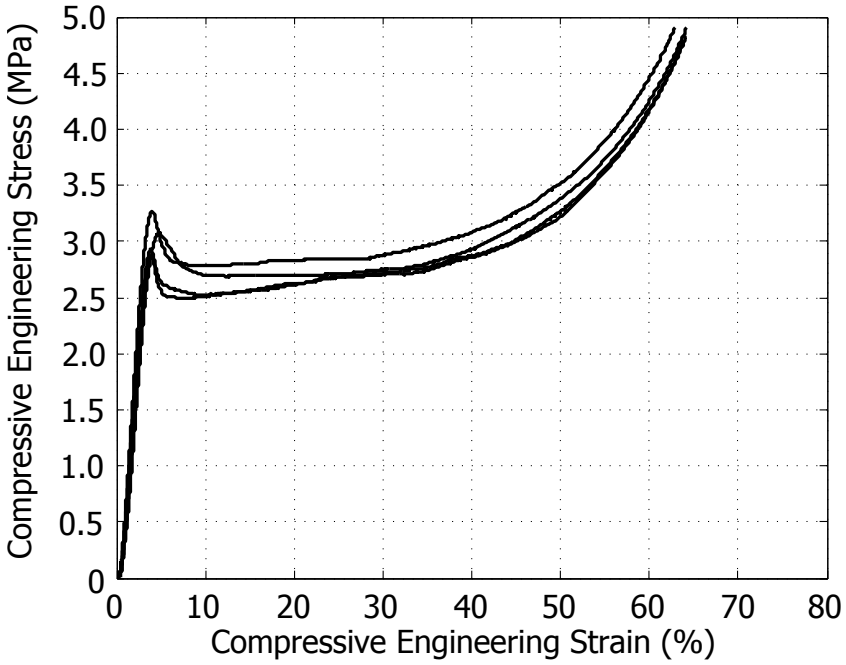


Figure 6.4: Engineering stress versus engineering strain for the three SAN Corecell M130 test samples.

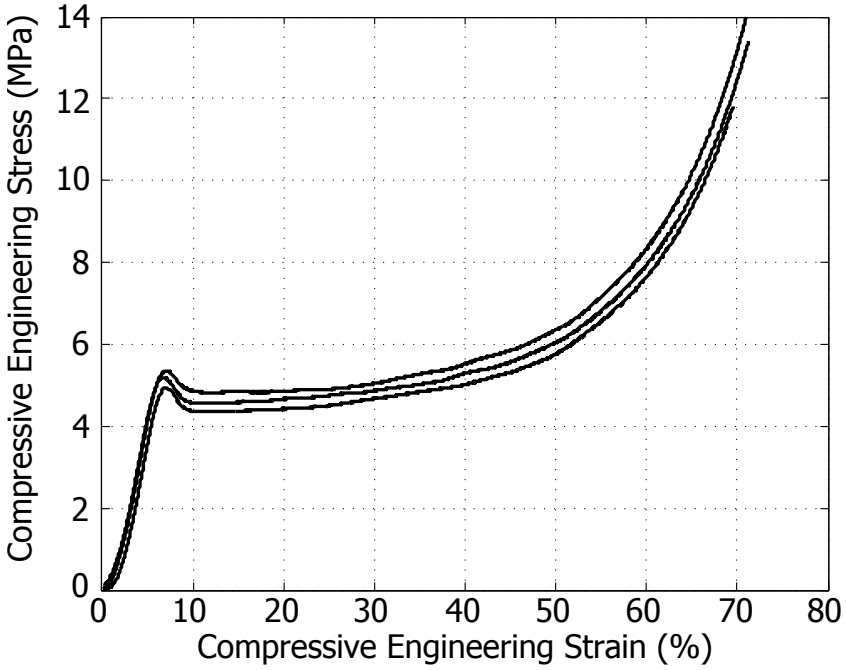


Figure 6.5: Engineering stress versus engineering strain for the three SAN Corecell M200 test samples.

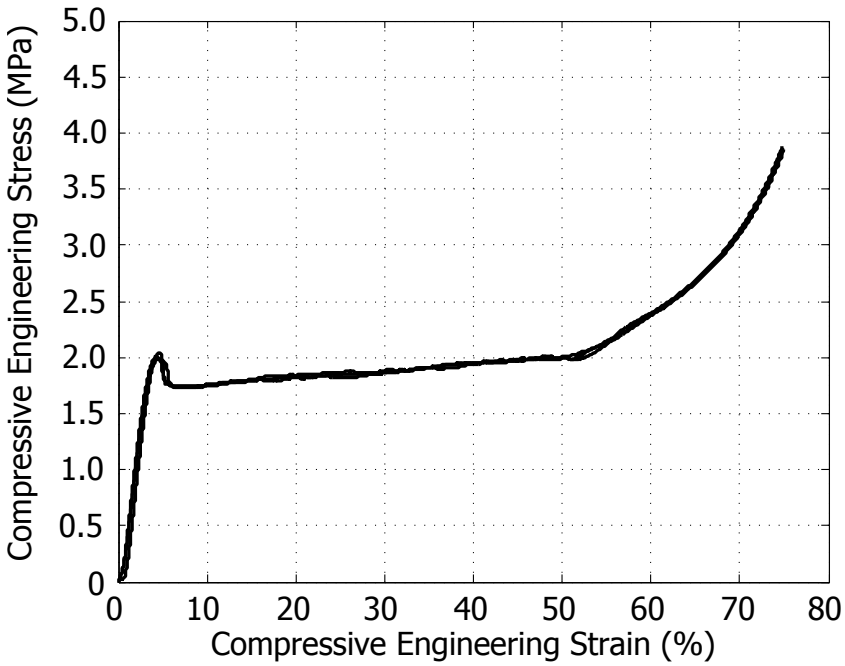


Figure 6.6: Engineering stress versus engineering strain for the three PVC Airex C70.90 test samples.

6.2.2.3 PMI Foam

The final foam to be tested in quasi-static compression was the PMI Rohacell 110SL foam which was 20 mm thick and tested at 0.5 mm/min. This foam was used in the 40 mm thick PMI blast panel, tested in the foam polymer type comparison, but the manufacturer also provided the foam in 20 mm thick sheets for laboratory testing. The results of the quasi-static compression tests are shown in Figure 6.7, and the main material characteristics summarised in Table 6.1. The modulus was calculated using DIC for strain and the load cell in the test machine for stress, and the crushing strain was measured using DIC.

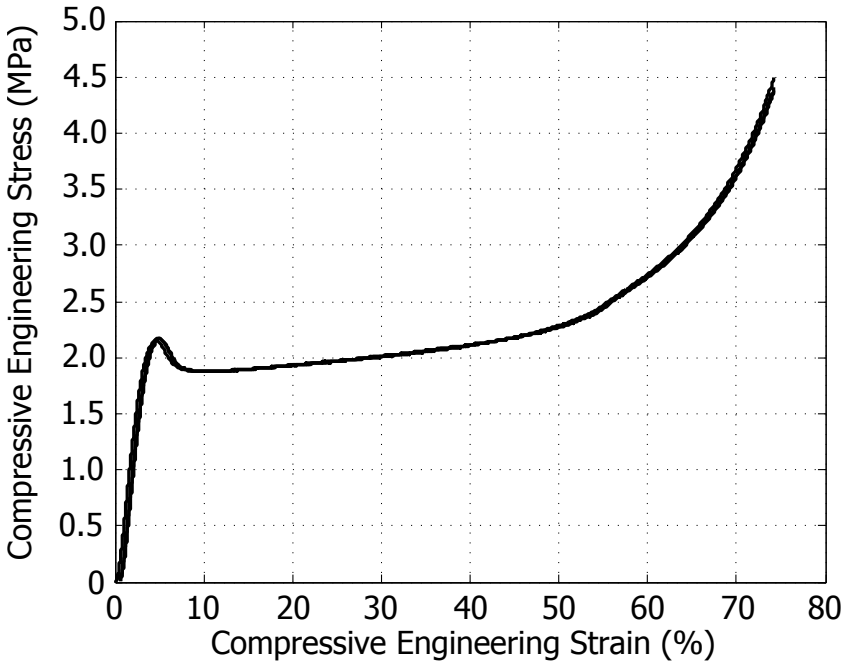


Figure 6.7: Engineering stress versus engineering strain for the three PMI Rohacell 110SL test samples.

Table 6.1: Summary of the quasi-static compressive properties of the five foam polymers used in air and underwater blast testing.

Foam	Density (kg/m^3)	Compressive Modulus (MPa)	Manufacturer Compressive Modulus (MPa)	Crushing Strength (MPa)	Manufacturer Compressive Strength (MPa)	Crushing Strain (%)	Plateau Stress (MPa)	Densification Strain (%)	Densification Constant, Q (MPa)	Densification Constant, λ
SAN M100	107.5 [100]	88 ± 5	107 [100]	1.79 ± 0.02	1.55 [100]	1.98 ± 0.06	1.5	39	1.51	9.98
SAN M130	140 [100]	126 ± 12	170 [100]	3.03 ± 0.17	2.31 [100]	2.34 ± 0.33	1.7	34	1.48	9.77
SAN M200	200 [100]	239 ± 43	317 [100]	5.15 ± 0.19	3.8 [100]	2.22 ± 0.01	4.7	38	2.06	9.57
PVC C70.90	100 [101]	88 ± 6	130 [101]	2.01 ± 0.03	2.0 [101]	2.41 ± 1.36	1.9	51	1.46	9.97
PMI 110SL	110 [102]	76 ± 2	88 [102]	2.16 ± 0.01	2.8 [102]	2.19 ± 0.02	2.0	45	1.41	8.93

6.3 Dynamic Compression Using a Split-Hopkinson Pressure Bar

6.3.1 Experimental Methods

The use of foam core sandwich composites in underwater blast scenarios relies upon crushing of the polymeric foam cores to absorb blast energy. In order to understand the extent of energy absorption, and the benefits of using a graded density foam core in underwater blast, SHPB tests were performed on the three SAN foam cores: Corecell M100; Corecell M130; and Corecell M200. The test design and data processing codes were developed by David R Sory and Professor William G proud, in the Royal British Legion Centre for Blast Injury Studies, Imperial College London. The SHPB was designed to test soft tissue subject to blast loading [112], [113] and was adapted for use with polymeric foam for this research. This design included the use of textured polypropylene (PP) pulse shapers to reduce the ramp gradient of initial loading on the specimen, to allow stress equilibrium to be achieved. A schematic of the SHPB test setup is shown in Figure 6.8. The Kulite S/UEP-350-090 semi-conductor strain gauges were situated in pairs, diametrically opposite on the aluminium bars, and the signals from these were amplified and recorded using a high frequency oscilloscope. The oscilloscope also had a transistor-transistor-logic (TTL) output port, which was used to trigger the high speed camera, as described subsequently. The striker bar was accelerated along a barrel using bottled compressed air, and was fired at varying pressure for different strain rate tests. The pulse shaper was developed by David R Sory and Professor William G Proud, and took the shape of a very thin polypropylene disc, containing small dimples, as shown in Figure 6.9. For the majority of tests performed, the transmission bar material was a 12 mm diameter aluminium tube, with an internal diameter of 9.5 mm, and an aluminium end cap press fitted into the tube. All aluminium materials used were 6063T5, and the bars sat in polished steel V shaped sliders, to ensure that the friction on the bars was minimal. Some tests were performed using a solid 12 mm diameter transmission bar with the higher density foams, to try to reduce the inaccuracies caused by wave dispersion. Data processing of the SHPB results used strain readings of the incidence pulse,

the reflected pulse and the transmitted pulse, read from the semi-conductor strain gauges. When both the incident and transmission bars were both solid the governing equations for the strain (ε_s), strain rate ($\dot{\varepsilon_s}$) and stress (σ_s) in the specimen, as outlined by Lifshitz and Leber, are provided by Equation (6.4), Equation (6.5) and Equation (6.6) respectively [73], where C_0 is the wave speed in the aluminium bars; A_A is the cross sectional area of the solid aluminium bars; A_s is the cross sectional area of the test specimen; l_s is the undeformed length of the specimen; ε_i, ε_r and ε_t are the incident, reflected and transmitted strain pulses at the specimen to bar interfaces respectively; and t is time.

In order to check for stress equilibrium in the specimen, the strain pulse at the end of each bar was checked for similarity to satisfy Equation (6.7). If strain equilibrium was achieved as specified by Equation (6.7), then the strain, strain rate and stress equations shown in Equation (6.4), Equation (6.5) and Equation (6.6) respectively were reduced to Equation (6.8), Equation (6.9) and Equation (6.10) respectively [73].

In the cases where a hollow transmission bar was used Equation (6.11) and Equation (6.12) were used to calculate the strain and strain rate in the specimen, where A_t is the cross sectional area of the hollow transmission bar. The same solid incident bar was used in these tests, so A_A was the same as in the cases with a solid transmission bar. The stress in the test specimen was then calculated using Equation (6.13), and stress equilibrium was checked for using (6.14) [70].

The strain measurements were also corrected for wave dispersion in the bars, using the method outlined by Lifshitz and Leber [73]. As the strain measured on the transmission bar was of very low amplitude, due to the low impendence of the foam tested, the strain readings contained a large amount of high frequency noise. A simple low pass moving average filter was applied to this data, to find the average data points across the trace.

$$\varepsilon_s(t) = \frac{C_0}{l_s} \int_0^t (\varepsilon_i - \varepsilon_r - \varepsilon_t) dt \tag{6.4}$$

$$\dot{\varepsilon_s}(t) = \frac{C_0}{l_s} (\varepsilon_i - \varepsilon_r - \varepsilon_t) \tag{6.5}$$

$$\sigma_s(t) = \frac{EA_A}{2A_s}(\varepsilon_i + \varepsilon_r + \varepsilon_t) \tag{6.6}$$

$$\varepsilon_i - \varepsilon_r = \varepsilon_t \tag{6.7}$$

$$\varepsilon_s(t) = -2\frac{C_0}{l_s}\int_0^t \varepsilon_r dt \tag{6.8}$$

$$\dot{\varepsilon_s}(t) = -2\frac{C_0}{l_s}\varepsilon_r \tag{6.9}$$

$$\sigma_s(t) = \frac{EA_A}{A_s}\varepsilon_t \tag{6.10}$$

$$\varepsilon_s(t) = \frac{C_0}{L_s}\left[\left(1 - \frac{A_A}{A_t}\right)\int_0^t \varepsilon_i dt - \left(1 + \frac{A_A}{A_t}\right)\int_0^t \varepsilon_r dt\right] \tag{6.11}$$

$$\dot{\varepsilon_s}(t) = \frac{C_0}{L_s}\left[\left(1 - \frac{A_A}{A_t}\right)\varepsilon_i - \left(1 + \frac{A_A}{A_t}\right)\varepsilon_r\right] \tag{6.12}$$

$$\sigma_s(t) = \frac{EA_t}{A_s}\varepsilon_t \tag{6.13}$$

$$\frac{A_A}{A_t}\left[\varepsilon_i - \varepsilon_r\right] = \varepsilon_t \tag{6.14}$$

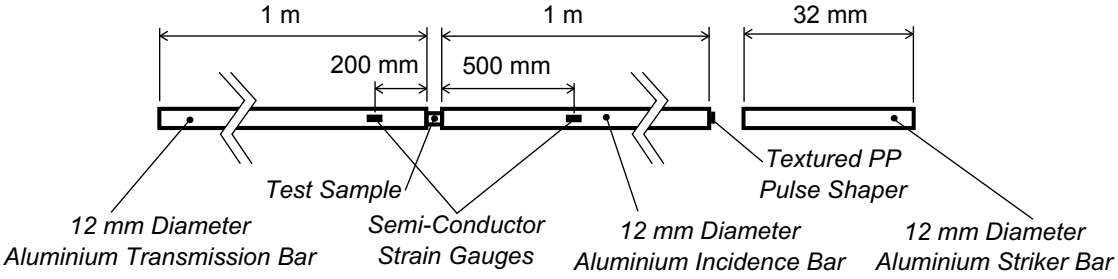


Figure 6.8: Schematic of the split-Hopkison pressure bar setup used to characterise SAN foams in dynamic compression.

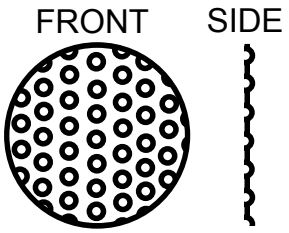


Figure 6.9: Schematic of the pulse shaper used in the SHPB tests. The diameter ranged from 4 mm to 10 mm depending on test parameters.

6.3.1.1 Digital Image Correlation

As stated by Song, Chen and Jiang [70], it is somewhat inaccurate to check for equilibrium in a soft specimen using the difference between the incident and reflected pulses compared to the transmitted pulse, due to the two very high magnitude incidence and reflected pulses, and the very low transmitted pulse. These strain pulse characteristics are caused by the low impendence of the test material. In order to further check for equilibrium, DIC was utilised to assess the strain distribution across the test specimens. A Phantom V12 high speed camera was used for this, with a frame rate of 84,104 s^{-1} and a resolution of 128 x 128 pixels. The results were then processed using the DIC software Aramis, with facet sizes of around 20 pixels and a step size of 1 pixel. This provided around 20 facets across the 6 mm long specimens. The high speed camera was triggered upon arrival of the strain pulse at the strain gauges on the incidence bar. As well as using DIC for checking equilibrium, it was also used to measure the strain during elastic loading, to determine the compressive modulus of the foam at dynamic rates. Due to the difficulties in aligning the high speed camera images with the data from the oscilloscope, the compressive modulus was calculated using Equation (6.1), where t is time, σ is the filtered stress readings; and ε is the strain measured from DIC.

6.3.1.2 Test Parameters

When performing SHPB tests it is important to select the diameter and thickness of the specimen to avoid severe radial and axial inertial effects, and frictional effects at the bar ends [114]. As stated by Chen and Song [114], the low Poisson's ratio of the foams during the cell collapse stage of deformation is close to zero,

meaning that the radial inertia and frictional effects are negligible. Furthermore, a very thin layer of silicon gel was placed between the test sample and bar material to reduce friction, and to also hold the specimen in place before testing. Axial inertial effects were successfully eliminated with the use of a pulse shaper, as the wave speed in the specimen was ramped up to the desired speed before yield of the foam took place, so that yield and cell collapse were at a constant strain rate. As researched by Dioh, Leevers and Williams [115], the thickness of the test sample can result in differing flow stresses, when testing various bulk polymers. Furthermore, due to the cells present in polymeric foams, it is important to test a large enough specimen to be representative of the bulk material. In order to establish a suitable material length, 10 images were taken with a microscope of 40 mm x 40 mm sections of three specimens of each foam, and an example image of each foam is shown in Figure 6.10. It was found that for the M100, M130 and M200 foams, the average cell diameters were 452 $\pm$ 111 μm, 354 $\pm$ 87 μm and 319 $\pm$ 109 μm respectively. The average cell wall thickness values for the three foams were 88 $\pm$ 45 μm, 87 $\pm$ 44 μm and 200 $\pm$ 89 μm respectively. Therefore, for the M100 foam polymer, a complete cell with half of the wall thickness surrounding it was allocated a 696 μm diameter, which is the upper bound of the cell diameter plus the upper bound of the wall thickness. The diameter of the sample chosen was 8 mm, and the length was 6 mm, providing 132 cells in the cross section, and 8 cells along the length of the sample, so 1,056 cells per sample. This does not account for partial cells at the boundaries, but assumes that all cell diameters and wall thicknesses are at the upper bound of the standard deviation. The samples were manufactured manually on a lathe. This was deemed sufficient to determine bulk material properties from the tests, as around 10 tests at each speed for each foam were performed.

In order to assess the effects of sample length on measured yield strength, M200 samples were also tested at 2 mm, 3 mm, 4 mm and 5 mm lengths. Striker bar pressures were set to test the foam specimens at approximately the following strain rates: 850 s^{-1}; 1,400 s^{-1}; 1,800 s^{-1}; 2,100 s^{-1}; 2,400 s^{-1}; and 2,700 s^{-1}.

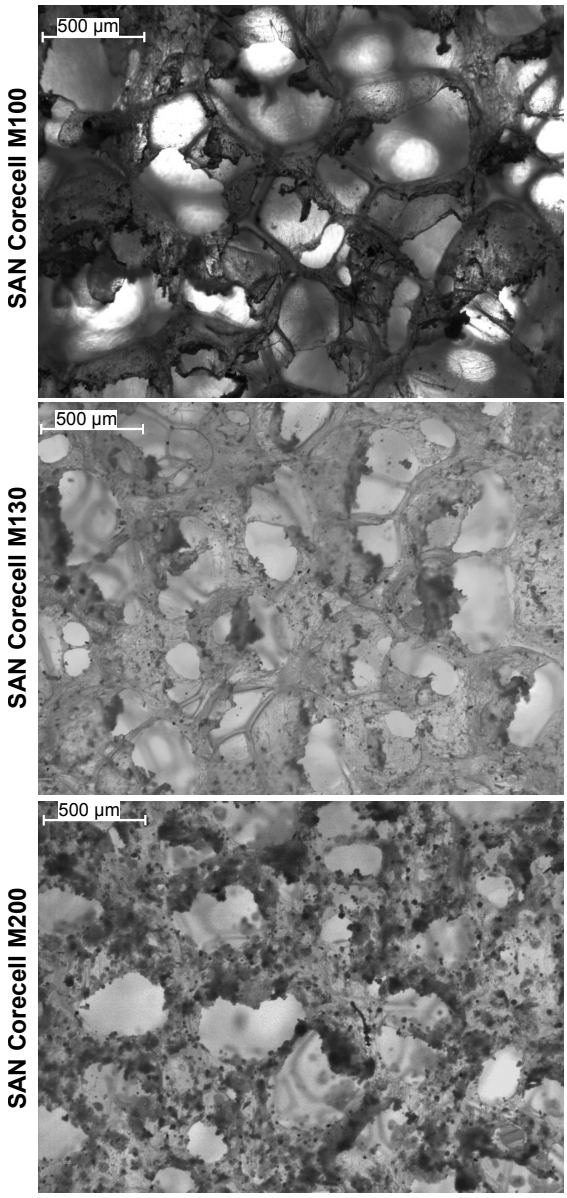


Figure 6.10: Images of the cell structure of the three foams tested using a SHPB. The images were captured using a microscope and show the SAN M100 foam structure in the top image; the SAN M130 foam structure in the middle image; and the SAN M200 foam structure in the bottom image.

6.3.2 Results

6.3.2.1 Raw Data

Raw voltage readings from the gauges on the incidence and transmission bar are shown in Figure 6.11. It can be seen from this plot that the strain on the specimen in the first pulse ramps up to a near plateau over the elastic section of the transmission bar reading. The equation for calculating the wave speed in the foam specimen material (C_s) is provided in Equation (6.15), where E_s is the elastic modulus of the specimen and ρ_s is the bulk density of the specimen. This equation is only an estimate, as wave travel through foam materials is complex due to the cell walls and cells of gas, but the method has been deemed suitable as an approximation by Gibson and Ashby [116]. Using the foam material properties provided in Chapter 3, it was found that wave speeds in the M100, M130 and M200 were approximately 1,002 m/s; 1,112 m/s; and 1,276 m/s respectively. Therefore, with a 6 mm length specimen used in the test shown in Figure 6.11, one elastic wave travelled across the specimen in 0.006 ms, meaning that 10 waves propagated in the ramp section of the loading. In research presented by Song and Chen [70], this was deemed a suitable number of oscillations for stress equilibrium to be achieved. The pulse shaper diameter was selected for each test parameter for each strain rate, to ensure at least six stress wave oscillations were achieved, indicating stress equilibrium in the test specimen.

$$C_s = \sqrt{\frac{E_s}{\rho_s}} \tag{6.15}$$

The governing equations for the SHPB tests are shown in Equation (6.4), Equation (6.5), and Equation (6.6) to calculate strain, strain rate and stress respectively. If stress equilibrium is satisfied (Equation (6.7)), then the strain, strain rate and stress terms reduce to Equation (6.8), Equation (6.9) and Equation (6.10) respectively. Therefore, the stress results obtained for the tests required the removal of high frequency noise, as they were calculated from the transmitted strain signal. The noisiest of the tests were in the M100 cases, as these samples transmitted the least energy to the transmission bar. An example of the engineering stress measured during a M100 test at 1430 s^{-1} is shown in Figure 6.12, and shown in

red is the filtered signal, with a moving average applied using MATLAB, with a span of 100 data points.

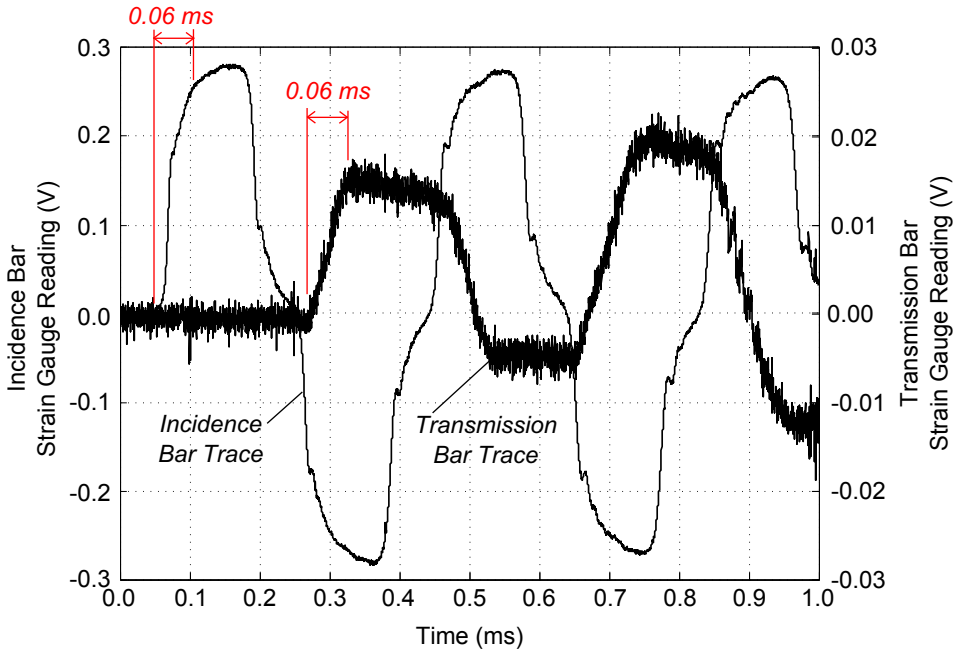


Figure 6.11: Raw Data of an M100 SHPB test at 1,430 s^{-1}.

6.3.2.2 Strain Equilibrium

Strain equilibrium in the test sample was initially measured using the traditional SHPB method, provided in Equation (6.7). As stated previously, this method is unreliable for soft materials, due to low transmitted strain pulses, so DIC was also used to check the distribution of strain across the specimen surface. An example of the DIC used to check strain equilibrium is shown in Figure 6.13, with the DIC contour plot of axial strain in the frame immediately before crushing shown. As can be seen from Figure 6.13 cell collapse began at various locations throughout the specimen and not at the incident bar, indicating stress equilibrium in the specimen. This was checked in every case, to ensure that the specimen was in stress equilibrium upon crushing.

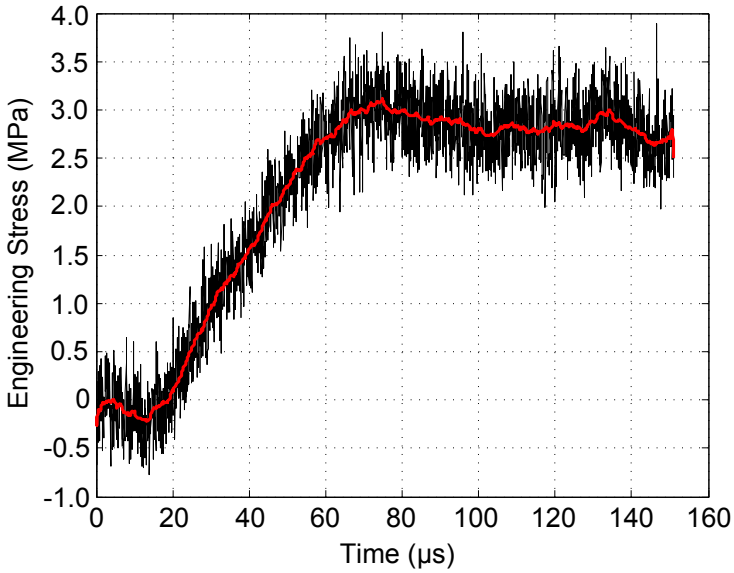


Figure 6.12: Test results of an M100 SHPB test at 1,430 s^{-1}, with a low pass moving average filter applied, using a 100 data point span.

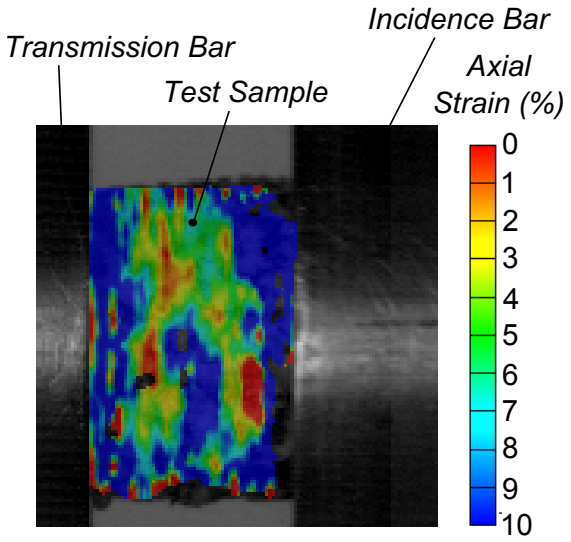


Figure 6.13: Equilibrium of an M130 sample tested at 2,710 s^{-1}, showing the DIC maximum principal strain contour plot in the frame immediately before crushing.

6.3.2.3 Compressive Modulus

The compressive modulus of foam is stated in the literature to be rate insensitive [116], as the ratio of bulk compressive modulus of the foam (E^*) to compressive modulus of the polymer from which the foam is produced (E_s), is given by Equation (6.16), where ϕ is the volume fraction of the foam material; ρ is density; ν is Poisson's ratio; and the superscript "*" and subscript "s" refer to the bulk material and polymer respectively. As also stated in Gibson and Ashby [116], the elastic modulus of common polymers shows negligible rate sensitivity, and by inspection of Equation (6.16) it can be seen that the modulus of the foam is also expected to be rate insensitive. The results of the M100 SAN foam compressive modulus with varying strain rates are shown in Figure 6.14, and from this graph it can be seen that there is no variation over the 2,000 s^{-1} range. However, the quasi-static compressive moduli presented in the previous section were 88 ± 5 MPa; 126 ± 12 MPa; and 239 ± 43 MPa for the M100, M130 and M200 foams respectively. The average moduli shown in Figure 6.14 are 63.7 ± 8.9 MPa; 107.4 ± 12.5 MPa; and 239.3 ± 40.5 MPa for the M100, M130 and M200 foams respectively. There was a small amount of discrepancy in modulus and this could be due to various factors, such as bedding in of the specimen at the start of loading, as witnessed in the quasi-static tests, or could have been caused by poorly manufactured specimens. The error present in the DIC data could also be the cause of the discrepancy as only between five and 10 frames were captured during the elastic part of the loading of the specimen. Finally, the most likely cause of the difference in measured moduli is due to size effects, as the length of the specimen has been shown to have significant effects on the measured properties of specimens in SHPB tests [115]. The compressive moduli of M200 foam samples made to thicknesses of 4 mm, 5 mm and 6 mm are shown in Figure 6.15. It can be seen that the compressive moduli of the 4 mm and 5 mm samples are fairly consistent, but that there is a clear increase in modulus in the 6 mm samples. An attempt was made to try to further investigate the hypothesis that by increasing the specimen length further the quasi-static compressive modulus would be reached, but it was discovered that stress equilibrium could not be achieved with the SHPB setup for lengths beyond

6 mm.

$$\frac{E^*}{E_s} = \phi^2 \left(\frac{\rho^*}{\rho_s}\right)^2 + (1-\phi)\frac{\rho^*}{\rho_s} + \frac{\rho_0(1-2\nu^*)}{E_s(1-\frac{\rho^*}{\rho_s})} \tag{6.16}$$

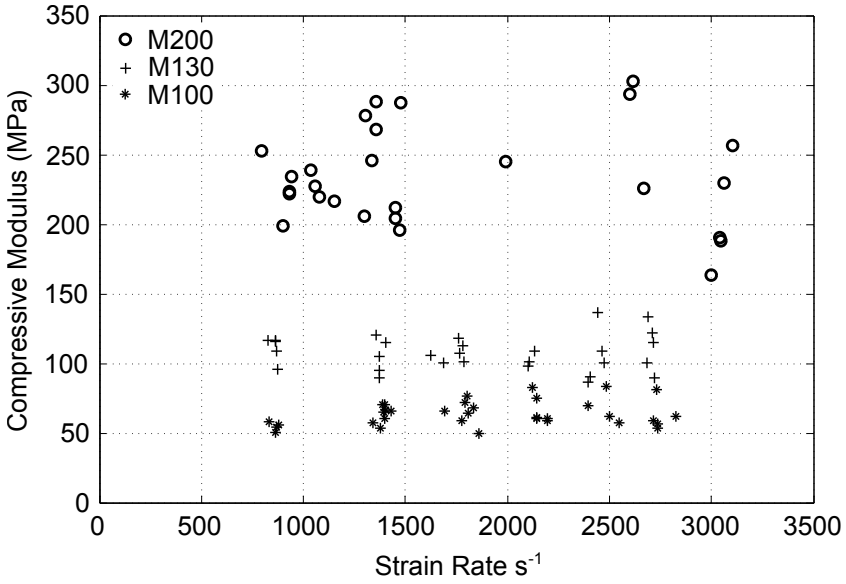


Figure 6.14: Compressive modulus versus strain rate of the SAN M200; M130; and M100 foam samples.

6.3.2.4 Crushing Strength

The strength of closed cell polymeric foams was predicted by Gibson and Ashby [116] by Equation (6.17), where σ is stress; Rc and $\dot{\varepsilon_0}$ are material constants; T_g is the glass transition temperature of the polymer; $\dot{\varepsilon}$ is the strain rate; Tm is temperature; and superscript "0" and subscript "*pl*" refer to quasi-static and crushing stress respectively. The crushing strengths of the M100, M130 and M200 foam samples are shown in Figure 6.16. There appears to be no increase in strength with strain rate for the M100 samples, and the M130 samples show a very slight increase which becomes insignificant compared to the spread of the data. The M200 data, however, show a more defined increase of crushing strength with strain rate. In order to determine any rate sensitivity information for the polymeric foams intermediate rates are required, which were not performed in this research. A

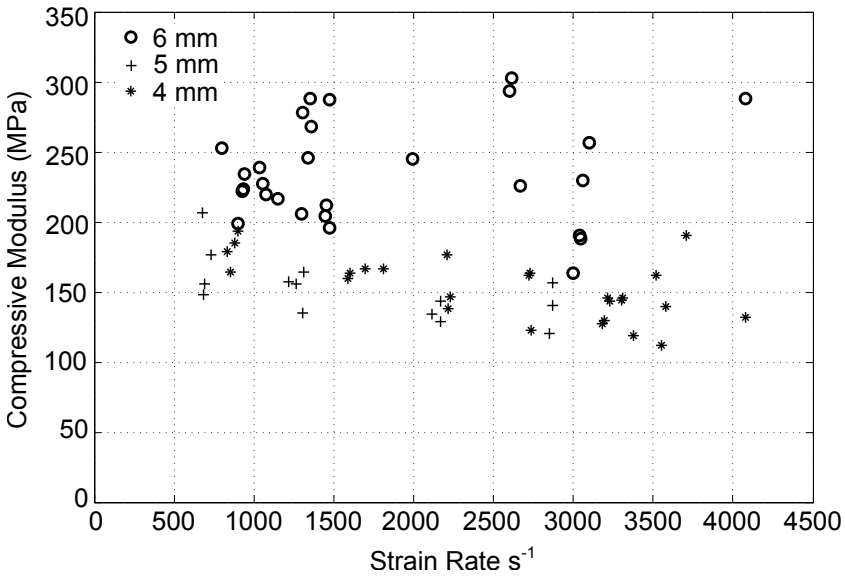


Figure 6.15: Compressive modulus versus strain rate of 4 mm, 5 mm and 6 mm thick SAN M200 foam samples.

sharp increase in strength with strain rate is expected for lower intermediate rates, reaching a plateau equal to the strength recorded in Figure 6.16. As with the compressive moduli data, the crushing strength has been plotted against the thickness of the SAN M200 test samples in Figure 6.17. In this case, there was no correlation between thickness and strength, unlike in the case of compressive modulus where increasing the thickness increased the modulus. The average crushing strengths for the M100, M130 and M200 foams were 3.4 ± 0.3 MPa; 5.5 ± 0.4 MPa and 10.8 ± 1.1 MPa respectively.

$$\sigma^*_{pl} = \left(\sigma^*_{pl}\right)^0 \left(1 - \frac{RcTm}{T_g} ln \frac{\dot{\varepsilon}_0}{\dot{\varepsilon}}\right) \tag{6.17}$$

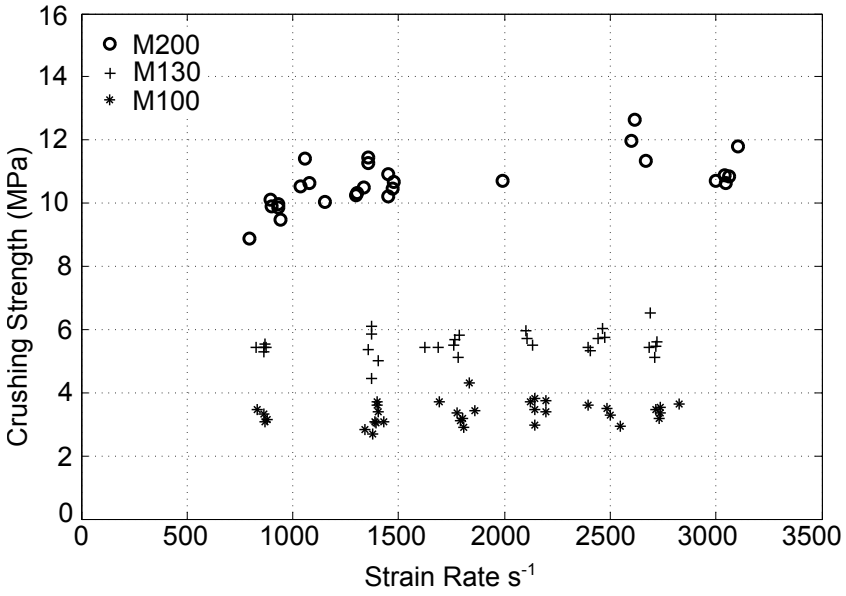


Figure 6.16: Crushing strength versus strain rate of the SAN M200; M130; and M100 foam samples.

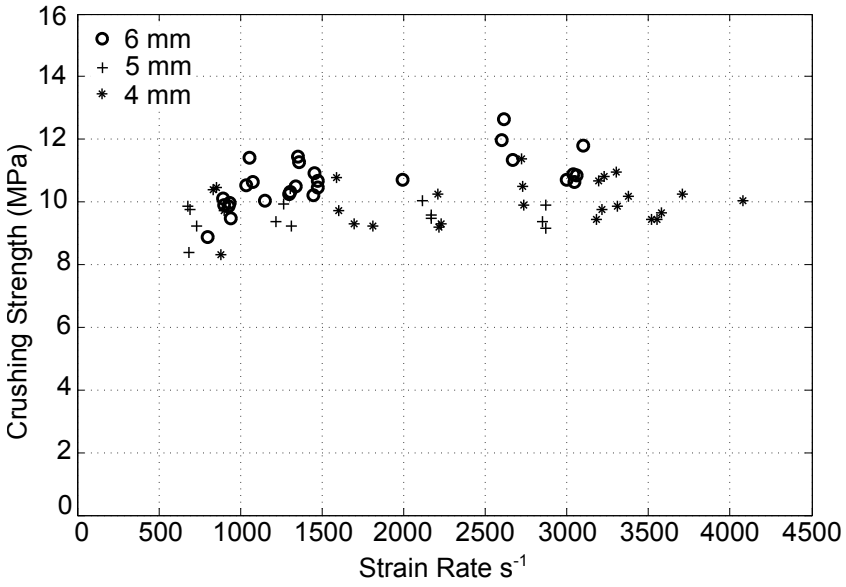


Figure 6.17: Crushing strength versus strain rate of 4 mm, 5 mm and 6 mm thick SAN M200 foam samples.

6.4 Quasi-Static Tension

6.4.1 Experimental Methods

As with the quasi-static compression data, quasi-static tension data is provided by the foam manufacturers, but it was decided to perform tests in this research to validate manufacturer data and to determine the full stress versus strain response of the materials. The testing was performed by cutting the foam into dog bone samples, with gauge sections of 10 mm wide by 6 mm thick, and 65 mm long. The specimens were cut using a router, with the foam specimen clamped to a guide to produce the same shape every time. A diagram of the foam dog bone samples is provided in Figure 6.18. The strain in these tests used DIC for the duration, as slip at the grips rendered the machine displacement unusable. The foams were initially tested using the ASTM C297/C297M standard [117], but it was found that a significant proportion of the tests failed at the adhered grips. It was found that using standard test grips on a 150 kN Instron 5984 universal testing machine caused failure in the gauge length every time, so this setup was used instead. An auxiliary 5 kN load cell was placed in the machine during testing, to reduce the errors in the results. As with the quasi-static compression tests, DIC images were captured with a Canon 350D SLR camera with the external "TriggerTrap" trigger, every 5 seconds. The elastic modulus was calculated using the gradient method outlined in Equation (6.1), to avoid issues with alignment of the frames with the load data. The strain to failure of the specimen was measured using the final photograph captured before the specimen fractured. The tests were performed at 1 mm/min, which equated to a strain rate of 0.015 s^{-1} and five specimens of each foam were tested.

6.4.2 Results

6.4.2.1 SAN Foam

The quasi-static tension results of the SAN M100 foam material are shown in Figure 6.19, and a summary of the mechanical properties are shown in Table 6.2. As with the quasi-static compression tests the importance of performing independent

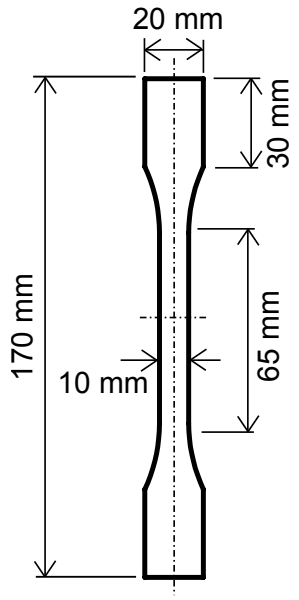


Figure 6.18: Dimensions of the quasi-static tension foam dog bone test specimens.

mechanical tests on the foams are important, as the measured values do not correspond well with the manufacturer data. The values in this table are averages of all five specimens, but as can be seen from Figure 6.19 there is a lot of spread in the fracture strain. The fracture stress, however, is at a plateau, so the stress versus strain response can be simplified to a linear elastic increase of stress to 2.8 ± 0.1 MPa, and then it remains at this stress with increasing strain until at least 5.5% where it breaks at some point. The elastic modulus of the SAN M100 foam, as measured using DIC and load cell data, was 88 ± 6 MPa.

The responses of the M130 and M200 SAN foams are shown in Figure 6.20 and Figure 6.21 respectively, and the mechanical properties are summarised in Table 6.2. As with the M100 foam, the M130 and M200 can be assumed linear elastic until a plateau stress of 3.8 ± 0.1 MPa and 5.7 ± 0.2 MPa respectively, and then they break at a strain of at least 6% and 5% respectively.

6.4.2.2 PVC Foam

Figure 6.22 shows the quasi-static tensile test results for the five PVC C70.90 tensile test specimens and the results are summarised in Table 6.2. This foam material showed much less of a plateau than the SAN foams, and failure occurred

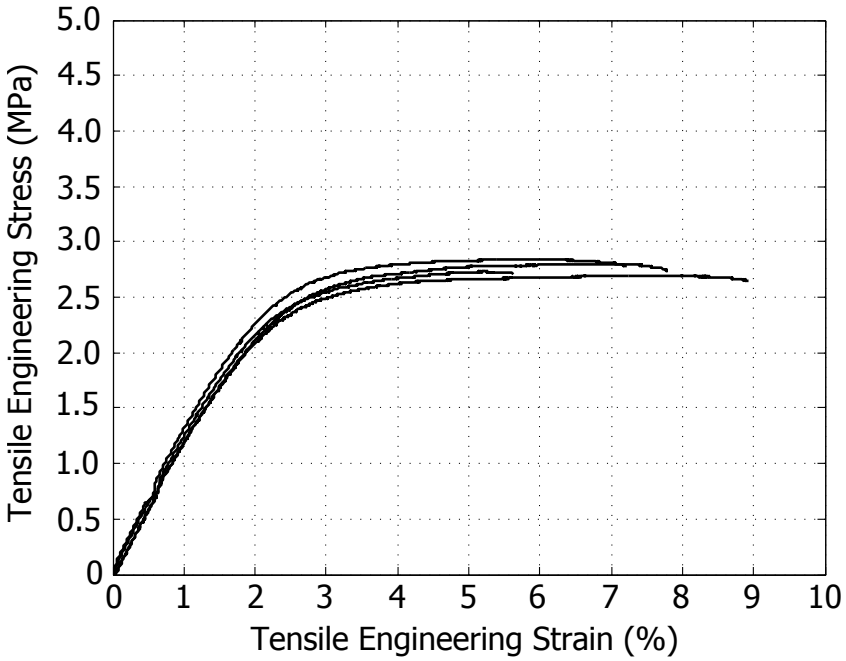


Figure 6.19: Quasi-static tension results of the SAN M100 foam.

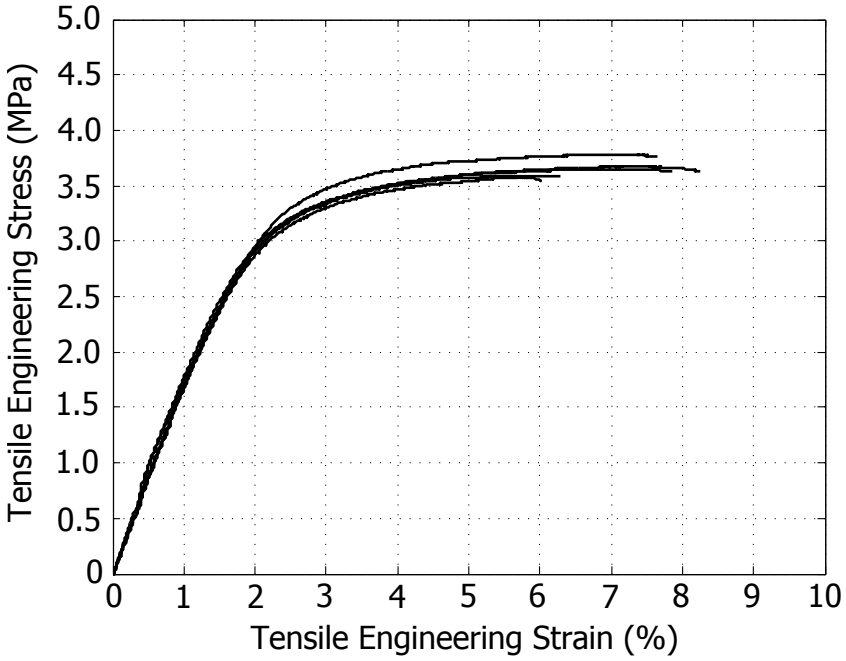


Figure 6.20: Quasi-static tension results of the SAN M130 foam.

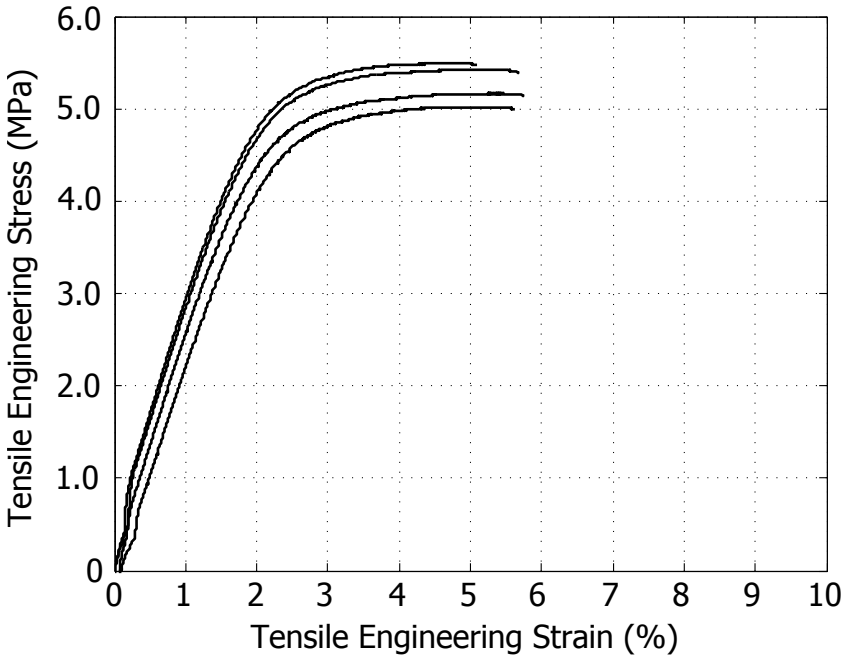


Figure 6.21: Quasi-static tension results of the SAN M200 foam.

at a minimum of 7%. The strain to failure was again very spread out, but the failure stress was consistent in every case.

6.4.2.3 PMI Foam

The response of the five PMI 110 SL foam specimens in tension are shown in Figure 6.23, and the mechanical properties are summarised in Table 6.2. The PMI samples showed much less plastic behaviour than the PVC and SAN foams, with the lowest fracture strain being at 4.7%. As with the PVC foam, the PMI foam did not show a plateau stress. However, the failure stress was fairly consistent across the specimens. An example PMI 110SL tensile test specimen is shown in Figure 6.24 with the DIC strain overlaid. The average DIC strain is shown above each photograph, where 2.0% is in the yielding zone and 6.2% is near to fracture. It can be seen that high strain bands form across the specimen when close to fracture, due to cells undergoing high strain. Fracture takes place when the cell walls in one of these high strain bands fractures and this was witnessed in all of the foam materials tested in quasi-static tension.

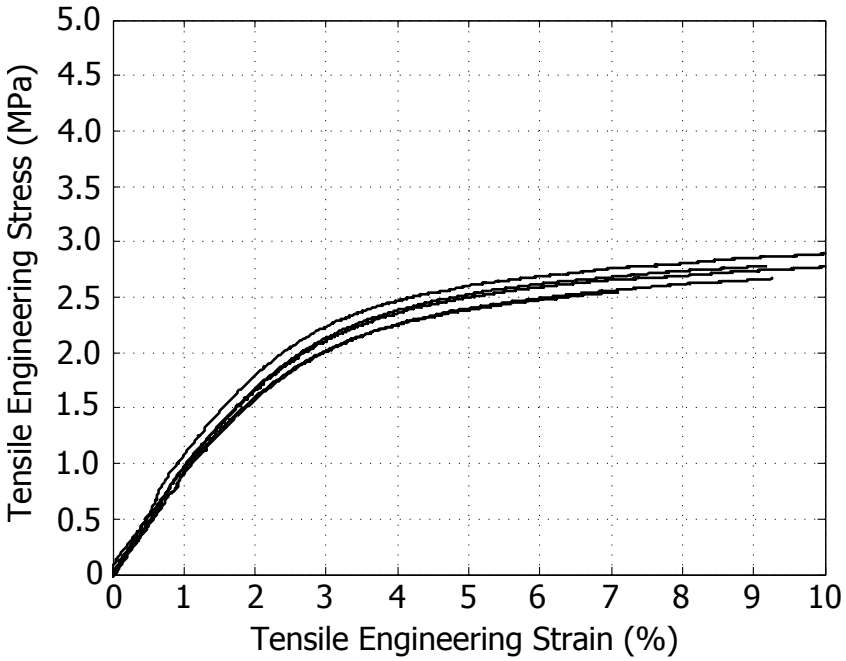


Figure 6.22: Quasi-static tension results of the PVC C70.90 foam.

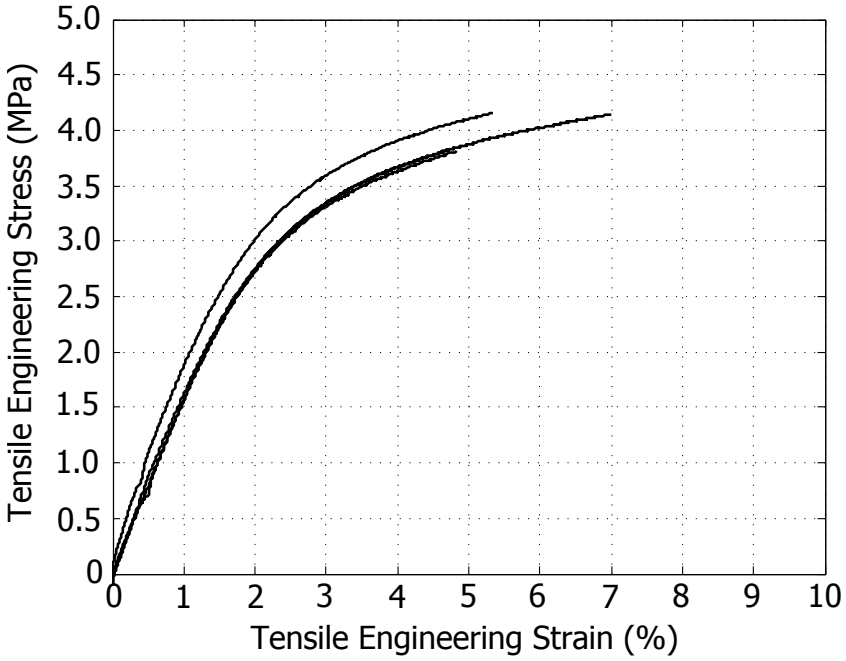


Figure 6.23: Quasi-static tension results of the PMI 110 SL foam.

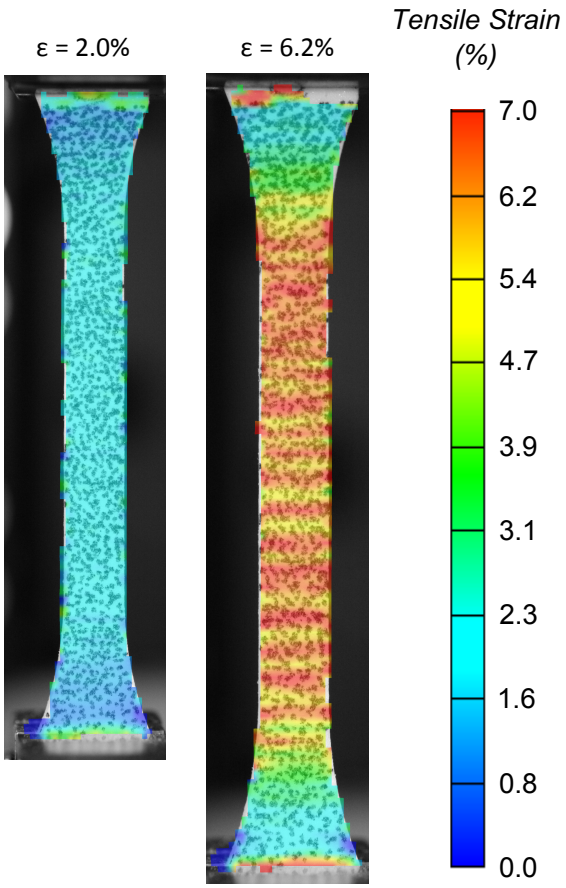


Figure 6.24: DIC contour plots of the quasi-static tensile strain in a PMI 110 SL foam sample. The average DIC strain in each image is shown at the top, where the 2.0% image was captured during the yielding of the material, and the 6.2% image was captured near to fracture.

Table 6.2: Summary of the quasi-static tensile properties of the five foam polymers used in air and underwater blast testing.

Foam	Density (kg/m^3)	Tensile Modulus (MPa)	Manufacturer Tensile Modulus (MPa)	Yield Stress (MPa)	Manufacturer Tensile Strength (MPa)	Yield Strain (%)	Fracture Stress (MPa)	Fracture Strain (%)
SAN M100	107.5 [100]	88 ± 6	109 [100]	2.4 ± 0.1	2.11 [100]	2.4 ± 0.1	2.8 ± 0.1	7.7 ± 1.5
SAN M130	140 [100]	133 ± 2	176 [100]	3.2 ± 0.1	2.85 [100]	2.2 ± 0.1	3.8 ± 0.1	7.2 ± 0.9
SAN M200	200 [100]	220 ± 15	334 [100]	4.9 ± 0.1	4.29 [100]	2.0 ± 0.1	5.7 ± 0.2	5.6 ± 0.3
PVC C70.90	100 [101]	71 ± 2	84 [101]	2.0 ± 0.1	2.7 [101]	2.6 ± 0.1	2.8 ± 0.1	9.3 ± 1.4
PMI 110SL	110 [102]	139 ± 4	202 [102]	2.7 ± 0.1	6.6 [102]	1.8 ± 0.1	4.1 ± 0.2	5.6 ± 0.9

6.4.3 Dynamic Tension

6.4.3.1 Experimental Methods

The final set of foam characterisation tests to be presented are from high speed tension tests. The tests were performed using a servo-hydraulic Instron VHS 8800 test machine capable of 400 mm of actuator travel, at 20 m/s, and a load of 15 kN. A 5 kN PCB 221B04 dynamic load cell was placed in the load train, between the test sample and the stationary machine bed. In order to achieve the desired test speed a lost motion device was attached to the top of the test specimen, allowing the actuator to reach the test velocity before catching the lost motion device and loading the specimen. Thin rubber washers were placed between the actuator and the flange of the lost motion device to dampen the impact, and allow the test specimen to be in equilibrium for the test. The test setup and sample dimensions are shown in Figure 6.25 and Figure 6.26 respectively.

Due to slippage at the grips during the dynamic tension tests, the strain was measured using a Miro 310 high speed camera, with a resolution of 192 x 304 pixels, and a frame rate of 41,000 s^{-1}. The samples were tested at actuator speeds of 5 m/s and 10 m/s, which correlated to strain rates of 180 s^{-1} and 365 s^{-1}, as measured with DIC. As with the quasi-static tests, the elastic modulus was measured using the gradient method outlined in Equation (6.1), using the strain measured from DIC and the stress calculated from the load cell. The load data was captured using an oscilloscope with a sampling frequency of 500 kHz and at least six specimens of each foam were tested. The data selected for use was from six samples, whose standard deviations were less than 10% of the average result, and this applied to the test rate measured from DIC, the elastic modulus, the fracture stress and the fracture strain.

6.4.4 Results

6.4.4.1 SAN Foam

The dynamic stress versus strain results of the SAN M100 foam are shown in Figure 6.27, where the data shown in Figure 6.27a is for the foam tested at 180 s^{-1}, and the data shown in Figure 6.27b is for the foam tested at 365 s^{-1}. It can be seen

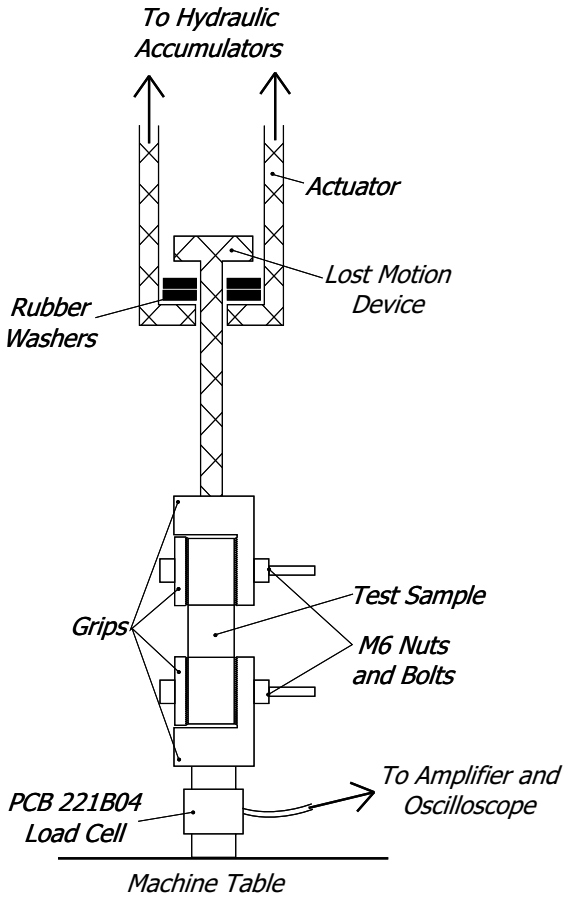


Figure 6.25: Schematic of the dynamic tension test setup.

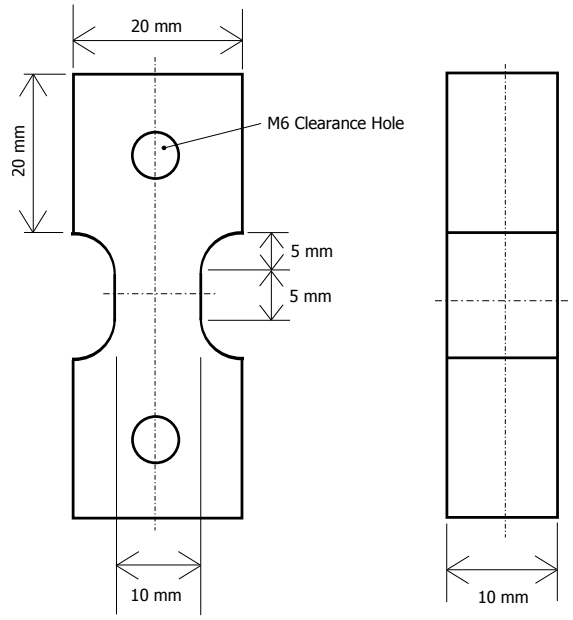


Figure 6.26: Dimensions of the dynamic tension test samples.

that in both cases the foam failed at around 6 MPa, and that the strain to failure was decreased by an increase in strain rate. From the previous section it can be seen that when tested under quasi-static conditions the foam failed at an average strain of 7.7%, so it is clear that this value reduces as the strain rate is increased. The strain to failure is of high importance in sandwich panel applications, as the stiffness of the face-sheets deems the foam stiffness insignificant, so until failure it merely acts to transmit shear load. The results of the SAN M130 foam samples are shown in Figure 6.28, with Figure 6.28a and Figure 6.28b showing results for 180 s^{-1} and 365 s^{-1} respectively. Similar results are observed here, where the strain to failure reduced with increased strain rate, as is also shown from the quasi-static results displayed in Table 6.2. The final set of SAN foam data is for the M200 samples, the results of which are shown in Figure 6.29, with the 180 s^{-1} and 365 s^{-1} strain rate data shown in Figure 6.29a and Figure 6.29b respectively. As in the M100 and M130 cases, the strain to failure was reduced with increasing strain rates. In all of the SAN results presented it is noticeable that the modulus varies significantly, and this was expected to be due to the low number of images captured during the elastic part of deformation. The total number of images

captured with the high speed camera varied between three for the lowest strain to failure at the higher strain rate, to 11 images with the greater failure strains tested at the lower strain rate. As a linear gradient with time was fitted to the DIC and load data, for use with Equation (6.1), this incorporated high errors into the results due to nonlinear loading initially caused by the rubber dampers in the lost motion device. These high errors are visible in the large standard deviations shown in Table 6.3 for the compressive modulus values. Equation (6.1) was used for calculating the modulus to remove uncertainty due to poor synchronisation of the DIC strain data and the stress calculated from the load cell reading. The failure strain was measured from the frame immediately before fracture was visible in the photographs, and the failure stress was calculated from a stress versus time plot, as the failure point was captured clearly. The results of the SAN foams tested in dynamic tension are summarised in Table 6.3.

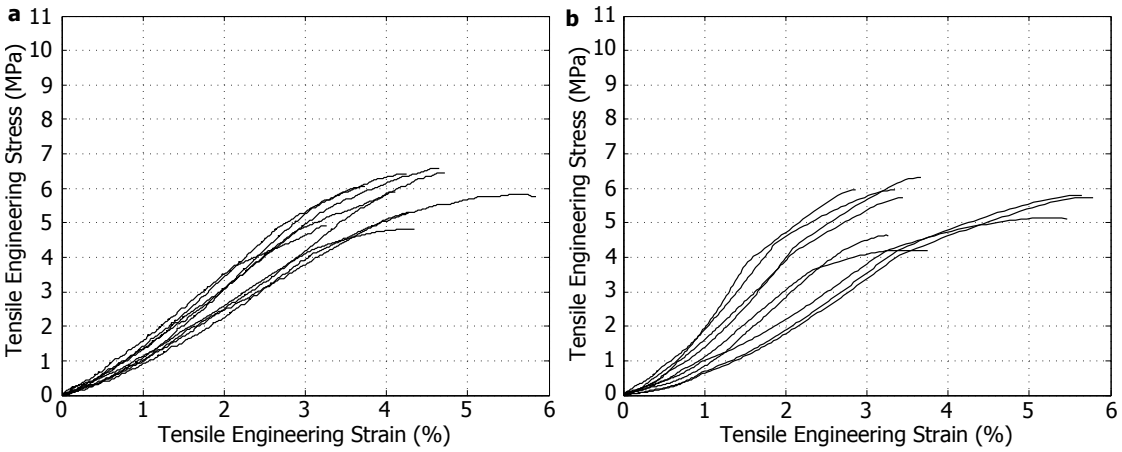


Figure 6.27: Tensile stress versus strain curves for the SAN M100 foam, tested at a) 180 s^{-1} and b) 365 s^{-1}.

6.4.4.2 PVC Foam

Figure 6.30 shows the dynamic stress versus strain results for the PVC C70.90 foam specimens, with the 180 s^{-1} and 365 s^{-1} strain rate data shown in Figure 6.30a and Figure 6.30b respectively. In this case, the strain to failure did not reduce between the two high speed test rates, but was significantly reduced from the quasi-static results shown in Table 6.2. Another noticeable aspect of this data is

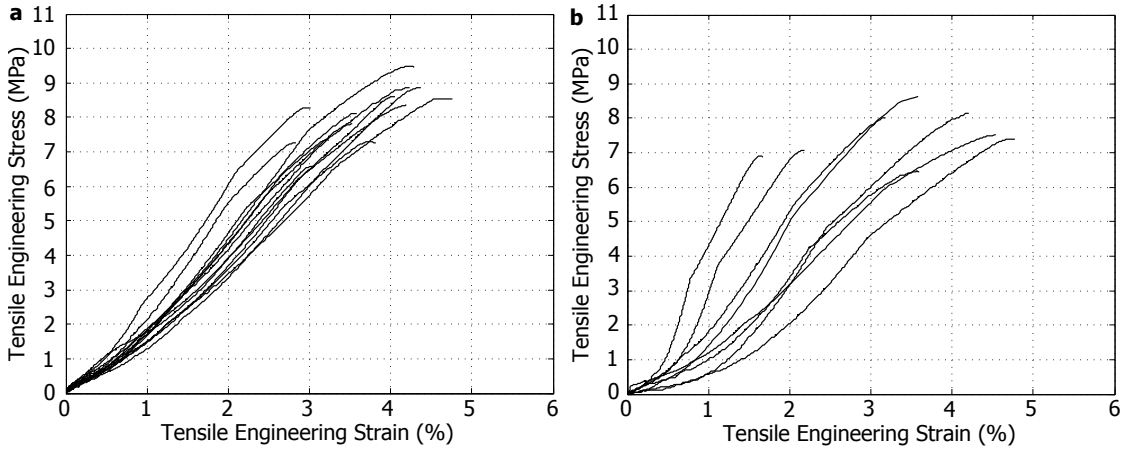


Figure 6.28: Tensile stress versus strain curves for the SAN M130 foam, tested at a) 180 s^{-1} and b) 365 s^{-1}.

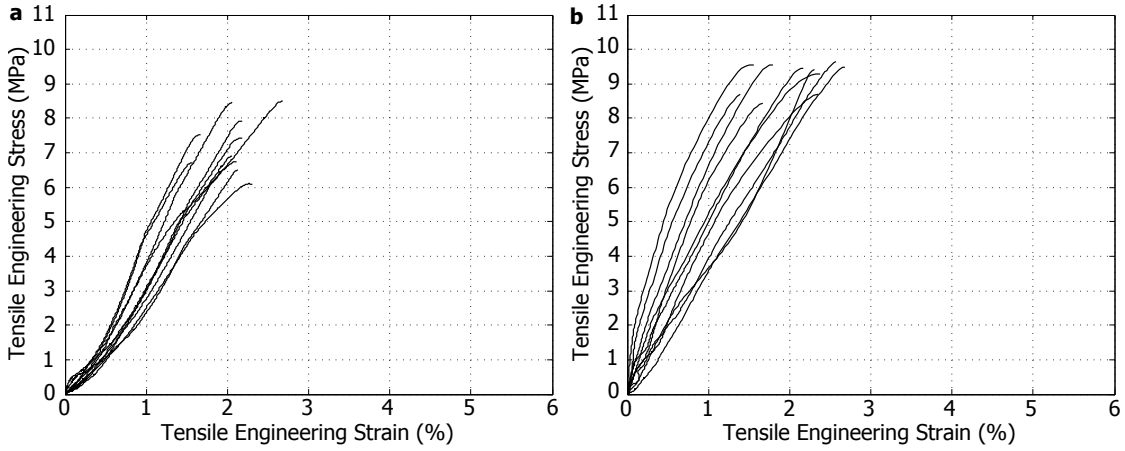


Figure 6.29: Tensile stress versus strain curves for the SAN M200 foam, tested at a) 180 s^{-1} and b) 365 s^{-1}.

that the moduli were much more closely matched, due to a higher frame rate on the high speed cameras, at the expense of resolution. This meant that there were fewer DIC measurement points across the sample, but there were still enough for average strain computations to be performed. Table 6.3 provides the summarised data obtained from the PVC high speed tension tests.

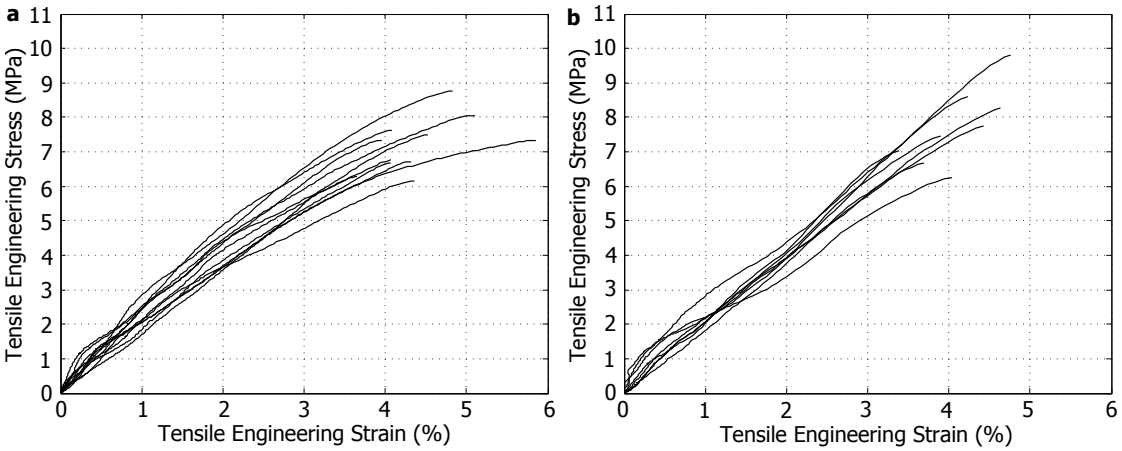


Figure 6.30: Tensile stress versus strain curves for the PVC C70.90 foam, tested at a) 180 s^{-1} and b) 365 s^{-1}.

6.4.4.3 PMI Foam

The final foam polymer to be tested in high speed tension was the PMI 110SL, the results of which are shown in Figure 6.31. Figure 6.31a shows the results for the 180 s^{-1} data, and Figure 6.31b for the 365 s^{-1} data. As with the PVC case, there was no visible reduction in strain to failure between the two test speeds, but a large reduction from the quasi-static tests. An example of the DIC contour plots for a PMI 110SL foam tensile sample, tested at 180 s^{-1}, is shown in Figure 6.32 and a build up of large strain is shown across the centre where fracture took place. Also visible is the large strain at the test grips, which highlights the importance of using DIC in the gauge section to establish the strain in the specimen. The average DIC strain in the specimen gauge section is shown above each image and the 1% strain is roughly halfway along the linear elastic loading, and the 2.3% image is immediately before fracture took place. All of the foams fractured fully within one frame of the high speed camera, so the frame immediately before fracture was

used to determine the fracture strain. There are only four data sets in the high speed tests presented here, due to the foam being much more brittle than the SAN and PVC foams, so failing at the tests grips much more frequently. The results of these tests are summarised in Table 6.3.

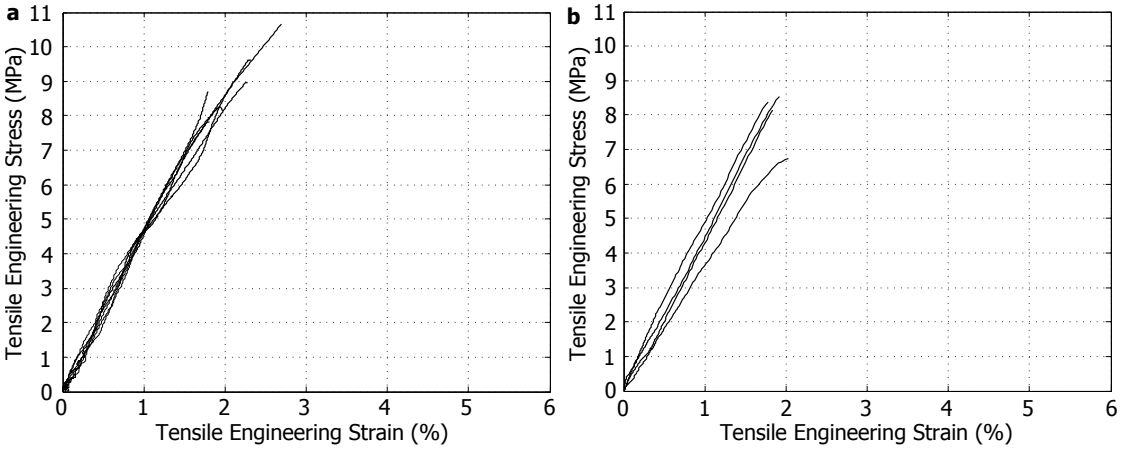


Figure 6.31: Tensile stress versus strain curves for the PMI 110SL foam, tested at a) 180 s^{-1} and b) 365 s^{-1}.

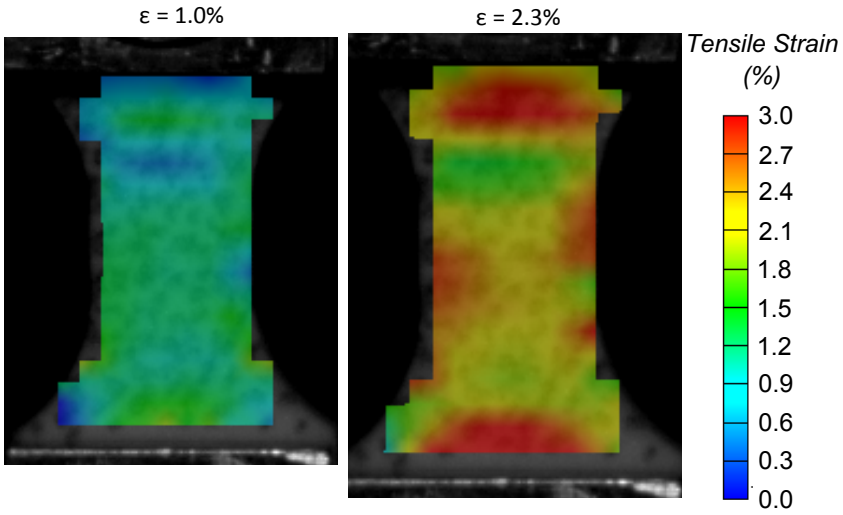


Figure 6.32: DIC contour plots of the 180 s^{-1} tensile strain in a PMI 110 SL foam sample. The average DIC strain in each image is shown at the top, where the 2.3% image was captured immediately before fracture.

Table 6.3: Summary of the dynamic tensile properties of the five foam polymers used in air and underwater blast testing. The dynamic tensile tests were performed at strain rates of 180 s^{-1} and 365 s^{-1}.

Foam	Density (kg/m^3)	Tensile Modulus at 180 s^{-1} (MPa)	Tensile Modulus at 365 s^{-1} (MPa)	Fracture Stress at 180 s^{-1} (MPa)	Fracture Stress at 365 s^{-1} (MPa)	Fracture Strain at 180 s^{-1} (%)	Fracture Strain at 365 s^{-1} (%)
SAN M100	107.5 [100]	162 ± 15	206 ± 53	5.7 ± 0.7	5.5 ± 0.7	4.5 ± 0.8	4.1 ± 1.1
SAN M130	140 [100]	267 ± 31	321 ± 101	8.1 ± 0.8	7.5 ± 0.7	3.8 ± 0.6	3.5 ± 1.1
SAN M200	200 [100]	436 ± 80	482 ± 97	7.3 ± 0.8	9.2 ± 0.4	2.0 ± 0.3	2.1 ± 0.4
PVC C70.90	100 [101]	164 ± 20	197 ± 20	7.2 ± 0.8	7.7 ± 1.1	4.4 ± 0.6	4.1 ± 0.5
PMI 110SL	110 [102]	417 ± 36	434 ± 50	8.7 ± 1.3	7.9 ± 0.8	2.2 ± 0.3	1.9 ± 0.1

6.5 Discussion

6.5.1 Quasi-Static Properties

The material properties provided for foam polymers by the manufacturers generally consist of elastic modulus and failure stress, but for this research the full stress versus strain curve was required. Also it was deemed as good practice to independently test the foam materials, and this was justified by the poor agreement witnessed between test data and manufacturer data. In this research the quasi-static material properties acted as a comparison for the dynamic properties, to understand how strain rate affects their performance. The full stress versus strain curves of the foams are also useful for future research, where analytical and numerical models of the sandwich constructions will be developed.

The quasi-static compressive properties were as expected, showing a linear elastic increase as the material was compressed elastically, followed by a plateau of stress with increasing strain as the cells began to buckle, followed by an exponential increase as the layers of foam polymer were compressed. The final stage of this was only approximated as exponential due to the complexities of the polymer layers contacting and the gas being displaced out of the foam, and if loading were continued a curve similar to the response of the virgin polymer would be witnessed. The full response of the foams in quasi-static compression were used to predict the full response in dynamic compression, by assuming the exponential increase began at the same strain. Therefore, using the plateau stress from the SHPB tests, the full dynamic response could be ascertained. The quasi-static compression tests were performed in the through-thickness direction of the foam sheets, to make use of the very flat surfaces produced by the foam manufacturing process. The foam was expected to be anisotropic in behaviour, but the material properties of interest were in the through-thickness direction, due to core crushing during underwater blast loading.

The behaviour of the three foam polymers in quasi-static tension was quite varied, with all of them exhibiting different amounts of plastic deformation before fracture. The SAN foams showed a linear elastic response, followed by a plateau up until fracture at 7.7 $\pm$ 1.5% strain. The PVC foam showed a gentle upward

slope before fracturing at 9.3 ± 1.4%. Finally, the PMI foam showed almost linear elastic behaviour up until fracture at 5.6 ± 0.9%. The lower strain to failure of the PMI foam is in line with the onset of damage witnessed during air blast, but the quasi-static tensile data would imply that the PVC foam would outperform the SAN foam, which was not the case. This finding illustrates the importance of testing the materials at higher strain rates, in order to explain the slightly better performance of the SAN foam to the PVC foam cores in air blast, and to characterise the materials for simulation purposes. The quasi-static tension tests were performed in-plane in the foam sheets, due to the low thicknesses available. This was acceptable as any tensile fracture of the foams in the sandwich panels would take place in bending, and thus in the in-plane direction.

6.5.2 Split-Hopkinson Pressure Bar

SHPB testing allowed strain rates up to 3,000 s^{-1} to be achieved, to allow the responses of the SAN foams to underwater explosive scenarios to be understood further. This strain rate is still much lower than that observed during the crushing phase of an underwater blast test, however. SHPB testing of low modulus materials such as foam is a challenging area of research and an area which has been the subject of a lot of studies. A textured PP pulse shaper was used to achieve stress equilibrium in the tests, and a hollow aluminium transmission bar, with semi-conductor strain gauges, was used to measure the response of the material. This set up still provided noisy data, which was then filtered using MATLAB, and it was also necessary to check for strain equilibrium using DIC, due to the low amplitude of the transmitted signal. Therefore the results presented in this thesis further the understanding of the foam materials as well as the understanding of testing them using a SHPB.

The compressive moduli of the SAN foams in dynamic compression showed no rate dependence, but did show a dependence on sample thickness. Due to this finding it was concluded that elastic modulus could not be determined from the SHPB tests, and it is expected that the error is either as a result of the silicon gel between the bar and the sample, or simply caused by the high sensitivity of measuring strain at such low magnitudes. However, the modulus is fairly insignif-

icant in underwater blast scenarios so the strain at which the quasi-static test samples began to crush was used alongside the SHPB crushing stress to calculate the elastic modulus. There was very little rate sensitivity observed in the crushing strength of the materials tested, albeit a slight increase in the strength of the M130 and M200 foams with increased rate. However, this was deemed too small to be conclusive. The quasi-static compressive strengths of the M100, M130 and M200 SAN foams were 1.8 MPa, 3.0 MPa and 5.2 MPa respectively, which increased to 3.5 MPa, 5.5 MPa and 10.5 MPa in the SHPB tests. This is a very large increase in crushing strengths, which is an important finding for underwater blast as it shows that much more energy is absorbed when crushing the foams at higher rates with an equal displacement.

In order to assess the full behaviour of the foams at high strain rates, the densification strain and exponential densification constants were taken from the quasi-static compression results and applied to the SHPB results. The plateau stress was assumed to be equal to the crushing stress, as the high strain rates make stress relaxation less likely. The stress versus strain responses of the three SAN foams, constructed from the SHPB and quasi-static compression tests, are shown in Figure 6.33. The curves have been shown up to a stress of 60 MPa as this was the peak pressure measured in the underwater blast tests, and constructed from a linear elastic increase of stress at the measured quasi-static modulus of the foams until the plateau stress measured in dynamic compression, followed by the densification strain and exponential densification response measured during quasi-static compression. As such, the key dynamic material property, measured using the SHPB, was the crushing stress, which was also used for the plateau stress. The energy absorbed in crushing the single density SAN M130 foams and the SAN graded density cores in the underwater blast test were calculated in Chapter 5. The energy absorbed per unit volume of the SAN M100, SAN M130 and SAN M200 foams, when loaded to 60 MPa, was 7.7 MJ/m^2, 9.3 MJ/m^2, and 11.9 MJ/m^2 respectively.

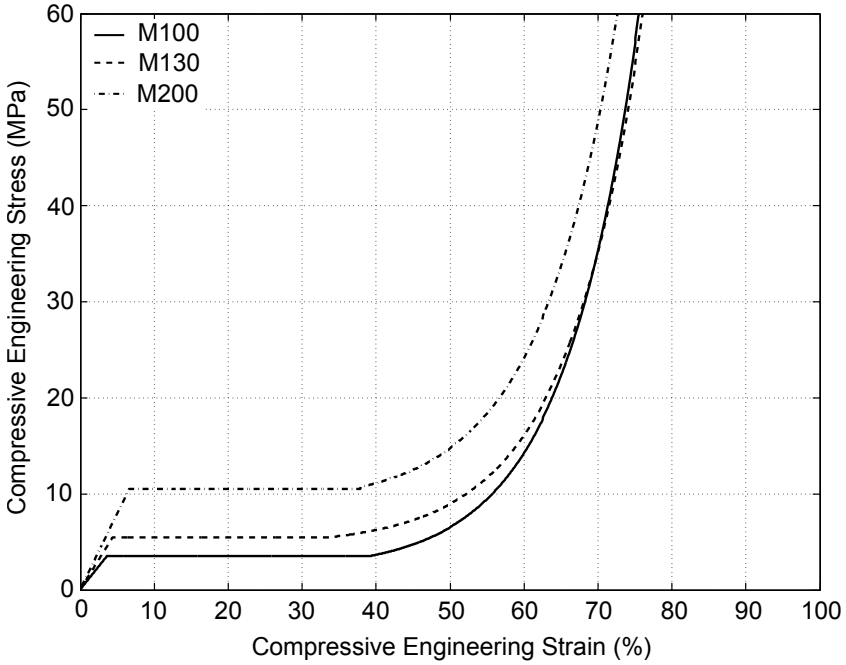


Figure 6.33: Dynamic compressive engineering stress versus engineering strain curves for the M100, M130 and M200 SAN foams, constructed from the strains measured in the quasi-static compression tests.

6.5.3 Dynamic Tension

Dynamic tension tests were performed to assess the different behaviours of the foam polymers when subjected to air blast loading. It was found in Chapter 3 that the shear strains at failure of the foams were fairly similar, so the different fracture properties were likely to be caused by tensile characteristics. All of the polymeric foams were found to be almost linear elastic when tested at 180 s^{-1} and 365 s^{-1}, and there was no difference in the responses between these two rates. The tests showed that the strains to failure of the foams were quite inconsistent, but when a higher frame rate on the high speed camera was used in the PVC and PMI cases, the elastic modulus was more consistent. The conclusion from this is that the highest possible frame rate should be used to capture the elastic properties of the foam during dynamic tests, to allow interpolation of the strain data over much smaller steps than those used to test the SAN foams. The strain to failure could also be deemed inconsistent due to misalignment in the grips, however, this is unlikely as the failure stress of the samples is consistent. The strain to failure was recorded as an average of the results, but this should be used with caution and more research should be performed with a higher frame rate of camera. As it is expected that the tensile modulus of the foams is rate insensitive, the recommended use of the tensile foam data in dynamic loading is a linear elastic response at the measured quasi-static tensile modulus, until the failure stress measured in the dynamic tensile tests is reached. This will then determine the strain to failure of the polymeric foams.

The PMI 110SL foam had a much greater elastic modulus than the PVC and SAN foams, and a lower strain to failure. This is the reason for the higher damage suffered in the PMI case during air blast loading. The SAN M100 and PVC C70.90 foams showed similar elastic moduli and strain to failures. In air blast testing the SAN foam outperformed the PVC case, and this is likely to be caused by a difference in fracture toughness, causing a more catastrophic failure in the PVC cores than the SAN cores. Another plausible explanation for the different responses could be a poorer bond between the face-sheets and PVC foam core than with the SAN M100 core, resulting in greater debonding in the PVC panel case. This would create more core cracks so result in much more damage overall.

The results of the three SAN foams showed that the elastic modulus of the M200 foam is over twice that of the M100 case. This aids in understanding the reduced cracking in the higher density rear foam layers in the graded density air blast test, as the mechanical properties are increased greatly by increasing foam density. By encouraging cracking in the weaker foams at the front, there is less energy to crack the stronger foam at the back, reducing damage in this region.

Due to the uncertainties in strain measured in the dynamic tensile tests it is recommended that the failure stress of the polymeric foams are used alongside the elastic tensile modulus measured in the quasi-static tensile tests. The dynamic tensile test results showed that the behaviour of the foams can be estimated as linear elastic, and Gibson and Ashby [116] expected that the elastic modulus of the foam is not rate sensitive. This allows an estimate of tensile failure strain to be determined from the quasi-static elastic modulus and the dynamic failure stress.

6.6 Conclusion

Characterisation of polymeric foams has been performed in order to understand the different responses of the materials to air and underwater blast loading. Quasi-static tensile and compressive tests were performed to provide the full stress versus strain responses of the material under static loading conditions, and to also verify or adjust manufacturer data.

From the quasi-static compression tests it was possible to measure the strain at which cell collapse began, the strain at which densification of the foam began, and the exponential shape of increased stress during densification. As these are macro effects on the foam structure, the strain values are expected to be consistent at all strain rates, so the collapse stress at elevated strain rates was measured using SHPB. From the values of collapse stress from SHPB, values of collapse strain from quasi-static tests and the densification properties from quasi-static tests it was possible to construct full stress versus strain curves at high strain rates, in order to compare the energy absorbed during crushing in underwater blast loading. This is detailed further in Chapter 5, and the curves are shown in Figure 6.33. Furthermore, the high rate compressive mechanical properties can be used in analytical and numerical modelling to predict the response of sandwich

panels to blast loading scenarios.

The polymeric foam materials were also tested in quasi-static and dynamic tension, and it was found that with increased loading rates the material behaviour was much more brittle. In both the quasi-static and dynamic test results the PMI foam showed a much lower strain to failure, which explains the lower blast resistance witnessed in Chapter 3. The strain to failure of the PVC and SAN M100 foams, however, were quite consistent, which leads to the hypothesis that the SAN M100 foam outperformed the PVC C70.90 foam for another reason such as a higher fracture toughness of the M100 foam, or better bonding between the M100 foam and the face-sheets. The elastic modulus of the M200 foam was much greater than the M100 and M130 materials, which explains why adding higher density foams to the rear of the sandwich panel encourages cracking in the front layers, and protects the back face.

Chapter 7

Finite Element Modelling

7.1 Introduction

This chapter presents research into finite element analysis (FEA) performed to simulate the response of polymeric foam core sandwich composite panels to air blast loading. The use of full scale blast tests provides a qualitative analysis of the resistance of the sandwich composites to blast, but by utilising the material properties found through laboratory testing, it was possible to simulate these responses using commercial finite element packages. By using the full scale blast tests to validate the FEA results, the simulation methods can be used to model different blast scenarios and geometries. The commercial FEA package used was Abaqus CAE and the solver was explicit in all cases. Elastic and inelastic simulations were performed in this research, and these were used to identify the onset of damage in the foam core. The simulations were only for the foam comparison study, considering the SAN Corecell M100 core sandwich panel and the PVC Airex C70.90 core sandwich panel. Due to time constraints the PMI Rohacell 110SL case was not simulated. Various load cases were performed and the onset of damage identified. The use of inelastic material models in FEA is non-trivial, so the research presented in this chapter acts as a starting point for further research into the damage modelling of sandwich composites under blast loading. The damage model presented in this chapter was in the form of a brittle cracking of the foam. In air blast there is no core crushing unless the peak pressure is greater than the

crushing stress of the foam, which it was not in the blast research presented in Chapter 3, but the core damage took the form of core shear cracking and core and face-sheet debonding. Debonding is very challenging to model, so it was omitted from the simulations presented in this chapter. The results presented take the form of pressure versus impulse damage curves, which show the onset of damage for the foam core. Also shown is a comparison of the digital image correlation (DIC) results to the actual air blast tests, for validation, and a boundary condition study, to assess how much of the structure needed to be simulated.

7.2 Simulation Methods

7.2.1 Finite Element Mesh

Due to the low thickness and large area of the fibre composite face-sheets, shell elements were used to model these. These were linear quadrilateral S4 shell elements. The sandwich core elements used were hexahedral 3D solid linear C3D8R elements, with reduced integration for increased computational speed. This selection of elements was the same in both the elastic and inelastic simulations. Furthermore, in all cases a tie contact was used between the face-sheets and the core, which allowed no movement of the nodes relative to each other. Due to uncertainty in suitable boundary conditions for the simulations, an elastic FEA was performed with one sixteenth of the cubicle front modelled, which was approximated as one quarter of a sandwich panel. This was then compared to a model which just contained the sandwich panel starting at the inside of the steel strips, and which contained encastre boundary conditions around the edges. This method would greatly reduce computational time, and it was theorised that it would only affect the response time of the sandwich panel, and not the overall displacements. The modelled area is shown in Figure 7.1 by the red square, which is simply drawn on top of Figure 3.6 from Chapter 3. The steel components in the model with the cubicle front were hexahedral 3D solid linear C3D8R elements, and the sandwich panel was fixed to the steel of the cubicle via tie constraints. The steel tubes used to prevent core crushing when tightening the panel to the cubicle were also included, to ensure that stress concentrations were correctly captured in the FEA. Due to

the complexity of the cubicle front, it was meshed as strips of steel tied together. The simulation was elastic, and the steel deflections were relatively small so this was adequate to capture the correct boundary conditions. The loading conditions in the simulations assumed a planar loading across the whole front of the test cubicle and the front of the sandwich panel, which followed a predicted form of the Friedlander equation shown in Equation (3.5) in Chapter 3. The modelled section of the cubicle front is shown in Figure 7.2, and Figure 7.2a shows the section of the cubicle front and sandwich panel that was measured, and Figure 7.2b shows the model with the mesh in place. Also shown in Figure 7.2 is the area of the sandwich panel which was modelled with the rest of the steel test cubicle omitted for computational efficiency.

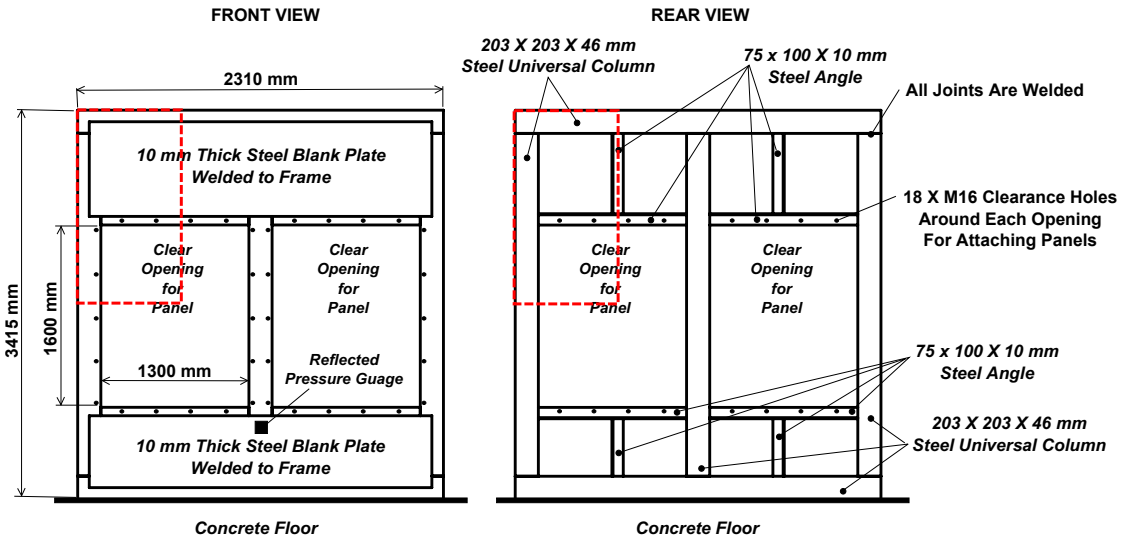


Figure 7.1: Schematic of the steel front of the test cubicle, with the section modelled with FEA highlighted in red.

7.2.2 Material Models

The direct strain rate in the foam cores was between the quasi-static and dynamic properties presented in Chapter 6, and from the contour plots of maximum principal strain (MPS) shown in Appendix A, this was around 15 s^{-1}. However, due to the effect of the GFRP face-sheets stabilising the foam core, and the in-

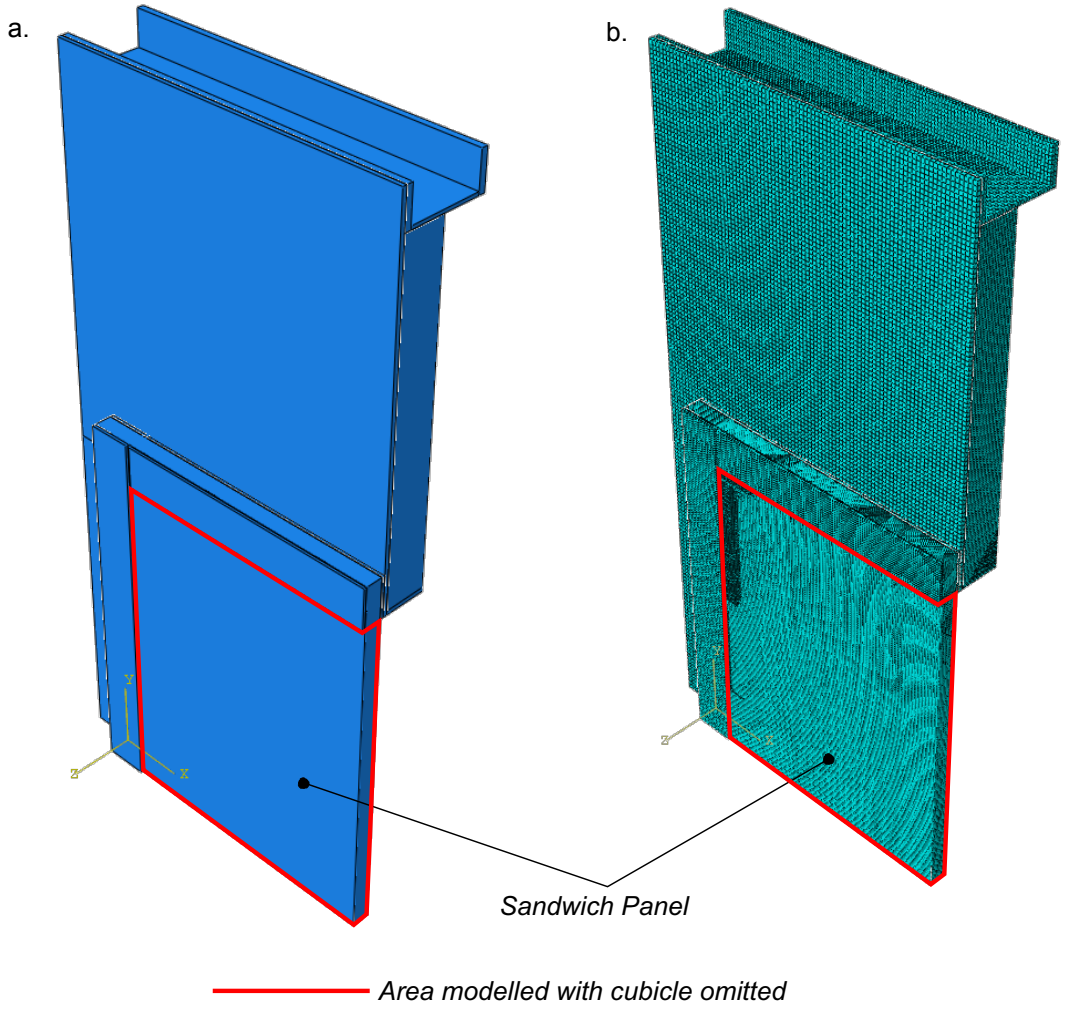


Figure 7.2: Screenshot of the Abaqus model of the cubicle front and sandwich panel as a) a solid model; and b) a meshed solid model. The red line indicates the area of the sandwich panel modelled with the test cubicle sections omitted.

sensitivity of the FEA simulations to the actual breaking stress of the foam, the fracture stress values used in the inelastic models were the dynamic properties found in the characterisation tests presented in Chapter 6. As recommended in Chapter 6 the dynamic elastic moduli were omitted from the models as they were likely to be inaccurate, due to low quality DIC in the laboratory tests, and it was expected that the elastic modulus should be the same as in the quasi-static tests. The strain to failure was calculated as the fracture stress from the dynamic tensile test results divided by the tensile modulus. The properties used for the face-sheet were as calculated in Chapter 3, and all of the material properties are summarised in Table 7.1, although damage in the face-sheets was omitted. The brittle cracking model was utilised for the foam core, which is designed for use with concrete. The brittle cracking model assumes a linear elastic response until a failure stress, where the element stiffness is reduced to zero [118]. As the foam density was so low, this caused excessive deformation upon fracture, unless a fairly large fracture toughness was implemented, to dampen the response at fracture. In order to optimise the response of this fracture process, the lowest fracture toughness was chosen which allowed the simulation to execute without becoming unstable due to excessive deformation speeds. The fracture toughness assumed in every case was 105 N/m, which was determined by incrementally increasing the fracture toughness until fracture in the foam took place in a stable manner. This value was chosen purely to achieve a stable simulation and had no bearing to real mechanical properties of the foam materials. Linear shear retention was assumed in the brittle cracking material model with complete shear stiffness reduction at a shear strain of 100%. Due to the low stiffness of the foam the response of the material was insensitive to changes in the shear retention model. This resulted in a linear reduction of shear modulus with crack opening until a maximum shear strain of one was reached. However, due to the low density and strength of the material, the model was completely insensitive to this parameter, so cracking was virtually instantaneous upon the cracking strain being reached, and the post-crack parameters merely provided a method to allow damage to take place in a stable manner.

Table 7.1: Material properties of the polymeric foams and GFRP face-sheets used in the finite element simulations.

Material	Density (kg/m^3)	Tensile Modulus (MPa)	Poisson's Ratio	Fracture Stress (MPa)	Fracture Strain (%)
SAN M100	107.5	88	0.3	5.7	6.5
PVC C70.90	100.0	71	0.3	7.2	10.1
GFRP QE1200	1730	15,900	0.3	-	-

7.2.3 Simulation Parameters and Results Processing

For both the elastic and the inelastic cases, the parameters from the blast wave of the 15 m stand-off 100 kg TNT equivalent charges were put into the model, to validate the FEA against the DIC results. This was done by both comparing contour plots of out-of-plane displacement and maximum principal strain, and by comparing the point plots of out-of-plane displacement at the centre and the quarter points. With the model validated, simulations were then performed with various amounts of peak pressure and impulse to create failure loci of pressure and impulse for each construction of sandwich composite.

The test cases performed were for TNT-equivalent charge sizes of 10 kg; 30 kg; 100 kg; 500 kg; and 1000 kg. The stand-off distances were then altered in increments of 1 m to find the combination at which damage took place. Abaqus input files of each pressure loading profile were created, so that the foam material properties could be altered easily, and a Windows batch script was created to run each simulation sequentially, using four processors on a local computer. The simulation times were 20 ms, and 100 field outputs were requested over the whole simulation, therefore at approximately 0.2 ms increments.

The maximum principal strains in the foam core and the maximum principal in-plane strains in each of the two face-sheets were then extracted for each frame, using a Python script to export a report for each frame, appended on to the report for the previous frame. A MATLAB script was then used to extract the

data from the exported reports, and to determine the closest charge size and stand-off distance combination to the failure point of the foam and each face-sheet. The failure decision was made via the strain as it was computationally much faster to extract strain data than stress data. As the failure models were linear elastic this was an acceptable method of inspection. Pressure versus impulse plots were then created for each combination of charge size and stand-off distance, to assess the effect of including damage into the FEA material models, and to compare the responses of the different foam core sandwich panels.

7.2.4 Results

7.2.4.1 Boundary Conditions

The first FEA simulation considered an eighth of the whole air blast test cubicle, as the boundary conditions during the test were known to be quasi-built in, due to the deflection in the steel frame. As the DIC results removed the steel frame deflections from the results, resulting in just the panel deflection relative to the panel edges, it was expected that by removing the steel cubicle from the simulations the deflection would remain the same but the response time would be much quicker. In Chapter 6 it was shown that the rate sensitivity of the foam was negligible when dynamic, so the response time of the panel was expected to have a negligible effect on damage initiation. For this reason, two elastic simulations were compared with the SAN M100 single core sandwich panels, with and without the steel cubicle. The simulations were elastic as this represented the smallest time saving, as the damage model would be much more computationally expensive.

With four processors assigned to each simulation, the computational time for the full test cubicle was 1.75 hours, and for just the panel was 0.60 hours, representing a reduction in computation time of 66%, or 1.15 hours. In order to determine the stand-off distance and charge sizes to cause damage approximately 40 simulations in each case were performed. With two simulated tests each performed with elastic properties and inelastic properties, this resulted in 160 simulations. This represented a minimum computational time saving of 184 hours, or 7.7 days. This was a minimum as it was based on the elastic cases and the inelastic cases were expected to result in greater time savings.

A comparison of the central displacements of the SAN M100 single core sandwich panel, tested with elastic properties, is shown in Figure 7.3. In the case of the steel cubicle being modelled, the displacement is the central point of the sandwich panel minus the central point of the central steel column. This position is highlighted in Figure 7.4 which also shows contour plots of the out-of-plane displacement of the test cubicle and sandwich panel. The out-of-plane displacement contour plots of the sandwich panel only are shown in Figure 7.5, again with the out-of-plane displacement measurement point highlighted. The central displacement plots in Figure 7.3 show that the central out-of-plane displacements are similar to the DIC results and that the panel only simulation had a faster response time than the steel cubicle simulations, which in turn was faster than the DIC response time. This is because in reality, the whole structure was elastic, whereas the FEA model with the steel front was fully built-in at the cubicle edges. It is shown in Figure 7.3 that by applying a correction factor (Cf) of 1.24 to the time axis in the steel cubicle front simulation, and a correction factor of 1.62 in the panel only simulation, the peak out-of-plane displacement times matched well with the DIC times. This number was chosen to illustrate the boundary effects only, and was chosen manually by fitting the displacement curves together. The rebound times, however, did not match well, due to the lack of damage in the FEA simulations, making the rebound much faster. The out-of-plane displacement of the simulations with the steel cubicle included overestimated that measured with DIC, and the simulations with the cubicle omitted underestimated the deflection. Over-deflection in the steel cubicle FEA case was expected to be because of the uneven pressure distribution in reality, transferring less energy to the cubicle front than in the FEA case where it was simply a planar pressure wave. This caused greater cubicle displacement in the FEA than witnessed in reality. The lower displacement in the panel only simulations was likely to be a combination of the effect of a purely elastic simulation, and the perfect boundary conditions. Due to the offset in deflection from DIC results with and without the steel cubicle modelled being similar, it was decided to omit the steel cubicle to gain computational speed.

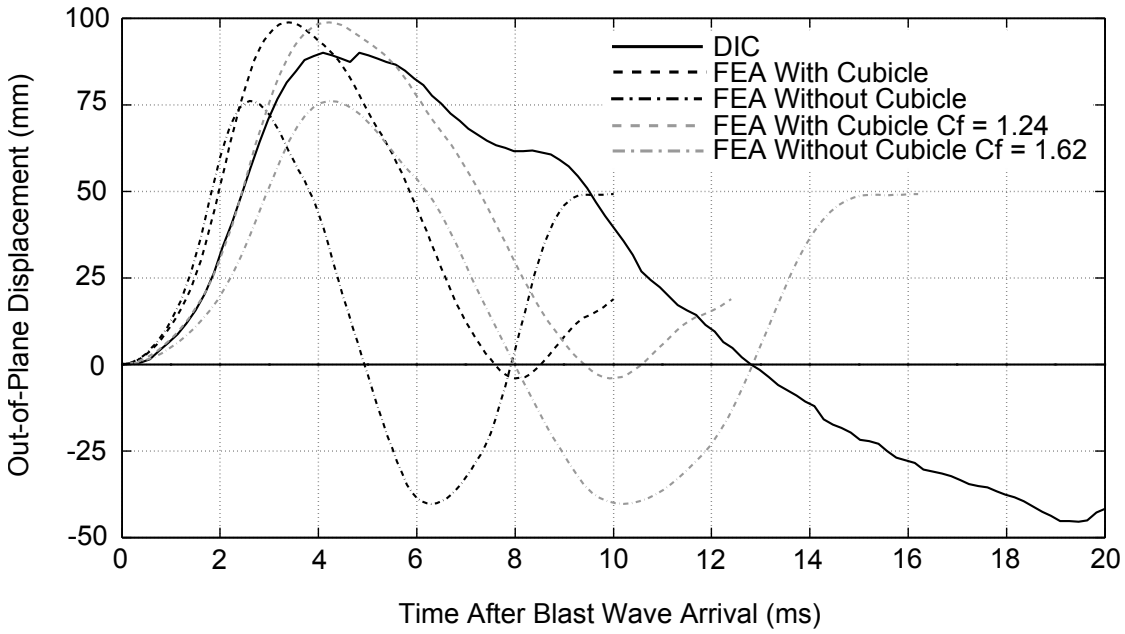


Figure 7.3: A comparison of the FEA plots with and without the test cubicle, and the results from the DIC. Also shown are plots of the central displacement with the response time factored down to match each other, to highlight the effect of the boundary conditions.

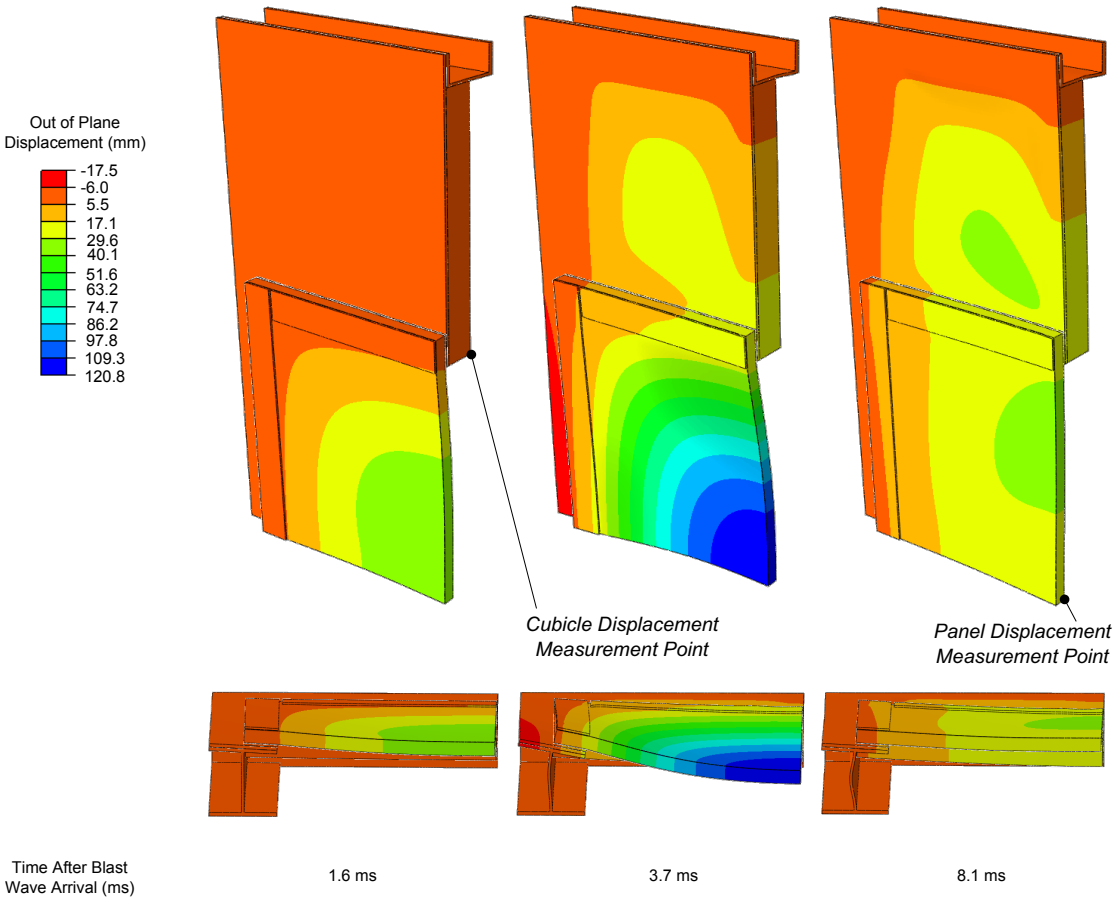


Figure 7.4: FEA results showing out-of-plane displacement of the SAN M100 single core sandwich panel with the steel test cubicle included, at 1.6 ms, 3.7 ms and 8.1 ms after the blast wave arrival. The sandwich panel displacement measurement point and steel cubicle displacement measurement point are also highlighted.

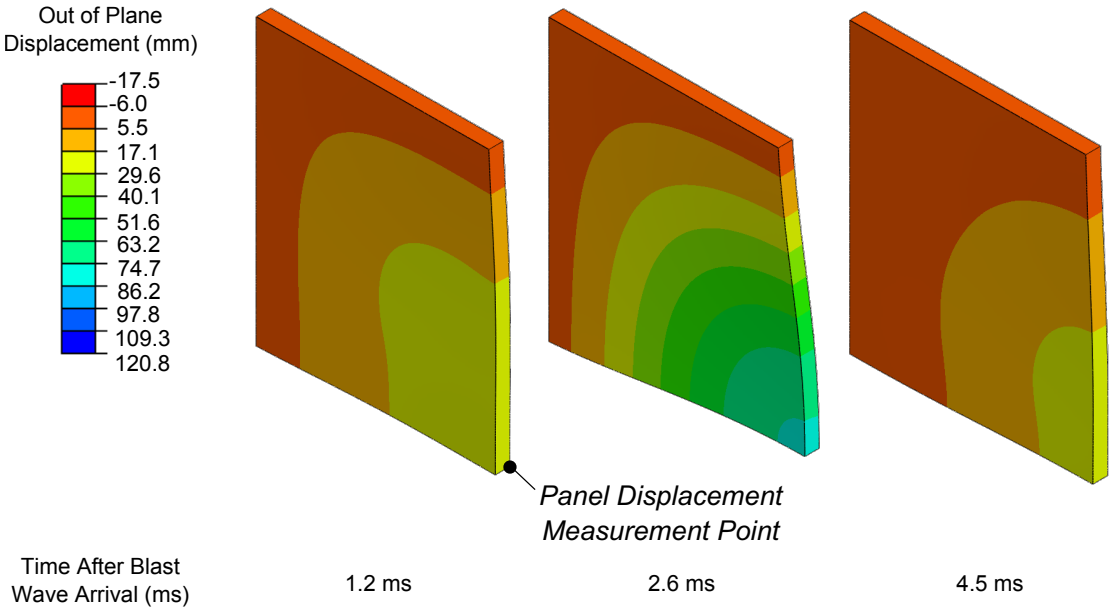


Figure 7.5: FEA results showing out-of-plane displacement of the SAN M100 single core sandwich panel at 1.2 ms, 2.6 ms and 4.5 ms after the blast wave arrival. The sandwich panel displacement measurement point is also highlighted.

7.2.4.2 Elastic Simulation Results

The first FEA study assessed the various peak pressure and impulse levels at which the sandwich panels failed when modelled with elastic material properties. Due to time constraints the study was only performed on the two of the three single core sandwich panels investigated in the air blast polymeric foam comparison detailed in Chapter 3. The cases studied were the SAN M100 sandwich panel and the PVC C70.90 sandwich panel. In order to verify the FEA results, the simulations were performed with 100 kg TNT equivalent charge sizes at a stand-off distance of 15 m, as in the air blast tests. The traces of the central and quarter point out-of-plane displacements for the DIC and FEA results are shown in Figure 7.6 for the SAN M100 case and in Figure 7.7 for the PVC C70.90 case. As can be seen in Figure 7.6 the displacements of the simulation are significantly less, due to the lack of damage in the sandwich panels and the fully elastic boundary conditions. The quarter point displacement is even further away from that measured with DIC, and this is due to the lack of "bathtub" deflections shape in the simulation, which caused by

cracking down the vertical edges of the panels in the experiments. The central displacement of the PVC C70.90 sandwich panel, shown in Figure 7.7, shows similar disagreement with the DIC results, as does the quarter point displacement, again due to the boundary conditions and the lack of damage modelling in the composite materials. The simulations results, however, are reasonably close in predicting the out-of-plane displacement, but the differences should be considered when drawing conclusions from the failure loci.

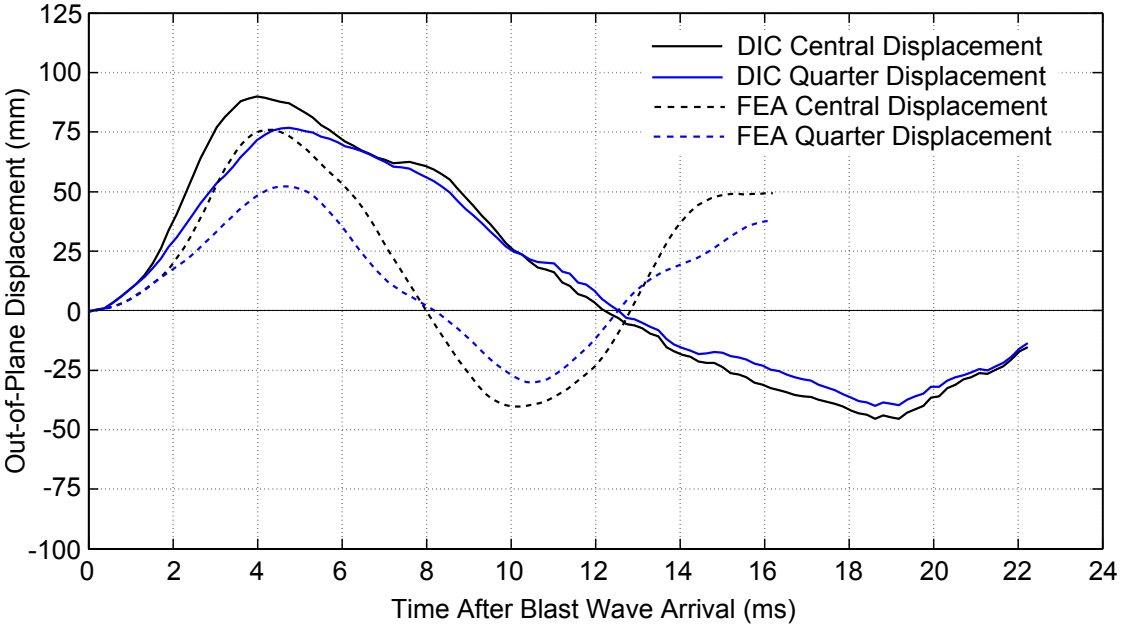


Figure 7.6: Central and quarter point out-of-plane displacements of the SAN M100 sandwich panel, from FEA results and DIC results.

Around 40 simulations were performed for each of the three elastic cases, and the results processed to find the failure points of each. Failure of each face-sheet and the foam core was identified using a MATLAB script, and the pressure versus impulse curves plotted. The pressure versus impulse curves for the SAN M100 core sandwich panel are shown in Figure 7.8 and for the PVC C70.90 sandwich panel in Figure 7.9. Also shown in the pressure versus impulse plots are the pressure versus impulse values for the charge sizes used in the simulations. The failure loci are connected with straight lines, as not enough data was available to plot smooth curves. The vertical lines extend to the pressure and impulse values for a 1 kg

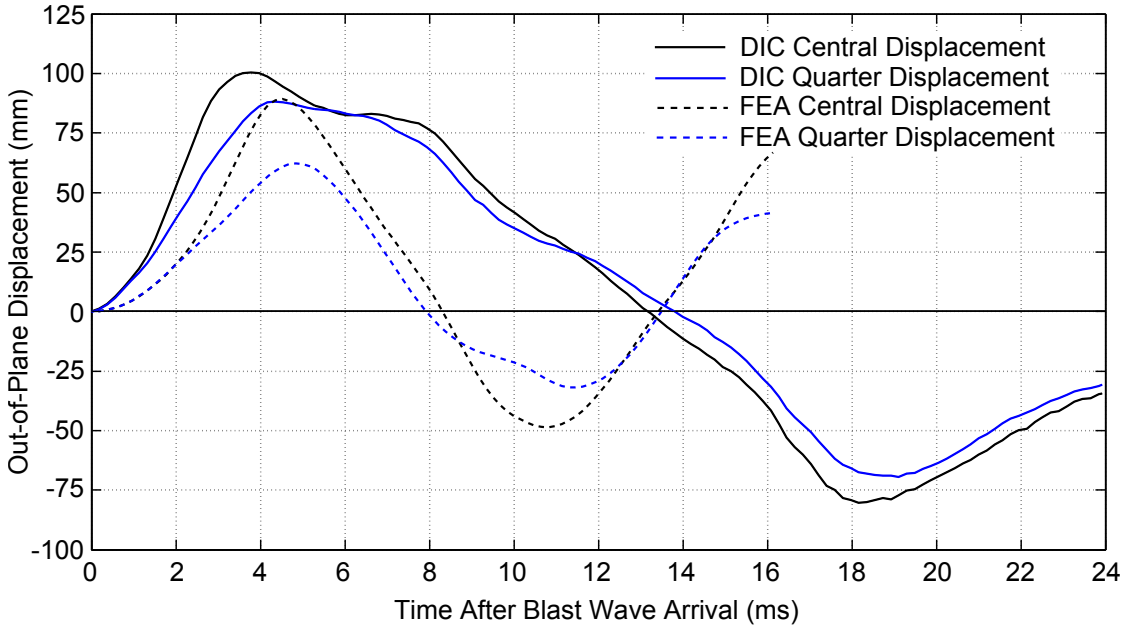


Figure 7.7: Central and quarter point out-of-plane displacements of the PVC C70.90 sandwich panel, from FEA results and DIC results.

charge situated at 1 m from the target, as this was found to be a point at which damage was caused in all of the sandwich panel simulations, and at such low charge sizes the stand-off distance variation for failure is low. The pressure and impulse values of a 1 kg charge at a 1 m stand-off distance are 8282 kPa and 286 kPa.ms respectively. These were not included in the study as small, close charges cause very localised loading in the sandwich panels, which are not considered in this research. The rear face-sheet failure curve in Figure 7.8 is greater than that for the PVC C70.90 case in Figure 7.9 and this is caused by the stiffer SAN foam. The higher strength of the PVC C70.90 foam is shown in the failure curve by the higher pressures at lower impulse values, although this result seems erroneous as the foam can withstand more than the back face-sheet. This inaccuracy is caused by the lack of damage material models, which cause unrealistic responses especially to higher pressure peaks which cause higher through thickness stresses. The front face-sheet failure curve is consistent in both plots and as such, this should be the failure point used if this method is used in design decisions.

It is expected that with significantly more simulations, the failure line with

increased impulse levels would plateau to a constant pressure, and this represents very large charge sizes with large stand-off distances. With close proximity charges the failure line would reach a constant impulse level with varying blast pressures. This would represent small charge sizes at very small stand-off distances. However, in the latter case the damage mechanism would become more intricate due to non-planar, concentrated pressure loading on the sandwich panel.

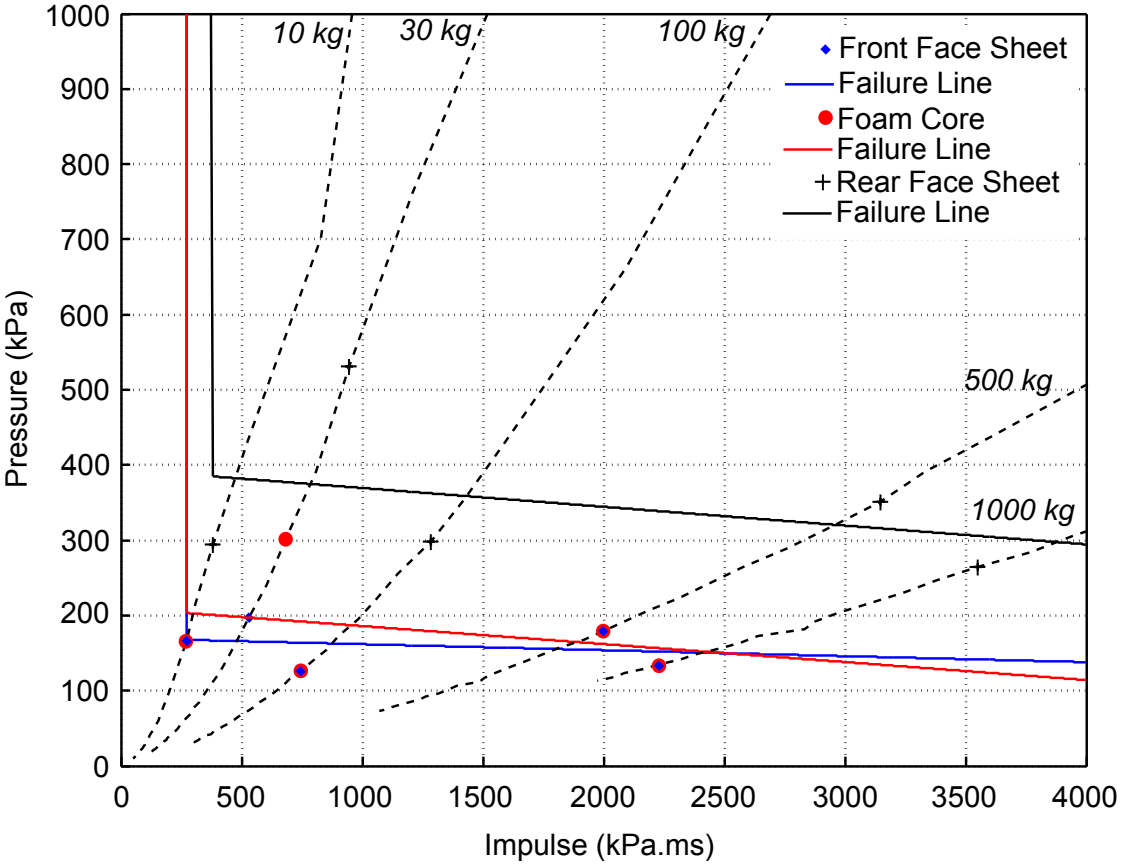


Figure 7.8: Pressure versus impulse curves for the front face-sheet, foam core and rear face-sheet in the SAN M100 simulations using elastic material models.

7.2.4.3 Damage Simulation Results

The damage modelling in Abaqus used a brittle cracking model for the polymeric foam core, which was intended for use with concrete. The crushable foam model was not used as the peak pressures witnessed in the air blast loading considered in

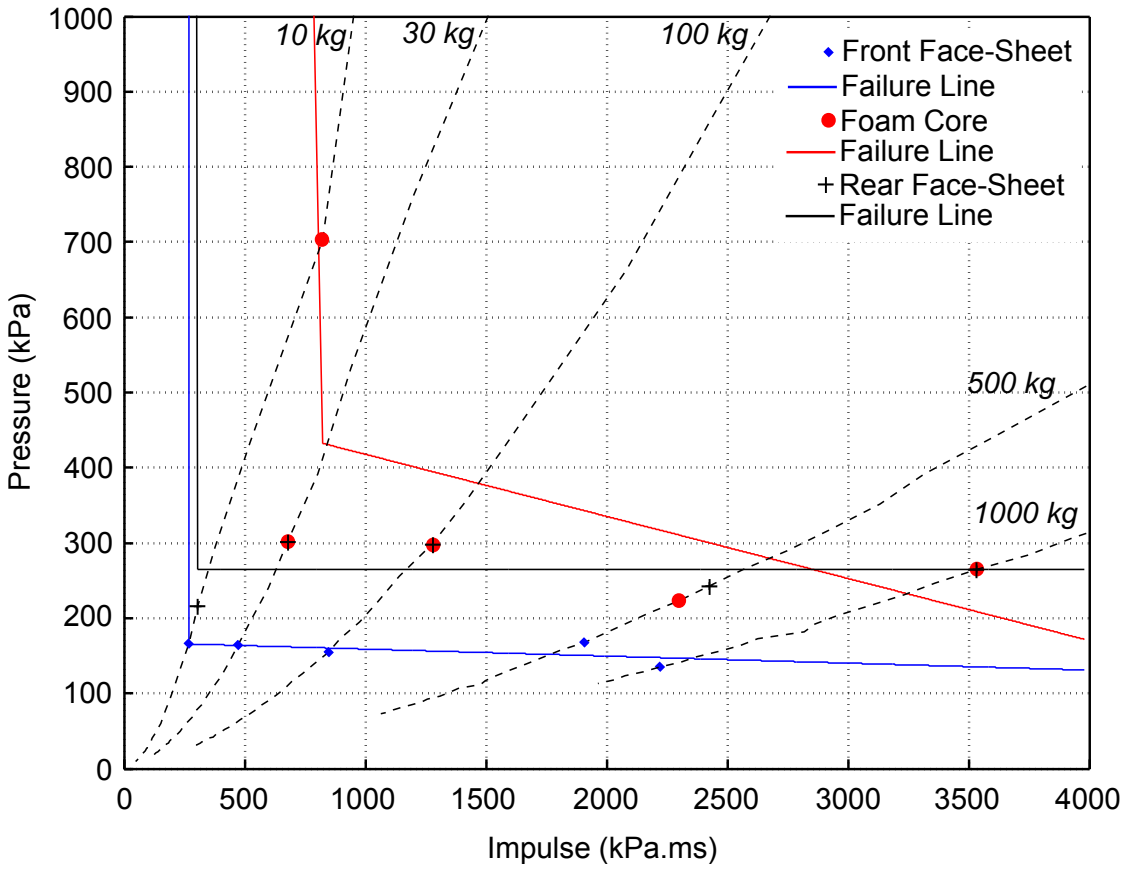


Figure 7.9: Pressure versus impulse curves for the front face-sheet, foam core and rear face-sheet in the PVC C70.90 simulations using elastic material models.

this research were not great enough to crush the foam cores. An edge profile of the SAN M100 sandwich panel during the core failure process is shown in Figure 7.10, which shows shear strain as the contour plot. Shear strain is shown as this makes failure most easily visible. The central and quarter point displacements of the FEA results in the SAN M100 core sandwich panel are compared to the DIC results in Figure 7.11 and it can be seen that the central displacement matches the DIC data much more closely than in the elastic case. Also visible is the deceleration of the sandwich panel at around 7 ms, caused by damage in the foam core. The quarter point displacement is still too low however, and it is expected that this is due to poor crack propagation across the foam inwards towards the centre of the sandwich panel, and the lack of debonding between the face-sheets and core in the FEA. The PVC C70.90 core sandwich panel comparison is shown in Figure 7.12, and this response is much less accurate than the elastic case. This is because the fracture stress of the PVC C70.90 material is greater than the SAN M100 material. However, the post-blast observations in Chapter 3 indicate more damage suffered in the PVC C70.90 test panel, which suggests that the initial damage could be caused by debonding which was not present in the FEA simulations. This conclusion is drawn based on the foam damage model being utilised, but the load not being great enough to cause damage of these types.

The pressure versus impulse failure curves of the SAN M100 and PVC C70.90 core sandwich panels are shown in Figure 7.13 and Figure 7.14 respectively for the front face-sheet, foam core and rear face-sheet. Also shown are curves for each charge size simulated. In both the PVC C70.90 and the SAN M100 core sandwich panel cases the failure loci for the front and rear face-sheets are separated by the same amount, implying that the incorporation of damage models into the foam aids in predicting face-sheet damage. The responses of the foam cores, however, appear slightly inaccurate with a steep gradient in the M100 case in Figure 7.13, and a positive gradient in Figure 7.14. In the SAN M100 case, the low impulse failure point has a greater peak pressure than all of the other plots, and this is likely to be caused by the higher stiffness of the SAN M100 foam. These results indicate that introducing core failure material models in the simulations helps to accurately predict the failure points of the face-sheets, but results in inaccurate core failure results due to poor propagation of brittle fracture through the core

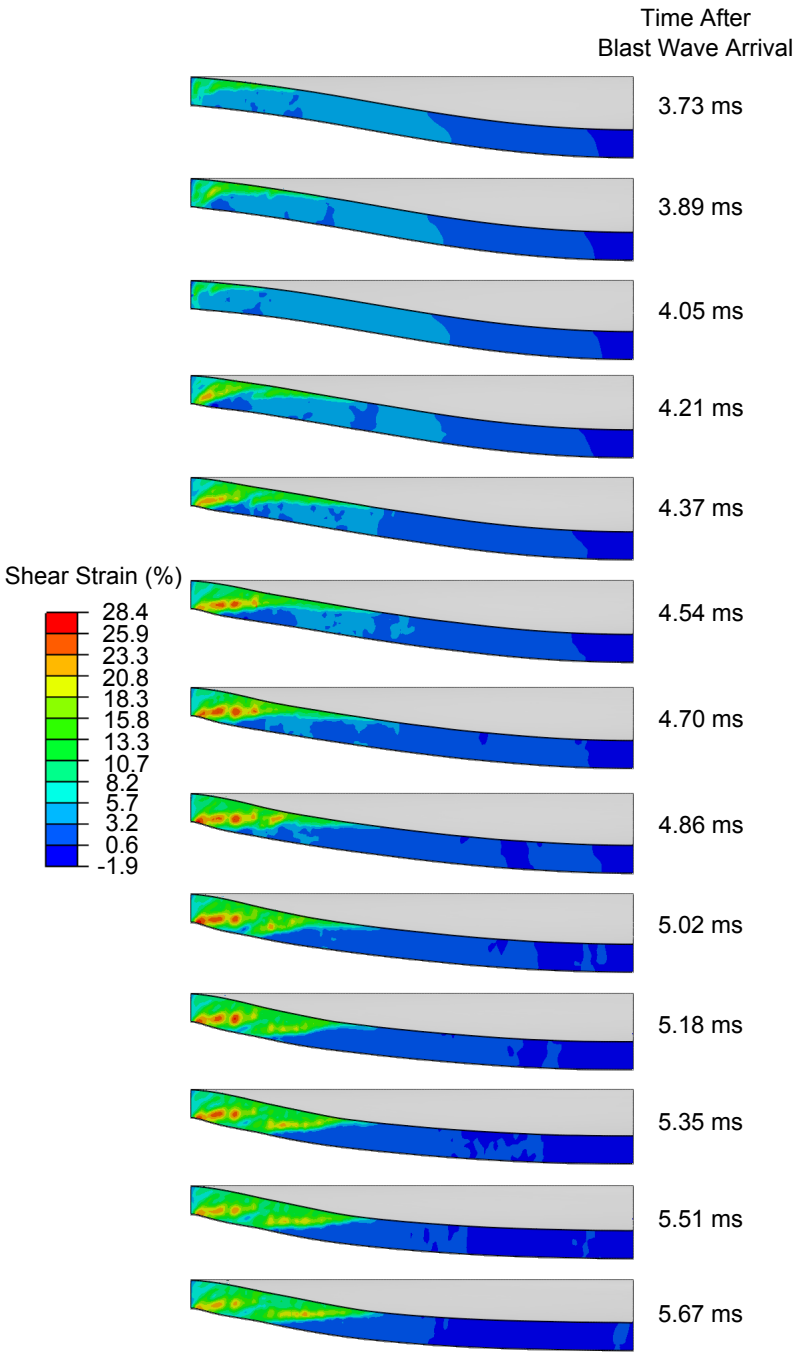


Figure 7.10: FEA deflection shape of the horizontal centre of the SAN M100 sandwich panel, subjected to a 100 kg charge at 15 m. The contour plots show shear strain in the sandwich panel.

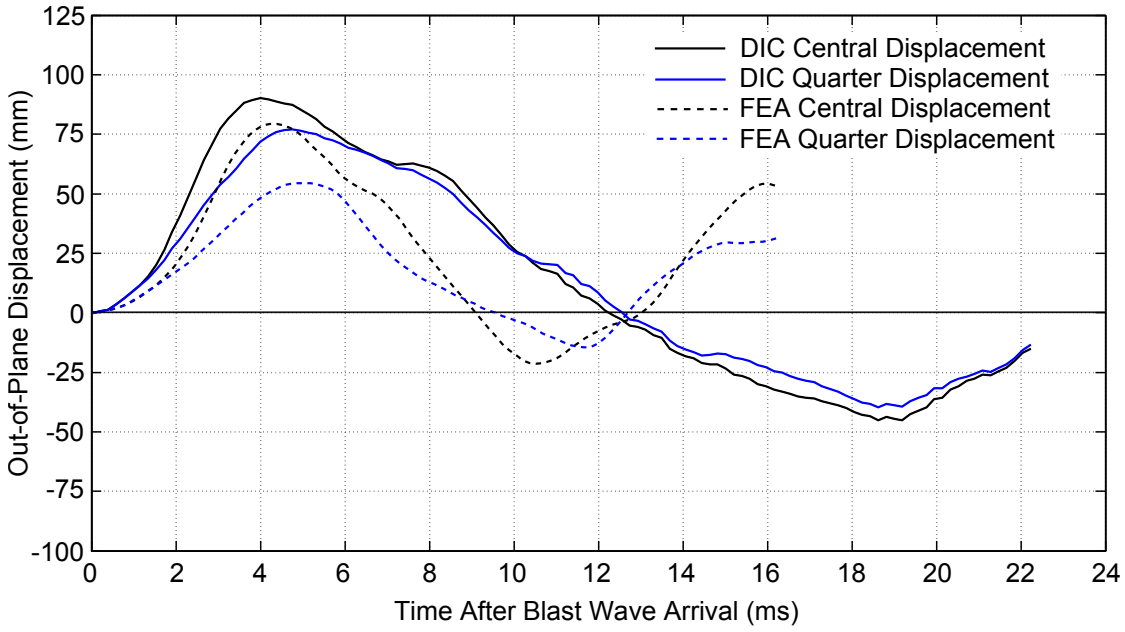


Figure 7.11: Central and quarter point out-of-plane displacements of the SAN M100 sandwich panel incorporating damage modelling, from FEA results and DIC results.

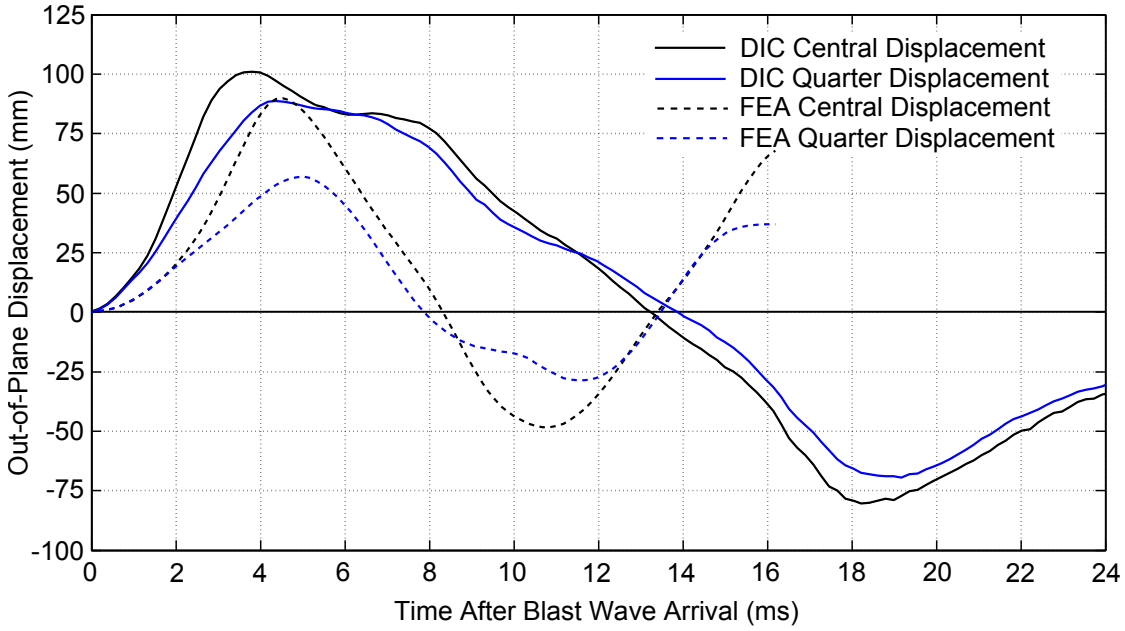


Figure 7.12: Central and quarter point out-of-plane displacements of the PVC C70.90 sandwich panel incorporating damage modelling, from FEA results and DIC results.

thickness.

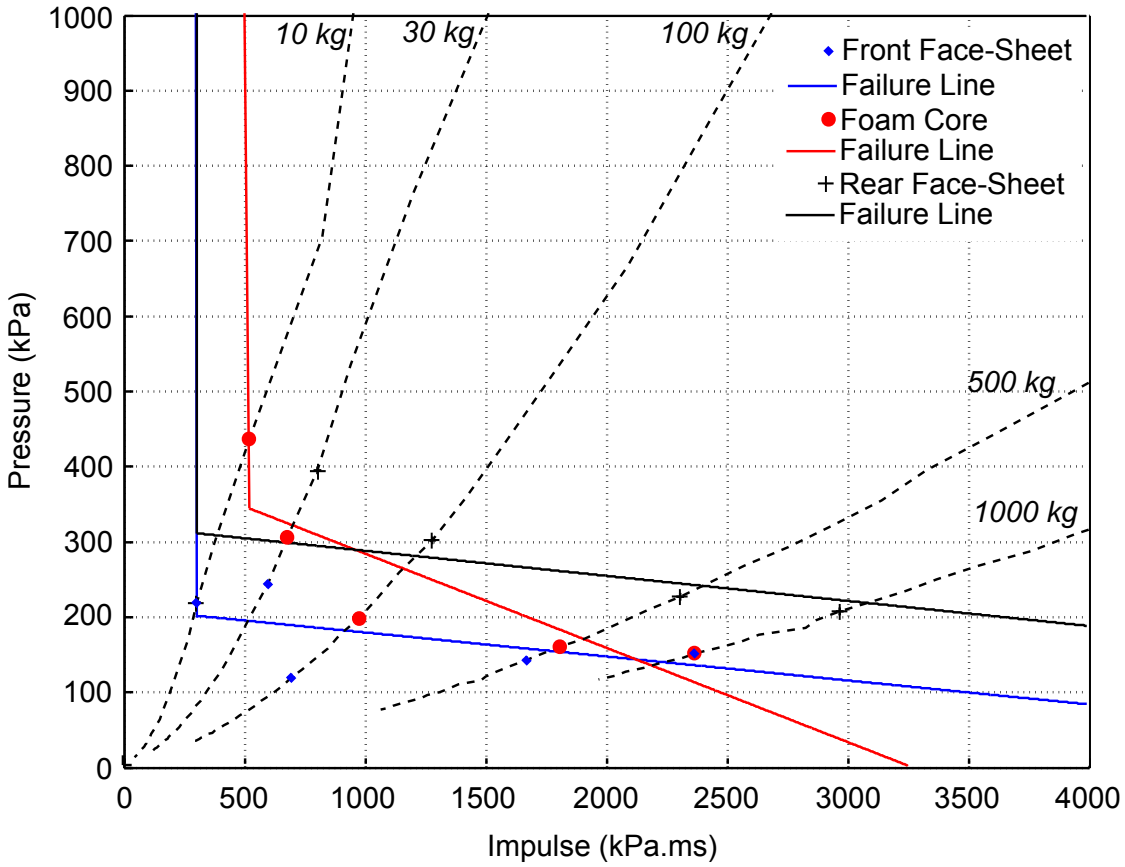


Figure 7.13: Pressure versus impulse curves for the front face-sheet, foam core and rear face-sheet in the SAN M100 simulations using material models incorporating damage.

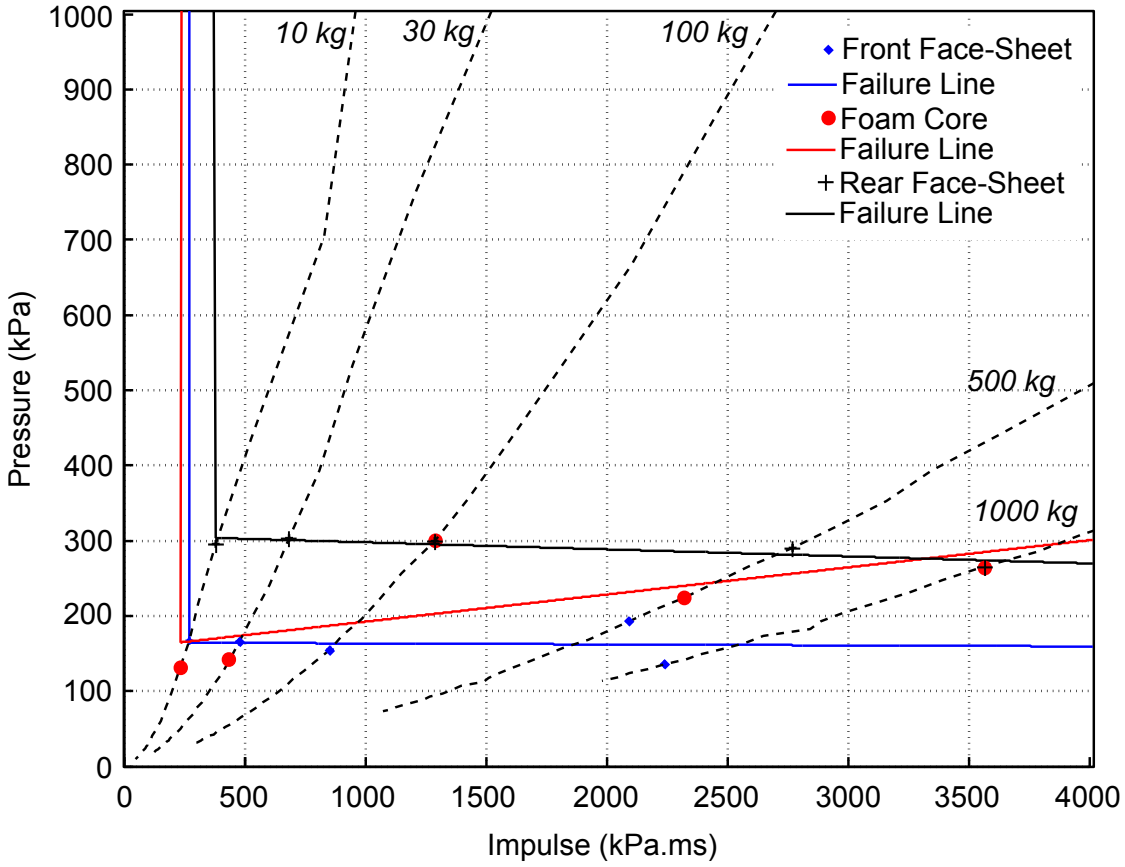


Figure 7.14: Pressure versus impulse curves for the front face-sheet, foam core and rear face-sheet in the PVC C70.90 simulations using material models incorporating damage.

7.3 Discussion

This chapter has provided the methods and results of simulating air blast loading of sandwich composite materials using FEA. The simulations were only performed for the single density foam core SAN M100 and PVC C70.90 cases, due to the computational time and post-processing time required. As this was the final stage of the research project, this resulted in a lack of time to complete FEA studies for all of the tests performed.

The findings in this FEA research provide an initial step in modelling sandwich composites to blast, by incorporating brittle cracking models into the polymeric foam core materials. As shown in Chapter 3 the foam materials fail as a result of combined shear and tensile loading, and the brittle cracking model provides tensile cracking and shear retention properties. As the material model was originally designed for use with concrete, Abaqus Explicit was unable to retain solution stability when cracking occurred due to the low density of foam. For this reason, a study was performed to identify the lowest fracture toughness possible to successfully model the whole response to blast. Fracture took place near the edges across the horizontal centre section, as expected from the air blast test results. Once fracture began the element stiffness reduced and the crack started to propagate, but did not travel very far before the displacement was dominated in the zones where cracking originally took place. This is a major disadvantage of the damage model, as in reality fracture travels across the horizontal section to around the quarter point. This did increase the out-of-plane displacement to closer to the values measured using DIC, so is a suitable first step in modelling brittle damage in the foam cores.

This research topic provided more conclusions with respect to modelling methods than the actual materials simulated, as the accuracy of the damage models was uncertain. The elastic comparison of the SAN M100 and PVC C70.90 sandwich panels showed similar pressure versus impulse failure loci, and the front face-sheet curve was the same in both. In the damage model cases the face-sheet failure loci were the same, but the core failure loci were inaccurate. As a result, it is concluded that the models could be used to predict face-sheet failure incorporating damage in the foam core, but not to draw any conclusions from the foam core

failure mechanism.

Further developments to this modelling system are recommended in the foam core response, and in the interfaces between the foam cores and face-sheets. In developing the FEA models visco-plastic damage was incorporated into the foam material model, as an alternative to the brittle cracking model. The fracture toughness in the plastic damage was assumed to be as low as possible, to encourage a brittle response, but it was found that the threshold for stability in the simulation was greater than with the brittle cracking model. Therefore the brittle cracking model was decided upon from the material models available in Abaqus. With the foam characterisation work began in Chapter 6 a recommended future development is the generation of a user defined material to specify the response of the polymeric foam. This material model could also include the crushable aspect of the foam for high pressure or underwater blast, a model which is already built into Abaqus. The interfacial fracture properties are key to accurately predicting sandwich panel response to air blast, as these regions account for around 50% of the total panel damage. An initial solution would be to define cohesive zones, specifically in the fractured areas if possible, although no work was performed in this area for this project.

7.4 Conclusion

The FEA research performed in this project was intended to develop the modelling method as opposed to providing valuable conclusions on the sandwich composite materials. Only two sandwich composite designs were tested, the SAN M100 foam core and the PVC C70.90 foam core cases subjected to air blast, as detailed in Chapter 3. Pressure versus impulse curves were produced for each sandwich panel, and a set of simulations were performed using elastic parameters, and a set with material models incorporating foam fracture. It was found that implementing foam fracture improved the consistency of face-sheet failure loci, but the foam failure loci became unrealistic. This was expected to be due to the unstable nature of fracture in the foam. The foam fracture began at the horizontal edges and started to propagate towards the centre as expected, but stopped propagating very quickly. This was either due to poor fracture toughness properties or the lack of interfacial

debonding between the face-sheets and core. The fracture toughness of the foam was set to be too high in the simulations, as a realistic value caused the simulation to become unstable and abort. The lowest fracture toughness possible was chosen, to allow the simulation to execute fully.

The future simulation work recommended is to characterise a new user material for the foam, from further characterisation laboratory tests. This would include shear properties as well as crushing under high pressure loads. Furthermore inter-facial fracture properties are recommended between the face-sheets and foam core, as this forms a significant proportion of the damage in air blast tests.

Chapter 8

Conclusions

The goal of the research performed in this project was to better understand the role of foam polymers in the blast response of foam core sandwich composites. The intended use of the sandwich composites is in naval vessels, to withstand blasts from sea mines detonated whilst not in direct contact with the ship hull. As such both air and underwater blast testing was performed. These tests were performed at a DNV GL test site in the Spadeadam Royal Air Force base. The blast tests considered the responses of sandwich panels with stepwise graded density foam cores, increasing in density away from the blast facing side. In the air blast tests, foam polymer types were compared, namely styrene acrylonitrile (SAN); polyvinyl chloride (PVC); and polymethacrylimid (PMI). The SAN foam polymers used in all studies were also characterised in quasi-static and dynamic compression and tension, and the PVC and PMI foam polymers used in the foam material comparison were characterised in quasi-static compression, and quasi-static and dynamic tension. Furthermore, all of the air blast test panels, except for the PMI core sandwich panel, were investigated in three point bending and edgewise compression, to determine their residual properties for continued service of naval vessels after withstanding blast loading. The PMI case was omitted as it had suffered too much damage to be sectioned into residual strength test specimens.

As well as investigating the foam core properties, an air blast test was carried out on a PVC core sandwich panel, with glass fibre reinforced polymer (GFRP) face-sheets, where the front (blast facing) face-sheet contained polypropylene (PP) plies interleaved between the GFRP plies. The intention of this construction was

to prevent through thickness cracking of the front face-sheet, due to the greater strain to failure of the front face-sheet caused by the PP plies.

Face-sheets were also investigated in the underwater blast tests, whereby carbon fibre reinforced polymer (CFRP) face-sheets were incorporated into a stepwise graded core and a single density core, and GFRP face-sheets were also incorporated on a stepwise graded core and a single core. This provided a comparison of the failure mechanisms of the CFRP panels versus the GFRP panels, caused by the dramatic increase in stiffness and strength. Furthermore, it allowed the advantage of using a stepwise graded density core with GFRP face-sheets and CFRP face-sheets to be compared.

8.1 Full Scale Air Blast Testing

Quantitative comparisons of the responses of the SAN, PVC and PMI foam core sandwich panels were performed during air blast with the use of paired high speed cameras for 3D digital image correlation (DIC). SAN and PVC materials are common in foam cores for marine applications and the air blast tests compared the two polymer types. PMI, a foam core material typically found in helicopter blades, was also compared, as it has greater strength and stiffness but is known to be more brittle than SAN and PVC. The maximum out-of-plane displacement of the SAN, PVC and PMI core sandwich panels were 90 mm; 101 mm; and 102 mm respectively. This shows that the SAN core suffered the least amount of damage, and this was further highlighted by the 46 mm maximum pull-out on the rebound of the sandwich panel, compared to the 81 mm and 90 mm pull-out measurements for the PVC and PMI sandwich panels respectively. The damage suffered during blast was also determined by sectioning the sandwich panels and photographing the edges, and the least damaged panel was with the SAN foam core, with 19% of damage over the whole panel, followed by the PVC panel with 40%; and then the PMI panel in which the amount was too great for the sandwich composite to be sectioned. The research objectives for this project expected to explain the different responses of the foam cores to blast loading with the use of dynamic tensile testing, as the shear properties were very similar, so different fracture properties were

expected to be a result of the tensile component of loading. This was achieved in the research project and it was found that the dynamic strain to failure of the PMI 110SL foam was the lowest, followed by the PVC C70.90 foam and then the SAN M100 foam. This corresponds to the damage witnessed in the air blast tests.

The graded density sandwich composite contained a stepwise graded density SAN foam core, with three layers each of 10 mm thickness. Due to triggering problems with the high speed cameras the 30 mm thick SAN M130 foam core sandwich panel to which it was compared revealed no DIC data. The post-blast damage assessment results, however, showed that the graded sandwich panel suffered greater damage than the single core panel. The graded panel showed 14% and the single M130 core panel showed 3.9%. However, this result was not conclusive without displacement results, and both sandwich panels contained no visible face-sheet damage. The out-of-plane displacement of the graded density sandwich panel was 102 mm, and the pull-out was 66 mm. These values are very similar to the 40 mm thick PVC and PMI core sandwich panels tested in the foam polymer comparison, despite being 10 mm thinner. The damage suffered was also significantly less. However, the out-of-plane displacement of the graded sandwich panel was greater than the 40 mm thick SAN M100 case, and the damage suffered was significantly less. The areal densities of the 30 mm thick graded density sandwich panel, the 30 mm thick SAN M130 sandwich panel and the 40 mm thick M100 sandwich panel were 11.57 kg/m^2; 10.86 kg/m^2; and 10.88 kg/m^2 respectively. Therefore the graded density core provided a suitable mass comparison to both panels.

It was hypothesised that the use of a stepwise graded density core in the sandwich panel would cause smoother rear face-sheet displacement due to cracking being encouraged in the lower strength foam layers on the blast side. This was witnessed in the test results and the rear face-sheet displacement profile of the graded core sandwich panel was much smoother than the single core cases. This is a positive result as it indicates that rear face-sheet damage is less likely as there are no regions of high strain.

The PVC foam core sandwich panel containing PP plies in the front face-sheet deflected less initially, and in pull-out than the identical sandwich panel containing no PP plies. The initial out-of-plane displacement of the compliant PP face-sheet panel was 90 mm, and the pull-out was 101 mm. However, this was likely to

be caused by the added flexural stiffness afforded by the thicker front face-sheet. The results of interest, however, were the very similar amount of damage suffered in each case. The compliant PP sandwich panel suffered 36% damage, and the comparison panel suffered 40%. The compliant PP sandwich panel suffered no front face-sheet cracking, unlike the PVC panel with only GFRP plies on the front-face-sheet. The deflection of the PP face-sheet panel was less, so this reduced the front face-sheet strain, but with high localised bending caused by core cracking it was expected that front face-sheet cracks occurred. However, these cracks in the GFRP were likely to be hidden by the undamaged PP plies. This is a positive result for naval engineering, because if the PP layers were present on a ship hull which was subjected to a large enough blast to fracture the front GFRP face-sheet, integrity of the face-sheet would be maintained such that water would not ingress into the sandwich structure.

8.2 Strength After Blast Testing

In order to determine the capabilities of the various sandwich constructions to continue in reduced service, after withstanding air blast loading, strength after blast tests were performed. The tests were performed on the 40 mm thick SAN core and PVC core sandwich panels used in the polymer comparison; the 30 mm thick graded core and M130 SAN core sandwich panels; and the PVC core sandwich panel containing PP fibres in the front face-sheet. The first study used a three point bending test setup, to assess the post-blast flexural properties of the sandwich panels, as a significant portion of the loading on a ship hull is from water on the side from buoyancy and waves. The lateral loading from the water on the ship hull is always dynamic due to wave slamming and the vertical movement of the ship as it travels over swells. Due to a lack of available test samples, it was decided to test the flexural samples in medium and high rates only, with no quasi-static tests being performed, except for in the rate sensitivity studies. This is due to the fact that the sandwich composites only exhibited rate sensitivity between quasi-static and dynamic test rates when no damage was present, and when there was no damage there was no rate sensitivity at all. It was therefore deemed unnecessary to test

damaged specimens in a quasi-static manner. The three point bending test results showed that with damage present, the sandwich panels showed no sensitivity to the amount of damage, in terms of flexural strength and flexural stiffness. All four sandwich panels tested displayed a damaged bending stiffness drop to around 8%, and a shear strength drop to around 15%. The shear strengths and face-sheet strengths in every damaged sample across the panel constructions were very consistent, with the only visible damage in stiffness properties. It was found that between the PVC and SAN foam core sandwich panels tested in the polymer foam comparison, the PVC sandwich panel retained higher shear and bending stiffness values, and the damaged shear and bending properties of the PVC sandwich panel with PP plies were lower than the PVC panel without PP plies. There was also found to be no benefit on residual properties from using a graded density foam core, as the shear and bending stiffness values reduced by the same amount as in the single density core cases.

The edgewise compression tests performed in the residual properties investigation were performed at quasi-static and dynamic rates. In edgewise compression the quasi-static properties were of high importance as the ship hull supports the weight of the vessel in the water, at the vertical section of the hull near the top of the cross-section. Medium rates were also tested as it was important to understand the performance of the composites when moving through the water, which causes oscillatory loading in edgewise compression. Due to the high loads required to perform these tests, machines were not available to perform tests above a medium rate, although high rate tests would have been beneficial due to large amplitudes of movements of ships in rough conditions.

In flexural testing it was found that the critical damage mechanism to cause a reduction in strength and stiffness was debonding of the face-sheets from the foam core. This decoupled the face-sheets, meaning that shear loads were not transmitted between them, greatly reducing the stiffness and strength. In edgewise compression the critical damage mechanism was more dependent on the distribution of debonding and cracks. The foam acted as an anti-buckling guide for the face-sheets, so the greater the length of face-sheets that is able to bow outwards, whether through core cracks or debonding, the more detrimental the effect of the damage on the residual properties.

8.3 Full Scale Underwater Blast Testing

Underwater blast testing was performed to assess the effect of implementing a stepwise graded density foam core, and to find out if this effect was greater with carbon fibre or glass fibre face-sheets. The underwater blast tests used a 1.0 kg plastic explosive 4 (PE4) charge, which had a TNT-equivalence of 1.3 kg, situated at 1 m from the front face-sheet of the sandwich panels. The responses of the sandwich panels to blast were recorded using electronic strain gauges on the front and rear face-sheets, and the panels were backed with air in a steel frame. The strain gauge data was interpolated across the thickness and over one quarter of each panel to calculate the central displacement, which provided the most useful comparison of the resistance of the sandwich constructions to blast.

It was found that the use of a graded density foam core reduced the central displacement of both the GFRP and CFRP sandwich panels. This was expected to be due to a mixture of greater energy absorption in crushing the graded core compared to the single core (123 kJ and 118 kJ respectively), and the fact that the bending response was smoothed by the progressive crushing of the panel. The bending of the sandwich panels began in the centre and the bending wave moved out to the boundaries. If the bending response was smoothed due to crushing of the lower density foam at the front, the bending wave would reach the edges with less central deflection, and due to the close proximity of the charge this would cause fracture at the edges. This is a positive result for the use of graded density foams as the greater energy absorption and slower response can be used when designing ship hulls, to mitigate bending of the hull which is the most likely cause of catastrophic damage.

In the comparison of CFRP versus GFRP face-sheets, the increased stiffness of CFRP caused the central deflection to be much lower, as the bending moment reached the boundaries with less central deflection. This caused the effect of the graded density core to be much more exaggerated due to the combined effect of the stiffness and the energy absorption in core crushing.

Overall it was concluded that a CFRP sandwich panel with a graded foam core would mitigate blast damage the most, and it would be beneficial to perform tests with varying panel sizes to assess the effect on boundary failure.

8.4 Foam Characterisation

The polymeric foam materials used in this research were characterised in quasi-static and dynamic compression, and quasi-static and dynamic tension. Quasi-static tests were performed to get the full strain response of the foams, and to compare to manufacturer data. It was then possible to reconstruct dynamic data to match the general strain response of the quasi-static data.

The tensile tests provided the elastic moduli of the foams, and the stress and strains at which they fractured. These were then used to inform the various fracture properties of the foams in the air blast tests, and to provide the inputs to the finite element simulations of the air blast tests. It was found that the tensile stress and strain to failure of the SAN M100 and PVC C70.90 foams were similar at around 4%, and the strain to failure of the PMI 110SL foam was around 2%. This explains why the PMI 110SL core sandwich panel suffered significantly more damage during blast than the PVC C70.90 and SAN M100 core sandwich panels. Furthermore, the fracture stress of the SAN M200 foam was significantly greater than the SAN M100 and SAN M130 foams, explaining why the back face-sheet displacement in the graded density core sandwich panel was much smoother than the single density case, as cracks were encouraged at the front of the sandwich panel.

A novel high speed split-Hopkinson pressure bar system was designed for testing the SAN M100, SAN M130 and SAN M200 foams used in the underwater blast tests. These tests were developed due to the extremely high strain rates present in the foams during underwater blast, in the order of 50,000 s^{-1}. However, the maximum strain rate achieved with a SHPB was 3,000 s^{-1}, so significantly less than that required to accurately capture the strain rates witnessed in underwater blast. From these tests, and the cell collapse and densification strains determined in the quasi-static compression tests, it was possible to construct a full dynamic compression curve for the three polymeric foams. This allowed the energy absorbed during blast to be estimated, and would also be useful in crushable foam models in Abaqus, to successfully model the response of the materials to underwater blast loading using finite element analysis (FEA).

8.5 Finite Element Modelling

FEA models were created as part of this research project, to simulate the response of the sandwich panels to air blast loading. As this was the final stage of the project to be completed time constraints resulted in only the SAN M100 single core sandwich panel, and the PVC C70.90 single core sandwich panel being modelled. The brittle cracking material model was utilised in Abaqus for simulating fracture in the foam core, and this helped to accurately predict the failure of the face-sheets under air blast loading. The actual fracture mechanism of the core, however, was fairly inaccurate due to the lack of interfacial debonding properties between the face-sheets and core, and an unrealistically high fracture toughness of the foam core. The high fracture toughness was implemented to allow the simulation to retain stability throughout, as the low foam density caused excessive deformation upon fracture.

The simulations performed were used to produce pressure versus impulse failure loci of the two face-sheets and the foam core. This was achieved by simulating charge sizes of 10 kg, 30 kg, 100 kg, 500 kg and 1000 kg at increasing stand-off distances, and then using a MATLAB script to determine the combination at which the sandwich panel was closest to failure. This produced coarse failure plots, but provided an initial assessment into the method of predicting damage for various charge size and stand-off distance combinations.

The recommended future developments in FEA of blast loaded sandwich composites is to further characterise the polymeric foam materials in the laboratory, to generate a user defined material. This would correctly predict failure under all loading conditions, and incorporate the correct fracture toughness of the polymeric foam. Furthermore, interfacial properties between the face-sheets and foam core should be implemented, as this debonding forms around 50% of the sandwich panel damage.

8.6 Future Work

The research performed in this project has contributed to the understanding of sandwich composite panel responses to air and underwater blast, and progress has been made in quantifying these responses with characterisation techniques.

Experimental laboratory work recommended for the future is to characterise the polymeric foam materials in quasi-static and high speed shear, and in quasi-static and high speed hydrostatic tension and compression. This will provide a full hydrostatic versus deviatoric response of the materials, which would be very beneficial in finite element and analytical modelling. It is also recommended that medium rate testing is performed, as the test results show that there is a change in material properties between quasi-static and dynamic speeds, but there is little rate sensitivity at dynamic rates. Therefore it would be beneficial to assess this change in properties over the medium strain rate range.

Progress in air and underwater blast testing could be made by placing electronic strain gauges inside the foam core of the sandwich panels, and between the foam core and face-sheets. This would provide information on the through thickness response of the sandwich panels to blast. In underwater blast tests, it would be very beneficial to perform digital image correlation, using a structurally sufficient air-tight box in which to house the high speed cameras. Another high speed camera focussed on the front of the sandwich panels would also be useful for quantifying cavitation during blast loading. In air blast loading a single panel test cubicle is recommended, to prevent asymmetry of the panel deflection. In underwater blast loading electronic strain gauges should be placed in the other quadrants simply to check for any asymmetry in the sandwich panels response, as the calculations performed in this research project relied upon symmetric loading of the sandwich panel. It would also be beneficial to situate the charge further away from the sandwich panel, to cause less catastrophic damage. Finally, computerised tomography scanning of the sandwich panels after blast would provide a more in-depth assessment of the damage present in the sandwich panels, after both air and underwater blast loading. This would allow the residual properties of the sandwich panels to be assessed against better quantified damage assessments.

Multiple loading is an area of proposed further research, to assess the residual

properties of the sandwich panels in response to blast loading. This would add to the residual strength properties calculated in this research, as it would assess if the panels could withstand a second blast, as well as assessing continued service capabilities as shown in this project.

A major area for progress in this research is in FEA. Material characterisation and full scale blast testing is both expensive and time consuming, and the ultimate goal is to reliably simulate the responses of the sandwich materials in real-life situations. The findings presented in this thesis provide material properties to generate FEA models with, and blast response results for validation of the simulation results. Initial FEA modelling was performed for air blast, in which damage was incorporated using an in-built Abaqus brittle cracking damage model. If the foam materials were characterised further a user defined material could be generated to simulate the material responses more accurately. This could include fracture, yield and crushing properties, as well as properties for the foam materials in a crushed state.

Once reliable finite element models are created, these can be fully validated against the results of full scale air and underwater blast tests. It would then be possible to vary the charge sizes and stand-off distance, as studied in this research project, but to also assess the effect of the response from changing the boundary conditions and sandwich panel geometries. It would also be possible to begin to construct models of actual ship hulls, including any reinforcements and the response to blast with other loads present such as wave slamming and the weight of the vessel.

8.7 Research Impact

This research project has investigated the benefits of using a graded density core, as proposed by Gardner, Wang and Shukla [109], when subjected to air and underwater blast loads. As expected, a stepwise graded core absorbs more energy in core compression under a high peak pressure underwater blast load, but it was also discovered that a much smoother rear face-sheet deflection is witnessed when the peak pressure is not great enough to cause core crushing. This is due to a higher

concentration of core cracks in the lower density foam materials on the blast side of the sandwich panel, so fewer cracks propagating to the rear of the sandwich panel.

A quantitative comparison of three foams commonly used in sandwich constructions was also provided, with SAN, PVC and PMI considered. It was found that the SAN foam outperformed the other two both in the air blast test results and in foam characterisation, with a greater strain to failure in tensile loading. This is an important property as fracture of the foam inside of a sandwich panel should be prevented where possible, to prevent high levels of localised bending in the sandwich panel, causing face-sheet fracture.

In order to better understand the energy absorbing characteristics of the foams when subjected to underwater blast, the three densities of SAN foams were tested in a SHPB. The SHPB used a hollow aluminium transmission bar to amplify the low energy transmitted pulse, and semi-conductor strain gauges to capture the very low transmitted strains. A high speed camera was also used as a secondary check for stress equilibrium, as the high noise of the transmitted pulse made it difficult to check for equilibrium by comparing the stress levels at each end of the specimen.

In the underwater blast tests presented in this project, a novel method of calculating the out-of-plane displacement of the sandwich panel using electronic strain gauges was developed. The average strain of the whole sandwich panel was measured from the strain at the same location on the front and rear face-sheet, and this was used to calculate the in-plane membrane strain of the sandwich panel, and as such the out-of-plane displacement. With this method, it was found that a graded density core reduced the central displacement of the sandwich panels dramatically, especially when CFRP face-sheets are used.

Finite element simulations were developed in this research project, using a brittle cracking model for predicting fracture of the foam core materials when simulating the air blast tests. The brittle cracking model was found to predict the onset of core damage well, but crack propagation was poor, resulting in less overall damage in the simulations than measured in the tests. The FEA research highlighted the necessity to incorporate debonding into the sandwich panels, but the core cracking model was useful to predict the onset of face-sheet damage.

The research presented in this thesis has contributed to the overall portfolio of potential composite constructions for use in naval vessels. The outcomes have shown that the use of a graded density core can protect the rear face-sheet from localised bending strains, and absorb a significant amount of blast energy due to incremental crushing and wave attenuation at the boundaries. The use of compliant fibre plies in the front face-sheet can also be used to prevent water ingress into the sandwich panel, even in the presence of heavy core and face-sheet damage. Overall, the findings have provided a qualitative comparison of various sandwich constructions to blast, and have provided mechanical properties of core materials, and of sandwich specimens with blast damage present. It is expected that the documented results could be used to develop numerical or analytical simulations from the mechanical properties presented, and use the full scale air and underwater results to validate the models for use in the design of a whole naval vessel. Furthermore, laboratory test methods have been developed for characterising foams and for quantifying residual properties of sandwich composites after blast, and advancements have been made in instrumentation for underwater blast testing.

References

[1] Defencyclopedia, The Ultimate Defence Encyclopedia. The ultimate showdown: (part-1) Arleigh Burke V/S Daring Class destroyers, 2015. URL https://defencyclopedia.com/2015/07/10/the-ultimate-showdown-part-1-arleigh-burke-vs-daring-class-destroyers/. Online, accessed June 2016. xiii, 3

[2] N. Crusham. Royal Navy Type 45 destroyer HMS Diamond, 2011. URL http://www.defenceimagery.mod.uk/fotoweb/fwbin/download.dll/45153802.jpg. Online, accessed June 2016. xiii, 3

[3] A. Boydston. Monthly feature, Zumwalt Class destroyer progression, 2014. URL http://liftndrag.blogspot.co.uk/2014/09/monthly-feature-zumwalt-class-destroyer.html. Online, accessed June 2016. xiii, 3

[4] J. Keller. Navy consideration of scrapping third ship of Zumwalt-class destroyer doesn't come as a surprise, 2015. URL http://www.militaryaerospace.com/articles/2015/09/zumwalt-class-destroyer.html. Online, accessed June 2016. xiii, 3

[5] E. W. Andrews and N. A. Moussa. Failure mode maps for composite sandwich panels subjected to air blast loading. *International Journal of Impact Engineering*, 36(3):418–425, 2009. xxvii, 25, 40, 42, 43

[6] Photron. FASTCAM SA1.1 specifications, . URL http://photron.com/

high-speed/cameras/fastcam-sa1-1/. Online, accessed September 2013. xxvii, 50

[7] Photron. FASTCAM SA5 specifications, . URL http://photron.com/high-speed/cameras/fastcam-sa5/. Online, accessed September 2013. xxvii, 50

[8] S. Bartlett and B. Jones. Composite ship structures. In *ASNE Day 2013*. www.navalengineers.org, Crystal City, 2013. 2

[9] www.naval-technology.com. Hamina Class, Finland, . URL http://www.naval-technology.com/projects/haminaclass/. Online, accessed June 2016. 2

[10] www.naval-technology.com. Skjold Class missile fast patrol boats, Norway, . URL http://www.naval-technology.com/projects/skjold/. Online, accessed June 2016. 2

[11] Mitch, D. Ada class corvettes of the Turkish Navy, 2015. URL http://navalanalyses.blogspot.co.uk/2015/06/ada-class-corvettes-of-turkish-navy.html. Online, accessed June 2016. 2

[12] Cobham Antenna Systems. Composite technologies from Cobham Antenna Systems. URL https://www.cobham.com/media/879571/cob_m09_composite_technologies_fa_v1.pdf. Online, accessed June 2016. 2

[13] www.naval-technology.com. US Navys DDG 1000 vessel receives composite deckhouse from HII, 2012. URL http://www.naval-technology.com/news/newsus-navys-ddg-1000-vessel-receives-composite-deckhouse-from-hii. Online, accessed June 2016. 3

[14] L. Carlsson and G. Kardomateau. *Structural and failure mechanisms of sandwich composites*. Springer, Dordrecht, first edition, 2011. ISBN 9781402032240. 5

[15] P. D. Smith and J. G. Hetherington. *Blast and ballistic loading of structures*. Butterworth-Heinemann Ltd, Oxford, first edition, 1994. ISBN 0750620242. 14, 40, 41, 137

[16] H. Arora, P. A. Hooper, and J. P. Dear. Dynamic response of full-scale sandwich composite structures subject to air-blast loading. *Composites Part A: Applied Science and Manufacturing*, 42(11):1651–1662, 2011. 14

[17] H. Arora, P. A. Hooper, and J. P. Dear. The effects of air and underwater blast on composite sandwich panels and tubular laminate structures. *Experimental Mechanics*, 52(1):59–81, 2011. 14

[18] H. Arora, P. A. Hooper, P. Del Linz, H. Yang, S. Chen, and J. P. Dear. Modelling the behaviour of composite sandwich structures when subject to air-blast loading. *The International Journal of Multiphysics*, 6(3):199–218, 2012. 15, 32, 131

[19] M. Kelly, H. Arora, and J. P. Dear. Blast resistance of polymeric composite sandwich structures. In P. W. R. Beaumont, C. Soutis, and A. Hodzic, editors, *Structural Integrity and Durability of Advanced Composites*, chapter 20, pages 513–538. Woodhead Publishing, London, first edition, 2015. ISBN 978-0-08-100137-0. 15

[20] S. A. Tekalur, K. Shivakumar, and A. Shukla. Mechanical behavior and damage evolution in E-glass vinyl ester and carbon composites subjected to static and blast loads. *Composites Part B: Engineering*, 39(1):57–65, 2008. 15

[21] J. LeBlanc, A. Shukla, C. Rousseau, and A. E. Bogdanovich. Shock loading of three-dimensional woven composite materials. *Composite Structures*, 79 (3):344–355, 2007. 15

[22] S. A. Tekalur, A. E. Bogdanovich, and A. Shukla. Shock loading response of sandwich panels with 3-D woven E-glass composite skins and stitched foam core. *Composites Science and Technology*, 69(6):736–753, 2009. 15

[23] N. Gardner, E. Wang, P. Kumar, and A. Shukla. Blast mitigation in a sandwich composite using graded core and polyurea interlayer. *Experimental Mechanics*, 52(2):119–133, 2011. 15

[24] E. Wang, N. Gardner, and A. Shukla. The blast resistance of sandwich composites with stepwise graded cores. *International Journal of Solids and Structures*, 46(18-19):3492–3502, 2009. 16, 31

[25] S. A. Tekalur, A. Shukla, and K. Shivakumar. Blast resistance of polyurea based layered composite materials. *Composite Structures*, 84(3):271–281, 2008. 16

[26] E. Wang and A. Shukla. Blast performance of sandwich composites with in-plane compressive loading. *Experimental Mechanics*, 52(1):49–58, 2011. 16

[27] N. Gardner, S. Gupta, E. Wang, and A. Shukla. Blast response of sandwich composites: effect of core gradation, pre-loading, and temperature. In A. Shukla, Y. D. S. Rajapakse, and M. E. Hynes, editors, *Blast Mitigation*, pages 279–330. Springer New York, 2014. ISBN 978-1-4614-7266-7. 16

[28] J. LeBlanc and A. Shukla. Dynamic response and damage evolution in composite materials subjected to underwater explosive loading: An experimental and computational study. *Composite Structures*, 92(10):2421–2430, 2010. 16

[29] F. Latourte, D. Grégoire, D. Zenkert, X. Wei, and H. D. Espinosa. Failure mechanisms in composite panels subjected to underwater impulsive loads. *Journal of the Mechanics and Physics of Solids*, 59(8):1623–1646, 2011. 16

[30] A. P. Mouritz. Ballistic impact and explosive blast resistance of stitched composites. *Composites Part B: Engineering*, 32(5):431–439, 2001. 17

[31] T. J. Cloete and G. N. Nurick. Blast tube loading of plates using an instrumented ballistic pendulum. In *proceedings of the IMPLAST 2010 Conference*. Society for Experimental Mechanics, 2010. 17

[32] G. N. Nurick, G. S. Langdon, Y. Chi, and N. Jacob. Behaviour of sandwich panels subjected to intense air blast Part 1: Experiments. *Composite Structures*, 91(4):433–441, 2009. 17

[33] S. Chung Kim Yuen and G. N. Nurick. Experimental and numerical studies on the response of quadrangular stiffened plates. Part I: subjected to uniform blast load. *International Journal of Impact Engineering*, 31(1):55–83, 2005. 17

[34] G. S. Langdon, S. Chung Kim Yuen, and G. N. Nurick. Experimental and numerical studies on the response of quadrangular stiffened plates. Part II: localised blast loading. *International Journal of Impact Engineering*, 31(1): 85–111, 2005. 17

[35] G. S. Langdon, Y. Chi, G. N. Nurick, and P. Haupt. Response of GLARE panels to blast loading. *Engineering Structures*, 31(12):3116–3120, 2009. 17

[36] G. S. Langdon, D. Karagiozova, C. J. Von Klemperer, G. N. Nurick, A. Ozinsky, and E. G. Pickering. The air-blast response of sandwich panels with composite face sheets and polymer foam cores: Experiments and predictions. *International Journal of Impact Engineering*, 54:64–82, 2013. 17, 27

[37] F. Zhu, L. Zhao, G. Lu, and Z. Wang. Deformation and failure of blast-loaded metallic sandwich panels - experimental investigations. *International Journal of Impact Engineering*, 35(8):937–951, 2008. 17

[38] F. Zhu, Z. Wang, G. Lu, and L. Zhao. Analytical investigation and optimal design of sandwich panels subjected to shock loading. *Materials & Design*, 30(1):91–100, 2009. 17

[39] J. Shen, G. Lu, Z. Wang, and L. Zhao. Experiments on curved sandwich panels under blast loading. *International Journal of Impact Engineering*, 37 (9):960–970, 2010. 18

[40] D. A. Kakogiannis, D. Van Hemelrijck, J. Wastiels, J. Van Ackeren, S. Palanivelu, W. Van Paepegem, J. Vantomme, G. N. Nurick, and S. C. Kim Yuen. Experimental and numerical study of pultruded composite tubes

under blast loading. In *proceedings of DYMAT 2009 - 9th International Conferences on the Mechanical and Physical Behaviour of Materials under Dynamic Loading*, pages 1677–1683. EDP Sciences, 2009. 18

[41] D. D. Radford, V. S. Deshpande, and N. A. Fleck. The use of metal foam projectiles to simulate shock loading on a structure. *International Journal of Impact Engineering*, 31(9):1152–1171, 2005. 18

[42] V. S. Deshpande, A. Heaver, and N. A. Fleck. An underwater shock simulator. *Proceedings of the Royal Society A: Mathematical, Physical and Engineering Sciences*, 462(2067):1021–1041, 2006. 18

[43] G. Caprino and R. Teti. Impact and post-impact behavior of foam core sandwich structures. *Composite Structures*, 29(1):47–55, 1994. 18

[44] G. Caprino, R. Teti, and I. de Iorio. Predicting residual strength of pre-fatigued glass fibre-reinforced plastic laminates through acoustic emission monitoring. *Composites Part B: Engineering*, 36(5):365–371, 2005. 19

[45] P. H. Bull and F. Edgren. Compressive strength after impact of CFRP-foam core sandwich panels in marine applications. *Composites Part B: Engineering*, 35(6-8):535–541, 2004. 19

[46] D. Zenkert, A. Shipsha, P. H. Bull, and B Hayman. Damage tolerance assessment of composite sandwich panels with localised damage. *Composites Science and Technology*, 65(1516):2597–2611, 2005. 20th Anniversary Special Issue. 19

[47] F. Edgren, L. E. Asp, and P. H. Bull. Compressive failure of impacted NCF composite sandwich panels - characterisation of the failure process. *Journal of Composite Materials*, 38(6):495–514, 2004. 19

[48] H. Arora, M. Kelly, A. Worley, P. Del Linz, A. Fergusson, P. A. Hooper, and J. P. Dear. Compressive strength after blast of sandwich composite materials. *Philosophical Transactions of the Royal Society of London A: Mathematical, Physical and Engineering Sciences*, 372(2015), 2014. 19

[49] T. E. Lacy and Y. Hwang. Numerical modeling of impact-damaged sandwich composites subjected to compression-after-impact loading. *Composite Structures*, 61(1-2):115–128, 2003. 20

[50] Z. Xie, A. J. Vizzini, and M. Yang. On residual compressive strength prediction of composite sandwich panels after low-velocity impact damage. *Acta Mechanica Solida Sinica*, 19(1):9–17, 2005. 20

[51] P. N. B. Reis, J. A. M. Ferreira, P. Santos, M. O. W. Richardson, and J. B. Santos. Impact response of kevlar composites with filled epoxy matrix. *Composite Structures*, 94(12):3520–3528, 2012. 20

[52] P. N. B. Reis, J. A. M. Ferreira, Z. Y. Zhang, T. Benameur, and M. O. W. Richardson. Impact response of kevlar composites with nanoclay enhanced epoxy matrix. *Composites Part B: Engineering*, 46:7–14, 2013. 20

[53] F. Sarasini, J. Tirill, M. Valente, L. Ferrante, S. Cioffi, S. Iannace, and L. Sorrentino. Hybrid composites based on aramid and basalt woven fabrics: Impact damage modes and residual flexural properties. *Materials & Design*, 49:290–302, 2013. 20

[54] G. A. O. Davies, D. Hitchings, T. Besant, A. Clarke, and C. Morgan. Compression after impact strength of composite sandwich panels. *Composite Structures*, 63(1):1–9, 2004. 20

[55] P. Wang, F. Pierron, and O. T. Thomsen. Identification of material parameters of PVC foams using digital image correlation and the Virtual Fields Method. *Experimental Mechanics*, 53(6):1001–1015, 2013. 21

[56] Dassault Systemes. Crushable foam plasticity models. In *Abaqus Analysis User's Manual*, chapter 22.3.5. Providence, 6.11 edition, . 22

[57] P. Viot. Hydrostatic compression on polypropylene foam. *International Journal of Impact Engineering*, 36(7):975–989, 2009. 22

[58] V. S. Deshpande and N. A. Fleck. Multi-axial yield behaviour of polymer foams. *Acta Materialia*, 49(10):1859–1866, 2001. 22

[59] R. C. Ostergaard, B. F. Sorensen, and P. Brondsted. Measurement of interface fracture toughness of sandwich structures under mixed mode loadings. *Journal of Sandwich Structures and Materials*, 9(5):445–466, 2007. 22

[60] W. J. Cantwell and P. Davies. A test technique for assessing core-skin adhesion in composite sandwich structures. *Journal of materials science letters*, 13:203–205, 1994. 22

[61] A. Patra and N. Mitra. Interface fracture of sandwich composites: Influence of MWCNT sonicated epoxy resin. *Composites Science and Technology*, 101: 94–101, 2014. 22

[62] A. Hernández-Pérez, F. Avilés, and L. A. Carlsson. Evaluation of the plate twist test to characterize mode III fracture of sandwich panels with a face/core interface crack. *Engineering Fracture Mechanics*, 104:41–55, 2013. 23

[63] F. Avils and L. A. Carlsson. Analysis of the sandwich DCB specimen for debond characterization. *Engineering Fracture Mechanics*, 75(2):153–168, 2008. 23

[64] A. Quispitupa, C. Berggreen, and L. A. Carlsson. Face/core interface fracture characterization of mixed mode bending sandwich specimens. *Fatigue & Fracture of Engineering Materials & Structures*, 34(11):839–853, 2011. 23

[65] M. Manca, C. Berggreen, L. A. Carlsson, and P. Bortolotti. Fatigue characterization of Poly Vinyl Chloride (PVC) foam core sandwich composite using the G-control method. *Journal of Sandwich Structures and Materials*, 2015. ePrint article. 23

[66] C. Lundsgaard-Larsen, B. F. Srensen, C. Berggreen, and R. C. stergaard. A modified DCB sandwich specimen for measuring mixed-mode cohesive laws. *Engineering Fracture Mechanics*, 75(8):2514–2530, 2008. 23

[67] W. Chen, F. Lu, and N. Winfree. High-strain-rate compressive behavior of a rigid polyurethane foam with various densities. *Experimental Mechanics*, 42(1):65–73, 2002. 24

[68] W. Chen, B. Zhang, and M. J. Forrestal. A split Hopkinson bar technique for low-impedance materials. *Experimental Mechanics*, 39(2):81–85, 1999. 24

[69] M. Shazly, Y. Bahei-El-Din, and S. Salem. Characterization of sandwich panels for indentation and impact. *Journal of Physics: Conference Series*, 451(1):1–8, 2013. 24

[70] B. Song and W. Chen. Split Hopkinson pressure bar techniques for characterizing soft materials. *Latin American Journal of Solids and Structures*, 2: 113–152, 2005. 24, 197, 199, 202

[71] B. Song, W. Chen, S. Dou, N. A. Winfree, and J. H. Kang. Strain-rate effects on elastic and early cell-collapse responses of a polystyrene foam. *International Journal of Impact Engineering*, 31(5):509–521, 2005. 24

[72] B. Song, W. Chen, and X. Jiang. Split Hopkinson pressure bar experiments on polymeric foams. *International Journal of Vehicle Design*, 2-3:185–198, 2005. 24

[73] J. M. Lifshitz and H. Leber. Data processing in the split Hopkinson pressure bar tests. *International Journal of Impact Engineering*, 15(6):723–733, 1994. 25, 197

[74] M. S. Hoo Fatt and K. S. Park. Dynamic models for low-velocity impact damage of composite sandwich panels - Part B: damage initiation. *Composite Structures*, 52(3-4):353–364, 2001. 25

[75] M. S. Hoo Fatt and L. Palla. Analytical Modeling of Composite Sandwich Panels under Blast Loads. *Journal of Sandwich Structures and Materials*, 11(4):357–380, 2009. 25

[76] M. S. Hoo Fatt and D. Sirivolu. Blast response of double curvature, composite sandwich shallow shells. *Engineering Structures*, 100:696–706, 2015. 25

[77] R. Li, G. A. Kardomateas, and G. J. Simitses. Nonlinear response of a shallow sandwich shell with compressible core to blast loading. *Journal of Applied Mechanics*, 75(6):1–10, 2008. 25

[78] R. Li and G. A. Kardomateas. Nonlinear high-order core theory for sandwich plates with orthotropic phases. *AIAA Journal*, 46(11):2926–2934, 2008. 25

[79] J. R. McConnell and H. Su. Design of cellular composite sandwich panels for maximum blast resistance via energy absorption. *Applied Composite Materials*, 23(3):375–396, 2016. 26

[80] R. Panciroli and S. Abrate. Dynamic response of sandwich shells to underwater blasts. *Central European Journal of Engineering*, 2(4):509–522, 2012. 26

[81] A. Schiffer and V .L. Tagarielli. The response of circular composite plates to underwater blast: experiments and modelling. *Journal of Fluids and Structures*, 52:130–144, 2015. 26

[82] X. Wei, P. Tran, A. de Vaucorbeil, R. B. Ramaswamy, F. Latourte, and H. D. Espinosa. Three-dimensional numerical modeling of composite panels subjected to underwater blast. *Journal of the Mechanics and Physics of Solids*, 61(6):1319–1336, 2013. 26

[83] R. W. McCoy and C. T. Sun. Fluid-structure interaction analysis of a thick-section composite cylinder subjected to underwater blast loading. *Composite Structures*, 37(1):45–55, 1997. 26

[84] V.A. Phadnis, P. Kumar, A. Shukla, A. Roy, and V. V. Silberschmidt. Optimising curvature of carbon fibre-reinforced polymer composite panel for improved blast resistance: finite-element analysis. *Materials & Design*, 57: 719–727, 2014. 26

[85] S. Li, Z. Wang, G. Wu, L. Zhao, and X. Li. Dynamic response of sandwich spherical shell with graded metallic foam cores subjected to blast loading. *Composites Part A: Applied Science and Manufacturing*, 56:262–271, 2014. 27

[86] S. Li, G. Lu, Z. Wang, L. Zhao, and G. Wu. Finite element simulation of metallic cylindrical sandwich shells with graded aluminum tubular cores subjected to internal blast loading. *International Journal of Mechanical Sciences*, 9697:1–12, 2015. 27

[87] W. Li, G. Huang, Y. Bai, Y. Dong, and S. Feng. Dynamic response of spherical sandwich shells with metallic foam core under external air blast loading - numerical simulation. *Composite Structures*, 116:612–625, 2014. 27

[88] Y. A. Bahei-El-Din, G. J. Dvorak, and O. J. Fredricksen. A blast-tolerant sandwich plate design with a polyurea interlayer. *International Journal of Solids and Structures*, 43(25-26):7644–7658, 2006. 27

[89] L. Librescu, S-Y. Oh, and J. Hohe. Linear and non-linear dynamic response of sandwich panels to blast loading. *Composites Part B: Engineering*, 35 (6-8):673–683, 2004. 27

[90] T. Hause and L. Librescu. Dynamic response of anisotropic sandwich flat panels to explosive pressure pulses. *International Journal of Impact Engineering*, 31(5):607–628, 2005. 27

[91] L. Librescu, S-Y. Oh, and J. Hohe. Dynamic response of anisotropic sandwich flat panels to underwater and in-air explosions. *International Journal of Solids and Structures*, 43(13):3794–3816, 2006. 27

[92] J. Hohe, L. Librescu, and S-Y. Oh. Dynamic buckling of flat and curved sandwich panels with transversely compressible core. *Composite Structures*, 74(1):10–24, 2006. 27

[93] D. Richardson. The fundamental principles of composite material stiffness predictions. *Univeristy of the West of England*. URL https://www.swcompositesgateway.co.uk/Property-Prediction.pdf. Online, accessed Jan 2015. 33

[94] AZoM.com Limited. E-glass fibre. URL http://www.azom.com/article.aspx?ArticleID=764. Online. 36, 134

[95] P. D. Soden, M. J. Hinton, and A. S. Kaddour. Lamina properties, lay-up configurations and loading conditions for a range of fibre-reinforced composite laminates. *Composites Science and Technology*, 58:1011–1022, 1998. 36, 134

[96] Sicomin Epoxy Systems. SR 8500 Versatile epoxy system for composite applications. URL http://www.sicomin.com/datasheets/product-pdf44.pdf. Online. 36, 134

[97] SP Gurit. ST 94 Single sided sprint. URL http://www.gurit.com/files/documents/st94pdf.pdf. Online. 36

[98] Granta Design. Polypropylene (PP). In *CES Edupack 2015*. Cambridge. 36

[99] Innegra Technologies. Composite panel data for FEA modelling. URL http://media.wix.com/ugd/6effc2_d563d1351819461193 90f6adbb27831a.pdf. Online. 36

[100] SPGurit. Gurit Corecell M The Marine Foam. URL http://www.gurit.com/files/documents/guritcorecell-mv8pdf.pdf. 38, 104, 136, 186, 195, 215, 223

[101] 3A Composites. Airex C70 Universal structural foam. URL http://www.airexbaltekbanova.com/downloads.html. Online. 38, 186, 195, 215, 223

[102] Evonik Industries. Technical information Rohacell SL. URL http://www.rohacell.com/sites/lists/PP-HP/Documents/ROHACELL-SL-mechanical-properties-EN.pdf. Online. 38, 186, 195, 215, 223

[103] T. A. Rose. Method of solution. In *Air3d Version 9 User's Guide*, chapter 2, pages 2–6. Cranfield, ninth edition. 39

[104] H. Arora. *Blast loading of fibre reinforced polymer composite structures*. PhD thesis, Imperial College London, 2012. 40, 42

[105] M. A. Sutton, J-J. Orteu, and H. W. Schreier. *Image correlation for shape, motion and deformation measurements*. Springer, Dordrecht, first edition, 2009. ISBN 9780387787466. 48

[106] GOM. Principle of deviation measurements. In *Aramis user manual - Software*, chapter A.5, pages 5–8. Braunschweig, 6.3 edition. 51

[107] ASTM International. ASTM C393/C 393 M - 06 Standard test method for core shear properties of sandwich constructions by beam. 1:1–8. 99, 100, 125

[108] ASTM International. ASTM C364-08 Standard test method for edgewise compressive strength of sandwich constructions. 07(Reapproved):24–31, 2010. 102, 103

[109] N. Gardner, E. Wang, and A. Shukla. Performance of functionally graded sandwich composite beams under shock wave loading. *Composite Structures*, 94(5):1755–1770, 2012. 131, 182, 263

[110] M. L. Minus and S. Kumar. The processing, properties, and structure of carbon fibers. *JOM Journal of the Minerals, Metals and Materials Society*, 57:52–58, 2005. 134

[111] ASTM International. C365-03 Standard test method for flatwise compressive properties of sandwich cores. pages 1–8, 2011. 187

[112] B. J. Butler, C. Bo, A. W. Tucker, A. P. Jardine, W. G. Proud, A Williams, and K. A. Brown. Mechanical and histological characterization of trachea tissue subjected to blast-type pressures. *Journal of Physics: Conference Series*, 500(18):1–6, 2014. 196

[113] C. Bo, A. Williams, S. Rankin, W. G. Proud, and K. A. Brown. Integrated experimental platforms to study blast injuries: a bottom-up approach. *Journal of Physics: Conference Series*, 500(10):1–7, 2014. 196

[114] W. Chen and B. Song. *Split Hopkinson (Kolsky) Bar: Design, Testing and Applications, Mechanical Engineering Series*. Springer, New York, 2011. ISBN 9781441979810. 199

[115] N. Dioh, P. Leevers, and J. Williams. Thickness effects in split Hopkinson pressure bar tests. *Polymer*, 34(20):4230–4234, 1993. 200, 205

[116] L. J. Gibson and M. F. Ashby. *Cellular solids*. Cambridge University Press, Cambridge, 1997. ISBN 9781139878326. 202, 205, 206, 229

[117] ASTM International. ASTM C297/C297M-04 Standard test method for flatwise tensile strength of sandwich constructions. 1:1–6, 2010. 209

[118] Dassault Systemes. Cracking model for concrete. In *Abaqus Analysis User's Manual*, chapter 22.6.2. Providence, 6.11 edition, . 235

A - Digital Image Correlation Contour Plots

This Appendix presents the raw digital image correlation (DIC) contour plots of out-of-plane displacement (U_Z) and maximum principal strain (MPS) for the five air blast tests. The contour plots are presented in Figure A1, and show the data before normalisation in MATLAB.

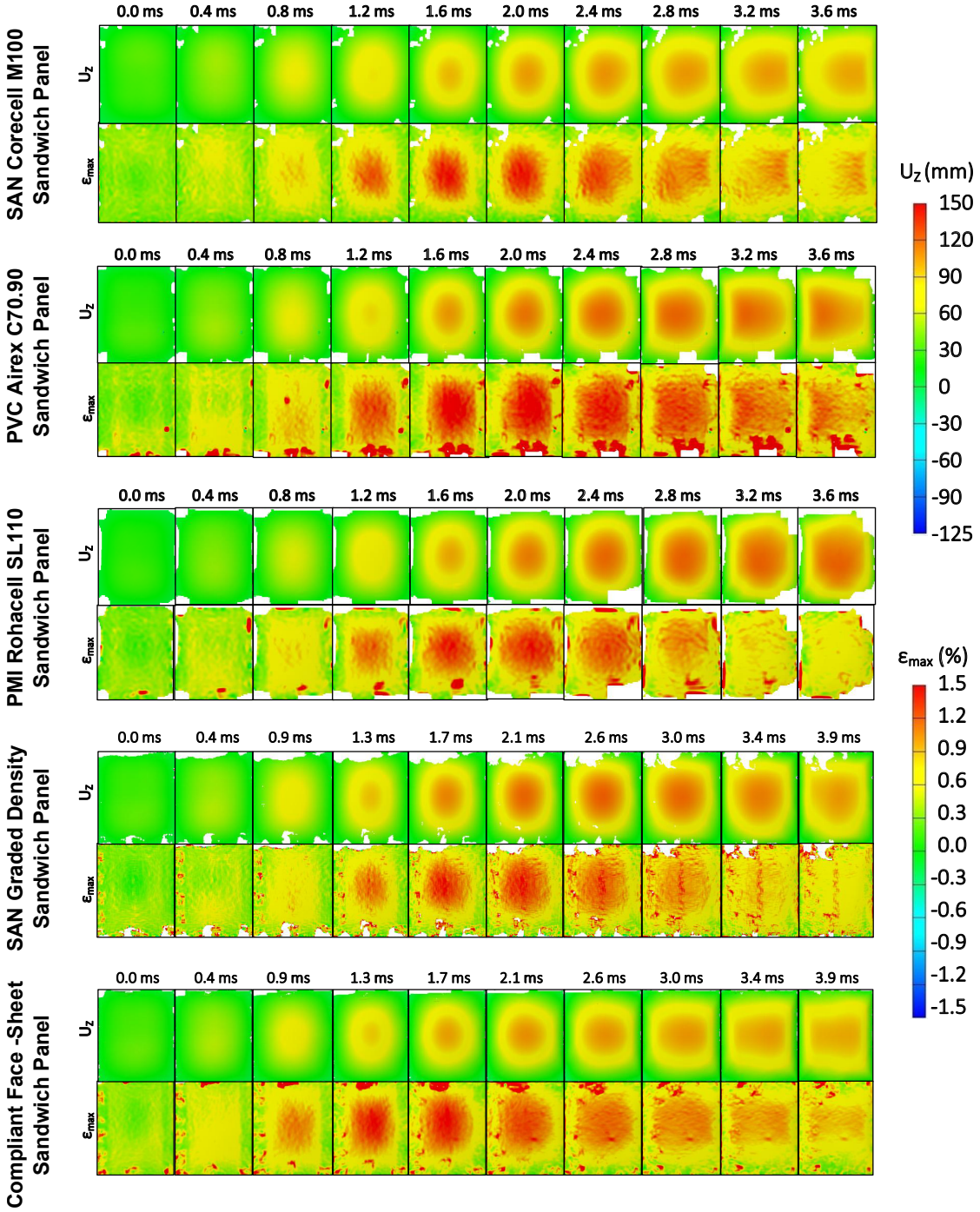


Figure A1: Out-of-plane displacement (U_Z) and maximum principal strain (MPS) DIC contour plots for the five air blasted sandwich panels. The reference to each test panel is shown on the left hand side, and the colour scales are shown on the right hand side.

B - Air Blast Digital Image Correlation Uncertainty Analysis

This appendix provides the uncertainty analysis for the digital image correlation (DIC) used to capture the response of the sandwich panels to air blast loading. The error terms were calculated based on Equation (B1), assuming that κ is a function of ζ, ξ and χ. The symbol "δ" denotes the absolute error term associated with the relevant variable. This Appendix provides the error term derivations for the out-of-plane and in-plane displacement of the sandwich panels. Also provided is a calculation of the uncertainty associated with the core shear strains measured during blast testing. The uncertainty analysis for the energy balance was omitted as the calculations are largely based upon assumptions on the pressure distribution over the sandwich panel during blast, which was determined through simulations.

$$\delta\kappa = \sqrt{\left(\frac{\partial\kappa}{\partial\zeta}\delta\zeta\right)^2 + \left(\frac{\partial\kappa}{\partial\xi}\delta\xi\right)^2 + \left(\frac{\partial\kappa}{\partial\chi}\delta\chi\right)^2} \tag{B1}$$

Digital Image Correlation Uncertainty

The air blast test measurements were all obtained using 3D DIC. The uncertainty associated with the DIC measurements was measured by assessing the noise in the data before the blast wave arrived at the test panel. This was possible from images saved during the pre-trigger from the high speed cameras, and accounts for uncertainty in the DIC calculations as well as errors caused by test factors

such as wind loading the sandwich panel. The quantification of the out-of-plane displacement of the sandwich panels for images captured before the arrival of the blast wave is shown in Figure B1, where the data point numbers have been interpolated from varying numbers of images. From this data a conservative estimate of ± 3.0 mm was concluded for the uncertainty in out-of-plane displacement measurements. The values of uncertainty required for the calculations performed in Chapter 3 were for out-of-plane displacement and in-plane horizontal displacement. The latter was determined using the same method as for the out-of-plane displacement to be ± 0.1 mm.

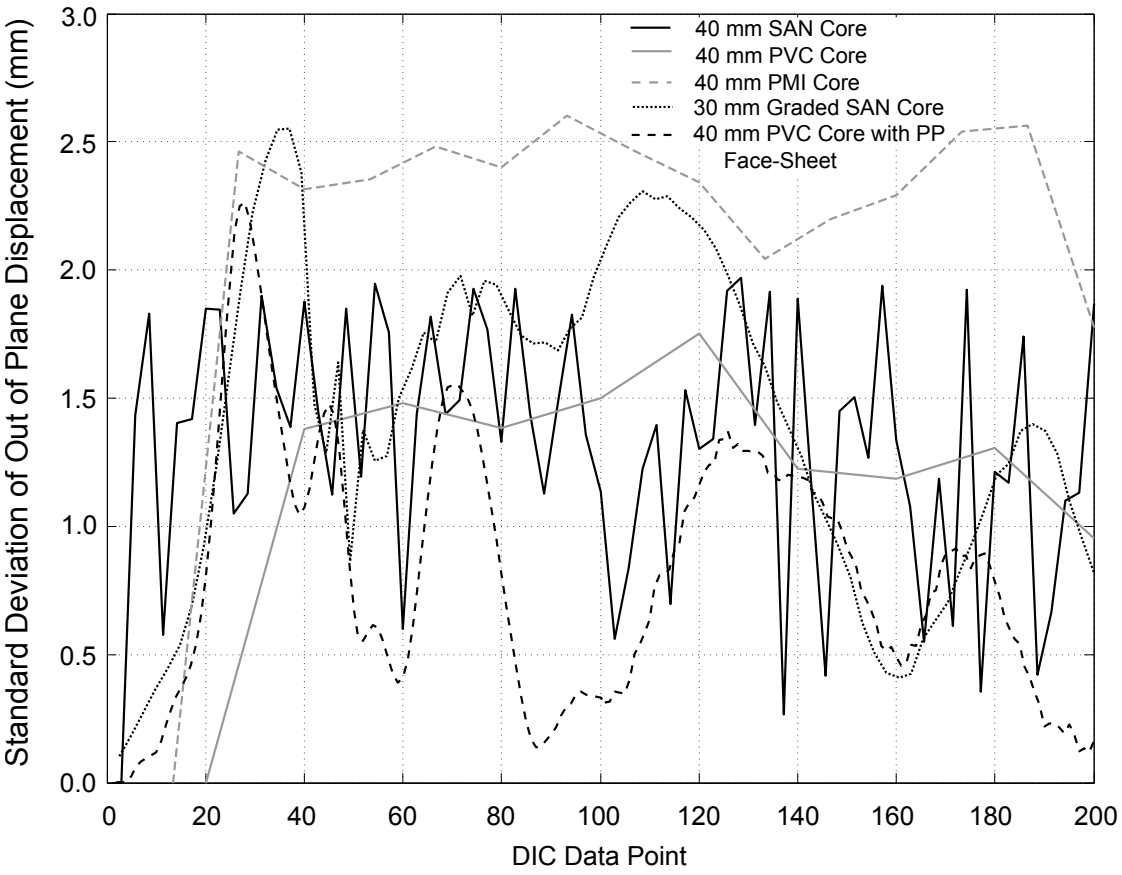


Figure B1: Standard deviation of out-of-plane displacement of the air blast test panels, measured prior to blast wave arrival.

Core Shear Strain

The core shear strain measurements derived from the 3D DIC results were split into α and β, and the error terms for these are shown in Equation (B2) and Equation (B3) respectively, where d is the out-of-plane displacement of a facet, x is the size of the facet (1 mm), h is the thickness of the foam core and Δx is the in-plane horizontal displacement of each facet. The subscript "n" refers to the facet location. When combined these lead to the total shear strain error term ($\delta\gamma$) in Equation (B4). The calculated errors associated with the α component of the shear strain are shown in Figure B2, and it can be seen that at the edges, where fracture occurred, the uncertainty is approximately $\pm$ 1.02°, but $\pm$ 1.06° was assumed for conservatism.

The equation for the error associated with the β component of shear strain, Equation (B3), is insensitive to low values of in-plane displacement (Δx). The error term was always calculated to be $\pm$ 0.005°. This resulted in the overall shear strain uncertainty, $\delta\gamma$, to have a value of $\pm$ 1.065° at the edges where fracture took place.

$$\delta\alpha = \frac{\sqrt{2}\, x\, \delta d}{d_{n+1}^2 + d_{n-1}^2 - 2d_{n+1}d_{n-1} + 4x^2} \tag{B2}$$

$$\delta\beta = \frac{2\, h\, \delta\Delta x}{h^2 + 4\,(\Delta x)^2} \tag{B3}$$

$$\delta\gamma = \delta\alpha + \delta\beta \tag{B4}$$

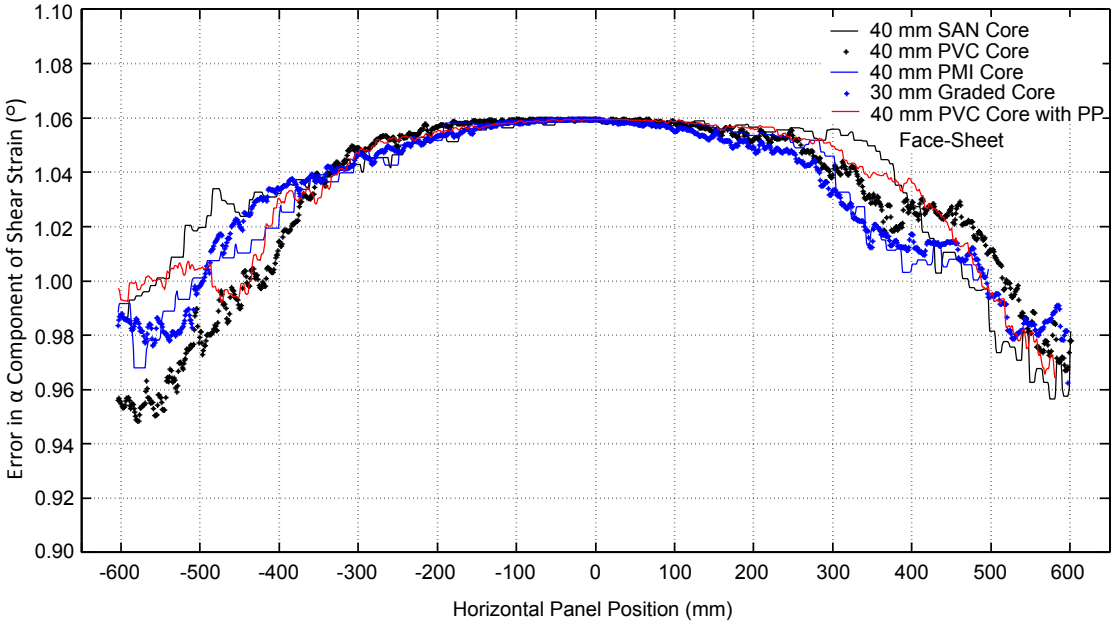


Figure B2: Error calculated in the α component of the shear strain, for each of the five air blast tested sandwich panels, across the horizontal centre section at maximum displacement.